Final Technical Progress Report
Differential Collision Cross-Sections for Atomic Oxygen

Contract NAS8-36955
Delivery Order 48

George C. Marshall Space Flight Center
Space Sciences Laboratory
National Aeronautics and Space Administration
Marshall Space Flight Center, Alabama 35812

by

Dr. Douglas G. Torr
Principal Investigator
The University of Alabama in Huntsville
Center for Space Plasma and Aeronomic Research and Physics Department
Huntsville, Alabama 35899

February 1991

330320
P. 138

NASA
National Aeronautics and Space Administration

Report Documentation Page

1. Report No.

2. Government Accession No.

3. Recipient's Catalog No.

4. Title and Subtitle
Final Technical Progress Report
Differential Collision Cross-Sections for Atomic Oxygen
Delivery Order 48

5. Report Date
February 19, 1991

6. Performing Organization Code

7. Author(s)
Dr. Douglas G. Torr

8. Performing Organization Report No.
OAL91-1

9. Performing Organization Name and Address
The University of Alabama in Huntsville
CSPAR/Physics Department
Research Institute C-10
Huntsville, Alabama 35899

10. Work Unit No.

11. Contract or Grant No.
Contract NAS8-36955
Delivery Order 48

12. Sponsoring Agency Name and Address
George C. Marshall Space Flight Center
Space Science Laboratory
National Aeronautics and Space Administration
Marshall Space Flight Center, Alabama 35812

13. Type of Report and Period Covered
Final Report
7-11-89 to 7-10-90

14. Sponsoring Agency Code

15. Supplementary Notes

16. Abstract
This report covers the technical progress for the duration of this contract (7-11-89 to 7-10-90)

17. Key Words (Suggested by Author(s))
Instrument, Ultraviolet Imaging, Auroral Modeling, Vehicle Contamination, Solar Terrestrail Physics, Chemical Releases

18. Distribution Statement
Unlimited

19. Security Classif. (of this report)
Unclassified

20. Security Classif. (of this page)
Unclassified

21. No. of pages
137

22. Price

Final Report on Delivery Order 48 of NAS8-36955

This contract supported four activities.

1. Differential Collision Cross-Sections

The primary purpose of this effort was to provide on-going support for Dr. Charles Keffer to establish a facility at MSFC for the measurement of differential collision cross-sections of O on N_2 and other gases of relevance to understanding vehicle-environmental contamination effects in orbit.

This work was initiated in 1988 under NAG8-100, entitled "Space Vehicle Contamination Study." During the period 6/1/89 to 11/6/90 the work was funded under D.O. 48, D.O. 59 and NAS8-37586. In June 1990, Dr. Keffer was awarded a grant with himself as Principal Investigator and has continued the work since that time in his own capacity without further assistance from D. G. Torr.

To place the flow of funding in perspective, Table 1 shows the percentage of Dr. Keffer's time charged to the above mentioned contracts in support of the fabrication of the cross-section facility. Also to provide some traceability of progress, we review briefly below the overall chronological evolution of the work, identifying what was specifically accomplished under D.O. 48. Also Dr. Keffer provided weekly written reports on his progress consistently and these are available on file.

The proposed experiments use a 5 eV atomic oxygen beam for differential scattering cross-section measurements. This 5 eV O beam is formed by focussing the output from a high energy pulsed CO_2 laser into the throat of a molecular oxygen nozzle beam source.

NAG8-100

Work on the cross-section facility was initiated under this grant in 1988. The final report on progress made was submitted on November 7, 1989. Essentially the conceptual design for the facility was developed, machining and welding were completed, and documentation generated. Signal to noise ratio estimates were calculated and writing of software for operation of the instrument initiated.

NAS8-37586

This contract supported Dr. Keffer from June 1 through September 30, 1989. During this period the cross-section chamber was assembled, and initial problems with the system debugged. By the end of the 4 month funding period the system was pumped down, but it was discovered that the chamber went out of alignment under vacuum conditions. Work on rectifying this problem was initiated under D.O. 48.

Work Accomplished Under D.O. 48

This phase started with an evaluation of the noise sources in the system, and in correcting the serious alignment problems identified under NAS8-37586.

The correction approach that was adopted was to adjust the assemblies attached to the bellow section. Following the alignment correction, the chamber was successfully aligned under vacuum on one axis. Vent and evacuation cycles were performed for

TABLE 1

FUNDING FLOW FOR CROSS-SECTION FACILITY

CONTRACT	NAS8-36955 D.O. 48	NAS8-36955 D.O. 59	(ISTP) NAS8-37586	NAG8-834 (KEFFER-P.I.)
MONTH	7/9/89 - 7/10/90	11/5/89 - 11/6/90	12/16/88 - 8/30/90	6/90 -
1989	PERCENT	CHARGED	(DR. KEFFER)	
6	0	0	100	0
7	0	0	100	0
8	0	0	100	0
9	0	0	100	0
10	100	0	0	0
11	100	0	0	0
12	100	0	0	0
1990				
1	100	0	0	0
2	0	100	0	0
3	100	0	0	0
4	100	0	0	0
5	0	100	0	0
6	0	100	0	0
7	30	0	0	70
8	0	0	0	100
9	0	100	0	0
10	0	100	0	0
11	0	0	0	100

alignment reproducibility. The alignment of the CO_2 beam was successful to the point of hitting the beam valve aperture with the focussed laser beam. However, the coating for the mirror which reflects the CO_2 laser beam was destroyed because of the high energy density of the beam.

Various materials were tested for CO_2 laser mirrors, and nickel copper mirrors with a gold coating were found to be successful.

Alignment tests were performed on the mass spectrometer housing, and work commenced with thermal scattering measurements. The testing indicated that all critical elements could be aligned. Estimates were made of the accuracy and uncertainty of the alignment. This was the status of the project on January 31, 1990.

During February work continued under D.O. 59. Under D.O. 59 work began on detecting a scattered signal from O_2 on N_2 collisions. However, the signal to noise was poor. Shielding of signal lines corrected the problem.

Work on the system operating software was re-initiated.

Work was started in a pulse mode of operation with crossed beams.

An anomalous result was obtained for the O_2-N_2 beams.

At this point funding was continued under D.O. 48.

The problem causing the anomalous results was identified and corrected and both beams exhibited sharp temporal and spatial profiles.

To increase sensitivity further the filament emission of the mass spectrometer was increased to give a factor of 10 improvement in detection efficiency. Also, the detector aperture was increased.

An anomaly in the results obtained was discovered in early March. This was eventually traced to a grounding problem in the instrument triggering circuit.

Action taken to improve S/N included:

Inhibition of the two pulsed valves controlling the sources of the crossed beams when data is not being taken.

An RF shield for the mass spectrometer data cable was added.

This was the status of the project at the end of April 1990, after which the project was funded under D.O. 59 until Dr. Keffer obtained independent funding to continue the work.

2. Groundbased Scientific Observations of Rocket Releases during NICARE-1

This project utilized the broadband imaging spectrometer referred to as the Compact Spectrometer developed in a colloborative effort with MSFC under NAG8-060. Since the Compact Spectrometer was the only instrument in existence capable of measuring a spectrum simultaneously across the wavelength range 3600 - 11,000 Å, UAH was approached by the Naval Research Labs (NRL) to monitor a rocket launched chemical release experiment in which the emissions of two new chemicals were to be identified. The spectra to be expected were essentially unknown. Thus the need for a broadband spectral imager.

The measurements were made from a naval station at Duck, North Carolina on October 22, 1989. The rocket was launched from Wallops Island, Virginia. Figures 1a show the twilight airglow spectrum recorded prior to launch. Figure 1 is the nightglow spectrum recorded two minutes prior to launch, and Figure 2, the same one minute after the flight. Figure 3 shows the spectral image recorded for 30 seconds immediately prior to the first release, which was a nickel carbonyl release. The natural airglow background has been removed. Figure 4 shows the spectral image recorded for 30 seconds commencing after the nickel carbonyl release. Figure 5 shows the same 60 seconds after the release. Emissions were only observed in the field of view of the mid-visible channel indicating that a sharp edge must characterize the cloud. The emissions appear to be a CO_2 continuum. Figures 6 and 7 respectively show the corresponding spatial distribution of the CO_2 continuum. The narrow width of the emission suggests that the rocket exhaust plume was being observed, and that no emissions from the release were observed. No emission was detected from release 2 which was a trifluromethyl bromide release. Figures 8 and 9 show a blow-up of the two CO_2 spectra.

These data were provided to NRL and the results were presented by Dr. Paul Bernhardt at the Fall 1990 Meeting of the American Geophysical Union. A copy of the printed abstract is attached.

3. Data Compression Study for the UVI

The purpose of this study was to evaluate ways by which the data rate generated by the detector readout could be matched to the telemetry transfer rate to the ground. The main goal was to determine what constraints the science requirements placed on temporal and spatial resolution, because the data rate can be reduced by increasing the CCD on chip integration time and by reducing spatial resolution requirements. Also placement (mapping) of the object dimensions in the image plane, i.e. a round earth on a rectangular image plane provides some additional freedom.

The pixel dimensions of the CCD are $244 \times 550 = 1.342 \times 10^5$ pixels per readout, digitized to 12 bits yields a data rate of 1.5×10^6 bits per readout. If no spatial compression could be tolerated, this would dictate an on-chip integration time of ~134 seconds to match the 12 kbps telemetry rate assigned to the UVI.

An evaluation of auroral dynamical time scales revealed two boundaries in this temporal regime: less than 1 second and greater than several tens of seconds. A thirty second integration time therefore requires a factor of 4.5 additional compression. The desired spatial resolution should be better than 40 km.

A factor of 2 can be obtained by noting that the pixel size of the Thomson TH 7866 CCD is 27 x 16 microns, which yields an undesirable elongated rectangular spatial resolution element. Thus it was decided to sum two of the 16 μm pixels to give a spatial resolution element of 32 x 27 μm as indicated in Figure 3.1. This image is fiber optically mapped from the CCD to the focal plane of the image intensifier as illustrated in Figure 3.2, yielding a focal plane spatial resolution element of 87.4 x 73.7 μm which matches the optical blur spot size of the instrument. The ground spatial resolution

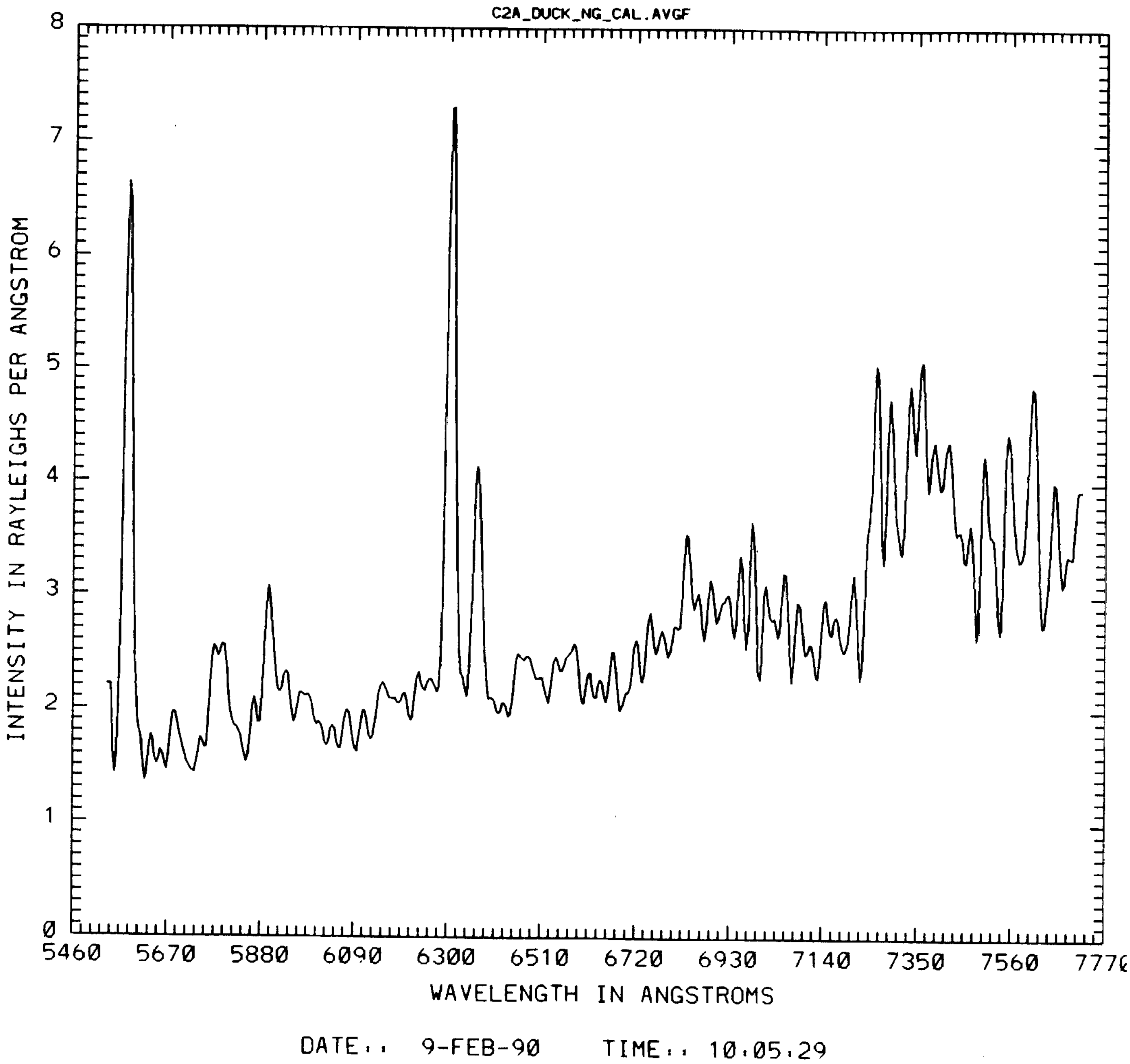

DATE.. 9-FEB-90 TIME.. 10.05.29

Figure 1a: An example of the late twilight spectrum imaged simultaneously by the Compact Spectrometer on October 22, 1989 at Duck, North Carolina at a solar zenith angle of ~108°.

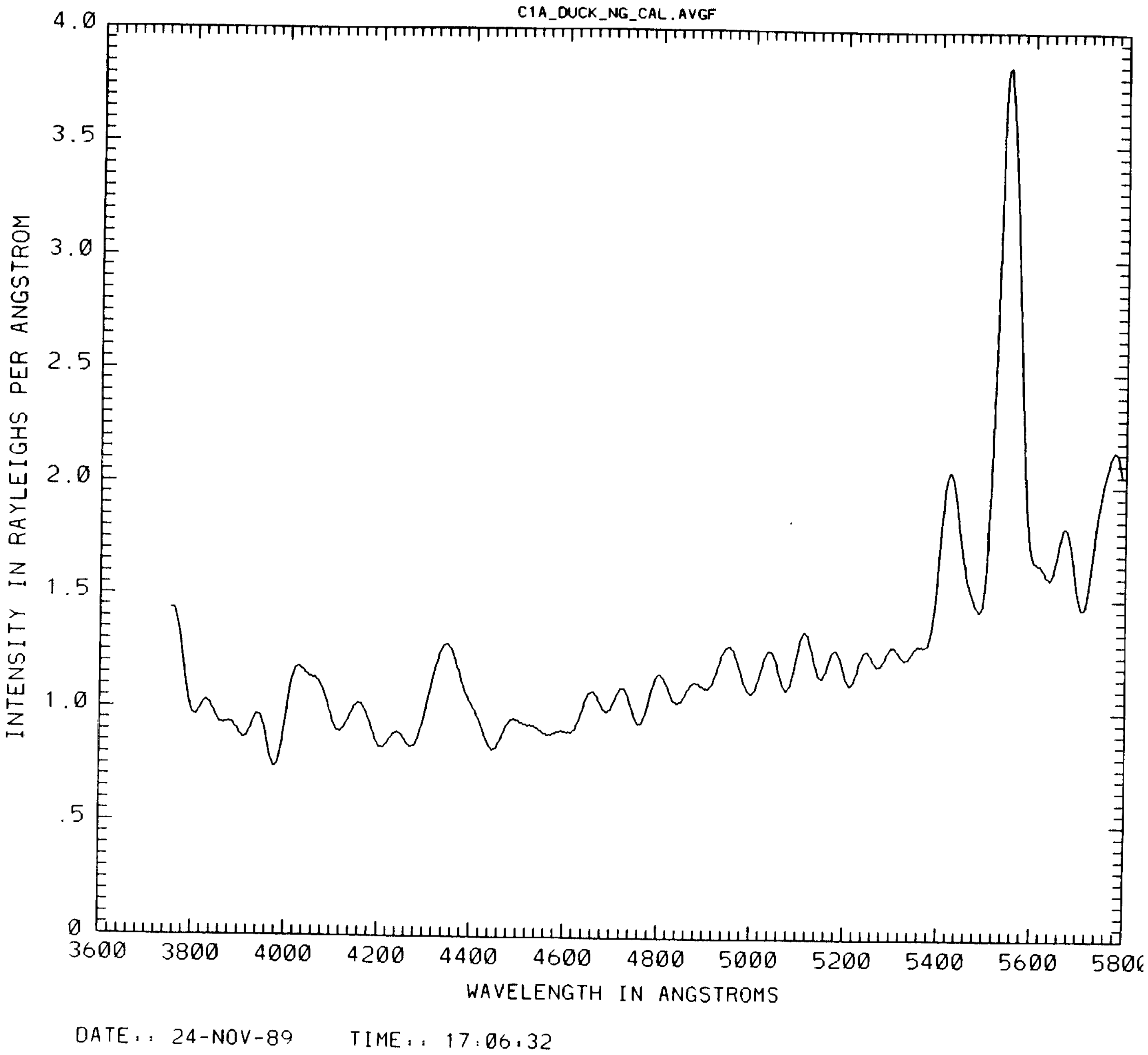

Figure 1a: An example of the late twilight spectrum imaged simultaneously by the Compact Spectrometer on October 22, 1989 at Duck, North Carolina at a solar zenith angle of ~108°.

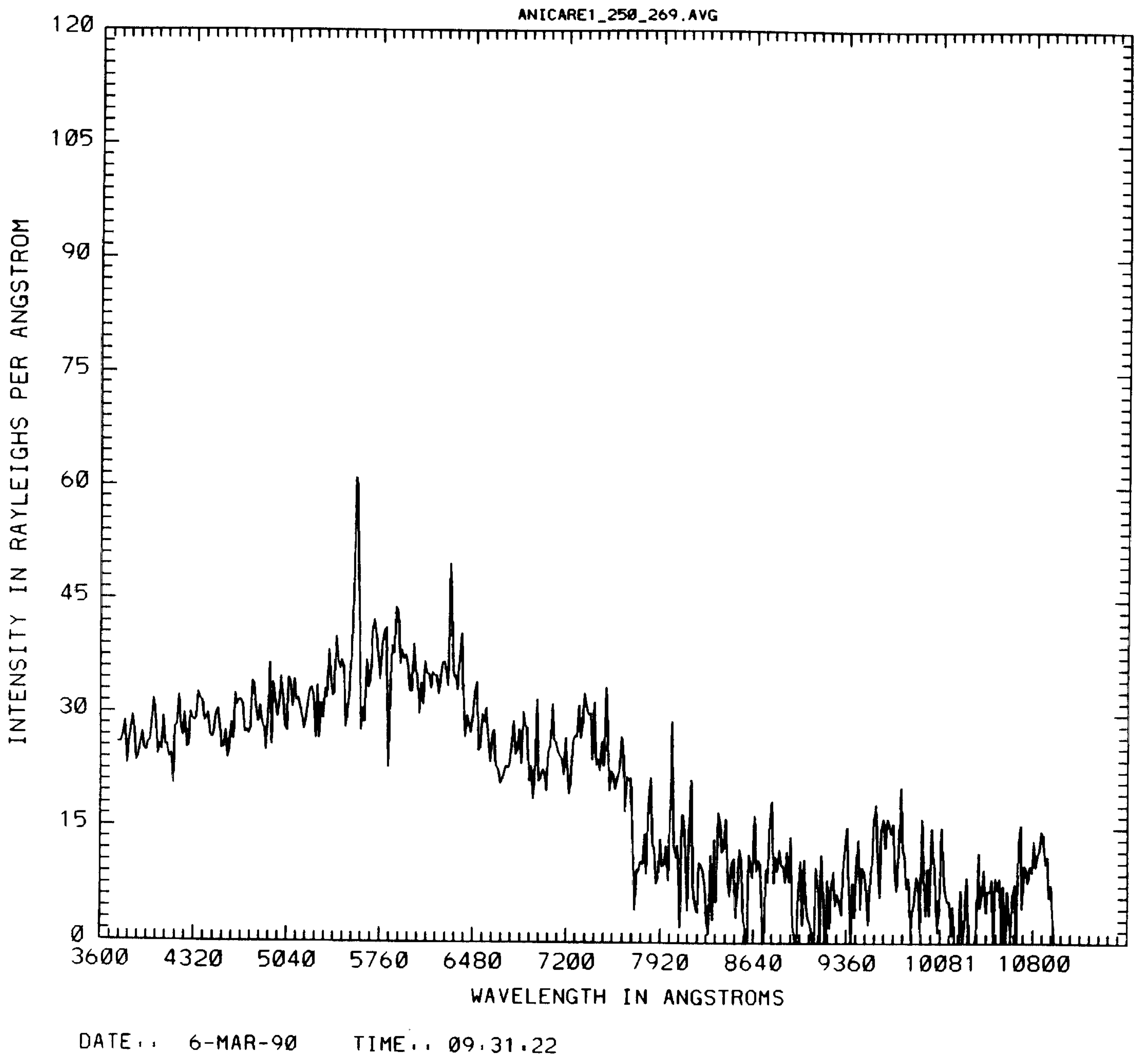

Figure 1: Uncalibrated nightglow recorded for two minutes prior to launch. A rough calibration in the visible was used to generate line intensities. The underlying continuum is unquantified. The instrument was pointed at the coordinates predicted for Release 1.

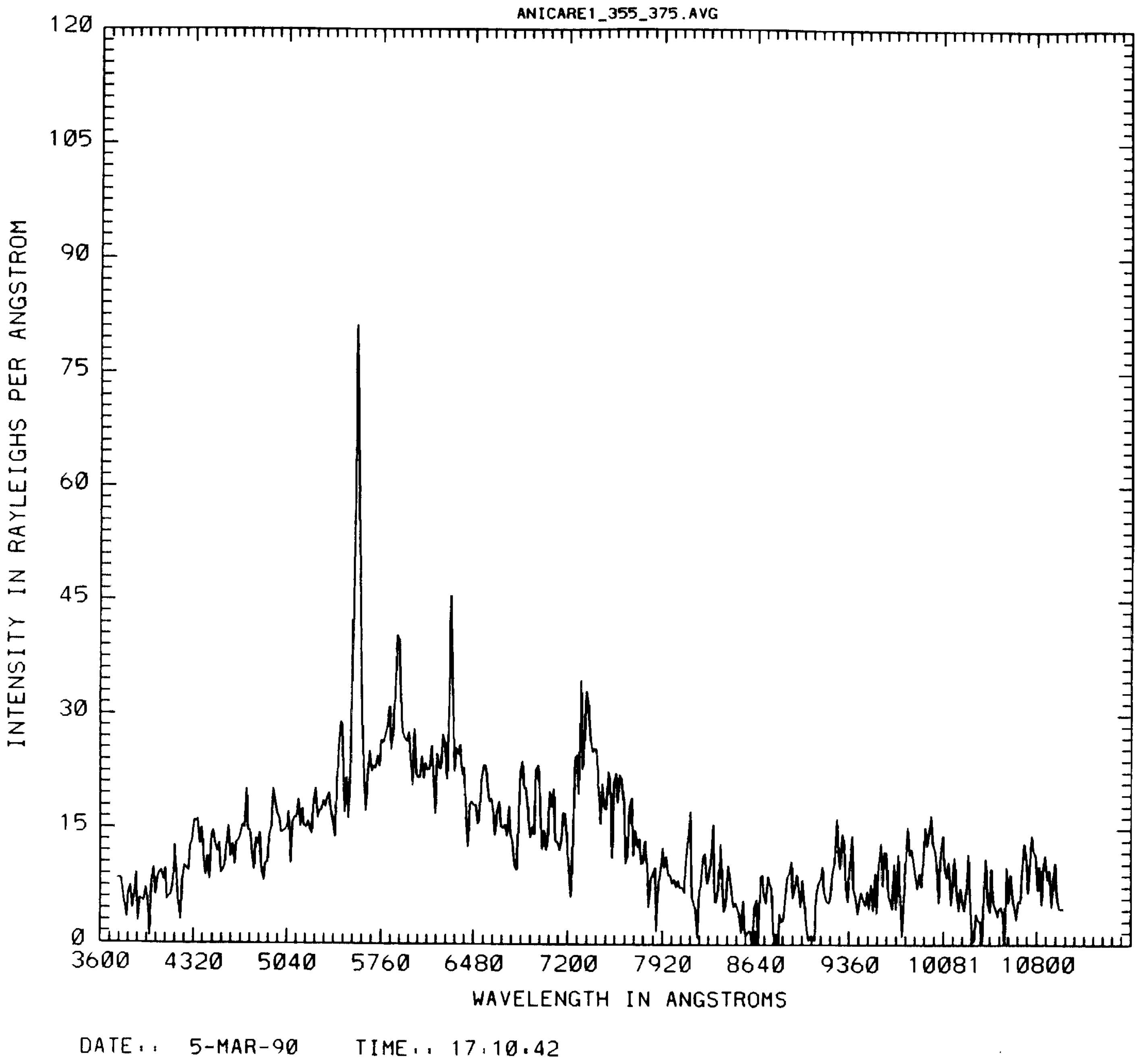

Figure 2: Uncalibrated nightglow recorded for one minute after the flight. The instrument was pointed in the last viewing direction.

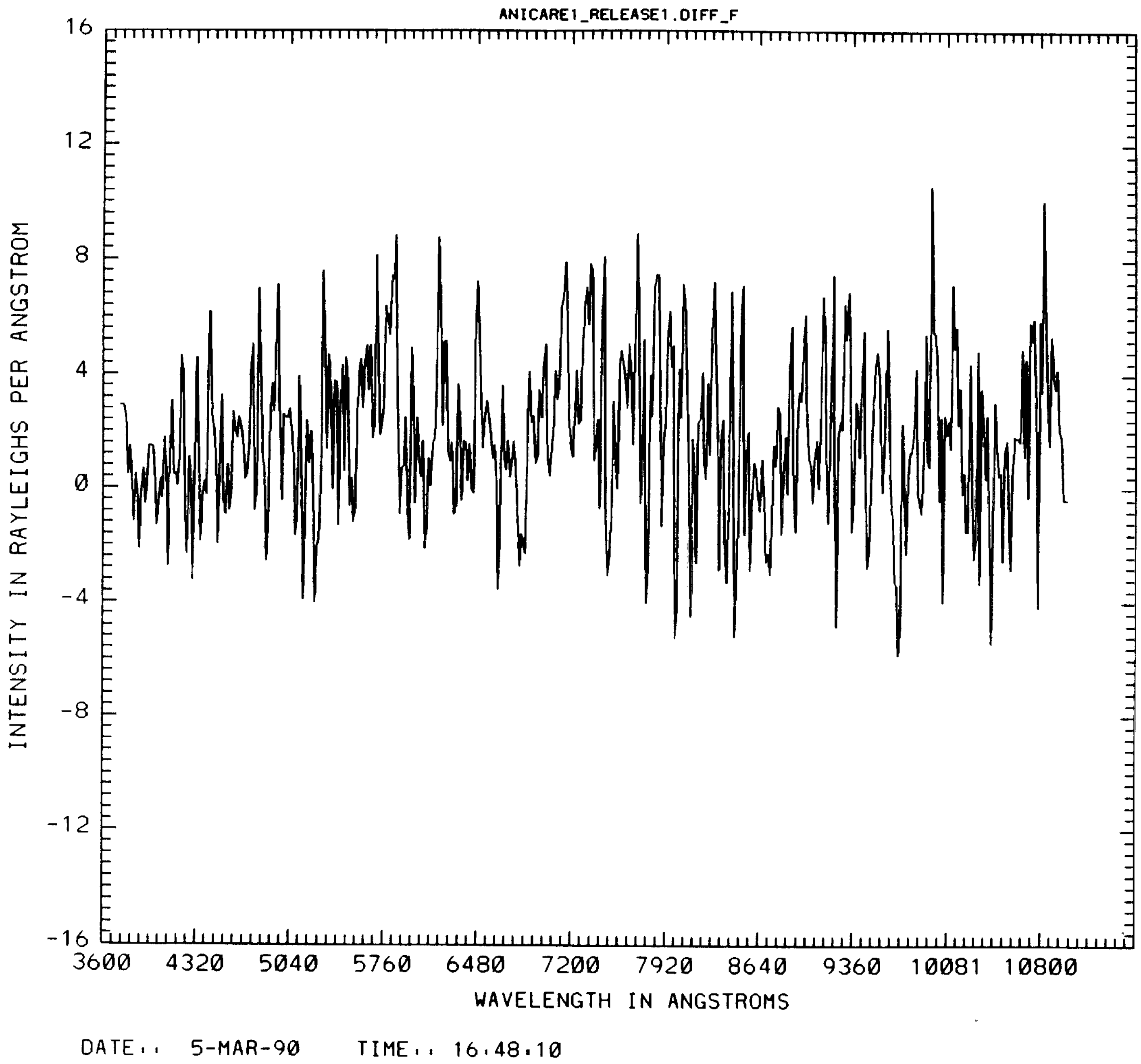

Figure 3: Spectral image recorded for 30 seconds immediately prior to Release 1 with nightglow subtracted.

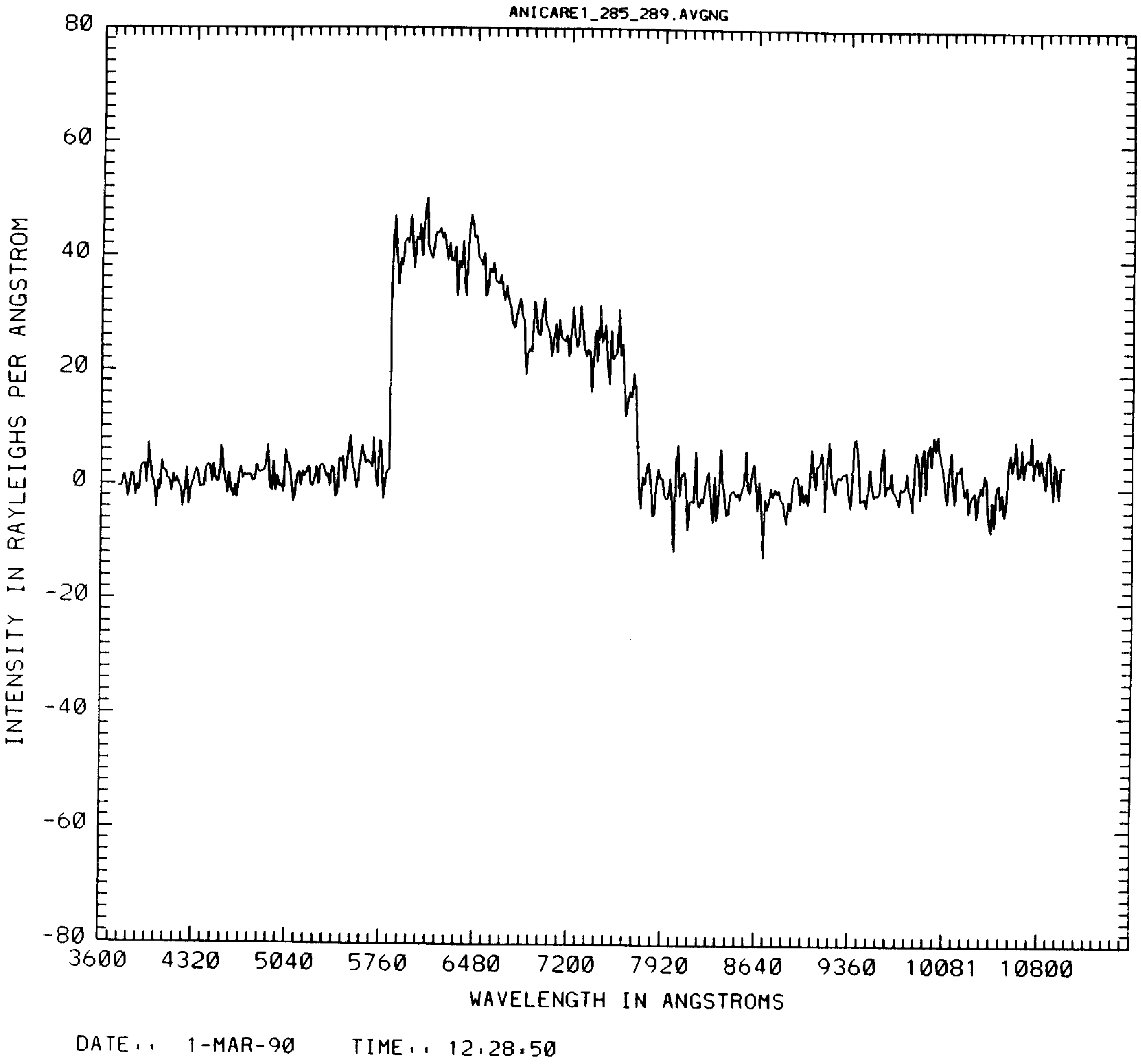

Figure 4: Spectral image recorded for 30 seconds commencing 30 seconds after Release 1. Emissions were only observed in the field of view of the mid-visible channel.

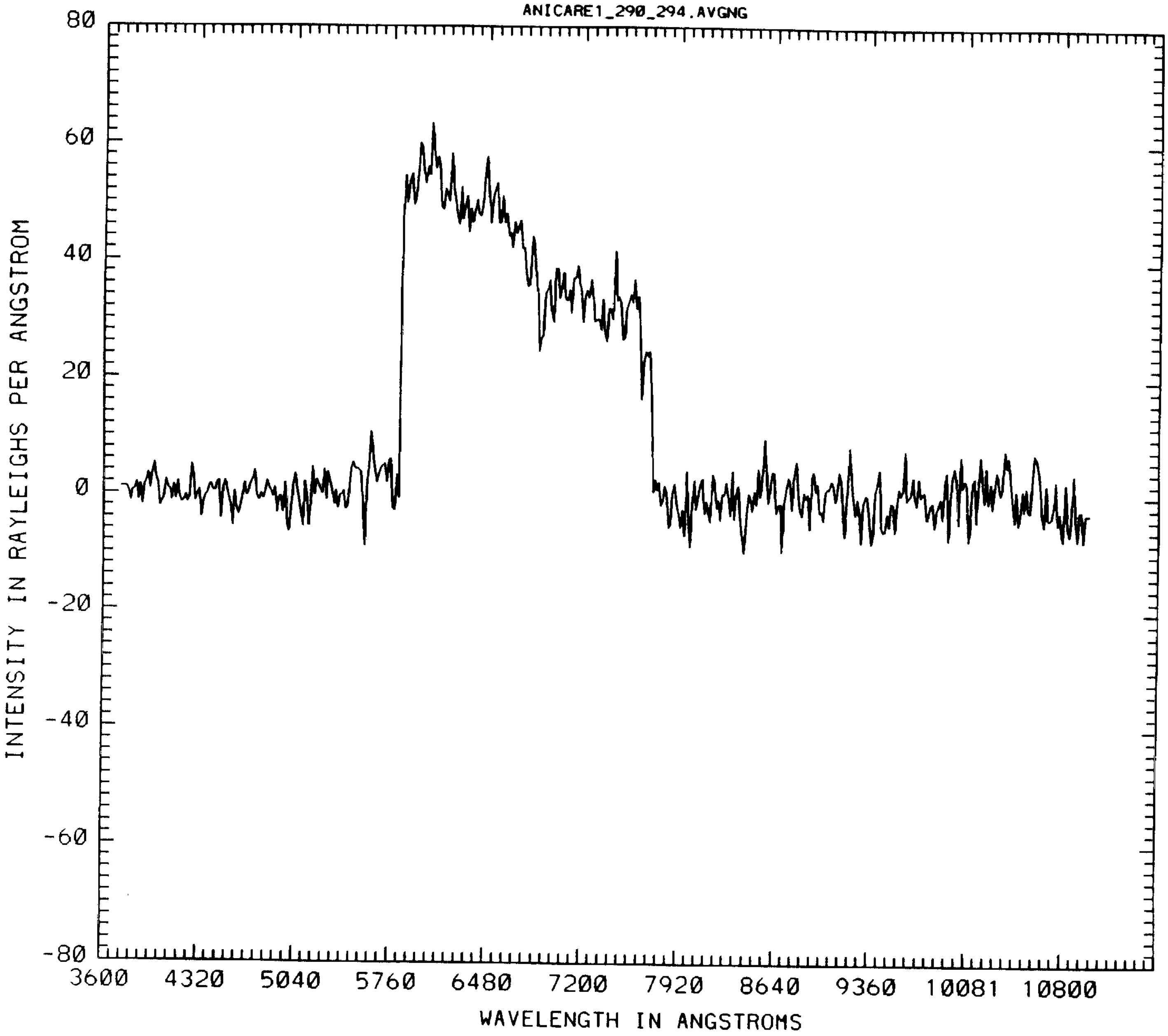

DATE:: 1-MAR-90 TIME:: 12:31:16

Figure 5: Spectral image recorded for 30 seconds commencing one minute after Release 1.

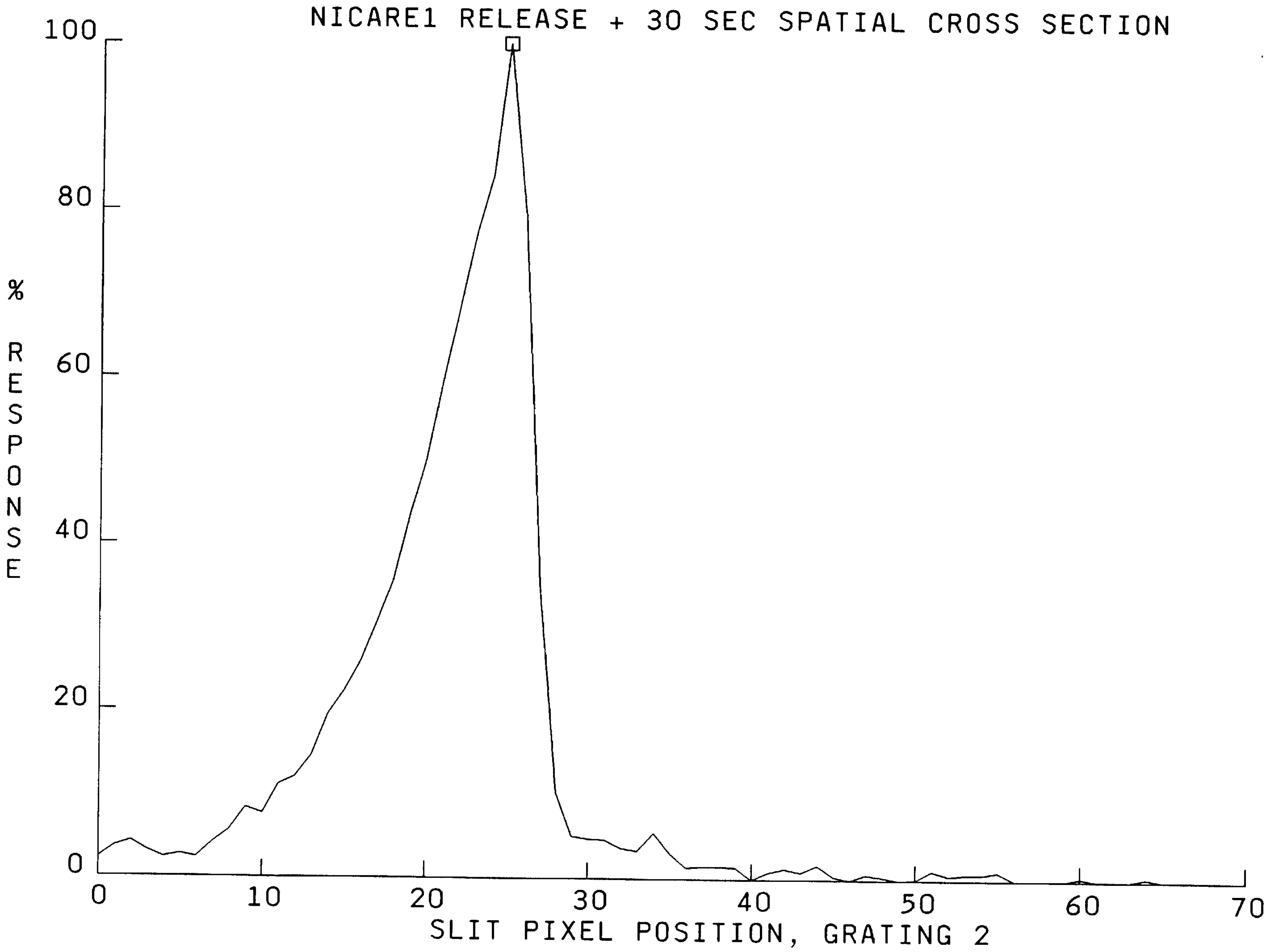
NICARE1 RELEASE + 30 SEC SPATIAL CROSS SECTION
% RESPONSE
100
80
60
40
20
0
0
10
20
30
40
50
60
70
SLIT PIXEL POSITION, GRATING 2

Figure 6

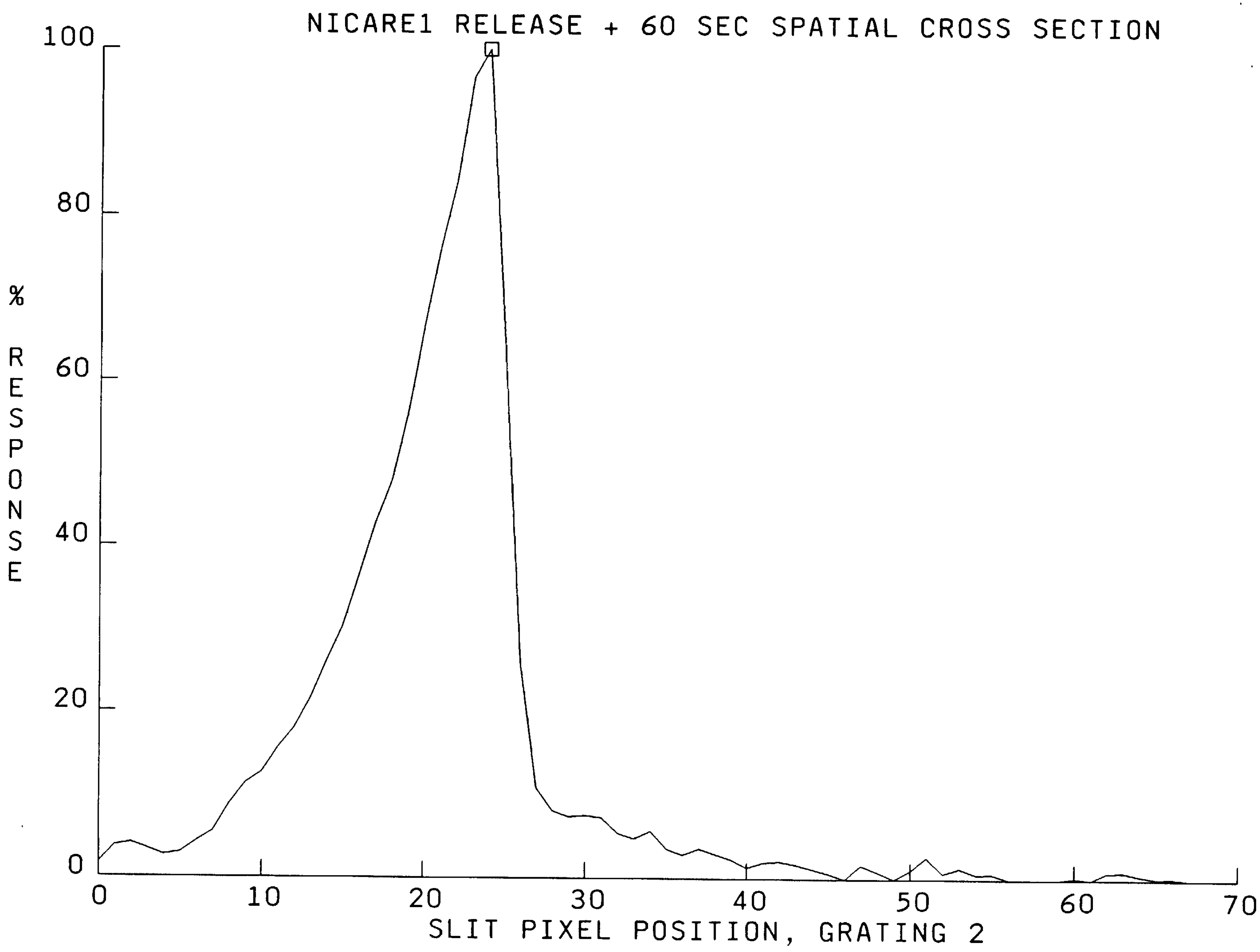
NICARE1 RELEASE + 60 SEC SPATIAL CROSS SECTION
% RESPONSE
100
80
60
40
20
0
0
10
20
30
40
50
60
70
SLIT PIXEL POSITION, GRATING 2

Figure 7

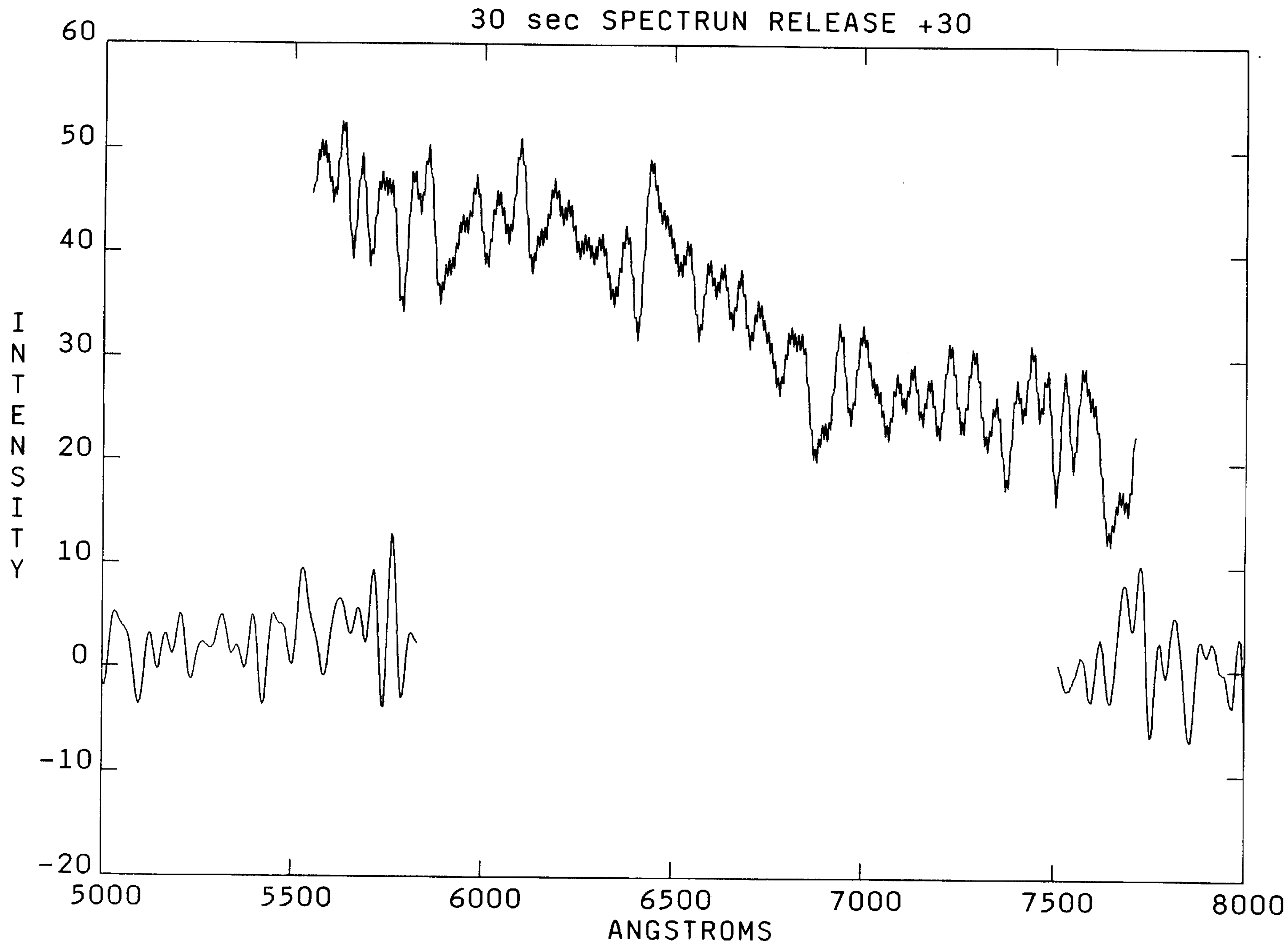
30 sec SPECTRUN RELEASE +30
INTENSITY
60
50
40
30
20
10
0
-10
-20
5000
5500
6000
6500
7000
7500
8000
ANGSTROMS

Figure 8

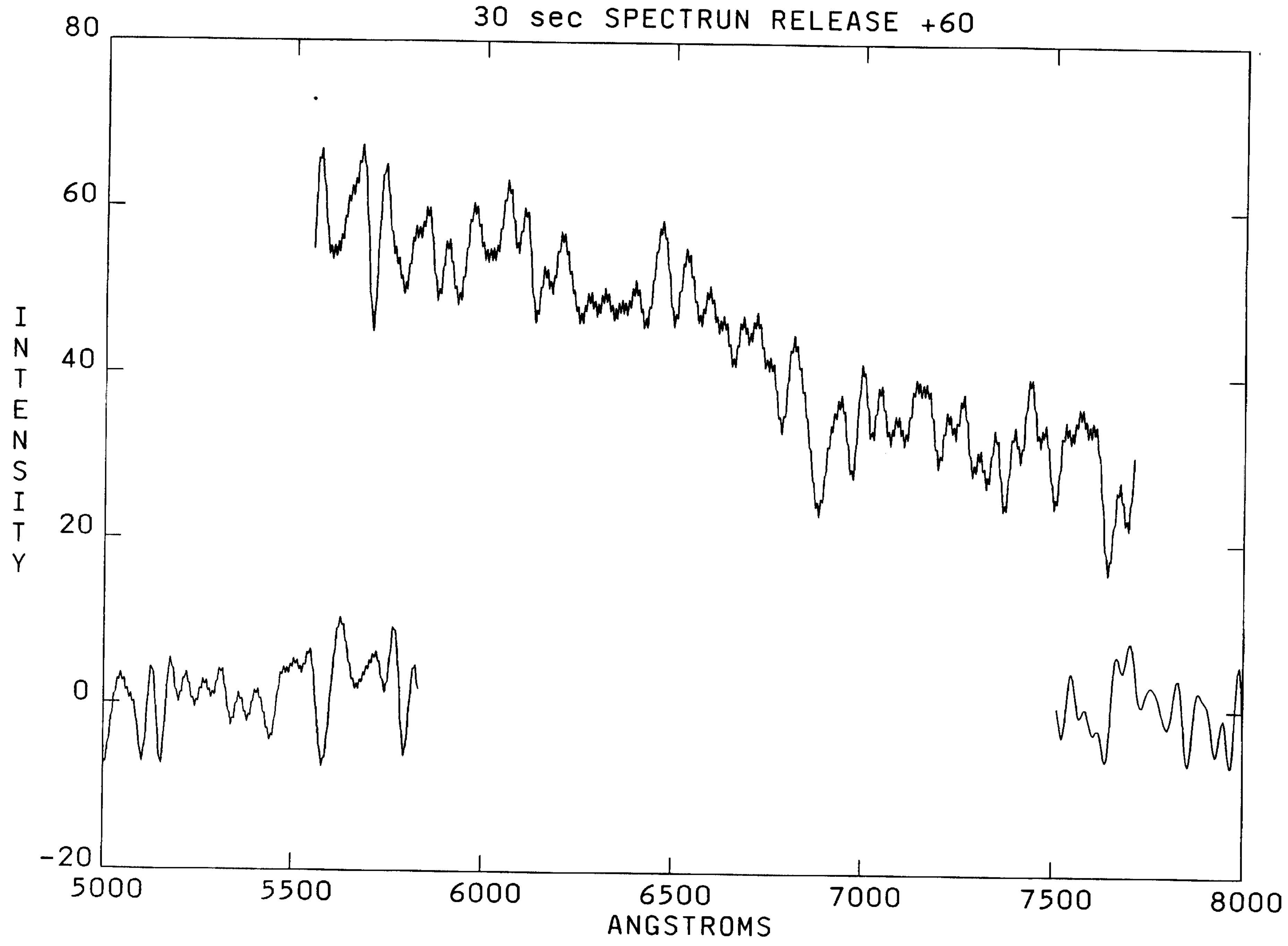
30 sec SPECTRUN RELEASE +60
INTENSITY
80
60
40
20
0
-20
5000
5500
6000
6500
7000
7500
8000
ANGSTROMS

Figure 9

PARAMETERS IN MAPPING OF PHOTOCATHODE TO CCD

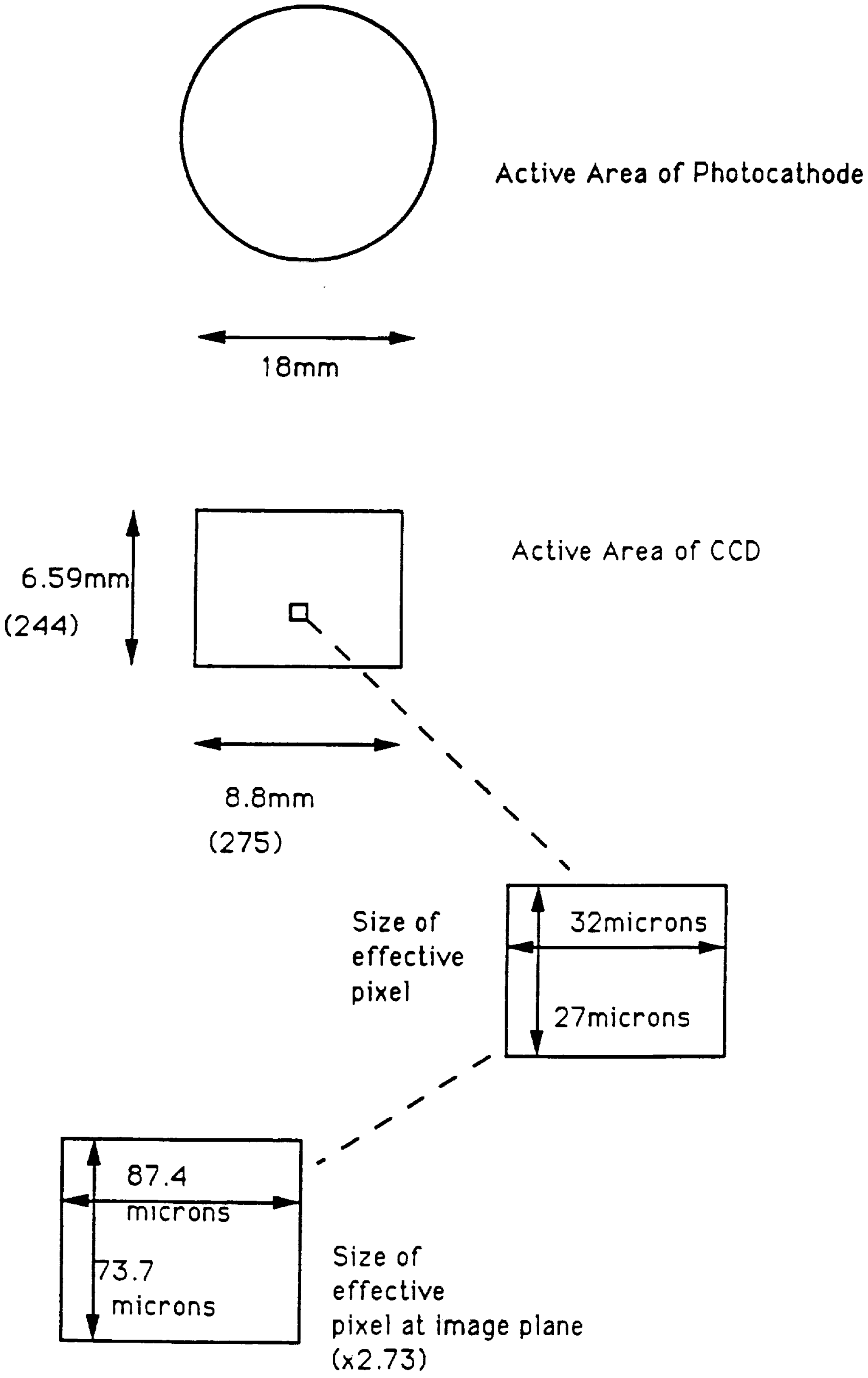

Figure 3.1

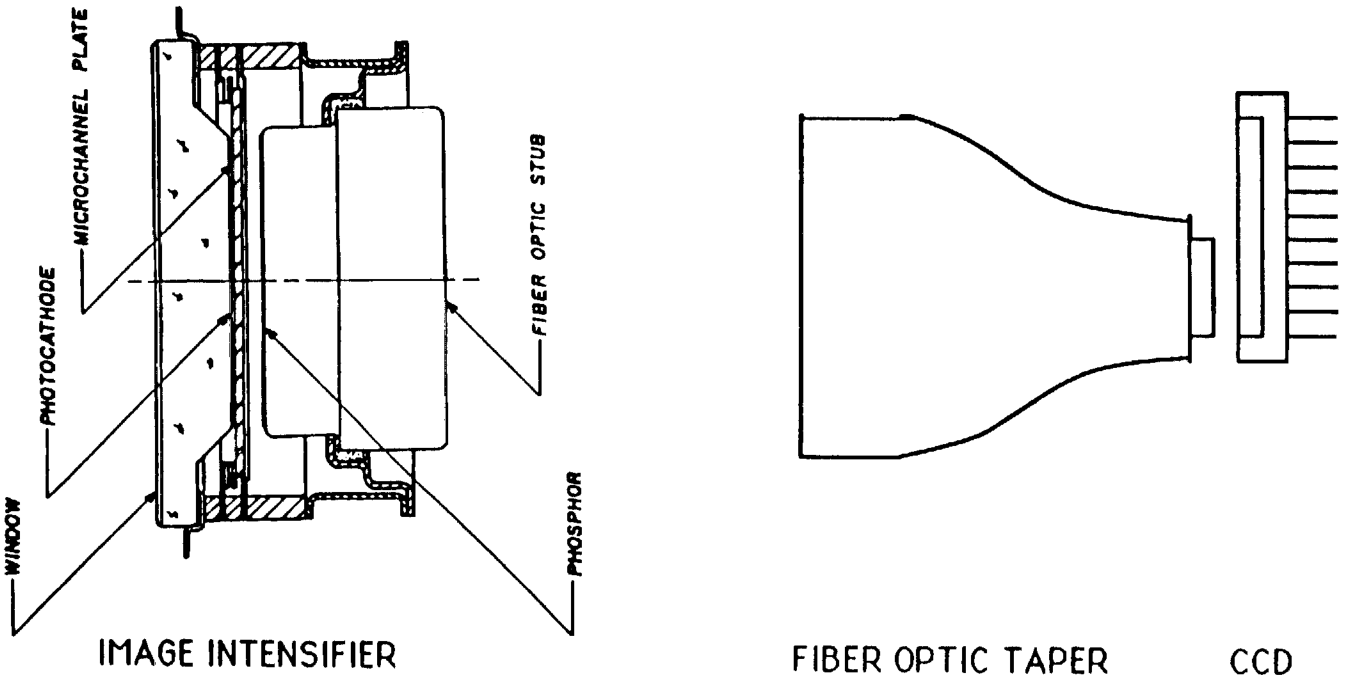
MICROCHANNEL PLATE
PHOTOCATHODE
WINDOW
FIBER OPTIC STUB
PHOSPHOR
IMAGE INTENSIFIER
FIBER OPTIC TAPER
CCD

Figure 3.2

achieved at 9 Earth radii is 25 km which meets the science requirements. Thus an additional factor of 2.2 compression is needed to match the telemetry rate.

This can be readily achieved with standard data compression techniques. For example, the first pixel in each row can be digitized to 12 bits, and then the intensities recorded with respect to the first expressed on a relative scale at lower quantization. Eleven bit digitization, for example yields a compression of a factor of 2. As a check for self-consistency the last pixel will also be digitized to 12 bits.

This study resolved the data compression issue. Figure 3.3 illustrates the placement of the image on the image tube focal plane.

4. Science Priorities for Ultraviolet Imaging in the Mid-1990's

This task was approached mainly from the perspective of the ionospheric priorities for global imaging, and not from the magnetospheric perspective because our expertise lies in ionospheric physics. The magnetospheric input was provided by other Co-investigators with expertise in magnetospheric physics.

The Earth's upper atmosphere is constantly undergoing periodic and aperiodic changes induced by solar eletromagnetic and corpuscular radiation.

The primary energy source is the absorption of solar ultraviolet radiation which under quiet conditions produces predictable cyclic patterns of behavior.

The solar wind introduces plasma into the terrestrial environment which energizes and penetrates into the Earth's magnetosphere where it is stored and then impulsively released creating, for example, the visual aurora.

These processes generate complex and variable electric potentials and currents which, in turn, result in large insertions of electrical and corpuscular energy to the upper atmosphere, greatly perturbing is quiet time behavior.

Figure 4.1 illustrates the energy sources to the ionosphere/thermosphere. Our goal is to determine the energy sources and their impact on the system.

To understand the significance of the role of the UVI Imager for the ISTP mission, one can pose the questions: what will the UVI do that has never been done before. The UVI will provide global coherent images of terrestrial emissions every 30 seconds, i.e. a full global snapshot of the entire earth repeated at 7 wavelengths. This has never been achieved before, because previous images of the earth had to be built up one pixel at at time by scanning a pencil beam field-of-view across the earth. It required 15 minutes on the Dynamics Explorer to build up single image at one color. Thus the coherence needed over time scales of the order of tens of seconds to understand the global behavior of the dynamic aurora could not be realized.

Second, the filter technology did not exist prior to UVI to separate out the ultraviolet wavelengths or colors emitted by the upper atmosphere, so that the full information of the spectral nature of the emissions could not be realized. (Note the dayside of the earth can only be viewed at VUV wavelengths). Thus the questions reduced to: what will coherent spectrally pure global imaging achieve?

To answer this question we examined the status of ionospheric research. Currently models exist which have the potential to describe the behavior of the global

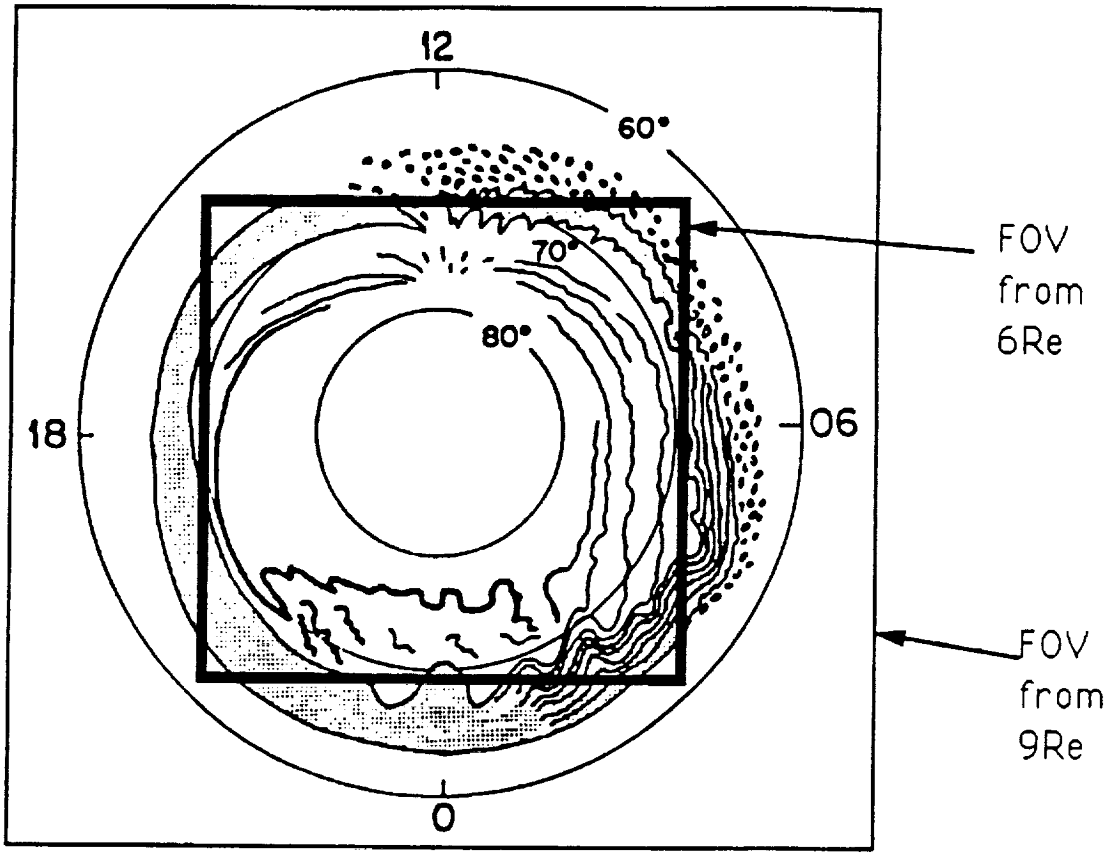

TYPICAL AURORAL OVAL WITH 8 x 8 degree FIELD OF VIEW FROM 6Re and from 9Re APPOGEE

Figure 3.3

SCIENCE OBJECTIVES: THE COUPLED IONOSPHERE THERMOSPHERE MESOSPHERE SYSTEM

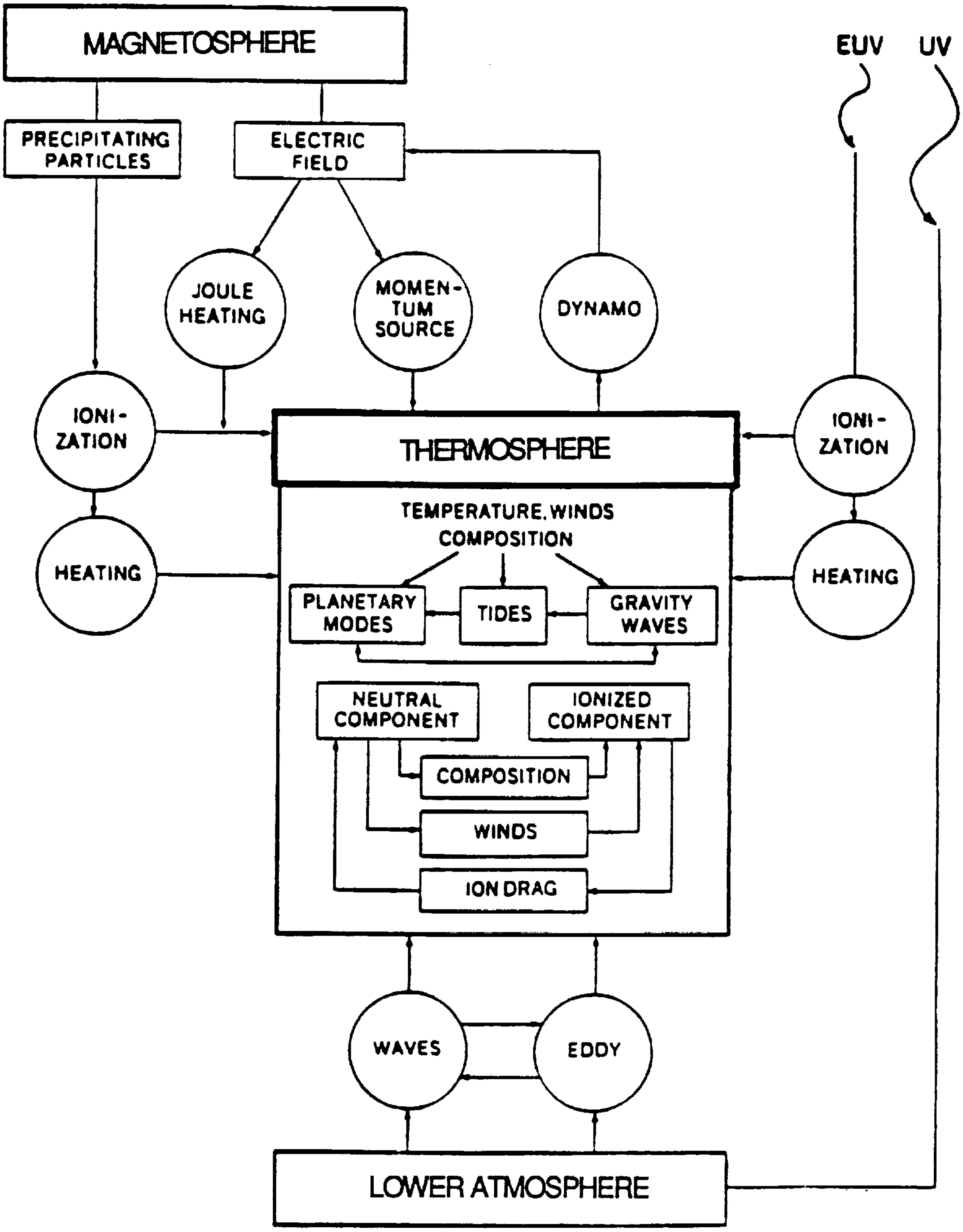

Figure 4.1

ionosphere. These ionospheric global models require the following fundamental input parameters:

- Solar EUV flux
- Global precipitated particle flux
- Upper atmospheric neutral winds
- Global electric field pattern
- Knowledge of the neutral atmosphere, i.e. composition and temperature

If the ionospheric models are combined with a thermospheric global circulation model (TGCM) then the required inputs reduce to

- Solar EUV flux
- Global precipitated particle flux
- Global electric field pattern

Under this contract we developed procedures to demonstrate that the UVI images can be used to provide the global precipitated particle flux and the global electric field pattern. These two parameters have been impossible to acquire on a global grid in the past, because the data are only useful if near simultaneous measurements can be made on a global scale.

Under D.O. 48 we demonstrated that coherent global imaging of spectrally pure emissions will provide the data needed to determine the particle fluxes and electric fields.

The first task to be performed was to determine what emissions could be used to characterize the particle energy influx. Using the auroral deposition code developed under NAS8-37586, the response of several candidate emissions to auroral particle energy input was evaluated. It was demonstrated that the molecular nitrogen Lyman-Birge-Hopfield bands in the Vacuum Ultraviolet (VUV) range 1200 - 1800 Å (termed $\mathrm{LBH}_{\mathrm{LONG}}$) vary linearly with the total precipitated particle energy flux. No other emissions exhibit this behavior. The results of these calculations are shown in Figure 4.2. These results were presented to the UVI Science Team on August 15-16, 1990. This success was fundamental to the science objectives that could be developed, and can be attributed directly to the successful development of a rectangular VUV filter under NAS8-37586 that straddled the $\mathrm{LBH}_{\mathrm{LONG}}$ wavelength range. A full scientific understanding was developed as to why the $\mathrm{LBH}_{\mathrm{LONG}}$ wavelengths respond in the desired way.

The next discovery proved to be equally significant, namely the ratio of two emissions were found which were sensitive only to the energy spectrum of the incoming particles, as defined by a "characteristic energy". Figure 4.3 shows the characteristic energy as a function of the ratio of the $\mathrm{LBH}_{\mathrm{LONG}}/\mathrm{LBH}_{\mathrm{SHORT}}$ emissions, where LBH short lie in the wavelength range 1400-1600 Å . Once again, the key to achieving this success is the ability to fabricate a filter that can spectrally isolate the $\mathrm{LBH}_{\mathrm{LONG}}$ and $\mathrm{LBH}_{\mathrm{SHORT}}$ emissions. The ratios of many emissions were investigated, and in each case with the

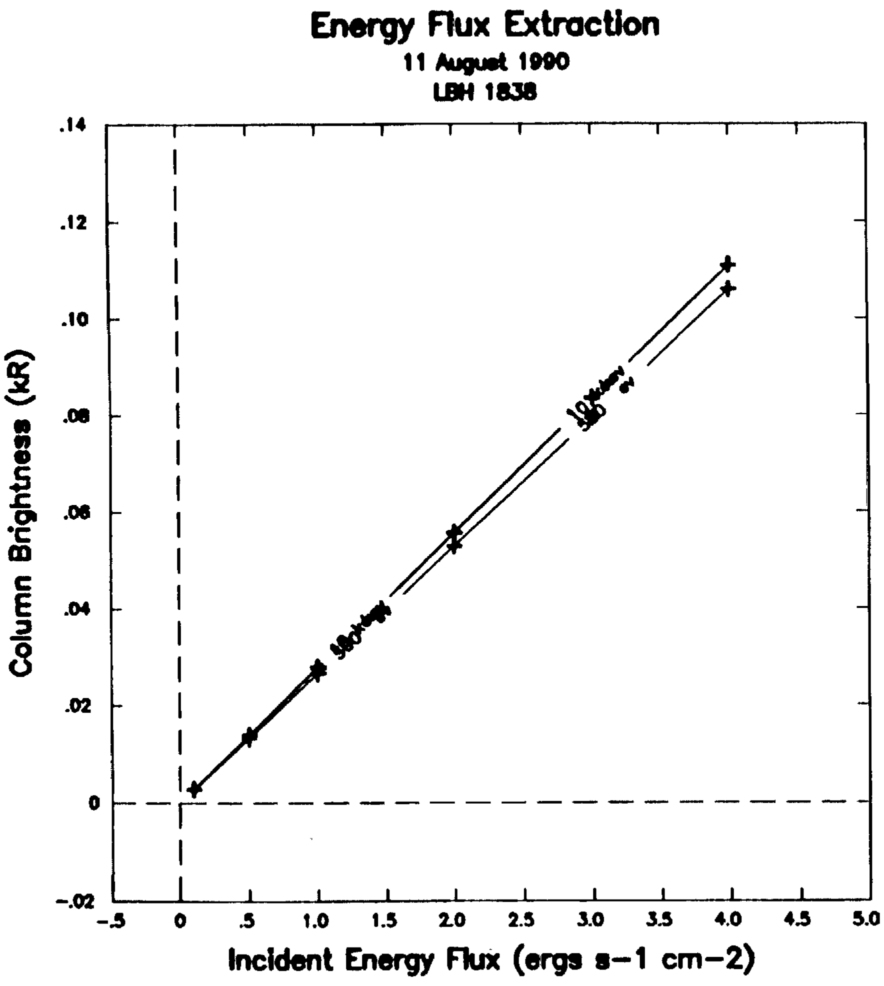
Energy Flux Extraction
11 August 1990
LBH 1838
Column Brightness (kR)
.14
.12
.10
.08
.06
.04
.02
0
-.02
-.5
0
.5
1.0
1.5
2.0
2.5
3.0
3.5
4.0
4.5
5.0
Incident Energy Flux (ergs s-1 cm-2)

Figure 4.2

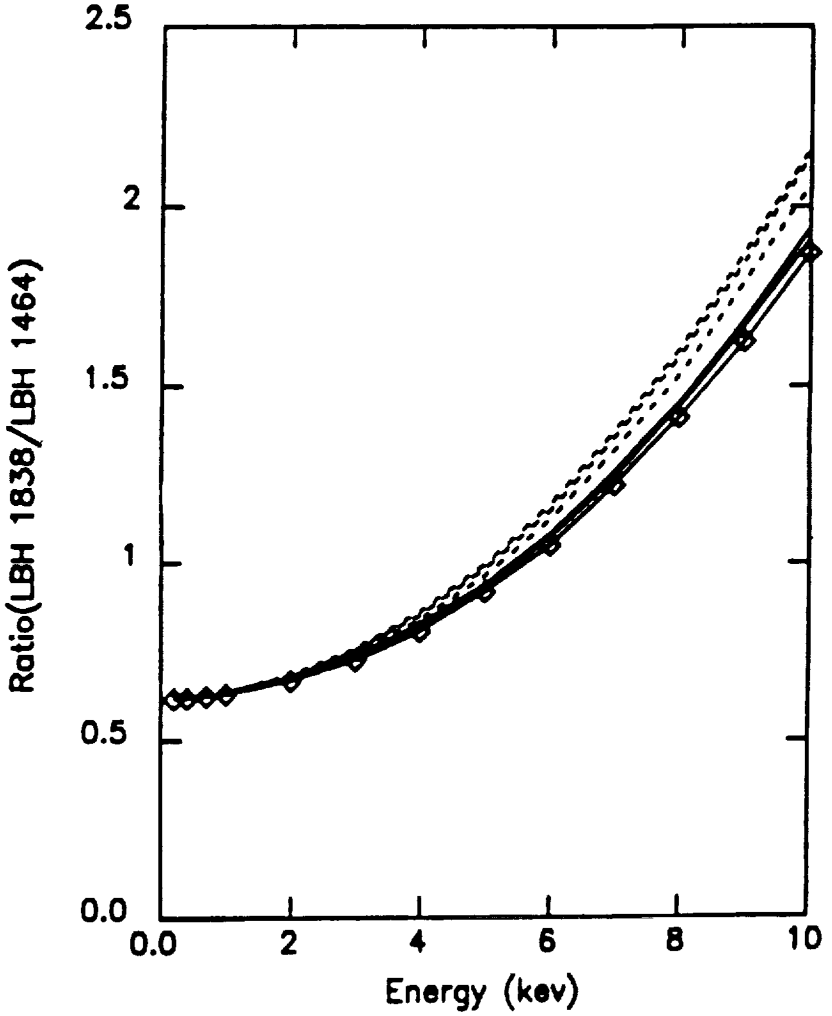

Figure 4.3

exception of LBH_{LONG}/LBH_{SHORT}, strong sensitivity to atmospheric composition and temperature were observed, which impacted their usefulness.

The above findings mean that the spectrum and energy flux of the incoming particles will be derived from the UVI images on a global scale, every 30 seconds. The impact of this data on modeling will be profound for the following reasons. The auroral code, referred to above, can now be used to calculate the global ionospheric corpuscular source function as a function of time. This will be the first time that real values for this critical ionospheric input parameter will be available. The corpuscular source accounts for about half the total energy input to the ionosphere and thermosphere and in the auroral zone it is the dominant energy source.

The results of this work were published in the Journal of Geophysical Research under the title, "The Dependence of OI 1356 and N_2 LBH Auroral Emissions on the Neutral Atmosphere", which is attached as Appendix A.

Figure 4.1 illustrates the energy input sources to the thermosphere/ionosphere system. An important goal in Solar Terrestrial Physics is to quantify the effects of coupling of magnetospheric electrical energy into the ionosphere. Under this contract we developed a strategy to use the imager to help define the global electric field system.

Current systems in the magnetosphere generated by interactions with the solar wind generate a cross-tail potential which maps down into the ionosphere, where it accelerates the ions. The ions collisionally impart momentum to the neutral atmosphere which sets up winds which typically can reach velocities of the order of kilometers per second. Thermally driven winds can also act on the ions generating ion drift motions. The effects of electric field are therefore manifested in ion and neutral motion. The former can be measured by groundbased incoherent scatter radars and the latter by Fabry-Perot interferometers which monitor a bright airglow feature at 6300 Å. Also, the current systems associated with the electric fields cause fluctuations in the earth's surface magnetic fields which can be observed by magnetometers. In addition, the electric field instruments on the ISTP spacecraft make direct *in situ* measurements of electric fields. All the above techniques can provide valuable spot (isolated) measurements of the global electric field. However, the imaging data can also be used to infer electric fields on a much broader scale. This statement is based on the fact that the ionosphere constitutes an important component of the magnetospheric electrical circuits. Currents can flow into and out of the ionosphere if the input and output points are electrically connected horizontally. The current carriers that close the loop are the electron-ion pairs that constitute the ionospheric plasma. Thus when auroral electron precipitation occurs, generating the auroral emissions, there is an associated production of electron-ion pairs. This production rate can be computed by the auroral deposition code from the UVI images as described above. Naturally, at night, data taken by the Iowa Visible Imager can also be used. This source function coupled with an ionospheric global model can be used to calculate the ionospheric electron density, i.e. the density of the current carriers, which means that the electrical conductivity of the circuit can be computed. These conductivities can then be used in an ionospheric electrodynamics model to infer the input electric fields.

Currently large scale potential patterns describing ionospheric convection patterns are estimated using statistical models for the ionospheric electrodynamics. One such model referred to as the Kamide-Richmond model, utilizes the following input data to infer the large scale potential pattern:

- Incoherent scatter radar convection observations
- Satellite direct field observations
- Ground and satellite magnetometer observations
- Ionosphere electrical conductance observations

The groundbased observations are capable of tracking rapid changes in electric fields and currents, conductivities and associated magnetic perturbations. The electrodynamics models can combine different kinds of electrodynamical data to infer the high-latitude electric potential patterns as they evolve in time. However, spatial coverage is limited so that many stations would be needed to obtain global coverage. By using the global conductances derived from the UVI/VIS images the input database can be greatly enhanced, and at much higher time resolution, allowing the time-evolution of the global ionosphere to be modeled.

Figures 4.4 - 4.9 illustrate our strategy for reaching a quantitative global modeling capability by the mid-1990's.

Figure 4.4. shows the basic starting point, discussed above. P. G. Richards and D. G. Torr have developed a global ionospheric model referred to as the Field Line Interhemispheric Plasma (FLIP) model. This model computes the global electron density as a function of height and time. It requires several inputs which are identified in Figure 4.5. As is evident from this figure, the FLIP model produces a large number of outputs. Figure 4.6 includes the need for these key inputs in the flow chart.

In addition to the auroral source function, the FLIP model requires as input the solar EUV flux, neutral winds and the neutral atmosphere. There are several ways to obtain these. The first option is to use empirical models which provide all three inputs as a function of geophysical indices such as magnetic and solar activity. However, these are essentially statistical models derived from existing databases, and do not necessarily accurately represent conditions on any specific day. The empirical models can be further constrained by groundbased airglow measurements as illustrated in Figure 4.7. UAH (our team) has been deeply involved over the last five years in developing techniques for deriving the solar EUV flux, the neutral atmosphere and winds from groundbased measurements of airglow and electron densities.

To include the effects of electric fields, the FLIP model is coupled to an ionospheric electrodynamics model (see Figure 4.8), which derives input from the groundbased network of radars, ionosondes, magnetometer chains and *in situ* ISTP E fields. The electrodynamics model provides the electric fields to the FLIP model which returns the global conductances to the electrodynamics model, thereby iteratively improving the global electric field calculation. The FLIP model predicts the electron density profile as a function of time at the locations of ~ 100 ionosonde and ~ 6 to 7 radar stations. Iteration is continued until the best electron density fit is obtained at all stations.

Finally, the entire system is coupled with a global thermospheric circulation model (TGCM) as illustrated in Figure 4.9. The TGCM utilizes the joule heat source and ion drag momentum source from the ionospheric models, and provides the neutral thermosphere and winds back to the ionospheric models. Iteration is continued until the global electron densities best fit the groundbased measurements.

ISTP CONTRIBUTION TO GLOBAL IONOSPHERE AND ELECTRODYNAMICS

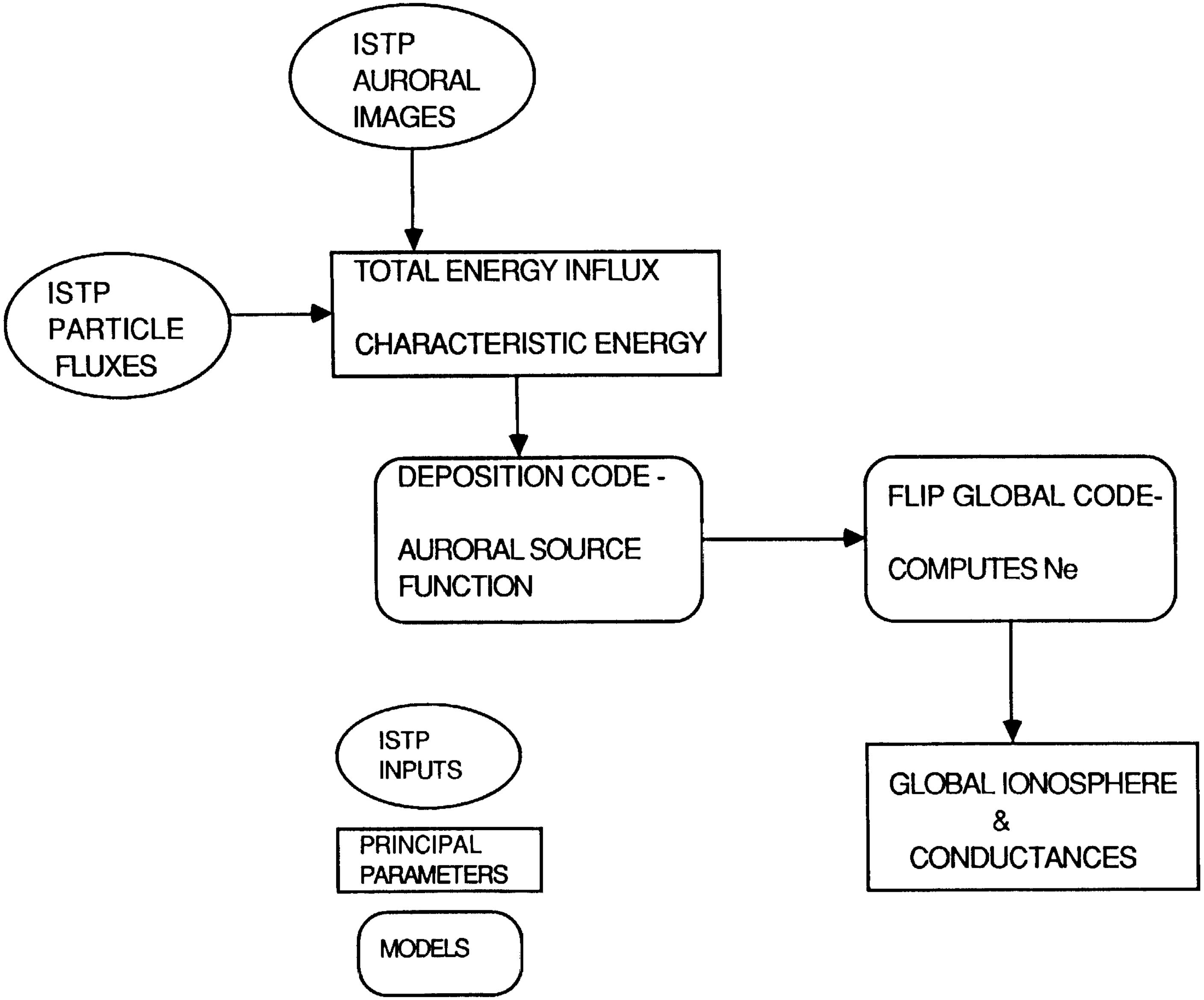

Figure 4.4

istpq001

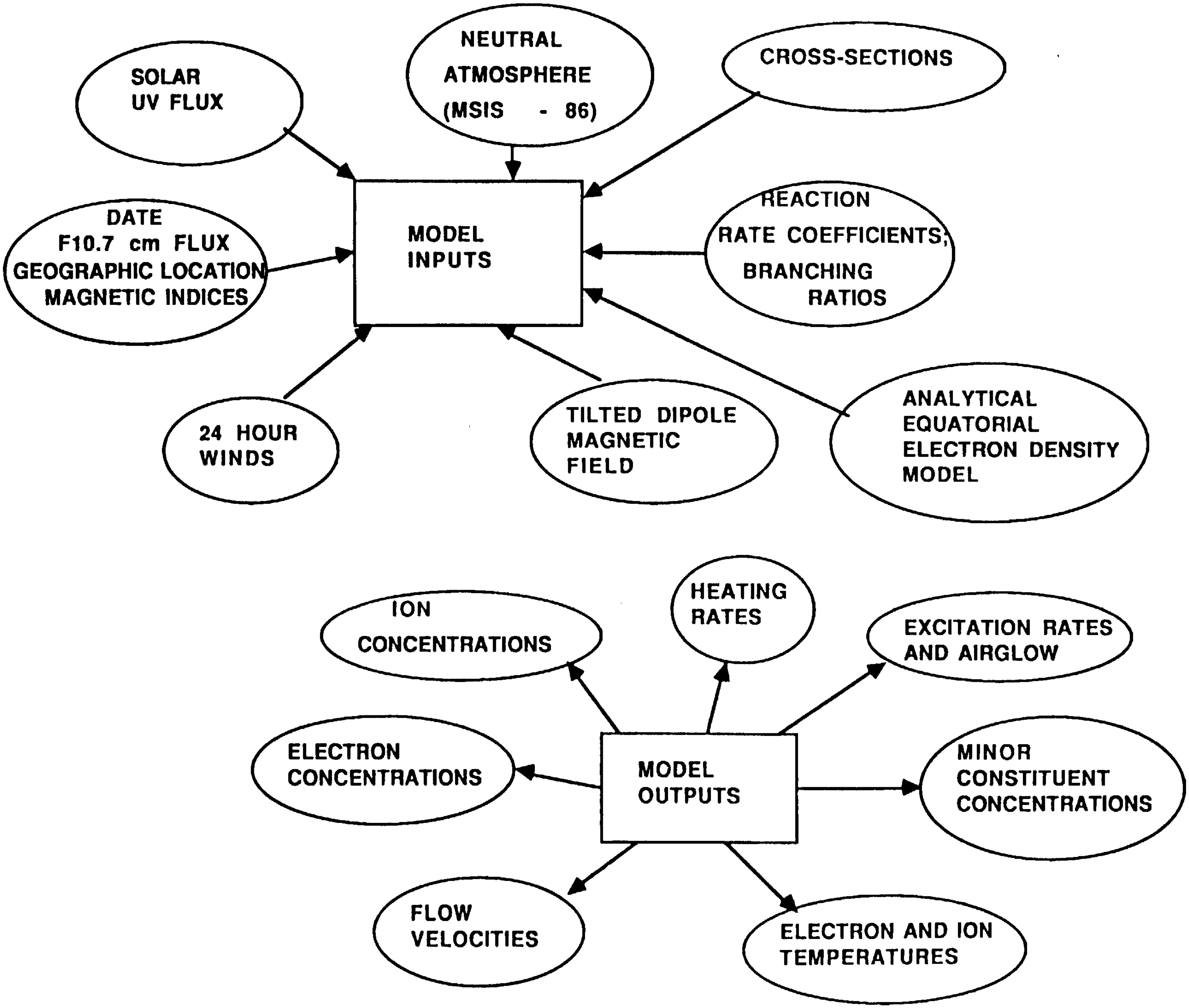

FLIP model inputs and outputs. An additional output not shown is the photoelectron flux.

Figure 4.5

ISTP CONTRIBUTION TO GLOBAL IONOSPHERE AND ELECTRODYNAMICS

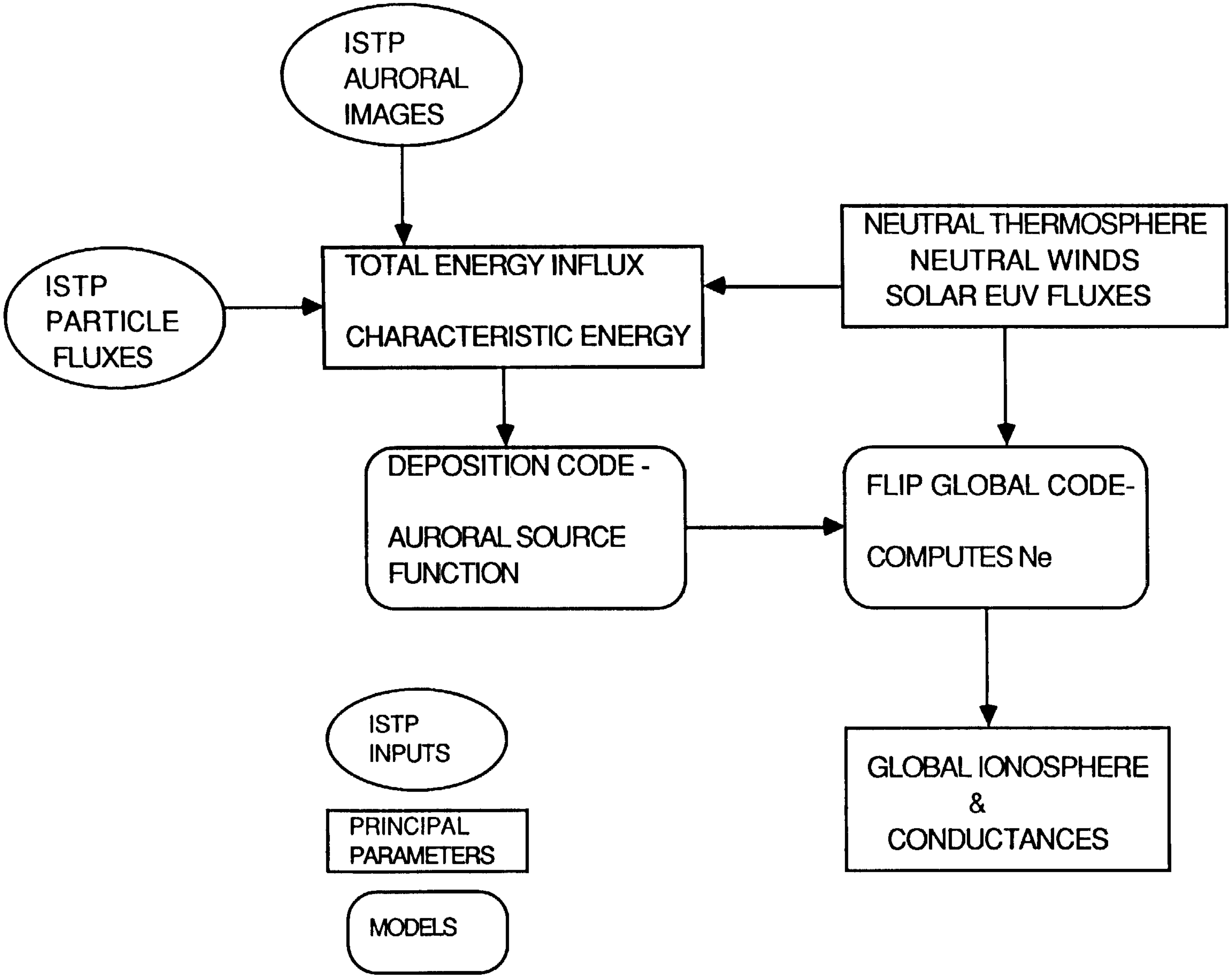

Figure 4.6

istpq002

ISTP CONTRIBUTION TO GLOBAL IONOSPHERE AND ELECTRODYNAMICS

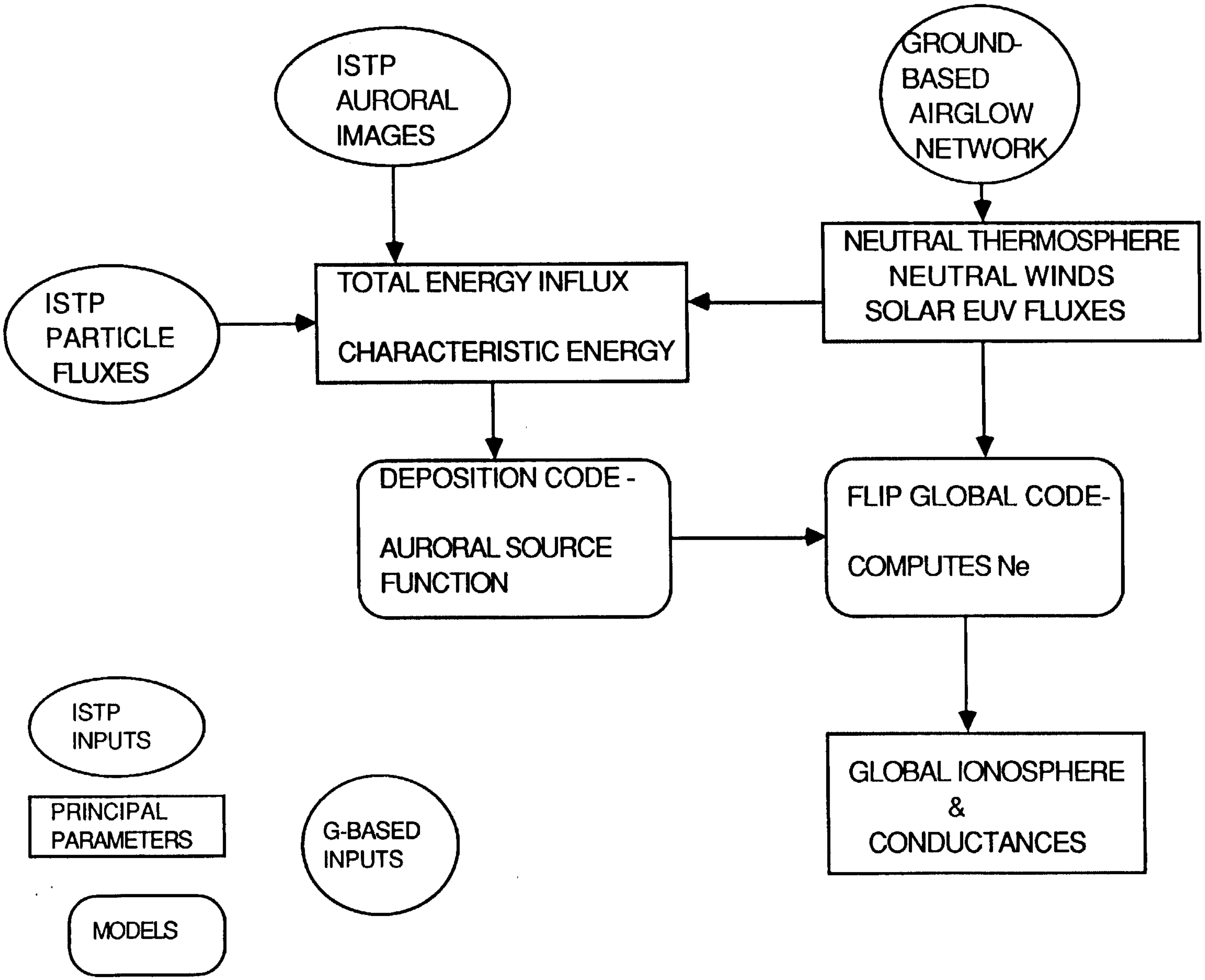

Figure 4.7

istpq003

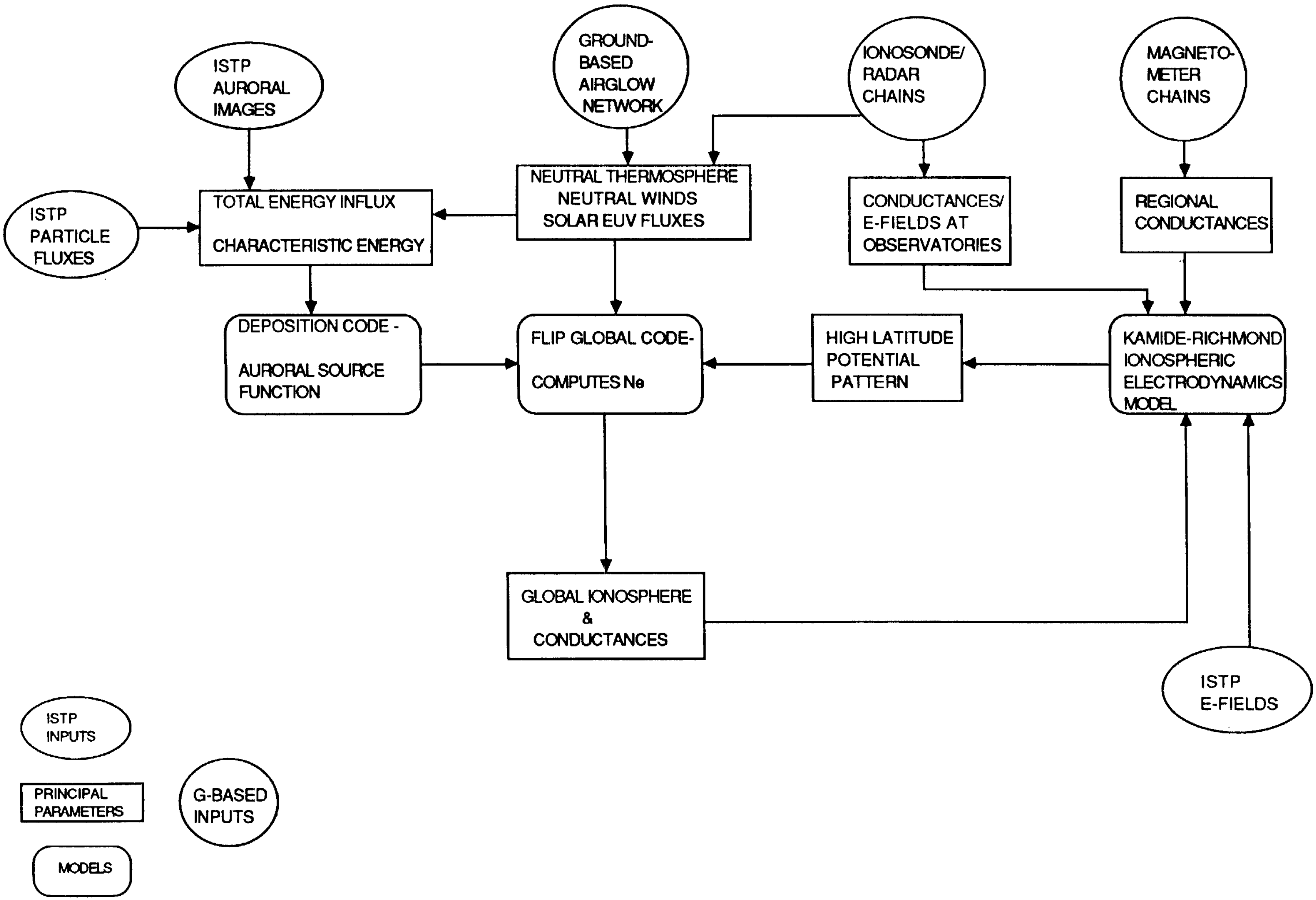

ISTP CONTRIBUTION TO GLOBAL IONOSPHERE AND ELECTRODYNAMICS

istpq004

Figure 4.8

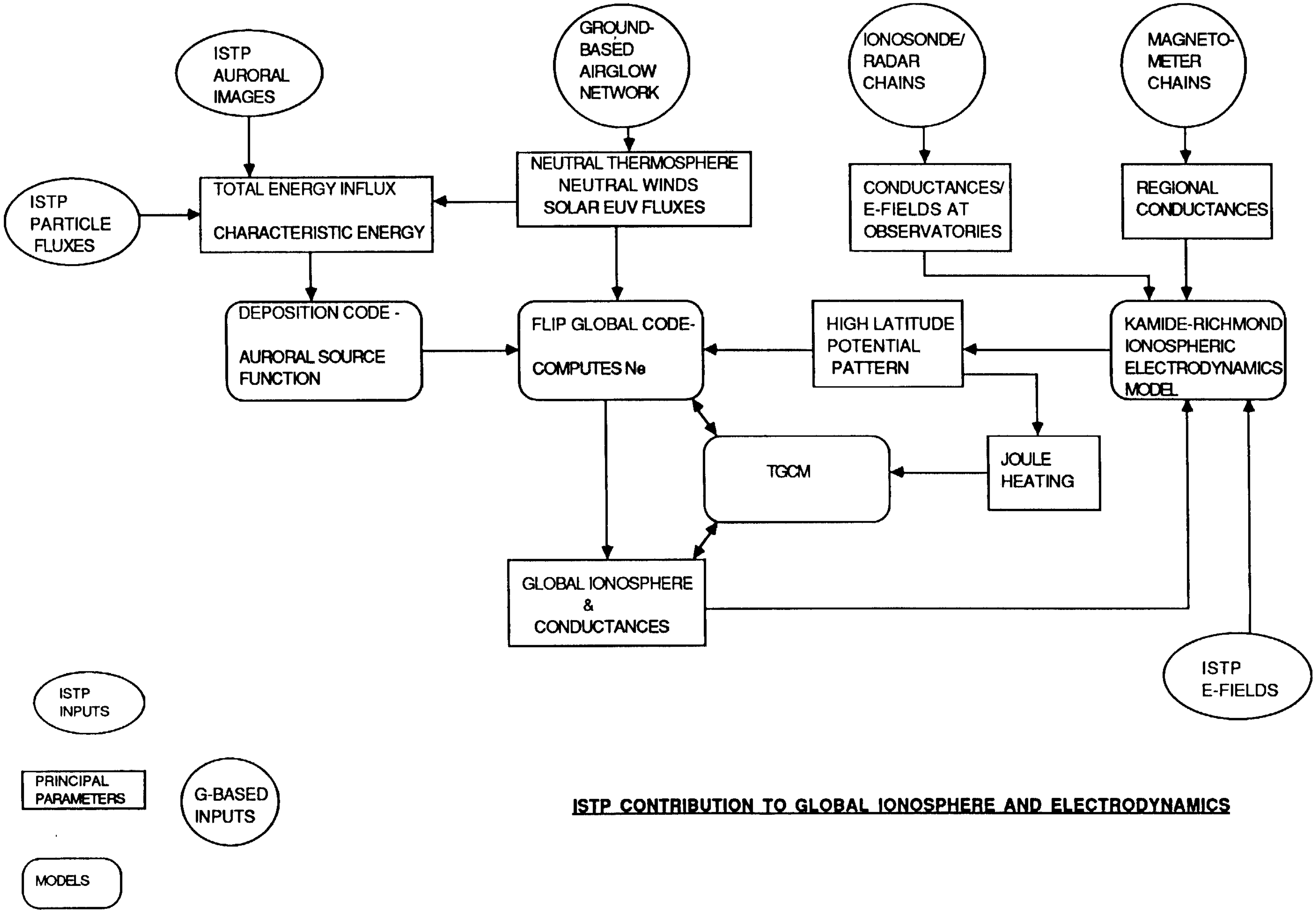

ISTP CONTRIBUTION TO GLOBAL IONOSPHERE AND ELECTRODYNAMICS

Figure 4.9

istpq005

We believe that the science priorities developed here will significantly advance our understanding of thermospheric, ionospheric magnetospheric coupling. The role of the ISTP database will be to provide near-continuous global coverage of key inputs to the system on a 30 second temporal grid allowing the actual response of the high and low latitude ionosphere and thermosphere to all significant energy sources to modeled in a time evolution manner.

This scheme is a very ambitious one, requiring large computing resources and excellent coordination between NASA and the NSF's groundbased network of aeronomy stations. However, it is highly viable. It can be done, and should be done.

Reprints of relevant papers published on this work are attached in Appendix A.

5. Assessment of Optimizations Possible in UV Imaging Systems

In this study, NASA's future needs in ultraviolet imaging were assessed, and possible optimizations evaluated. The following instrumental requirements were identified for the post ISTP area in order to meet the scientific goals of the future.

1. A capability will be needed to image the weak aurora from space.

2. It was noted that strategic planning activities by NASA Headquarters during the late 90's had identified imaging of magnetospheric extreme ultraviolet emissions as a key goal for the future. At that time, however, the technology did not exist to provide the spectral purity and sensitivity needed to successfully image the key ions of the magnetosphere. Specifically, emissions of ionized helium and atomic oxygen at 304 Å and 834 Å respectively were identified as the prime emissions for imaging. Two-dimensional imaging of the magnetosphere could provide the first coherent 3-D picture of the ion populations by tomographic inversion of the images.

The above two goals translate into the following new technology requirements:

- Better VUV filters than those developed for ISTP

- A new class of instrument is needed with 100 times greater sensitivity than the existing EUV capability, with 50 Å spectral filtering.

A study was carried out to investigate ways of increasing further the performance achieved with the ISTP filters developed mainly under NAS8-37586. This problem was solved with two new technology developments:

1. The development of Π multilayer coatings - a new design concept.

2. The use of multiple reflectors to improve resolution.

A detailed report on the approach has been submitted for publication in Applied Optics under the title, "Multiple Reflectors as Narrowband and Broadband VUV Filters".

This technology resulted in a decrease in bandwidth of the ISTP filter at 1356 Å, for example, from ~5.0 nm to 3.2 nm with an increase in transmission from ~25% to ~40%. The work was also presented at the Fall Meeting of the American Geophysical

Union in San Francisco, California, December 1990. A copy of these reports is attached as Appendix B.

In addressing the question of extreme ultraviolet imaging, the thin film design program developed for the VUV was applied to the EUV region at 83.4 nm. Materials were identified which could serve as multilayer coatings in this wavelength regime.

Coatings with 60% reflectance at 83.4 nm with out-of-band reflectance of 5% were designed. These coatings were incorporated into an EUV imager design in a highly innovative way; the design requires no actual filters in the system. The ISTP UVI instrument was selected for the imager optical design. This is a three-mirror system. It was found that by placing the reflective filter coating directly on the mirror surfaces, the mirrors could be used simultaneously as both the imaging and filtering elements. The design yielded a net system efficiency of ~20% compared with ~0.2% achieved with existing technology, thus providing two orders of magnitude improvement in sensitivity, which meets the sensitivity specifications for magnetospheric imaging of O^+ ions.

This work was reported in a CSPAR presentation to the University President, Mr. J. Moquin, on January 22, 1991. Copies of the relevant charts used are included in Appendix C.

SA51A-8 1052h

Evolution of Three-Dimensional Plasma Clouds in the Ionosphere

T-Z Ma and R W Schunk (Center for Atmospheric and Space Sciences, Utah State University, Logan, Utah 84322-4405)

A three-dimensional time-dependent model for the motion of plasma clouds in the ionosphere has been developed. In the model, the ions created from the released neutral gas and the background ions are treated separately so that the acceleration of the background ions and the deceleration of the cloud ions can be calculated. The model takes account of the finite conductivity along the magnetic field, pressure gradients, stress tensor, inertial effects, collisions, thermospheric winds, and current coupling between the cloud and background ionosphere. Studies are being conducted to contrast the expansion characteristics of both negative and positive ion clouds, long thin cloudlets and nearly spherical clouds, clouds with and without background neutral winds, and clouds that are both preionized and photoionized. Some of the cloud expansion features will be presented.

SA51A-9 1106h

Numerical Simulations of Expansion of a Plasma Cloud

C B Chen and N Singh (Department of Electrical and Computer Engineering, University of Alabama in Huntsville, Huntsville, AL 35899; 205–895–6678)

The dynamics and expansion of plasma clouds created by chemical releases in space is a complex problem. Some kinetic aspects of the dynamics are examined by means of one– and two–dimensional numerical simulations using Vlasov and PIC codes. The role of electron dynamics in the expansion is examined through the evolution of the electron velocity distribution function inside the cloud. The two–dimensional PIC code is used to predict the potential structure when the size of the cloud is varied. The evolution of the perpendicular electric fields near the boundaries of the cloud and their penetration into the ambient plasma affect the composite potential structure, which, in turn, affects the field–aligned plasma expansion. Conditions under which field–aligned plasma expansion is the main feature of the dynamics of the cloud will be presented.

SA51A-10 1120h

Generation of Equatorial Spread-F by Cosmoids - Comparison of Theory and Recent Experiments

M Dubin (NASA/Goddard Space Flight Center, Code 916, Greenbelt, MD 20771; 301-286-5475)

A theory for the formation of equatorial spread-F from the interaction in the F region of hypervelocity particle streams formed from dispersed long-period meteoroids, cosmoids, was presented several years ago, but evidence for a cosmoid population was assumed and the upward motion of spread-F observed with incoherent scatter techniques could not be explained. The theory, however, was able to explain the formation of the electron bite-outs or bubbles, the pre-midnight occurrence, the seasonal variations and latitude dependence of spread-F. The theory explained the ion composition as the presence of Fe^+, the fine structures observed with radar and the scintillations at GHz frequencies. Recent analysis of Pioneer 10 and 11 measurements has supplied evidence for the existence of cosmoids in interplanetary space and their dispersion characteristics. A radar meteor signature of dispersed cosmoids has at last been detected at 2 MHz to 140 km altitude. Chemical release experiments were used to demonstrate the formation of bite-outs by electron attachment and to detect Joule heating in the spread-F region. Shaped-charge chemical releases produced measurable ionization, demonstrating the ease of ion pair formation from critical velocity effects, thus explaining the upward motions measured with incoherent scatter radar. Furthermore, the discovery of sudden neutral sodium layers and sporadic Fe layers related to sporadic E represent another signature of the cosmoid population in the E region. An overview of the theory and experimental evidence will be presented.

SA51A-11 1134h

Electric Field Formation at Solar Cell Edge Regions

H Thiemann (Thiemann & Noack, Längenhardstr. 9, D-7800 Freiburg, West Germany)
R W Schunk (Center for Atmospheric and Space Sciences, Utah State University, Logan, Utah 84322–4405)

Ground tests of negatively biased solar array test modules in a simulated LEO-plasma environment identified the solar cell edge region as a critical location. Arc discharges cause carbonization spots along the cell peripheries at the Kapton substrate. Long-term exposure of solar arrays under such conditions will lead to short circuits and, eventually, a complete solar array power loss. For a quantitative assessment of this problem, we performed appropriate self-consistent computer experiments, simulating the solar cell-substrate-interface. The interaction is controlled by the electrical and the secondary emission properties of the target. We will present results on the formation of strong electric fields, their dynamic features, strengths, directions and locations.

SA51A-12 1148h

The Dynamics of Finite-Sized, Low-β, Plasma Clouds Injected at an Angle to a Background Magnetic Field

T Neubert and R H Miller (Both at: Space Physics Research Laboratory, University of Michigan, Ann Arbor, MI 48109-2143)
O Buneman (Space, Telecommunications, and Radioscience Laboratory, Stanford University, Stanford, CA 94305-4055)
K-I Nishikawa (Department of Physics and Astronomy, University of Iowa, Iowa City, Iowa 52242)
R Roussel-Dupre (Space Science and Technology, Los Alamos National Laboratory, Los Alamos, NM 87545)

The dynamics of finite-sized, low-β, plasma clouds moving at angles to a background magnetic field have been studied by means of a new three-dimensional electromagnetic particle simulation code. The onset of electric and magnetic fields, the formation of charge layers, and the "braking" of the plasma cloud are studied for a range of ambient plasma and beam parameters. The electromagnetic radiation for a finite-sized cloud is compared with earlier two-dimensional analytical and numerical results and to observations from sounding rockets, space shuttles and satellites in the Earth's ionosphere and magnetosphere.

SA52A CA: 313 Fri 1330h

Chemical Release Experiments in Space II

(joint with SM)

Presiding: P A Bernhardt, Naval Research Lab

SA52A-1 1330h INVITED

The NICARE Experiments - An Overview

D.G. Tall

Paul A Bernhardt (Space Plasma Branch, Plasma Physics Division, Naval Research Laboratory, Washington, DC 20375; 202-767-0196)

The releases of electron attachment materials into the mid-latitude and equatorial ionospheric have been shown to be effective generators of (1) large scale plasma depletions, (2) enhanced plasma waves, and (3) bright airglow clouds. During the Negative Ion, Cation Release Experiments (NICARE-1 and -2), nickel carbonyl, triflurومethyl bromide, and sulfur hexafluoride were released between 300 and 380 km altitude into the dusk ionosphere. The experiments were conducted from rockets launched from the Wallops Flight Facility, Virginia and from the Kwajalein Missile Range, Marshall Islands. For comparison, NICARE-2 also contained a chemically inert, atomic release to estimate the effect of "snow-plow" density changes. The electron attachment molecules produced localized density reductions with factors ranging between 10^2 and 10^4. The density changes were measured with in situ Langmuir probes, radio beacon signals, and incoherent scatter radar signals. Plasma waves from DC to over several MHz were stimulated by the releases. Some of the new wave modes can be directly traced to the presence of negative ions in the plasma. Enhanced optical emissions were the result of chemiluminescent reactions between the neutral and plasma components of the releases and background environment.

Research supported by ONR and NASA.

SA52A-2 1350h

Simulations of High (Orbital) Velocity Releases of Electron Attachment Materials in the Ionosphere*

W A Scales and P A Bernhardt (Space Plasma Branch, Plasma Physics Division, Naval Research Laboratory, Washington DC 20375; 202-767-3630)

Two-dimensional numerical simulations of high (orbital) velocity releases of electron attachment material clouds across the geomagnetic field in the *F* region are presented. The electrostatic simulation model includes electron attachment and mutual neutralization chemistry, self-consistent electric fields, three species transport and ion inertia. The dynamics of the plasma irregularities produced are studied at early and at late times after release. At early times, the plasma enhancement produced shows steeping of the backside and generation of vortices due to a Kelvin-Helmholtz instability. At late times when the cloud has slowed due to collisions, the plasma depression produced shows structuring due to the E × B interchange instability if a background neutral wind is present. The effects of the variation of the ion-neutral collision frequency with altitude on the irregularity structuring will be discussed in detail.

*Research sponsored by ONT

SA52A-3 1405h

Electric Field and Langmuir Probe Measurements in Chemically Modified Ionospheres*

C L Siefring, P Rodriguez, D G Haas, M M Baumback, D N Walker, P A Bernhardt, (Space Plasma Branch, Plasma Physics Division, Naval Research Laboratory, Washington, DC 20375-5000)

A sophisticated set of in-situ plasma diagnostics have been developed to study the perturbation effects of chemical releases on the ionosphere. Electric field, plasma wave and Langmuir probe data taken during the NICARE 1 & 2 experiments will be discussed with an emphasis on newly developed measurements. The Langmuir Probe measurements characterize the electron density depletions or enhancements and electric field measurements provide information on cloud polarization. Electrostatic plasma oscillations are almost always found in the highly disturbed regions near a chemical releases. Our plasma wave receiver can provide information on the spectral, temporal and k-space characteristics of the plasma waves over a broad frequency range (DC to 10 MHz). We believe these measurements will answer many critical questions relating to effectiveness of various chemicals as ionospheric perturbation sources.

*Research supported by ONR and NASA.

SA52A-4 1420h

Negative Ion Plasma Waves Observed in the NICARE Chemical Release Experiments*

P Rodriguez, C L Siefring, D G Haas, P A Bernhardt, P V Nuygen, M M Baumback, D N Walker, (Space Plasma Branch, Plasma Physics Division, Naval Research Laboratory, Washington, DC 20375-5000)

The release of several electron-attachment chemicals (SF_6, $Ni(CO)_4$, and CF_3Br) in the ionosphere by the NICARE 1 and 2 sounding rockets have produced local plasmas in which the negative charge is carried by a heavy ion and in which there are none or very few electrons present. Such a plasma corresponds to a new environment for space experiments and we have observed several varieties of low frequency electrostatic waves which appear to be "negative ion plasma waves." We report the observations of waves based on electric field and plasma density measurements taken with the NRL electric field sensors and current probes. Electric field and plasma density fluctuations within the electron-depleted ionospheric "hole" are discussed, with an illustration of the evolution of the wave spectrum as the diagnostic vehicle leaves the region of electron depletion and re-enters the normal background ionosphere. The possible effects of wave normal orientations on the measured spectrum are discussed. It is believed that these experiments have produced the first collisionless space plasma in which negative ion plasma waves have been detected.

*Research supported by ONR and NASA.

SA52A-5 1435h

Far Ultraviolet Spectrometer Observations for the NICARE Rocket Experiment

A B Christensen and J B Pranke (Both at: Space Sciences Laboratory, The Aerospace Corporation, PO Box 92957, Los Angeles, CA 90009)
P A Bernhardt (Naval Research Laboratory, 4555 Overlook Avenue, SW, Washington, DC 20375-5000)

A 1/8 m Ebert-Fastie spectrometer which scanned the far ultraviolet wavelength range from 125 to 149 nm at 1.0 nm spectral resolution was included in the NICARE rocket payload launched 23 October 1989 from Wallops Island, VA. The instrument viewed perpendicular to the rocket spin axis and recorded emissions from OI (130.4), OI (135.6) and a feature near 148.0 nm, possibly a carbon line, that were enhanced during some of the chemical releases. The absolute intensity of the emissions and comparison with expected airglow emission rates will be presented.

SA52A-6 1450h

HF Observations of Ionospheric Depletions Produced by Chemical Releases

T. J. Fitzgerald, P. A. Argo, and R. C. Carlos (Los Alamos National Laboratory, SST-7, MS D466, P.O. Box 1663, Los Alamos, New Mexico 87545; (505) 667-1542)

We have made observations of the ionospheric depletions produced by the NICARE I and II chemical releases using

APPENDIX A

JOURNAL OF GEOPHYSICAL RESEARCH, VOL. 95, NO. A7, PAGES 10,337–10,344, JULY 1, 1990

Auroral Modeling of the 3371 Å Emission Rate: Dependence on Characteristic Electron Energy

P. G. RICHARDS

Computer Science Department and Center for Space Plasma and Aeronomic Research
University of Alabama in Huntsville

D. G. TORR

Physics Department and Center for Space Plasma and Aeronomic Research
University of Alabama in Huntsville

We have developed an efficient two-stream auroral electron model to study the deposition of auroral energy and the dependence of auroral emission rates on characteristic energy. This model incorporates the concept of average energy loss to reduce the computation time. Our simple two-stream model produces integrated emission rates that are in excellent agreement with the much more complex multistream model of Strickland et al. (1983) but disagrees with a recent study by Rees and Lummerzheim (1989) that indicates that the N_2 second positive emission rate is a strongly decreasing function of the characteristic energy of the precipitating flux. Our calculations reveal that a 10 keV electron will undergo approximately 160 ionizing collisions with an average energy loss per collision of 62 eV before thermalizing. The secondary electrons are created with an average energy of 42 eV. When all processes including the backscattered escape fluxes are taken into account, the average energy loss per electron-ion pair is 35 eV in good agreement with laboratory results.

1. INTRODUCTION

There is currently renewed interest in the use of auroral optical emission rates to deduce the characteristics of the precipitating particle fluxes, and ultimately, the global auroral energy input to the Earth's upper atmosphere. Images from the Dynamics Explorer satellite have been used by *Rees et al.* [1988] to calculate the energetic electron flux and its characteristic energy. Imaging instruments planned for the ISTP mission will monitor key UV emissions on a global scale for the express purpose of determining the global energy input.

Early work in determining auroral particle characteristics from emissions concentrated on the use of the ratios of atomic oxygen emission rates (6300 Å, 5577 Å) to molecular nitrogen ion emission rates (3914 Å, 4278 Å) to deduce the incident auroral spectrum [*Rees and Luckey*, 1974; *Vallance Jones*, 1975; *Shepherd et al.*, 1980; *Strickland et al.*, 1983]. The higher energy auroral electrons penetrate deeper into the thermosphere where the relative proportion of atomic oxygen is smaller. Thus the ratio of atomic to molecular emission rates decreases with increasing electron energy. Unfortunately, chemical processes play an important role in the atomic oxygen emissions and it is difficult to separate the effects caused by the characteristics of the auroral energy flux from the effects caused by changes in the atmospheric composition. Therefore, it would be useful to find an emission rate ratio that is sensitive to the auroral characteristics but which is not complicated by chemical factors.

Recently, *Rees and Lummerzheim* [1989] suggested that the ratio of the second positive to first negative emission rates could be used to determine the characteristic energy of the auroral electron flux. Using an auroral electron model developed by *Lummerzheim et al.* [1989], *Rees and Lummerzheim* [1989] found that the N_2 second positive (3371 Å) emission rate decreases substantially with increasing characteristic energy of the auroral electrons while the N_2^+ emission rates are almost constant. This ratio would be an attractive alternative to those used previously because it would be independent of atmospheric composition and both emissions are prompt, thus eliminating chemical effects. Unfortunately, the calculations of *Rees and Lummerzheim* [1989] are in conflict with the earlier calculations by *Daniell and Strickland* [1986] who found that the 3371 Å emission rate was nearly independent of the characteristic energy.

The experimental evidence also seems to be in conflict. *Rees and Lummerzheim* [1989] present data from high flying aircraft that support their theoretical calculations. On the other hand, *Solomon* [1989] presented data from the visible airglow instrument on the Atmosphere Explorer C satellite showing that the ratio of the N_2 3371 Å to N_2^+ 4278 Å emission rates has only a small dependence on the characteristic energy, which can be accounted for by contamination of the 3371 Å second positive emission by the Vegard-Kaplan (0-9) band. The VAE data support the earlier calculations of *Daniell and Strickland* [1986] and *Strickland et al.* [1983]. Solomon was able to reproduce the observed ratios using his own two-stream auroral electron deposition code. We note that the experimental data presented by *Solomon* [1989] for the ratio of N_2 3371 Å to N_2^+ 4278 Å is in excellent agreement with the ratio of N_2 3371 Å to N_2^+ 3914 Å that was measured on a 1974 rocket flight by *Sharp et al.* [1979].

Paper number 90JA00233.
0148-0227/90/90JA-00233$05.00

The source of the discrepancy between the models is difficult to understand. Both *Rees and Lummerzheim* [1989] and *Strickland et al.* [1983] use relatively complete multi-stream models. The model used by *Solomon* [1989] is a simpler two-stream model and his calculations are in agreement with the calculations of *Strickland et al.* [1983] and *Daniell and Strickland* [1986] which show little variation in the 3371 Å to 3914 Å emission rate ratio as a function of characteristic energy. In this paper we present calculations of a number of important emission rates obtained from a two-stream auroral electron model that we have developed. The calculated emission rates for the 3371 Å emission rate and a number of other emission rates are in accord with the earlier calculations of *Strickland et al.* [1983] and *Daniell and Strickland* [1986] for the dependence on characteristic energy of the precipitating flux. However, mainly due to the use of a revised cross section, our atomic oxygen 1356 Å emission rate is a factor of 2.5 lower than that calculated by *Strickland et al.* [1983].

2. MODEL

2.1. *General Principles*

The model that we have developed is based on the two-stream photoelectron flux model of *Nagy and Banks* [1970] that was subsequently extended to 500 eV and combined with a continuous energy loss model to calculate auroral electron fluxes by *Banks et al.* [1974]. Although both our model and the model of *Solomon et al.* [1988] have origins in the *Nagy and Banks* [1970] two-stream model, they have evolved substantially along entirely separate paths. Our model owes much to our earlier work with the ionospheric photoelectron flux [*Richards and Torr*, 1984; 1985a].

By incorporating a variable energy grid developed by *Swartz* [1985] and a variable altitude grid we have been able to extend the two-stream model up to energies greater than 20 keV. This has eliminated problems encountered by *Banks et al.* [1974] in matching the continuous slowing down approach that they used above 500 eV with the two-stream approach they used below 500 eV. The continuously variable altitude grid allows altitude steps of less than a kilometer below 90 km up to 50 km at 500 km with a manageable number of grid points.

Further economy in computer time is achieved by introducing the concept of an average energy loss for an excitation or an ionization event. This concept allows the use of only the total excitation and ionization cross sections instead of treating each partial excitation or ionization process separately. That is, the excitation (or ionization) is treated as arising from a single average state for each thermospheric species. The average energy loss depends on the species and also on the energy of the primary electron. The calculation of the emission rates then becomes a two stage process with just the total cross sections being needed to calculate the electron flux as a function of energy and altitude in the first stage. In the second stage, the partial cross sections are folded with the electron fluxes to produce the excitation rates.

For each of the 3 main neutral atmospheric components (O, O_2, N_2) the total cross sections are made up of partial cross sections from the numerous electronic states of each species each corresponding to a different energy state of the atom or molecule. In addition, each electronic state of a molecule can be created in any one of a large number of vibrational energy states. A complete evaluation of the electron flux would require the separate accounting of all these energy losses which we have replaced with a single, energy dependent average energy loss for the excitation and ionization of each of the three main thermospheric species O, O_2, and N_2.

The treatment of excitation processes is relatively straightforward; the average energy loss is specified and the electrons deposited in the correct lower energy bin. However, ionizing collisions are more complex because of the production of secondary electrons which may be produced with energies ranging from 0 up to $E_p - I_i$ where E_p is the energy of the primary electron and I_i is the ionization potential of the state i being produced. We follow the approach of *Banks et al.* [1974] and designate the higher energy electron as the degraded primary and the lower energy electron as the secondary. This means that the maximum secondary energy is then $(E_p - I_i)/2$ as is the minimum energy of the degraded primary. We treat ionization as arising from a single state with an average ionization potential I and we use the measured secondary electron distributions of *Opal et al.* [1971] to determine the average energy E_s of the secondary electrons produced by an electron of energy E_p (we note that the measured secondary electron distributions are in fact a sum of the contributions from all the ionization states). The average energy of the degraded primaries is then $E_p - I - E_s$. A separate ionization potential could be used for each species but a further improvement in computational efficiency can be made by observing that the ionization potentials and secondary electron distributions are similar enough that a single ionization potential and secondary electron distribution for all 3 major species will suffice. Since N_2 is the most important species in aurora, we adopt the N_2 ionization characteristics. At each electron energy, the total number of secondary electrons from O, O_2, and N_2 is calculated and then they are distributed according to the measured secondary electron distributions of *Opal et al.* [1971]. The model has been found to conserve energy to better than 5% for characteristic energies in the range .1 to 20 keV.

2.2. *Average Ionization Potentials*

The calculation of the average ionization potential follows from the knowledge of the ionization potentials and the partial cross sections for the various ionization states of each of the thermospheric species. For example, N_2 ionization results in the formation of the X, A, and B states of N_2^+ and also N^+ which arises from several higher lying states that dissociate. The ionization potentials for the X, A, and B states are 15.6, 16.8, and 18.8 eV respectively while the bulk of the N^+ probably arises from a state with a threshold near 37 eV [*Erdman and Zipf*, 1986]. The actual energy lost by the primary electrons may be greater than threshold due to the ions being vibrationally excited and because, in the case of dissociative ionization, the atomic fragments are observed to carry substantial kinetic energy [*Liliana and Stockdale*, 1975]. To complete the calculation of the average ionization energy for N_2 we also need the ratios of the partial cross sections. We examine the high energy case first where the proportions of the various partial cross sections are practically constant and the calculation is straightforward. Above approximately 100 eV, dissociation accounts for ~20% [*Rapp et al.*, 1965] and the B state ~10% [*Borst and Zipf*, 1970] of the total cross section. According to *Cartwright et al.* [1975], the X and A state cross sections are approximately equal (that is, ~35%). Using these percentages for the partial cross sections and ionization potentials given above, the average ionization potential is ~20 eV for high energy electron impact ionization of N_2. We now examine the low energy average energy loss per collision. The average ionization potential begins at 15.6 eV at threshold when the X state is produced but increases to ~16 eV above 17 eV when the A state threshold is reached. There is only a marginal increase when the B state threshold is reached at 18.8 eV because it accounts for less than 10% of the total cross section at these energies and the energy loss of 18.8 eV is only marginally larger than 16.8 eV. After about 30 eV dissociative ionization becomes important. The ionization potential then rises steadily to approximately 19 eV at 50 eV before leveling off toward 20 eV at high energies.

A similar calculation yields an average ionization potential of approximately 18 eV for both O and O_2, at high energies. Because N_2 is the dominant constituent and all three ionization potentials are similar, we use the average N_2 ionization potential for all three species. This simplifies the calculation and reduces the computation time without introducing significant errors. The adopted ionization and excitation energy losses as a function of primary electron energy are shown in Figure 1. This figure also shows the average energy of the secondary electrons as a function of the primary energy. Below 25 eV the ionization potential is assumed to be 16 eV while above 25 eV it is represented by $10\,(1+(1-15/E)^{1/2})$ eV.

2.3. *Average Secondary Electron Energy*

To obtain the secondary electron distribution we adopt the *Banks et al.* [1974] parameterization of the *Opal et al.* [1971] measured distributions. The probability of a secondary electron of energy E_s is given by

$$P_s(E_s) = \frac{A}{1+(E_s/\bar{E})^2} \qquad (1)$$

where $A = [(\bar{E}\arctan(E_m/\bar{E})^{-1}]$ is a normalization factor that ensures a total probability of unity when integrated over all secondary energies from 0 to $E_m = (E_p - I)/2$ and $\bar{E}$=14 is an empirical normalization factor. The product of E_s and Equation 1 integrated over energy yields the average secondary electron energy for a primary energy E_p as

$$E_{av} = 0.5\ A\ \bar{E}^2 \ln\left(1+(E_s/\bar{E})^2\right) \qquad (2)$$

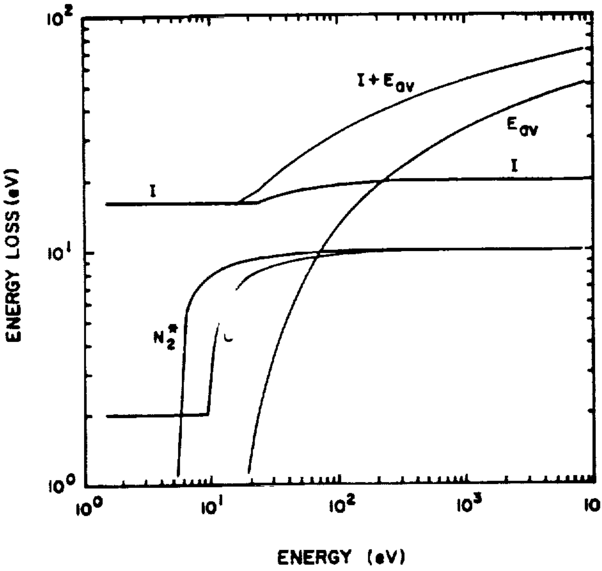

Fig. 1. Average energy losses per collision and average secondary electron energies (E_{av}) as a function of primary electron energy. The average ionization potential is labelled I and the total energy loss per ionization is labelled I+E_{av}. The average excitation potentials are indicated by an asterisk and the O_2 excitation potential is set equal to that of N_2. Note that below 5 eV, the N_2 excitation potential is set at 1 eV.

The dependence of the average secondary energy on the primary energy is shown in Figure 1 along with the average total energy loss of the primary ($I + E_{av}$). The average energy of the secondaries increases steadily from 0 near threshold to 52 eV for 10 keV primary electrons. The total energy loss per ionizing collision for 10 keV electrons is 72 eV, when the 20 eV ionization potential is included. The average energy of the secondaries is approximately equal to the ionization energy for 200 eV primary electrons.

A quantity of interest, in relation to energy degradation of high energy electrons, is the average energy required to produce each electron-ion pair. The average energy required to produce each electron-ion pair is a quantity that is independent of electron energy and is also remarkably independent of the species being ionized. The experimental value for the energy lost per electron-ion pair for high energy electron is 35 eV [*Valentine and Curran*, 1958]. This energy loss per electron-ion pair was used in early auroral electron deposition codes [Rees, 1963; *Rees et al.* 1969; *Rees and Jones*, 1973].

An approximate value for the energy loss per electron-ion pair can be deduced by using the average energy losses depicted in Figure 1, assuming that for electron energies above approximately 100 eV the energy lost to excitation collisions is small and can be neglected. With this assumption, it requires about 160 ionizing collisions to thermalize a single 10 keV electron. Thus, on the average, 62 eV is lost in the creation of each of the 160 electron-ion pairs. Since the ionization energy is 20 eV for electron energies above 100 eV, the average energy of the secondaries is ~42 eV. This means that the 160 secondary electrons are sufficiently energetic to create one more electron-ion pair each. If all secondaries created an additional electron-ion pair, the total number of pairs would be 320 and the average energy per electron-ion pair would decrease from 62 to 31 eV. In reality this does not happen because, below 100 eV, excitation processes begin to compete effectively with the ionization processes for the available electron energy and the number of additional electron-ion pairs produced by the secondary electrons would be less than 160. In fact, for a 42 eV electron the total ionization and excitation cross sections are approximately equal and only half the secondaries could be expected to produce an additional electron-ion pair. This agrees with our previous calculations that show that a third rather than a half, of the total ionization is created by degraded primaries and secondaries with energies below 100 eV [*Richards and Torr*, 1985b]. Thus the original 10 keV electron would ultimately produce about 240 electron ion pairs and yield an average energy loss per electron-ion pair of 42 eV. This is only an estimate of the energy lost per electron-ion pair and a more detailed calculation including transport is required to determine the actual value. It was pointed out by *Banks et al.* [1971] that escaping backscattered electrons will be lost to the system and act to increase the energy loss per electron-ion pair.

We have summed the total ion production rate in our full auroral calculation, and we obtain an average energy loss per electron-ion pair of 35 eV, which is smaller than our estimate but in agreement with the laboratory measured value. A slightly higher value of 37 eV was obtained by *Fox and Victor* [1988] using their discrete local energy loss method. The reason that the energy lost per electron-ion pair is not a strong function of electron energy has to do with the relationship between the average secondary electron energy and the primary electron energy. Electrons with higher initial energies suffer a greater energy loss per collision as they degrade but they produce higher energy secondaries which are more likely to generate secondary ionization. For example, a 1 keV electron will undergo only 22 ionizing collisions with an average energy loss of 45 eV before it thermalizes. Thus, the secondary electrons have an average energy of only 25 eV compared to the 42 eV for the 10 keV electrons and are much less likely to produce additional ions.

2.4. *Cross Sections*

In a number of previous studies of the ionospheric photoelectron flux we have chosen measured total excitation cross sections that produce good agreement between theory and the photoelectron spectrometer measurements from the AE-E satellite [*Lee et al.*, 1980]. At low altitudes where N_2 is the dominant species, the total cross section obtained from electron mobility studies by *Pitchford and Phelps* [1982] was found to be compatible with the PES measurements. At high altitudes where atomic oxygen is the dominant species, the emission cross sections measured by Zipf and co-workers produced good agreement between theory and PES measurements. These total cross sections for energies below 100 eV have been published by *Richards and Torr* [1988]. Basically the same cross sections have been used in this study but they have been reparameterized to extend them to higher energies.

Above 100 eV, the excitation cross sections decay rapidly with increasing energy and are much less important than the ionization cross sections both because they are smaller and because the energy loss per collision is smaller. The total ionization cross sections are better established than the total excitation cross sections although there are some differences [*Kieffer and Dunn*, 1966]. We have adopted the N_2 and O_2 total ionization cross sections of *Rapp and Englander-Golden* [1965] which have also been used by most other modelers. The total ionization cross section for O is from *Brook et al.* [1978]. The elastic cross sections are very important because of their role in inhibiting transport. We have used the elastic cross sections of *Solomon et al.* [1988] and also their elastic backscatter coefficients. The total cross sections used in our auroral model are shown in Figure 2. Our N_2 total excitation cross section is comparable to that of *Solomon et al.* [1988] below 25 eV but is smaller at higher energies. The differences at high energies have little effect on the calculated fluxes because the excitation cross section is smaller than the ionization cross section. However, differences in cross sections below 30 eV produce comparable differences in fluxes. The N_2 total excitation cross section of *Strickland et al.* [1983] is almost a factor of two larger than ours at all energies and their fluxes would be a factor of two lower below 30 eV, at least below 200 km where N_2 is the dominant species. The cross sections of *Solomon et al.* [1988] and *Strickland et al.* [1983] were obtained by summing the partial cross sections and there is the possibility of double counting some cross sections; for example, those that lead to dissociation. Moreover, *Strickland et al.* [1983] included large

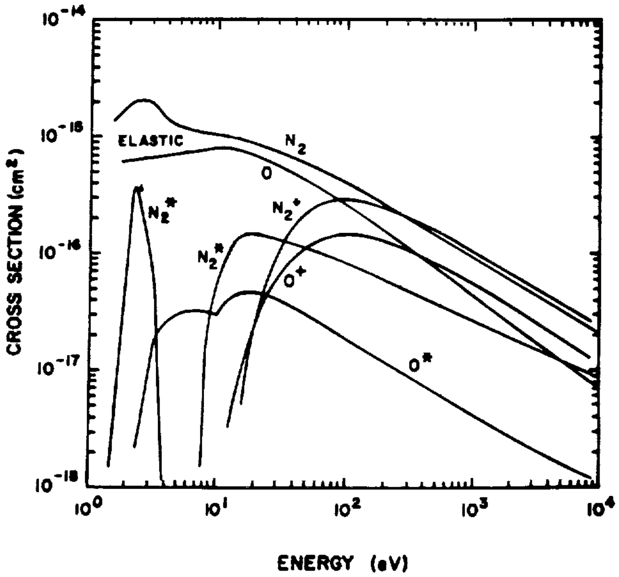

Fig. 2. Total elastic, excitation, and ionization cross sections employed in the model. The ionization cross sections are indicated by a plus while the excitation cross sections are indicated by an asterisk.

Rydberg cross sections from *Green and Stolarski* [1972] which have been revised sharply downward by *Porter et al.* [1976]. There is now good agreement between the total cross section of *Pitchford and Phelps* [1982] and the sum of the partial excitation cross sections of *Cartwright et al.* [1977a,b] as revised by *Trajmar et al.* [1983], below 20 eV. Above 20 eV, the ionization cross section becomes an increasingly important component of the total inelastic cross section and it is not easy to compare the two cross sections.

The total atomic oxygen excitation cross section employed by *Solomon et al.* [1988] is a factor of 2 larger than ours above 15 eV and will produce a similar difference in flux above 250 km where O is the dominant species but the atomic oxygen cross section has little effect on the integrated emission rates. Our atomic oxygen excitation cross section was obtained by summing the measured emission cross sections for 1304, 1356, and 1027 Å [*Zipf and Erdman*, 1985], the 989 cross section from *Gulcicek and Doering* [1988], and the theoretical ^1D and ^1S from *Henry et al.* [1969]. Implicit in this procedure is the assumption that the higher lying triplet and quintet states are included in the 1304 and 1356 emission cross sections via cascade. We have left out some theoretical Rydberg cross sections proposed by *Jackman et al.* [1977] and some minor states that radiate directly to the ground state but for which there is no experimental data. Thus, our cross section must be regarded as a lower limit.

Figure 3 shows the excitation cross sections for the second positive ($C^3\pi_u$) and Lyman-Birge-Hopfield ($a^1\pi_g$) systems of N_2. Also shown is the cross section used for calculation of the $O(^5S)$ 1356 Å emission rate. We obtained this cross section by reducing the measured cross section of *Stone and Zipf* [1974] by the factor 3.1 which is the same factor that the 1304 Å emission cross section of *Stone and Zipf* [1974] was reduced by *Zipf and Erdman* [1985]. The ($C^3\pi_u$) cross section was obtained by multiplying the 3371 Å cross section of *Imami and Borst* [1974] by 4 and the ($a^1\pi_g$) cross section is from *Ajello and Shemansky* [1985].

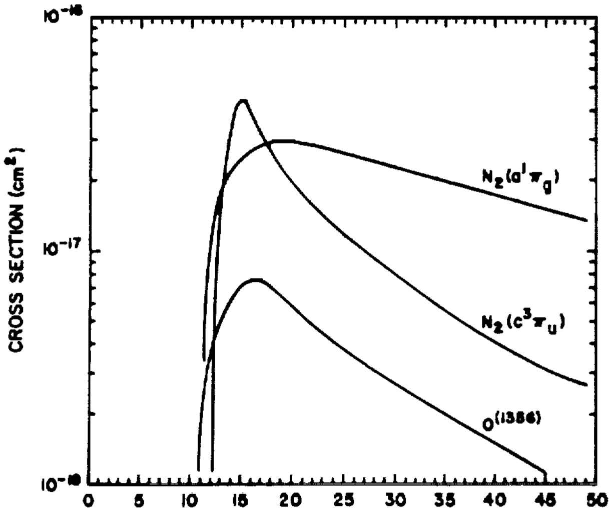

Fig. 3. Cross sections for the three excited states giving rise to the emissions studied in this paper.

We have examined the sensitivity of the emission rate ratios to cross sections and this will be discussed later. In all these calculations we have used the 1 erg cm^{-2}s^{-1} Gaussian incident flux distribution, and the neutral atmosphere employed by *Strickland et al.* [1983].

3. RESULTS

3.1. *Comparison With Previous Work*

We have calculated the N_2 3371 Å, N_2^+ 3914 Å, N_2^+ 4278 Å, O 1356 Å, and several N_2 LBH band emission rates as a function of energy and these are shown in Figure 4. This figure shows that both the 3371 Å and 3914 Å emission rates are independent of the characteristic energy of the precipitating flux for energies above 2 keV in agreement with the results of *Strickland et al.* [1983] and *Daniell and Strickland* [1986]. Not only is the shape in good agreement but, except for the 1356 Å emission rates, the magnitudes are also in good agreement. Although the shape of the 1356 Å curve is in good agreement with that of *Strickland et al.* [1983], the magnitude is a factor of 2.5 lower owing to the use of the revised cross section of *Zipf and Erdman* [1985].

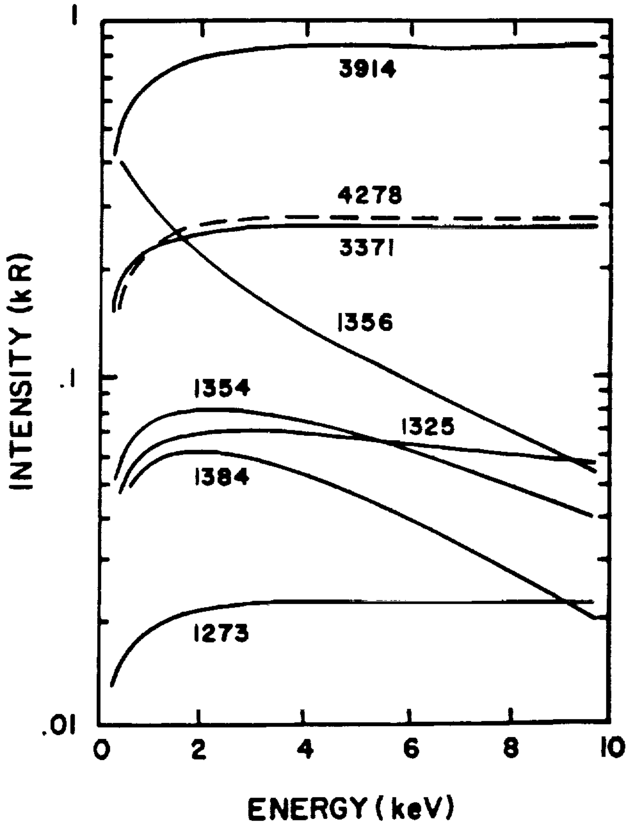

Fig. 4. Calculated emission rates as a function of the characteristic energy for a Gaussian energy distribution with a total incident energy flux of 1 erg cm^{-2} s^{-1}. When differences in cross sections are taken into account, there is excellent agreement with the calculations in Figure 8 of *Strickland et al.* (1983) and Figure 11 of *Daniell and Strickland* (1986).

We have included O_2 Schuman-Runge absorption which affects both the 1356 Å and the 1200-1600 Å LBH bands when the characteristic energies are high and the electrons penetrate to lower altitudes [*Strickland et al.*, 1983]. The ratios of the LBH bands are taken from *Ajello and Shemansky* [1985].

Our calculated second positive to first negative emission rate ratios are within 20% of the measured values for the N_2 emissions. At 10 keV, our 3371 Å to 3914 Å ratio is 0.3 compared to 0.25 from *Sharp et al.* [1979] and our 3371 Å to 4278 Å ratio is 0.98 compared to 0.8 from *Solomon* [1989]. Solomon obtained better agreement between his model ratios and the measured ratios but there is sufficient uncertainty in the input parameters to account for the differences.

3.2. *Sensitivity of Ratios*

We have performed some parameter studies to characterize the sensitivity of the ratio of the second positive to first negative integrated emission rates to possible errors in the model inputs. Obviously, a reduction of 20% in the 3371 Å emission rate cross section would bring the calculated and measured values into excellent agreement but a 30% increase in the N_2 total excitation cross section has a similar effect by decreasing the low energy electron flux which is responsible for most of the 3371 Å emission. Likewise, a 30% increase in the N_2 total ionization cross section above 100 eV reduces the ratio from 0.3 to 0.25 by increasing the 3914 Å production rate. The integrated ratio is not sensitive to changes of up to a factor of two in most other parameters including: the atomic and molecular oxygen inelastic cross sections, the O, O_2, and N_2 elastic cross sections and backscatter coefficients, and the relative concentrations of the species. We estimate a possible error of 10% in our computed average excitation and ionization potentials but this has negligible effect on our computed ratios.

3.3. *Energy Budget*

The incident electron energy flux is initially partitioned into a large number of excitation and ionization processes before it finally emerges as heat for the thermosphere or is radiated into space. Figure 5 shows the gross energy partition amongst ionizations, excitations, thermal electron heating and backscattered escape flux as a function of characteristic energy. N_2 ions capture the greatest share of the available energy (35%). Excitation of N_2 is next with (20%) while only 15% is lost through the escaping backscattered flux. This escape flux is much smaller than the 45% obtained by *Banks et al.* [1974], possibly as a result of the use of different cross sections and backscatter coefficients. Below 1 keV, ionization and excitation of atomic oxygen absorption are important energy sinks for the electron energy, but they become small for high energy incident fluxes. Absorption in molecular oxygen shows the opposite trend, becoming more important with the deeper penetration of the higher energy fluxes. Thermal electrons capture a greater proportion of the available energy, the lower the characteristic energy.

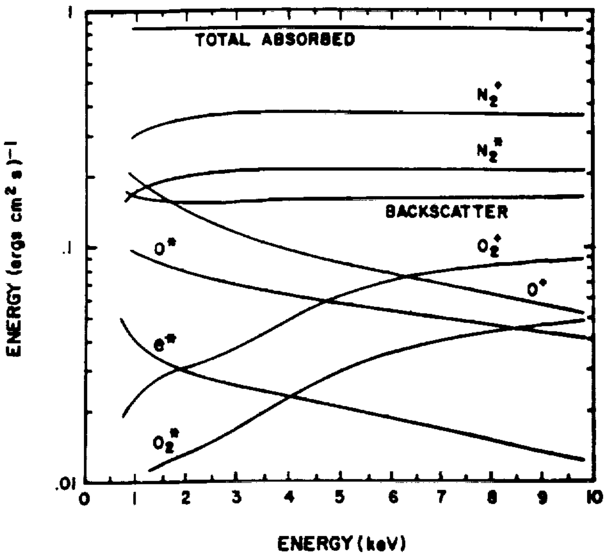

Fig. 5. The initial partitioning of the incident 1 erg cm^{-2} s^{-1} energy flux between ionization, excitation, thermal electron heating, and backscatter as a function of characteristic energy. The largest proportion of the energy (~35%) goes initially into the ionization potential of the N_2^+ while (~20%) goes into N_2 excitation. Only (~16%) is backscattered out of the thermosphere. O is an important absorber of energy at the lowest energies while O_2 becomes increasingly important as the characteristic energy increases.

3.4. *Electron Flux Spectra*

Downward moving fluxes at 120, 174, 223, and 326 km are shown in Figure 6 for a 5 keV incident Gaussian flux with an energy flux of 1 erg $cm^{-2}s^{-1}$. The incident flux can be seen centered at 5 keV in Figure 6. At the two highest altitudes, there is very little degradation of this initial flux but the degradation is noticeable at 174 km and pronounced at 120 km. Because there is so

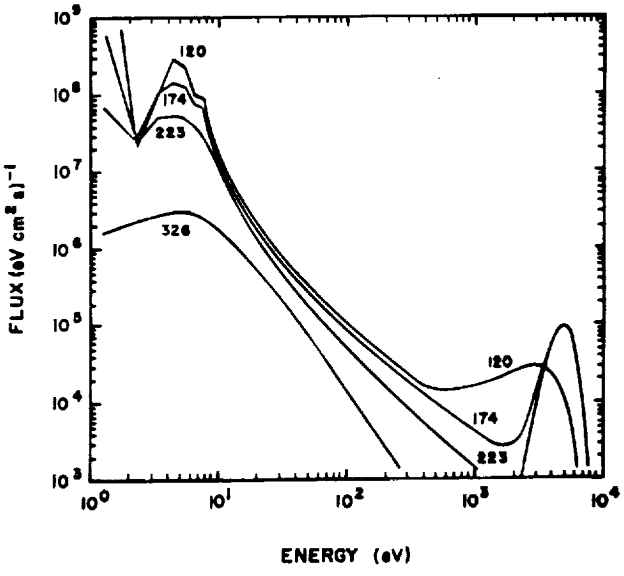

Fig. 6. Downward moving electron flux spectra at several altitudes for a 5 keV Gaussian incident flux. The incident energy flux is 1 erg cm^{-2} s^{-1}.

little interaction with the thermosphere for high energy electrons at the high altitudes, there are few degraded primaries to fill in the region between 300 eV and 5 keV. However, at the lowest altitudes this intermediate energy range is filled in. Comparison of the downward fluxes in Figure 6 with the upward fluxes in Figure 7 reveals that, below 225 km, where transport is inhibited, the electron flux is isotropic for energies less than 300 eV. At 326 km, the upward (escape) flux is a factor of 2 larger than the downward flux at low energies and orders of magnitude larger at intermediate energies.

4. CONCLUSIONS

We have developed an efficient two-stream auroral electron model that incorporates the concept of average energy loss. This model produces integrated emission rates that are in excellent agreement with the more sophisticated multi-stream model of *Strickland et al.* [1983] but is in disagreement with the model of *Rees and Lummerzheim* [1989] with regards to the energy dependence of the N_2 3371 Å second positive emission rate. Our calculations give a value of 35 eV for the average energy lost per electron-ion pair produced independent of primary electron energy and we have explained this behavior in terms of the variation in the energy of the secondary electrons. We find that more than 30% of the initial energy flux is stored initially as ionization energy of N_2^+ while about 20% goes into excited states of N_2 while only 15% is backscattered out of the thermosphere. All other processes are minor except at low incident energies where 20% of the energy is stored in atomic oxygen ions.

Acknowledgments. This work was supported by NSF grants ATM-8713693, ATM-8716036, ATM-8907808, and ATM-8714461; and NASA grants NAGW-922, and NAGW-996 at The University of Alabama in Huntsville.

The Editor thanks R. E. Daniell and M. H. Rees for their assistance in evaluating this paper.

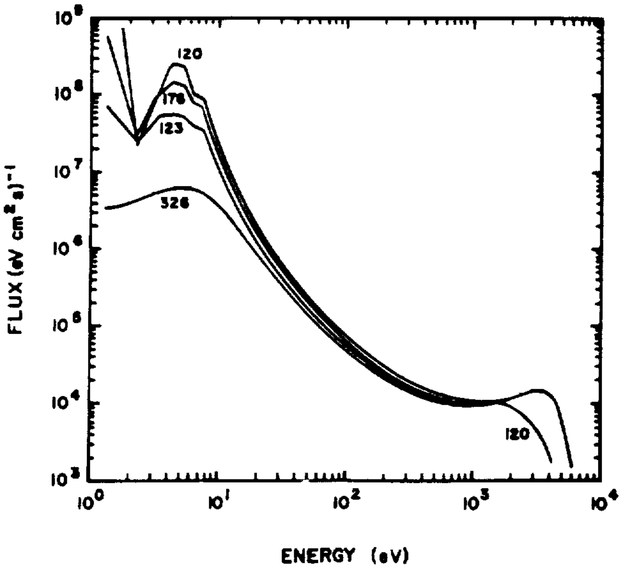

Fig. 7. Upward moving electron flux spectra for the 5 keV Gaussian incident flux shown in Figure 6.

REFERENCES

Ajello, J. M., and D. E. Shemansky, A reexamination of important N_2 cross sections by electron impact with application to the dayglow: The Lyman-Birge-Hopfield band system and N I (119.99 nm), *J. Geophys. Res.*, *90*, (A10), 1985.

Banks, P. M. and C. R. Chappell, and A. F. Nagy, A new model for the interaction of auroral electrons with the atmosphere: spectral degradation, backscatter, optical emission, and ionization, *J. Geophys. Res.*, *79*, 1459, 1974.

Borst, W. L., and E. C. Zipf, Cross section for electron-impact excitation of the (0,0) first negative band of N_2^+ from threshold to 3 keV, *Phys. Rev. A*, *1*, 834, 1970.

Brook, E., M. F. A. Harrison, and A. C. H. Smith, Measurements of the electron impact ionisation cross sections of He, C, O and N atoms, *J. Phys. B*, *11*, 3115, 1978.

Cartwright, D. C., W. R. Pendleton, and L. D. Weaver, Auroral emission of the N_2^+ Meinel bands, *J. Geophys. Res.*, *80*, 651, 1975.

Cartwright, D. C., A. Chutjian, S. Trajmar, and W. Williams, Electron impact excitation of the electronic states of N_2, I, Differential cross sections at incident energies from 10 to 50 eV, *Phys. Rev. A*, *16*, 1013, 1977a.

Cartwright, D. C., S. Trajmar, A. Chutjian, and W. Williams, Electron impact excitation of the electronic states of N_2, II, Integral cross sections at incident energies from 10 to 50 eV, *Phys. Rev. A*, *16*, 1041, 1977b.

Daniell, R. E., and D. J. Strickland, Dependence of the auroral middle UV emissions on the incident electron spectrum and neutral atmosphere, *J. Geophys. Res.*, *91*, 321, 1986.

Erdman, P. W., and E. C. Zipf, Dissociative excitation of the $NI(^5S)$ state by electron impact on N_2: Excitation function and quenching, *J. Geophys. Res.*, *91*, 1986.

Fox, J. L., and G. A. Victor, Electron energy deposition in N_2 gas, *Planet. Space Sci.*, *36*, 326, 1988.

Garstang, R. H., Multiplet intensities for lines $^4S-^2D$ of SII, OII and NI, *Astrophys. J.*, *115*, 506, 1952.

Green, A. E. S. and R. S. Stolarski, Analytic models of electron impact excitation cross sections, *J. Atmos. Terr. Phys.*, *34*, 1703, 1972.

Gulcicek, E. E., and J. P. Doering, Absolute differential and integral electron excitation cross sections of the atomic oxygen ^3P and ^5P states at 30 eV, *J. Geophys. Res.*, *92*(A4), 3445-3448, 1988.

Henry, R. J. W., P. G. Burke and A. L. Sinfailam, Scattering of electrons by C, N, O, N^+, O^+ and O^{++}, *Phys. Rev.*, *178* 218, 1969.

Jackman, C. H., R. M. Garvey, and A. E. S. Green, Electron impact on atmospheric gases, I. Updated cross sections, *J. Geophys. Res.*, *82*, 5081-5090, 1977.

Kieffer, L. J., and G. H. Dunn, Electron impact ionization cross section data for atoms, atomic ions and diatomic molecules: I. experimental data, *Rev. Mod. Phys.*, *38*, 1, 1966.

Lee, J. S., J. P. Doering, T. A. Potemra, and L. H. Brace, Measurements of the ambient photoelectron spectrum from Atmosphere Explorer, I, AE-E measurements below 300 km during solar minimum conditions, *Planet. Space Sci.*, *28*, 947, 1980.

Liliana, D, and J. A. D. Stockdale, Dissociative ionization of molecules by electron impact, II, Kinetic energy and angular distributions of N^+ and N^{++} ions from N_2^+, *J. Chem. Phys.*, *63*, 3898-3906, 1975.

Lummerzheim, D., M. H. Rees, and H. R. Anderson, Angular dependent transport of auroral electrons in the upper atmosphere, *Planet. Space Sci.*, *37*, 109, 1989.

Mahmood, I, and Walter L. Borst, Electron excitation of the (0,0) second positive band of nitrogen from threshold to 1000 eV*, *J. Chem. Phys.*, *61*, 1115, 1974.

Nagy, A. F., and P. M. Banks, Photoelectron fluxes in the ionosphere, *J. Geophys. Res.*, *75*, 6260, 1970.

Opal, C. B., W. K. Peterson, and E. C. Beaty, Measurements of secondary-electron spectra produced by electron impact ionization of a number of simple gases, *J. Chem. Phys.*, *55*, 4100, 1971.

Pitchford, L. C., and A. V. Phelps, Comparative calculations of electron swarm properties in N_2 at moderate E/N values, *Phys. Rev. A 25*, 540, 1982.

Porter, H. S., C. H. Jackman, and A. E. S. Green, Efficiencies for production of atomic nitrogen and oxygen by relativisitic proton impact in air, *J. Chem. Phys.*, *65*, 154-167, 1976.

Rapp, D., and P. Englander-Golden, Total cross sections for ionization and attachment in gases by electron impact I, Positive ionization. *J. Chem. Phys.*, *43*, 1464, 1965.

Rees, M. H., Auroral ionization and excitation by incident energetic electrons, *Planet. Space Sci.*, *11*, 1209, 1963.

Rees, M. H. and R. A. Jones, Time dependent studies of the aurora, II, Spectroscopic morphology, *Planet. Space Sci.*, *21*, 1213, 1973.

Rees, M. H., and D. Luckey, Auroral electron energy derived from the ratio of spectroscopic emissions, 1, Model computations, *J. Geophys. Res.*, *79*, 5181, 1974.

Rees, M. H., and D. Lummerzheim, Characteristics of auroral electron precipitation derived from optical spectroscopy, *J. Geophys. Res.*, *94*, 6799, 1989.

Rees, M. H., D. Lummerzheim, R. G. Roble, J. D. Winningham, J. D. Craven, and L. A. Frank, Auroral Energy deposition rate, characteristic electron energy and ionospheric parameters derived from Dynamics Explorer 1 images, *J. Geophys. Res.*, *93*, 12841, 1988.

Rees, M. H., A. I. Stewart, and J. C. G. Walker, Secondary electrons in aurora, *Planet. Space Sci.*, *17*, 1997, 1969.

Richards, P. G., and D. G. Torr, An investigation of the consistency of the ionospheric measurements of the photoelectron flux and solar EUV flux, *J. Geophys. Res.*, *89*, 5625, 1984.

Richards, P. G., and D. G. Torr, The altitude variation of the ionospheric photoelectron flux: a comparison of theory and measurement, *J. Geophys. Res.*, *90*, 2877, 1985a.

Richards, P. G. and D. G. Torr, On the production of N^+ by energetic electrons, *J. Geophys. Res. 90*, 9917, 1985b.

Richards, P. G., and D. G. Torr, Ratio of photoelectron to EUV ionization rates for aeronomic studies *J. Geophys. Res.*, *93*, 4060, 1988.

Sharp, W. E., M. H. Rees, and A. I. Stewart, Coordinated rocket and satellite measurements of an auroral event, 2, The rocket observations and analysis, *J. Geophys. Res.*, *84*, 1977, 1979.

Shepherd, G. G., J. D. Winningham, F. E. Bunn, and F. W. Thirkettle, An empirical determination of the production efficiency for auroral 6300- Å emission by energetic electrons, *J. Geophys. Res.*, *85*, 715, 1980.

Solomon, S. C., Auroral excitation of the N_2 2P(0,0) and VK(0,9) bands, *J. Geophys. Res.*, *94*, 17215, 1989.

Solomon, S. C., P. B. Hays, and V. J. Abreu, The auroral 6300 Å emission: Observations and modeling, *J. Geophys. Res.*, *93*(A9), 9867, 1988.

Stone, E.J., and E.C. Zipf, Electron-impact excitation of the $^3S^o$ and $^5S^o$ states of atomic oxygen, *J. Chem. Phys.*, *60*, 4237, 1974.

Strickland, D. J., J. R. Jasperse, and J. A. Whalen, Dependence of auroral FUV emissions on the incident electron spectrum and neutral atmosphere, *J. Geophys. Res.*, *88*, 8051, 1983.

Swartz, W. E., Optimization of energetic electron energy degradation calculations, *J. Geophys. Res.*, *90*, 6587, 1985.

Trajmar, S., D. F. Register, and A. Chutjian, Electron scattering by molecules, II, Experimental methods and data, *Phys. Rep.*, *97*, 219, 1983.

Vallance Jones, A., A model for the excitation of electron aurora and some applications, *Can. J. Phys.*, *53*, 2276, 1975.

Zipf, E. C., and P. W. Erdman, Electron impact excitation of atomic oxygen: Revised cross sections, *J. Geophys. Res.*, *90*, 11087, 1985.

P. G. Richards and D. G. Torr, University of Alabama, Research Institute C-10, Huntsville, AL 35899.

(Recieved October 18, 1989;
accepted November 28, 1989.)

JOURNAL OF GEOPHYSICAL RESEARCH, VOL. 95, NO. A6, PAGES 7725–7733, JUNE 1, 1990

The Dependence of Modeled OI 1356 and N_2 Lyman Birge Hopfield Auroral Emissions on the Neutral Atmosphere

G. A. GERMANY AND M. R. TORR

Space Science Laboratory, NASA Marshall Space Flight Center, Huntsville, Alabama

P. G. RICHARDS AND D. G. TORR

University of Alabama in Huntsville, Huntsville, Alabama

Images of the entire auroral oval at carefully selected wavelengths contain information on the global energy influx due to energetic particles and some information on the characteristic energy of the precipitating particles. In this paper we investigate the sensitivity of selected auroral emissions to changes in the neutral atmosphere. In particular, we examine the behavior of OI 1356 A and two Lyman Birge Hopfield (LBH) bands and their ratios to each other with changing atmospheric composition. The two LBH bands are selected so that one lies in the region of strong O_2 absorption (1464 A) and one lies at a wavelength where O_2 absorption is effectively negligible (1838 A). We find that for anticipated average uncertainties in the neutral atmosphere (factor of 2 at auroral altitudes), the resultant change in the modeled intensities is comparable to or less than the uncertainty in the neutral atmosphere. The smallest variations, for example, are for I 1838 (approximately 10 to 20%) while the largest variation is seen in the OI 1356 A emission which is linear with [O] to within 20%. We have also investigated the dependence of these intensities, and their ratios, to much larger changes in the composition (i.e., $[O]/[N_2]$) such as might be encountered in large magnetic storms, or over seasonal or solar cycle extremes. We find that the variation in the I 1356/I 1838 ratio over the equivalent of a solar cycle is less than 50%. The summer-to-winter changes are approximately a factor of 2. The I 1356/I 1838 ratio is a very sensitive indicator of the characteristic energy, showing a change of 13 over the energy range 200 eV to 10 keV. The corresponding change in the LBH long-to-short wavelength ratio is much less (about a factor of 3). However, the latter is insensitive to changes in the neutral atmosphere (<20% changes in LBH emission ratio for large changes in N_2). The three emissions therefore potentially provide a most valuable diagnostic of particle characteristic energy and energy flux.

1. INTRODUCTION

While in situ observations of energetic particles provide accurate information on the particle characteristics at the point of measurement, imaging from space of the entire auroral oval holds the potential for providing details on total auroral energy influx, estimates of the characteristic energy of the auroral particles, and the capability to map and relate the footprint of this derived information back along the magnetic field lines to various regions of the magnetosphere. Auroral imaging in the vacuum ultraviolet permits observations of the regions of interest under both day and night conditions. Work by *Rees and Luckey* [1974] on the ratios of visible emissions, UV emission intensity calculations by *Strickland et al.* [1983], and analysis of UV auroral spectra by *Ishimoto et al.* [1988] all indicate the potential value of using ratios of emission intensities to study auroral processes. A major focus of work in this area at the present time is to establish the quantitative footing on which such determinations can be placed.

With the exception of HI Lyα, the OI multiplets at 1304 Å and 1356 Å and the N_2 Lyman Birge Hopfield (LBH) bands are the most prominent vacuum ultraviolet auroral emissions. The OI 1304 Å emission has a high efficiency for multiple scattering. As a result, it has limited use for actual auroral imaging, although it does have potential value as an indicator of the O concentration. While the 1356 Å emission does undergo multiple scattering, the efficiency is relatively small [*Strickland and Anderson*, 1983] and we ignore multiple scattering for I 1356 for this study. Similar considerations allow us to also ignore multiple scattering for the N_2 LBH emissions that are also considered in this study. The OI 1356 Å emission is absorbed increasingly by O_2 with decreasing altitude. Thus its intensity varies strongly (inversely) with increasing depth of penetration of the incident auroral electrons and hence with increasing energy. The N_2 LBH transitions are electric dipole forbidden and the only prominent excitation mechanism is electron impact. The LBH emission may therefore serve as a direct measure of the total energy flux of charged particles into the atmosphere. The longer wavelength LBH bands, which lie outside the region of substantial O_2 absorption, are useful indicators of the total energy influx, while the long-to-short wavelength LBH intensity ratio provides information on the O_2, and thus also some information on energy. These are the emissions (OI 1356, long and short wavelength LBH) on which we shall concentrate in this study.

The purpose of this paper is to examine the sensitivity of these emissions to both likely uncertainties and anticipated changes in the neutral atmosphere. This is just one step in the process of making quantitative interpretations of auroral images, but an important one. We will consider other aspects (energy spectral characteristics and wavelength spectral extraction) elsewhere. In this paper we conduct a series of sensitivity studies using an auroral emission code that has been developed by our group [*Richards and Torr*, 1990]. The results are discussed below.

2. DESCRIPTION OF AURORAL CODE

The behavior of auroral OI 1356 and N_2 LBH emissions has been studied with the use of an auroral computer model. The model is a two-stream auroral electron energy loss code that determines the energy degradation of the primary spectrum as a func-

Paper number 89JA03771.
0148-0227/90/89JA-03771 $05.00

tion of energy and altitude and determines the production rates of prominent auroral emissions. A more complete description of the program, the selected cross sections, and comparison with other auroral models is given by *Richards and Torr* [1990]. The N_2 ($a^1\pi_g$) cross section, as well as the ratios of the individual LBH bands are taken from *Ajello and Shemansky* [1985]. Attenuation due to molecular oxygen absorption is explicitly computed with O_2 absorption cross sections taken from *Ogawa and Ogawa* [1975] and *Hudson* [1971]. The model currently assumes that O_2 absorption at wavelengths beyond 1750 Å can be ignored.

The model is optimized by incorporating variable energy bins [*Torr et al.*, 1974; *Swartz*, 1985] for the energy grid. To prevent numerical instabilities and violation of energy conservation, the altitude grid is variable to allow small grid steps (less than 1 km) at low altitudes. As a result, energy is typically conserved to within 10%. The code utilizes either the MSIS-86 neutral atmosphere [*Hedin*, 1987] or a user-supplied atmosphere. Either monoenergetic fluxes or a specified energy spectrum may be used. The incident energy spectrum may be modeled as a Gaussian or Maxwellian distribution, after *Strickland et al.* [1983] (hereafter *SJW*), or a user-supplied distribution may be used. All simulations reported below employed a 1 erg cm^{-2} s^{-1} Gaussian incident flux distribution. The Gaussian scale parameter, labeled *W* in *SJW*, has been set equal to 0.25 E_{char} which yields a full width at half maximum of 0.5 $[\ln 2]^{1/2}$ E_{char}, where E_{char} is the characteristic energy.

3. SENSITIVITY STUDIES

The emission studies reported here involved modeling auroral emissions at local midnight at 60 degrees north latitude. Table 1 lists the MSIS parameters used in this study as well as detailing the range of solar activity investigated in the latter part of the study.

TABLE 1. MSIS Model Parameters

	Solar Activity		
	Minimum	Moderate	Maximum
$F_{10.7}$ cm Flux Index	75	110	200
Average $F_{10.7}$ cm Index	75	110	200
Ap Magnetic Activity Index	4	20	100

Geographic latitude, 60 degrees; geographic longitude, 0 degrees; solar apparent time, 0.0 hours; days 173, 356.

Three emission ratios were studied. The first ratio was OI 1356/LBH_{long}, where LBH_{long} designates an N_2 LBH emission not strongly dominated by O_2 absorption. Specifically, the (2,8) band at 1838 Å was chosen for this purpose. Second, the ratio OI 1356/LBH_{short} was also modeled to investigate the relative influence of absorption by molecular oxygen. Here, LBH_{short} is represented by the (1,1) band at 1464 Å. By analogy with the previous definition LBH_{short} is an LBH emission which is strongly absorbed by O_2. The final ratio studied was LBH_{long}/LBH_{short}. The volume emission rates integrated over altitude give the surface brightness or column intensity of the emission which we shall designate I 1356, I 1464, and I 1838. These are the intensities that would be seen by a nadir viewing instrument from above the emission layer.

3.1. *Sensitivity to the Uncertainty of a Single Constituent*

The first question we chose to investigate was the dependence of the selected emissions and emission ratios on the uncertainties at any given time in our knowledge of the neutral atmosphere. We have assumed for this purpose that if we base our calculations on the MSIS-86 model atmosphere, the concentrations of O, O_2, or N_2 at auroral altitudes may on the average be uncertain by as much as a factor of 2. There will be occasions on which the uncertainty will exceed a factor of 2, but typically it will be less. This is similar to studies performed in *SJW*, but extends the investigation to study the dependence of auroral emissions to each of the major atmospheric constituents. In addition, in section 3.2 below, we further extend the study to include larger compositional variations due to seasonal and solar cyclic variations.

The unperturbed, or reference, atmosphere is an MSIS model for high solar activity at summer solstice. Figure 1. Figure 2

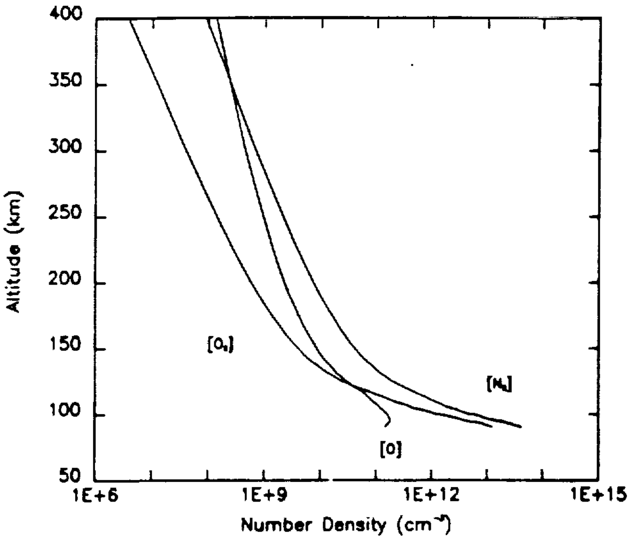

Fig. 1. MSIS-86 reference atmosphere used as the standard case in this study (Day = 173, $F_{10.7}$ = 200, Ap = 100).

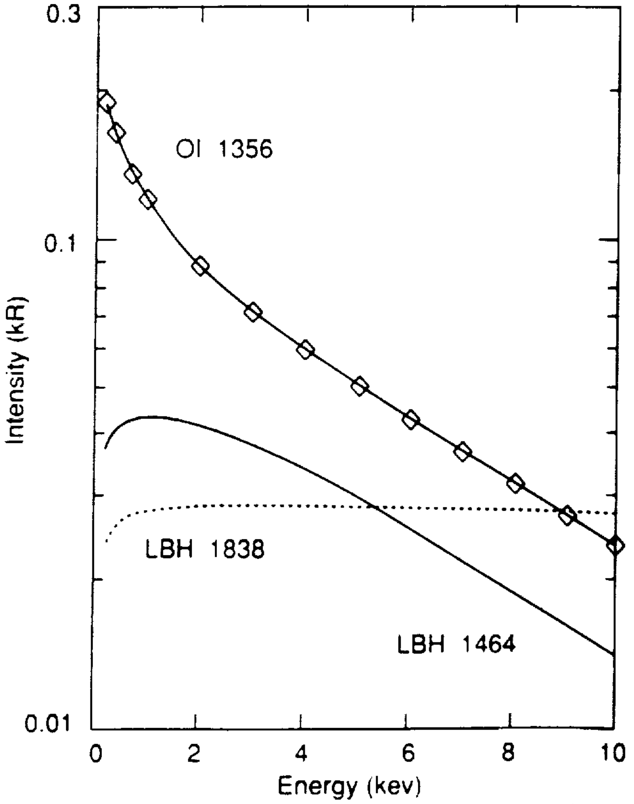

Fig. 2. Nadir viewing column brightnesses (I 1356, I 1464, and I 1838) calculated using the reference atmosphere shown in Figure 1. The diamonds here and in the remainder of the figures show the selected Gaussian characteristic energies for the incident electron energy distribution.

shows the computed I 1356, I 1464, and I 1838 intensities for this model atmosphere as a function of energy over the range 200 eV to 10 keV as determined by our auroral code. In what follows we shall compare these results with those obtained when each of the atmospheric constituents (O, O_2, N_2) is, in turn, individually multiplied by 2 at all altitudes, while the other two are held constant.

Before examining the results of these atmospheric changes, let us consider the possible impact of the changes. Doubling the concentration of a constituent might at first be expected to double the effect of that specie on the column brightness of the monitored auroral emissions. In reality, however, there are a number of possible options in the interaction of the penetrating electrons and the atmospheric gases that render the situation more complex. An electron of a given initial energy will undergo a fixed number of collisions in a particular gas before thermalizing. Thus in the very simple case of a single constituent atmosphere, changing the concentration simply raises or lowers the altitude of the peak energy loss (and peak emission). This example (single-constituent atmosphere) is representative of those altitudes in which the concentration of one atmospheric constituent dominates. From Figure 1 it can be seen that (for the conditions chosen) O tends to dominate above 400 km and N_2 tends to dominate below 300 km. In a mixture of gases, increasing the concentration of one specie relative to the others may also have the effect of raising the penetration depth. However, the gases will compete for incoming electrons in proportion to their mixing ratios and collision cross sections, and the ratio of the resulting emissions changes accordingly.

Figure 3 shows the volume emission rate profiles for OI 1356 Å photons for the reference atmosphere case for selected energies. Only the very soft electrons (<200 eV) lose their energy in the altitude region where O is the major species. All other energies lie in altitude regions where the various gases can compete for collisons with the precipitating electrons. Thus, for example, increasing the concentration of N_2 will result in a decrease in the production of OI 1356 Å photons, because electrons that would have collided with O atoms now have an increased probability of colliding with N_2 molecules. The results of changing the O, O_2, and N_2 concentrations individually by a factor of 2 are shown in Figures 4 and 5.

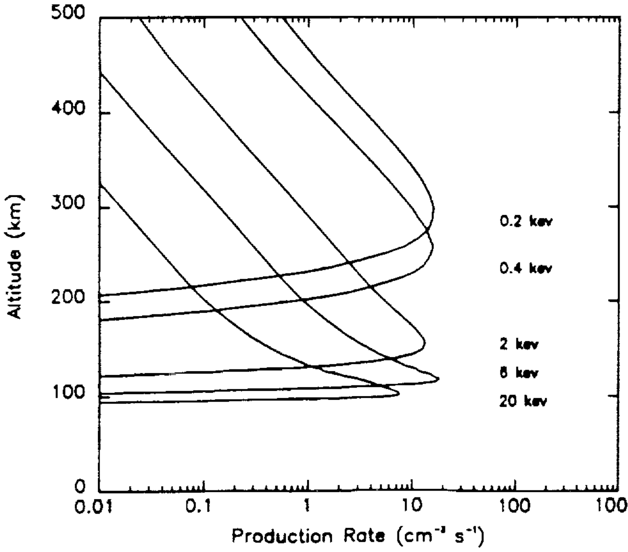

Fig. 3. Volume emission rate profiles for OI 1356 Å for the reference atmosphere shown in Figure 1.

Figures 4a and 5a show the impact on the computed OI 1356 Å and LBH surface brightness of the doubling of [N_2]. The 1356 Å intensity at 2 keV drops to 65% of the reference model, and then rises back to 86% of the reference model by 10 keV. The I 1356 is reduced at all modeled energies due to the fact that there are now more collisions with N_2, with a corresponding decrease in the production of O emissions. The decrease is not a full factor of 2 because of the abundance of atomic oxygen at the higher altitudes. For the very lowest energies (highest altitudes), where [N_2] is much less than [O], the I 1356 should tend to an intensity level unchanged from the standard case, as the emission is simply raised in altitude. The modeled emissions do not include initial energies less than 200 eV which would lose their energy above 400 km, but the lowest energy emissions do show this trend. At the higher energies, the emission is produced primarily at altitudes where N_2 is the major constituent and increased N_2 does not result in a significant change in the competition between O and N_2.

For the LBH 1464 Å emission, doubling the N_2 reduces the relative concentration of the dominant absorber, O_2. Thus for the higher energies which penetrate to greater depths, the emission from the increased N_2 overwhelms the O_2 absorption. Absorption by O_2 is not significant for the LBH 1838 Å emission; there is thus little dependence on the energy of the incident electrons.

Doubling the O_2 density (Figures 4b and 5b) increases the absorption of I 1356 and I 1464 at the higher energies (lower altitudes) resulting in reduced column brightnesses. The LBH 1838 Å emission is relatively unaffected by O_2 absorption and is influenced only by increased competition for collisions of the energetic particles with O_2 molecules. However, since [N_2] remains the major specie relative to [O_2], I 1838 shows only small changes.

The effect of doubling the [O] is shown for I 1356 in Figure 4c and for the LBH emissions in Figure 5c. For I 1356 the effect is close to a factor of 2 increase in the emission at all energies, while for the LBH emissions there is almost no effect at all energies. For the very low energies (not modeled) where O is the major constituent, the effect of doubling the O is simply to raise the altitude of the 1356 Å emission. The trend to an unchanged emission can be seen at the lower energies. For the LBH emissions, the effect of doubling the O concentration is only seen at the very low energies (high altitudes) where the competition with N_2 is further increased. In the altitude regimes where N_2 is a larger component, the O does not play a significant role.

From the results shown in Figures 4 and 5 it can be seen that uncertainties of a factor of 2 in any of the principal neutral atmospheric species translate into uncertainties of less than 20% for I 1838. The LBH 1464 Å emission shows variations up to 70% for factor of 2 uncertainties in [N_2] and less than 40% variation due to other constituents. OI 1356 is weakly sensitive to changes in O_2 and N_2, but varies almost in direct proportion to changes in O.

3.2. *Sensitivity to Larger Compositional Changes*

The neutral atmosphere exhibits relatively large compositional changes in the course of the seasonal, solar cyclic and magnetic storm variations. In this section we report the results of our assessment of the dependence on the computed emissions chosen for this study to changes of this magnitude. In order to simulate changes we have varied the input parameters ($F_{10.7}$, Ap, day of year) to the MSIS-86 model atmosphere, yielding neutral atmospheres at summer and winter solstice for conditions corresponding to low, moderate, and high solar activity (Table 1). The relative

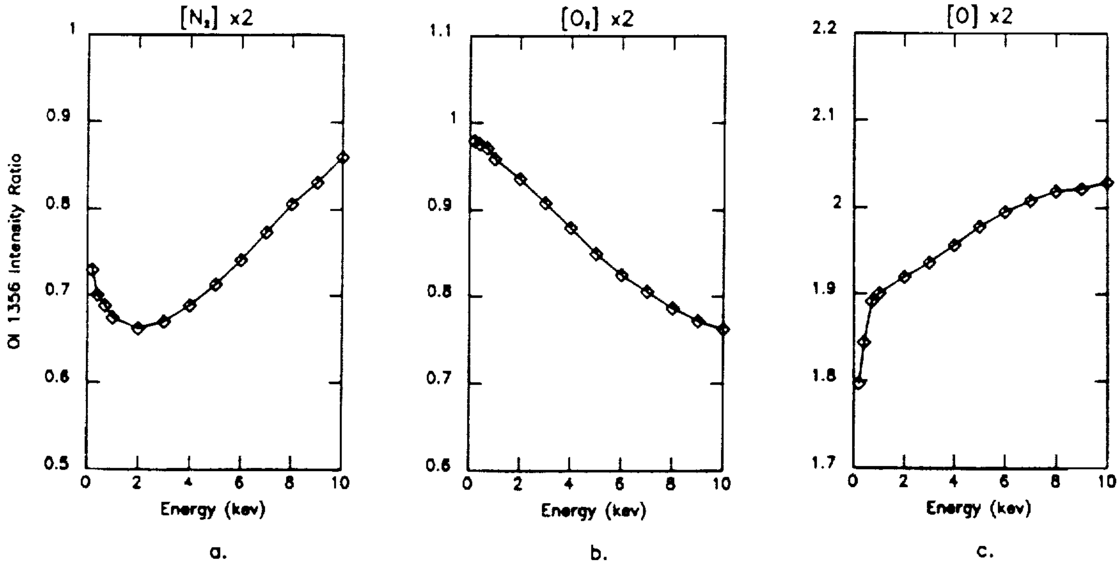

Fig. 4. OI 1356 dependence on [O], [O$_2$], and [N$_2$]. Each curve shows I 1356 for the doubled constituent case divided by I 1356 from the standard (unchanged) case.

compositional changes produced by these cases are illustrated in Figure 6.

The variations in the emission ratio of OI 1356 Å to LBH 1838 Å due to such composition changes are illustrated in Figure 7. This particular ratio is very sensitive to incident energy. For any given atmospheric conditions, the ratio varies by a factor of 13 over the energy range shown in the figure. What is interesting to note in Figure [illegible] is that the variation due to the compositional changes produced by solar activity variations (low, moderate, and high $F_{10.7}$ cm flux) are small ($\leq 30\%$), while the variations resulting from compositional changes of the type produced by seasonal variations are much larger (about a factor of 2). In Figure 8 we show the energy dependence for these various composition cases for the individual I 1356 and I 1838 intensities. The LBH intensity is relatively insensitive to the changing atmospheric conditions, while the OI 1356 is found to be primarily responsible for the variations shown in Figure 7.

The reason for this can be seen in Figure 9 which shows the ratio of the individual concentration changes relative to the standard case. Figure 9*a* shows that the atomic oxygen concentration (for altitudes below 300 km, which correspond to the initial energies modeled here) is significantly higher for the winter cases than the summer cases.

Figure 10 shows the modeled volume emission rate altitude profiles for the solar minimum and solar maximum summer cases. As the atmosphere expands under the influence of increased solar activity, the production rate for a given energy peaks at higher altitudes. Of note is the fact that the behavior of the production

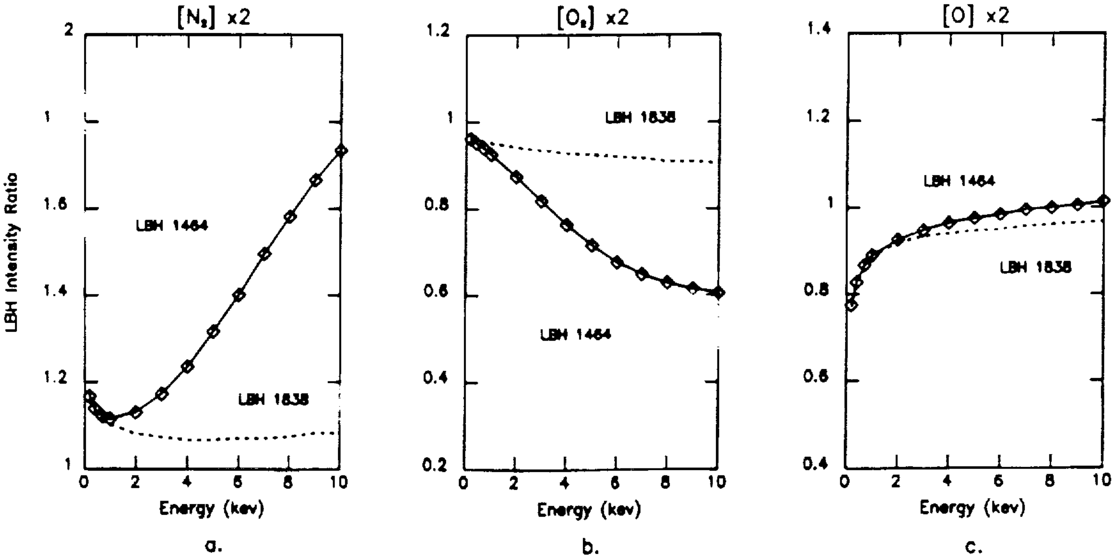

Fig. 5. LBH dependence on [O], [O$_2$], and [N$_2$]. Each curve shows the LBH intensity for the doubled constituent case divided by the LBH intensity from the standard (unchanged) case.

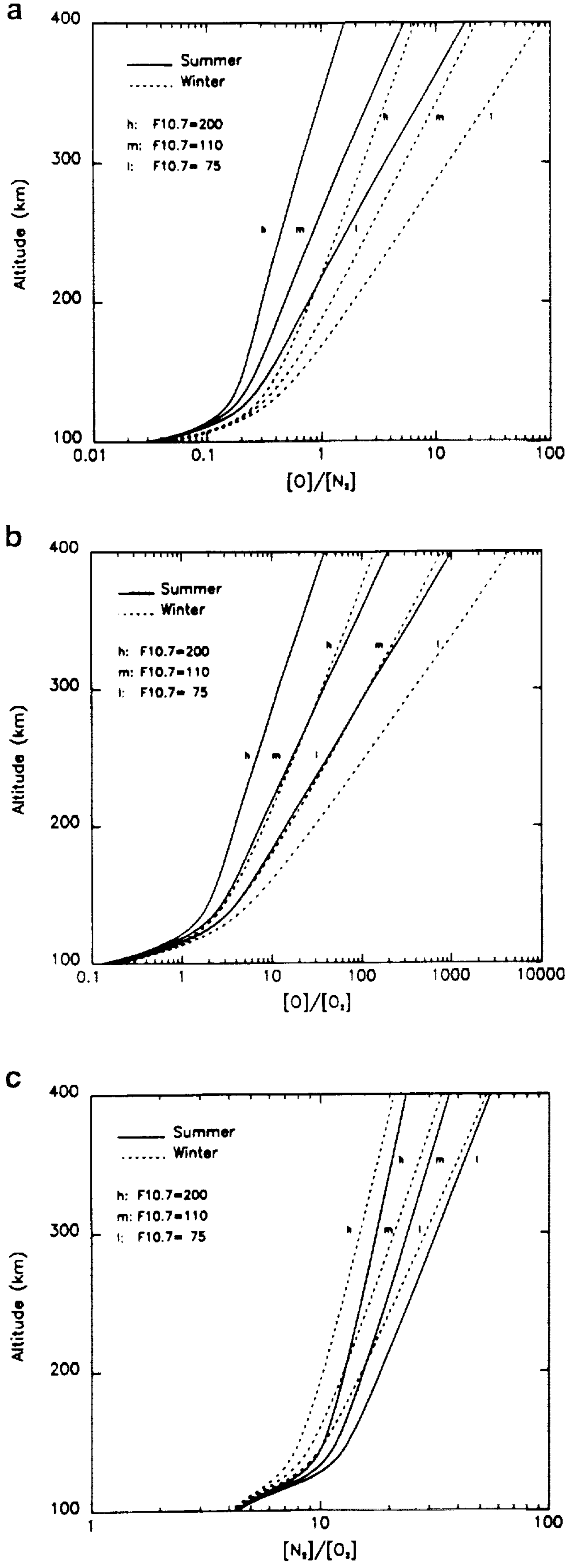

Fig. 6. Relative altitude density profile variations as a function of solar activity and seasonal variation.

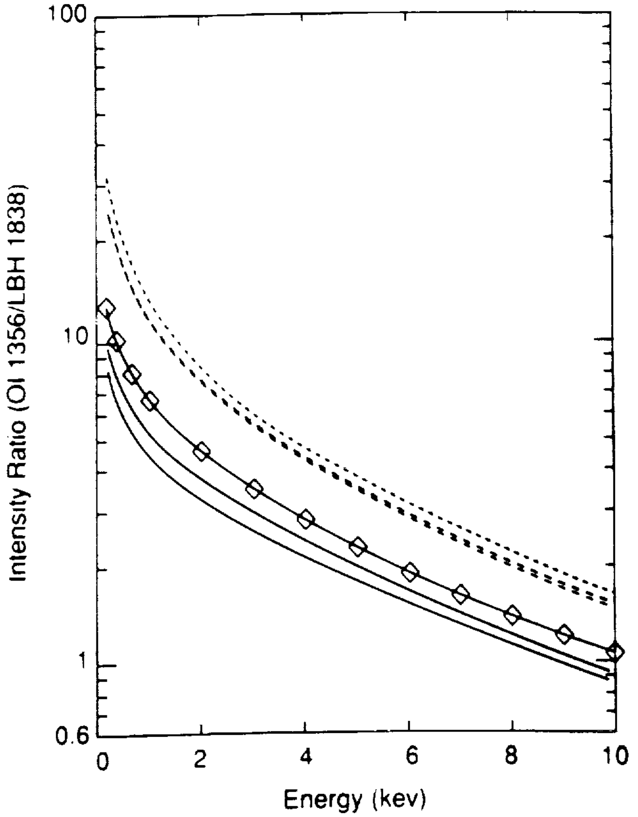

Fig. 7. Sensitivity of the OI 1356/LBH 1838 intensity ratio to solar activity and seasonal variation. Solid lines indicate summer conditions; dashed lines are for winter. Within each seasonal set of curves, the largest intensity ratios are obtained at solar minimum activity; the smallest ratios occur at solar maximum.

rate profiles for electron energies below 2 keV is markedly different from that above 2 keV. The altitude at which this energy loss peaks is approximately 140 km. This is the altitude below which O_2 becomes a competitive constituent (see Figure 1).

Figure 11 illustrates the effect of local O_2 absorption. As would be expected, for emissions lying outside the region of O_2 absorption (LBH 1838), the production rates are unchanged by local O_2 absorption. For emissions within the Schumann-Runge absorption continuum, however, the shape of the emission rate profiles is changed significantly due to local O_2 absorption.

The final ratio modeled was LBH$_{long}$/LBH$_{short}$ (Figure 12). The ratio of LBH 1838 to LBH 1464 shows a dependence on the incident electron energy that varies only slightly with solar activity. As above, this variation can be explained by the relative densities of N_2 and O_2. The observed variability from solar minimum to solar maximum is due to changes in the O_2 column density and hence in the O_2 absorption.

4. DISCUSSION

We have shown the intensity ratio OI 1356/LBH$_{long}$ to be a useful diagnostic for determining the characteristic energy of the auroral particles using LBH$_{long}$ to be LBH 1838. The I 1356/I 1838 ratio is a very sensitive indicator of characteristic energy, changing by a factor of 13 or more over the range 200 eV to 10 keV, but this ratio can vary by up to factors of 2 with changes in the neutral atmosphere. Almost all the change is due to variations in I 1356. In addition, the I 1838/I 1464 ratio shown in Figure 12

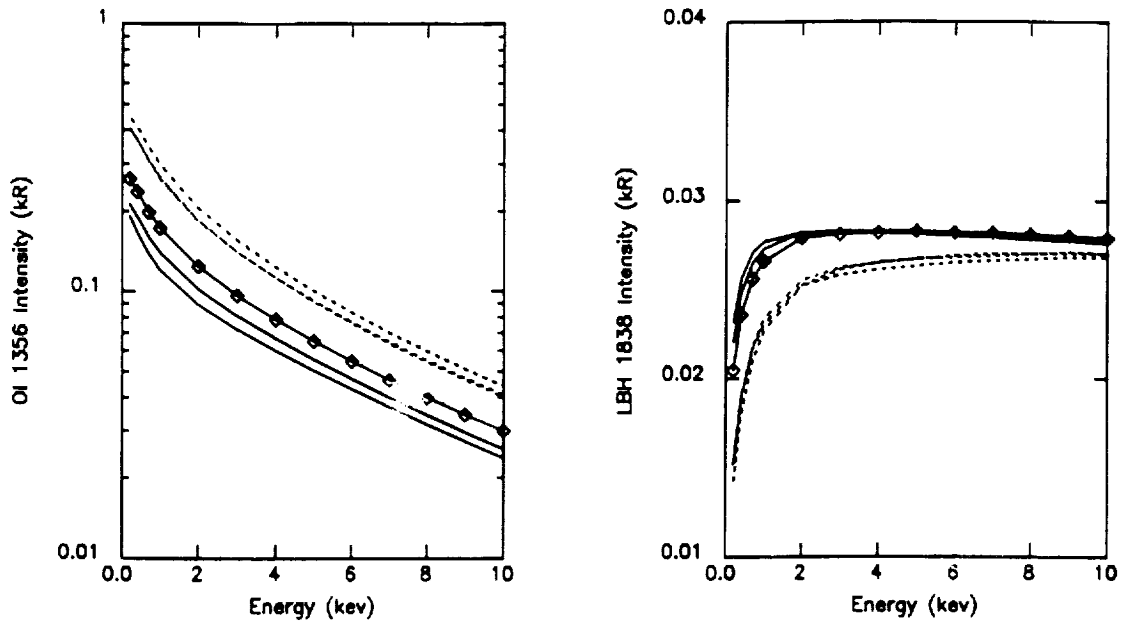

Fig. 8. Dependence of LBH 1838 and OI 1356 on solar activity and seasonal variation. The curves have the same interpretation as in Figure 7.

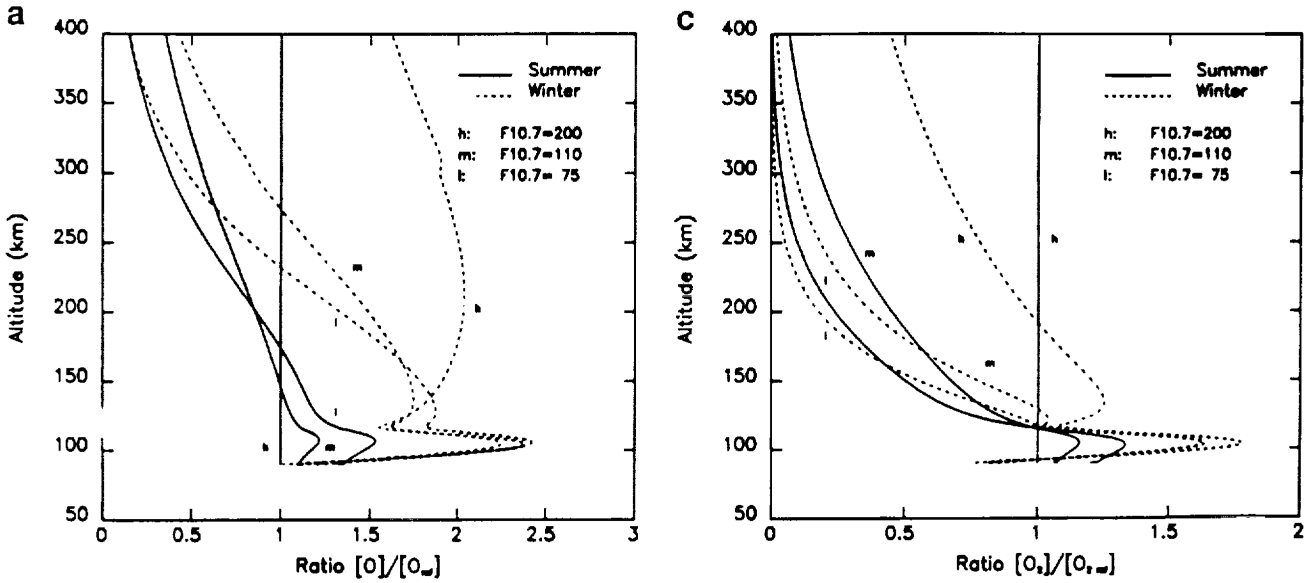

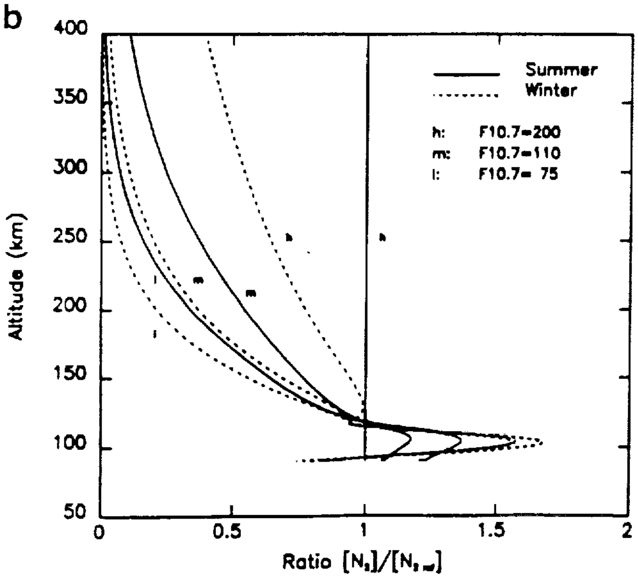

Fig. 9. Variation of altitude density profiles as a function of solar cyclic and seasonal variations. The profiles have been normalized to the standard case (summer, $F_{10.7} = 200$).

is found to be another potentially useful determinant of characteristic energy. The N_2 LBH long-to-short wavelength ratio varies by about a factor of 3 between 0.2 and 10 keV but, unlike the OI 1356 emission, is almost insensitive to changing atmospheric composition. The longer wavelength LBH bands are also useful indicators of the total energy influx, while the long-to-short wavelength LBH intensity ratio provides information on the O_2.

Other workers have also attempted to use optical emissions to characterize the auroral electron precipitation. For example, *Ishimoto et al.* [1988] studied a similar ratio (OI 1356/LBH 1928) using a recent version of the Strickland model. Their modeled emission ratio shows a sensitivity of 9 between 1 and 10 keV, in good agreement with our results. In their description of the auroral code used in this study, *Richards and Torr* [1990] conduct a comparison between the two-stream model used here and the

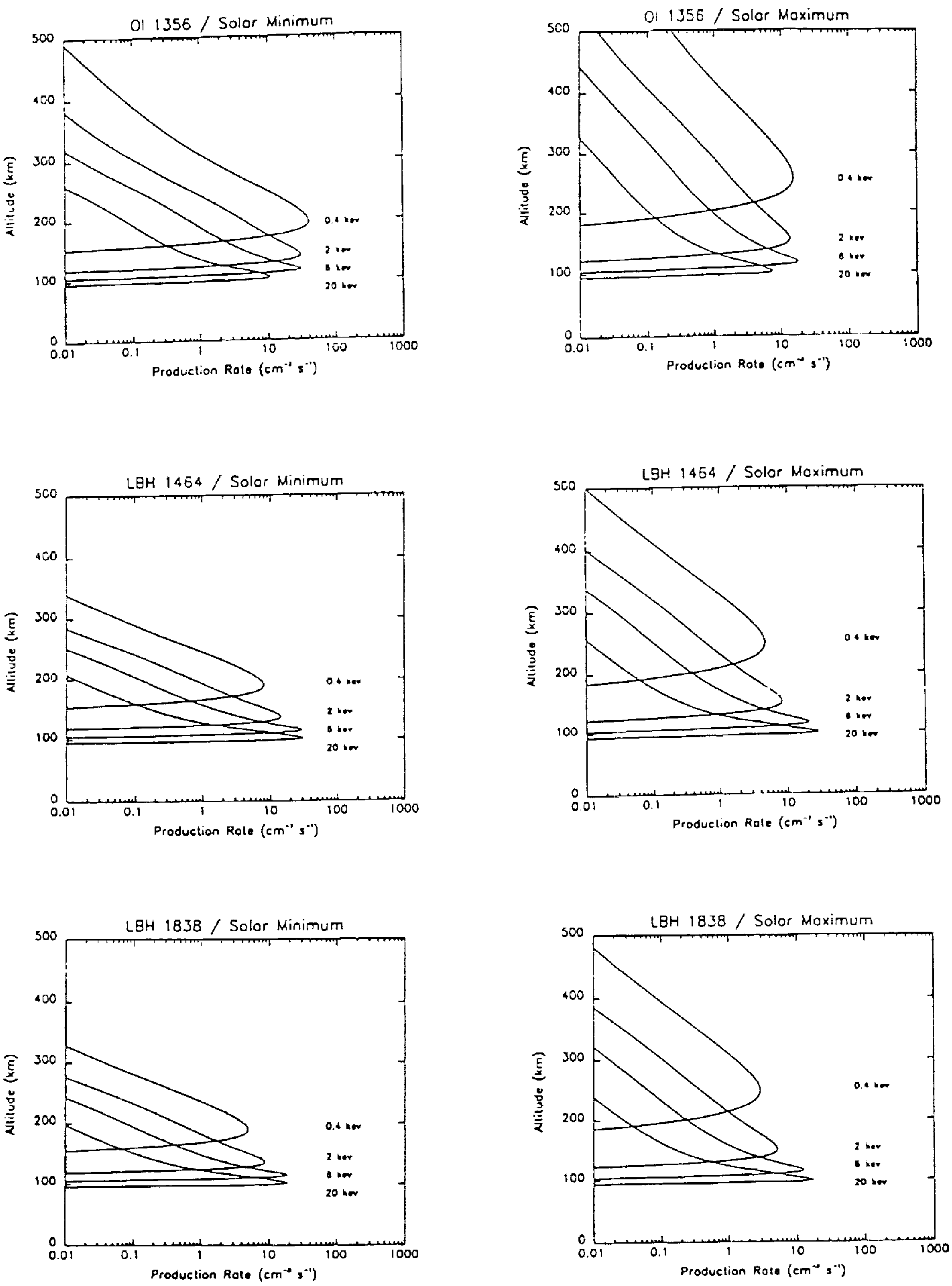

Fig. 10. Emission production rate altitude profiles for OI 1356 and LBH.

more sophisticated multi-stream model of *SJW* and find good agreement in the shape of the OI 1356 emission curve. (Differences in magnitude are due to the use of revised OI cross sections in our model.) In addition to these studies, *Rees and Lummerzheim* [1989] have suggested the N_2 3371/N_2^+ 4278 emission ratio as a determinant of the incident auroral energy. Their results, however, disagree with calculations by *SJW* and with our model, which shows the 3371 emission to be independent of characteristic energy above 0.5 keV [*Richards and Torr*, 1990].

We have investigated the sensitivity of OI 1356 Å, LBH 1464 Å, and LBH 1838 Å auroral emissions to changes in the neutral atmosphere. Our studies show that OI 1356 varies linearly with [O] to within 20% and shows much less variation with other atmospheric constituents. The LBH 1838 Å intensity is relatively insensitive to typical uncertainties in the neutral atmosphere (factor of 2 at auroral altitudes). I 1464 shows larger variations because of its additional interaction with O_2. Our results are in good agreement with similar sensitivity studies performed by *SJW*

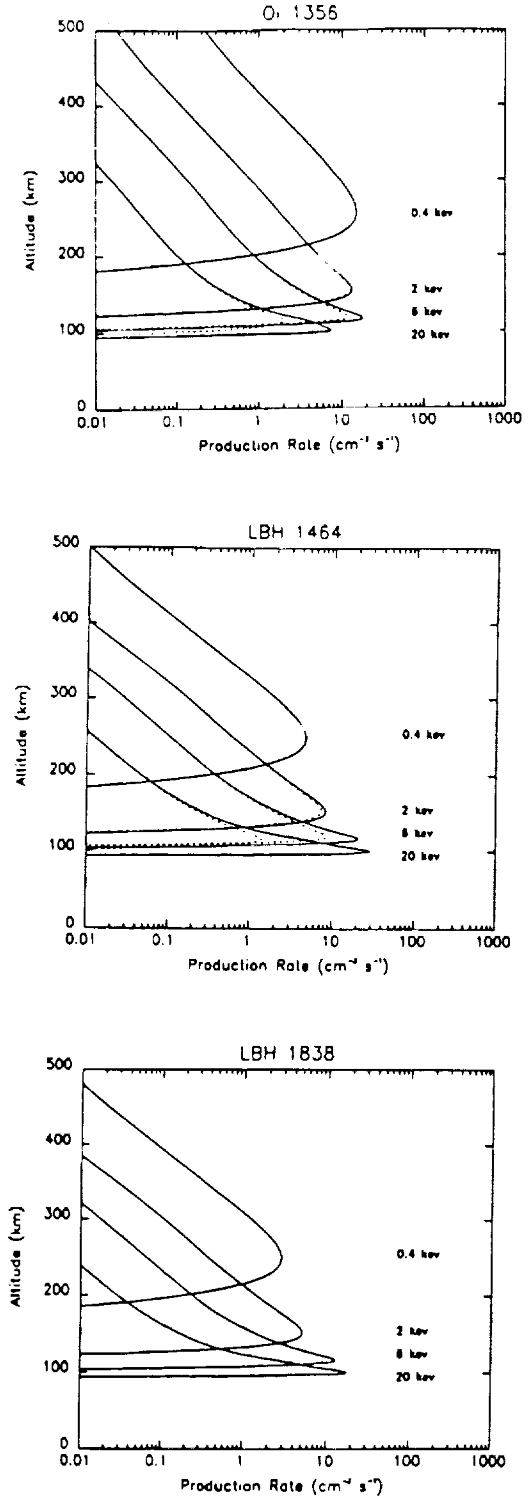

Fig. 11. Same as Figure 10 (solar maximum), but illustrating the effects of local O_2 absorption. The dashed curves are with local O_2 absorption.

who used a Jacchia model atmosphere [*Jacchia*, 1977] to model OI 1356 dependence on [O]. The dependence of these intensities on much larger changes in the composition such as might be encountered over seasonal or solar cycle extremes has also been investigated. It is found that the OI 1356 Å intensity is sensitive to compositional changes while the N_2 LBH long wavelength emission is relatively insensitive to such changes.

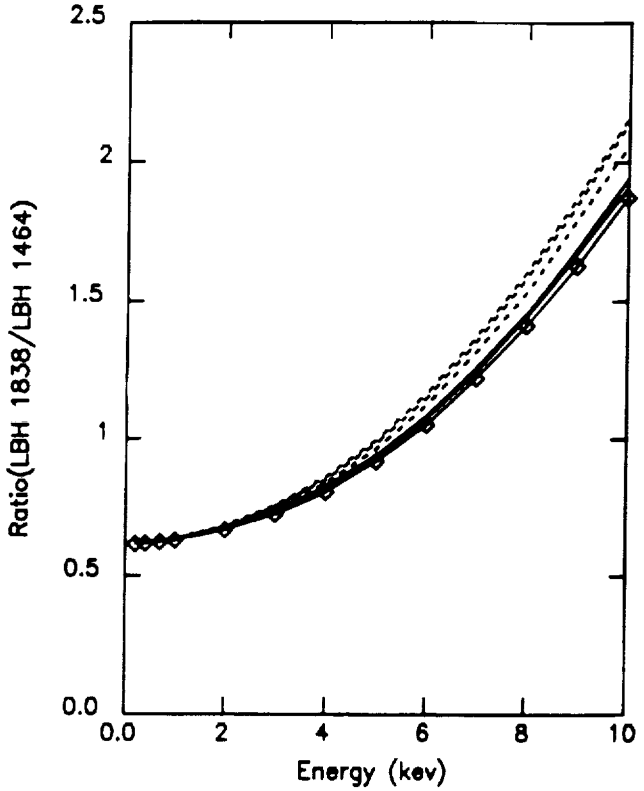

Fig. 12. Sensitivity of LBH_{long}/LBH_{short} intensity ratio to solar activity and seasonal variation. The curves have the same interpretation as in Figure 7.

Acknowledgments. This work was supported by NASA contracts NAS8-36955 and NAS8-37586, NASA grant NAGW-996, and NSF grant ATM 8713693 to the University of Alabama in Huntsville. This work was done while one of the authors (GAG) held a National Research Council–NASA Research Associateship.

The Editor thanks Manfred Rees and Donald Shemansky for their assistance in evaluating this paper.

REFERENCES

Ajello, J. M., and D. E. Shemansky, A reexamination of important N_2 cross sections by electron impact with application to the dayglow: The Lyman-Birge-Hopfield band system and NI (119.99 nm), *J. Geophys. Res.*, *90*, 9845, 1985.

Hedin, A. H., MSIS-86 thermospheric model, *J. Geophys. Res.*, *92*, 4649, 1987.

Hudson, R. D., Critical review of ultraviolet photoabsorption cross sections for molecules of astrophysical and aeronomic interest, *Rev. Geophys.*, *9*, 305, 1971.

Ishimoto, M., C.-I. Meng, G. J. Romick, and R. E. Huffman, Auroral electron energy and flux from molecular nitrogen ultraviolet emissions observed by the S3-4 satellite, *J. Geophys. Res.*, *93*, 9854, 1988.

Jacchia, L. G., Thermospheric temperature, density, and composition: New models, *Spec. Rep. 375*, Smithsonian Astrophys. Observ., Cambridge, Mass., 1977.

Meier, R. R., D. J. Strickland, P. D. Feldman, and E. P. Gentieu, The ultraviolet dayglow, 1, Far UV emissions of N and N_2, *J. Geophys. Res.*, *85*, 2177, 1980.

Ogawa, S., and M. Ogawa, Absorption cross sections of $O_2(a^1\Delta_g)$ and $O_2(X^3\Sigma_g)$ in the region from 1087 to 1700 Å, *Can. J. Phys.*, *53*, 1845, 1975.

Rees, M. H., and D. Luckey, Auroral electron energy derived from ratio of spectroscopic emissions, 1, Model computations, *J. Geophys. Res.*, *79*, 5181, 1974.

Rees, M. H., and D. Lummerzheim, Characteristics of auroral electron precipitation derived from optical spectroscopy, *J. Geophys. Res.*, *94*, 6799, 1989.

Richards, P. G., and D. G. Torr, Theoretical modeling of the dependence of the N_2 second positive 3371 Å auroral emission on characteristic energy, *J. Geophys. Res.*, in press, 1990.

Strickland, D. J., and D. E. Anderson, Jr., Radiation transport effects on the OI 1356 Å limb intensity profile in the dayglow, *J. Geophys. Res.*, *88*, 9260, 1983.

Strickland, D. J., J. R. Jasperse, and J. A. Whalen, Dependence of auroral FUV emissions on the incident electron spectrum and neutral atmosphere, *J. Geophys. Res.*, *88*, 8051, 1983.

Swartz, W. E., Optimization of energetic electron energy degradation calculations, *J. Geophys. Res.*, *90*, 6587, 1985.

Torr, M. R., J. C. G. Walker, and D. G. Torr, Escape of fast oxygen from the atmosphere during geomagnetic storms, *J. Geophys. Res.*, *79*, 5267, 1974.

G. A. Germany and M. R. Torr, Space Sciences Laboratory, NASA Marshall Space Flight Center, Huntsville, AL 35812.

P. G. Richards and D. G. Torr, The University of Alabama in Huntsville, Huntsville, AL 35899.

(Received October 6, 1989;
revised December 13, 1989;
accepted December 14, 1989.)

JOURNAL OF GEOPHYSICAL RESEARCH, VOL. 95, NO. A12, PAGES 21,147–21,168, DECEMBER 1, 1990

Mid- and Low-Latitude Model of Thermospheric Emissions
1. $O^+(^2P)$ 7320 Å and N_2 (2P) 3371 Å

MARSHA R. TORR
Space Science Laboratory, NASA Marshall Space Flight Center, Huntsville, Alabama

D. G. TORR AND P. G. RICHARDS
University of Alabama in Huntsville

S. P. YUNG
Boeing Corporation, Huntsville, Alabama

The capability has been developed to model thermospheric airglow emissions on a semiglobal scale ($L < 5$). This model produces volume emission rates as a function of altitude, latitude, longitude, and local time for any selected date, and solar and magnetic conditions. The model can thus be used to provide three-dimensional maps of the selected emission for comparison with data obtained from orbiting vehicles. As such it becomes an essential tool in the planning and interpretation of airglow observations. A unique feature of the model is that it incorporates full interhemispheric coupling by solving all the appropriate coupled equations along the magnetic flux tubes from the mesosphere in one hemisphere to the mesosphere in the other hemisphere. As a result the effects of conjugate photoelectrons (and heat fluxes) can be fully explored. In this paper we select two thermospheric emissions with which to demonstrate the capability. The first is the 7320-Å emission from the metastable $O^+(^2P)$. The second is the permitted emission at 3371 Å from the N_2 second postive 0–0 band. These two emissions, for which the photochemistry is relatively well understood, are used to show the seasonal, diurnal and solar cyclic variations on a scale that covers mid- and low-latitudes, and the effects of interhemispheric coupling (conjugate photoelectrons).

INTRODUCTION

Airglow emissions are important indicators of atmospheric composition and the mechanisms responsible for the production and loss of the particular excited state from which the airglow is radiated. For example, the 0–0 band of the N_2 second positive system, which radiates at 3371 Å, is excited in the airglow by photoelectron impact, and is lost only by radiation. As a result, this emission is an excellent indicator of the photoelectron excitation rate [*Kopp et al.*, 1977]. The $O^+(^2P)$ metastable state, which radiates at 7320 Å, is excited both by photoelectrons and by extreme ultraviolet photons. However, because it is a long-lived state, it is lost by quenching by O, N_2, and electrons in addition to radiation. Thus at high altitudes, where radiation is the dominant loss mechanism, the 7320-Å emission can be used to infer either the atomic oxygen concentration or the solar ultraviolet flux if the other is known [*Meriwether et al.*, 1978; *Rusch et al.*, 1976].

In the past, a number of detailed studies of these emissions have been made using measurements of the surface brightness altitude profiles obtained from orbiting spacecraft (see, for example, *Walker et al.* [1975] and *Rusch et al.* [1977]). In this study we have globally modeled these two emissions for a variety of conditions.

The model we have used here is one that we have steadily developed over the years. We solve the coupled time dependent energy, momentum, continuity, and photoelectron transport equations from 80 km in one hemisphere, along a field line to 80 km in the other hemisphere (Figure 1) [*Young et al.*, 1980*a*,*b*; *Richards and Torr*, 1985*a*, 1988]. The equations that are solved are summarized below:

1. Ion continuity equation for major ions is given by

$$\frac{\partial N_i}{\partial t} = Q_i - L_i N_i - \nabla \cdot \phi_i \qquad (1)$$

where N_i is the concentration of the ith major ion. Q_i and L_i are its production and loss frequency, respectively, and ϕ_i is the ion flux defined below. The electron density is assumed to be equal to the sum of the ion densities.

2. Momentum equation is given by

$$\phi_i = N_i U_i \qquad (2)$$

where

$$U_i = \left(\frac{\nu_{ij}}{\Sigma(\nu)}\right)U_j - D_i\left(\frac{1}{N_i}\nabla N_i - \frac{m_i G}{kT_i} + \frac{1}{T_i}\nabla T_i + \frac{T_e/T_i}{n_e}\nabla N_e + \frac{1}{T_i}\nabla T_e + \frac{N_j}{N_i + N_j}\left(\frac{\alpha_{ij}}{T_i}\nabla T_i - \frac{\alpha_{ij}^*}{T_i}\nabla T_j\right)\right) + \left(\frac{\nu_{in}}{\Sigma(\nu)}\right)U_n \qquad (3)$$

where U_n is the neutral wind velocity and where the subscripts i and j are applied first to O^+ and H^+ respectively, and then to H^+ and He^+ respectively. O^+, H^+, and He^+ are coupled through collisions and the polarization electric fields. Since the influence of O^+ and He^+ on H^+ becomes significant in different altitude regimes and since the effect of He^+ and O^+ is small due to their mass ratio, this decoupling of a system of three major ions into 2 pairs of major ions considerably simplifies the numerical calculation of the major ion densities. Here α_{ij} and α_{ij}^* are thermal diffusion coefficients and D_i is the ordinary ion diffusion coefficient of species i, as in the work by *St. Maurice and Schunk* [1977].

Paper number 90JA01010.
0148-0227/90/90JA-01010$05.00

3. The thermal electron energy equation is

$$\frac{3}{2} N_e k \frac{\partial T}{\partial t} = -N_e k T_e \nabla \cdot U_e - \frac{3}{2} N_e k U_e \cdot \nabla T_e - \nabla \cdot q_e + \Sigma Q_e - \Sigma L_e \tag{4}$$

4. The ion energy equation is

$$\frac{3}{2} N_i k \frac{\partial T_i}{\partial t} = -N_i k T_i \nabla \cdot U_i - \frac{3}{2} N_i k U_i \cdot \nabla T_i - \nabla \cdot q_i + \Sigma Q_i - \Sigma L_i \tag{5}$$

5. The ion heat flow equation is

$$q_i = \frac{1}{1-\xi} \left(-\lambda_i \nabla T_i - \frac{N_i m_i \nu_{ij}'}{N_j m_j \nu_j} \lambda_j \nabla T_j \right) \tag{6}$$

6. The electron heat flow equation is

$$q_e = -\lambda_e \nabla T_e \tag{7}$$

The thermal conductivity coefficients λ_i and λ_e, and the term

$$\xi = \nu_{ij}' \nu_{ji}' / (\nu_i' \nu_j')$$

where ν_{ji}', ν_{ij}', ν_i', and ν_j' are the effective collision frequencies, are given by *St. Maurice and Schunk* [1977]. The ion-neutral collision frequencies ν_{in} are from *Schunk and Nagy* [1980].

7. The photoelectron Liouville equation is given by

$$B \frac{d}{ds} \frac{\Phi^+}{B} = -T_2 \phi^+ + T_1 \phi^- + \frac{q}{2 < \cos \theta >} + \frac{q^+}{< \cos \theta >'} \tag{8}$$

$$-B \frac{d}{ds} \frac{\Phi^-}{B} = -T_2 \phi^- + T_1 \phi^+ + \frac{q}{2 < \cos \theta >} + \frac{q^-}{< \cos \theta >} \tag{9}$$

where

$\phi^+(E,s)$	photoelectron flux outward along s;
$\phi^-(E,s)$	photoelectron flux inward along s;
$q(E,s)$	photoelectron production rate in the range E to $E+dE$ due to direct ionization processes;
$q^\pm$	photoelectron production in the range E to $E+dE$ due to cascading from higher energy photoelectrons undergoing inelastic collisions;
$< \cos \phi >$	average cosine of pitch angle;
B	magnetic field strength;

$$T_1 = \sum_k n_k p_e^k \sigma_e^k;$$

$$T_2 = \sum_k n_k [\sigma_e^k + p_e^k \sigma_e^k];$$

and

n_k	kth species number density;
p_e^k	photoelectron backscatter probability for elastic conditions with the kth species;
σ_e^k	photoelectron total scattering cross section for elastic conditions with the kth species;
σ_a^k	inelastic cross section for excitation of the kth particle species.

The model includes an option to increase the O^+–O collision frequency as recommended by *Burnside et al.* [1987]. The use of the *Schunk and Nagy* [1980] values here does not significantly influence the results of this paper.

The above formulation corresponds to conditions where the differences between species temperatures and flow velocities are assumed to be small, i.e., stress and nonlinear acceleration terms are neglected. In addition, density and temperature gradients normal to the geomagnetic field lines are neglected and we assume that the electron and ion temperature distributions are isotropic.

The continuity equation is solved using a rather unique approach. We can rewrite (1) in terms of a function F:

$$dF = \frac{\partial N_i}{\partial t} + \nabla \cdot (N_i U_i) - Q_i + L_i N_i \tag{10}$$

Then, using a Newton iterative procedure to find the minimum of F, we solve for the density at the grid point, j. Figure 2 shows how the field line is divided into elements about the actual grid point j. The lower limit of the element (ℓ) is placed midway between the grid points j and $j-1$, and the upper limit (u) is placed midway between j and $j+1$. The lower limit of one element is the upper limit of the preceding element. We then integrate (10) between u and ℓ, and obtain the densities by solving

$$F = \int_\ell^u \frac{1}{B} \left(\frac{\partial N_i}{\partial t} - Q + L \right) ds + \left(\frac{N_{iu} U_{iu}}{B_u} - \frac{N_{i\ell} U_{i\ell}}{B_\ell} \right) = 0 \tag{11}$$

where B is the amplitude of the magnetic field. The values of $\partial N / \partial t$, Q, and L are obtained at the limits of integration, u and ℓ, by interpolation between the actual grid points.

In the past, many models have encountered numerical problems above about 3000 km, due to the large diffusion coefficient in this region which results in small density changes producing large changes in velocity. At lower altitudes, both ion-ion and ion-neutral collisions are important, while at greater altitudes, collisions become less important and the plasma can be accurately

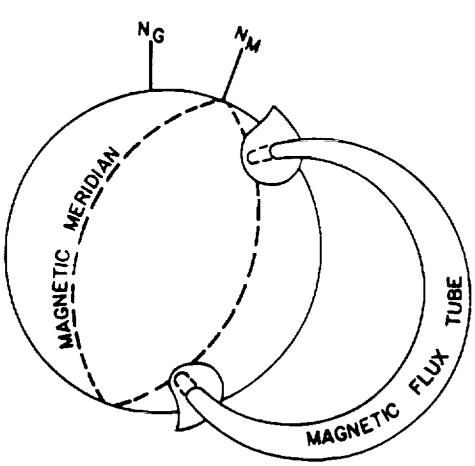

Fig. 1. Illustration of the interhemispheric nature of the code in which the coupled and time dependent equations are solved from 80 km in one hemisphere, along a field line, to 80 km in the conjugate hemisphere.

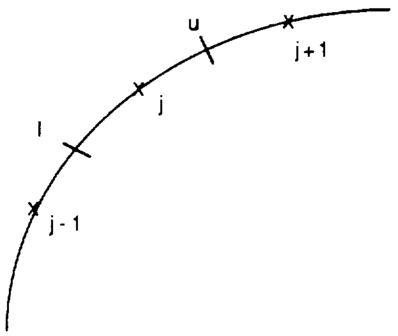

Fig. 2. The numerical grid scheme used for the solution of the continuity equation.

described using a diffusive equilibrium approach. The solution of (11) distinguishes this model from previous methods which evaluate the terms of the integral at only one point. As can be seen from (11) and Figure 2, the flux at the upper limit of one element becomes the flux at the lower limit of the next element. These fluxes must be identical and hence this method has been called the "flux preserving scheme." Furthermore, the flux at any grid point is closely tied to the flux at neighboring grid points, allowing stable solutions even for regions where large changes would give rise to unstable solutions with other numerical methods.

The model starts at noon with "best guess" initial values. It is allowed to run for 12 hours (in local time) before results are used in order to reduce dependence on initial conditions. It has been found that the ionospheric densities over a midnight to midnight diurnal cycle typically repeat with only small differences due, for example, to plasmaspheric refilling. The plasmaspheric H^+ and He^+ contents are initially low, and the flux tubes are allowed to fill continuously. The transport equations for the three major ions, He^+, H^+, and O^+, are carried out in two steps. As mentioned above, the coupled O^+ and H^+ equations are solved first, followed by the He^+ and H^+ equations, where the latter use the O^+-H^+ results. Thus the equations for the three major ions are essentially solved in a simultaneous manner. Below approximately 180 km, NO^+ and O_2^+ become major ions, but are obtained from photochemical equilibrium calculations.

The numerical solution of these equations, boundary conditions and other details are further discussed by *Young et al.* [1980*a*,*b*].

The full interhemispheric coupling is difficult to handle, but once incorporated it imposes no artificial upper boundary conditions for both thermal and photoelectron fluxes. This is most important for thermal coupling and the proper treatment of conjugate photoelectrons [*Richards and Torr*, 1985*b*] which can be significant in the calculation of airglow emissions. Typically, attenuation of the conjugate photoelectron flux by Coulomb collisions results in approximately 5% energy loss. The model includes the option to specify loss due to pitch angle scattering which we assumed to be zero for this paper. A tilted dipole approximation is used for the Earth's magnetic field [*Richards and Torr*, 1986*a*].

The concentrations of the major neutral species are provided by the MSIS-86 [*Hedin*, 1987] to the model which then computes the concentrations of minor and excited state species and major ions [*Torr*, 1985; *Richards et al.*, 1982*a*, 1986*b*]. In this paper a simple model giving daytime poleward winds and equatorward neutral winds was employed. This behavior is consistent with the results obtained using the method of *Richards and Torr* [1986*b*] and *Miller et al.* [1986]. The model includes the option to use model winds of *Hedin et al.* [1988], *Killeen et al.* [1987] and Killeen (private communication 1989). Note, if the *Hedin et al.* [1988] model is used, the O^+–O collision frequency of *Burnside et al.* [1987] should be used in order to produce the observed h_mF2 at night.

The chemistry of all significant emitting species is incorporated in detail, including the excitation of the metastable states [*M. R. Torr and Torr*, 1982] and vibrational states [*Richards et al.*, 1986*a*; *Richards and Torr*, 1986*c*], and the odd nitrogen chemistry [*Richards et al.*, 1981, 1982*b*; *Richards*, 1986]. The vibrational population distributions of N_2 are determined, an important factor in calculating the ionospheric O^+ and N_e concentrations. The model also includes calculation of the vibrational populations of N_2^+, but this does not significantly affect the results reported here. The photochemistry is that described by *Torr* [1985] as updated and shown here in Table 1 and illustrated in Figure 3. At equatorial latitudes, where electric fields play an important role, the electron concentrations are obtained from the fully analytical ionospheric model of *Anderson et al.* [1989]. Elsewhere, the electron densities are computed self-consistently by this model. The transition occurs between $L = 1.5$ and 1.8 with interpolation between these L shells. The major elements of the code are shown in Figures 4*a* and 4*b*. The solar EUV flux is obtained in the following way. For solar minimum ($F10.7 = 71$) the model utilizes the F74113 reference spectrum from *Torr et al.* [1979], with the fluxes below 250 Å doubled as recommended by *Richards and Torr* [1984] and supported by *Ogawa and Judge* [1986]. For other levels of solar activity, each of the 37 wavelength intervals is scaled linearly as a function of $F10.7$ using the solar maximum measured flux at $F10.7 = 206$ given by *Torr and Torr* [1985]. For further details, see *Richards and Torr* [1988], which also provides the cross sections used.

The main outputs of the model include ion densities (O^+, $O^+(^4S)$, $O^+(^2D)$, $O^+(^2P)$, H^+, He^+, N^+, NO^+, N_2^+, N_2^{+*}), neutral densities ($N(^4S)$, $N(^2D)$, $N(^2P)$, NO, $O(^1D)$, $O(^1S)$, $N_2(A^3\Sigma_u^+)$, N_2^*), electron and ion temperatures and flow velocities, the photoelectron flux, and a large number of emissions (see Figure 4*a*).

During the Atmosphere Explorer C, D, and E program, numerous studies were conducted which compared the photochemistry of the code with in situ measurements of species concentrations. The photochemistry yields results consistent with the data base taken over the lifetime of the AE satellites. Generally, very good agreement with measurements has been obtained with regard to all parameters with the exception of high altitude electron temperatures in the plasmasphere and ionosphere [*Newberry et al.*, 1989]. The model has been extensively tested against comprehensive satellite and incoherent scatter radar data bases [*Young et al.*, 1980*a*,*b*; *Chandler et al.*, 1983; *Richards and Torr*, 1988; *Newberry et al.*, 1989; *Horwitz et al.*, 1990; *Richards et al.*, 1989]. Apart from the input parameters (such as data and location) the only free parameter in the code is the pitch angle scattering of photoelectrons in the plasmasphere. In its present form, the model is ideally suited for studies of the airglow emissions.

The code is run on the Marshall Space Flight Center CRAY XMP computer. Values of output parameters are provided on a global grid of points, providing results in a latitude, longitude, altitude, and local time mesh for any selected date, or solar or magnetic conditions. For the cases discussed in this paper, we have run the model for 144 flux tubes, which corresponds to 144 northern and 144 southern hemisphere locations. Figure 5 shows the locations of the field lines along which the equations are solved. These are constrained to $L \leq 5$.

We have chosen the $O^+(^2P)$ emission at 7320 Å and the N_2 second positive 0–0 band emission at 3371 A for the initial global modeling. The calculations have been made for November 28, 1983 for which the $F10.7$ cm flux was 89, and the Ap index was 23. Thus the November 1983 calculations correspond to a period of relatively low solar activity. An earlier example of the results for the 7320 Å case has been shown by *Torr et al.* [1990]. The results shown here represent a significant improvement over the *Torr et al.* [1990] case, in that we have added approximately 50 more flux tubes at low latitudes (144 versus 96). In addition we have used much smaller time steps through the twilight conditions (5 minutes versus 20 minutes). For comparison, we have also run the calculations for the same day of year, but for conditions

TABLE 1. Summary of Photochemistry Used in the Interhemispheric Model

Reaction Number	Reaction	Rate Coefficient (cm^3 s^{-1}) or Rate (s^{-1})	Reference
1.	$O^+ + e^- \rightarrow O + h\nu$	$\sim 4 \times 10^{-12} (T/300)^{0.7}$	*Torr* [1985]
2.	$O_2^+ + e^- \rightarrow O + O$	$1.6 \times 10^{-7} (300/T_e)^{0.55}$ for $T_e \geq 1200$ K $2 \times 10^{-7} (300/T_e)^{0.7}$ for $T_e < 1200$ K	*Torr and Torr* [1981]; *Mehr and Biondi* [1969]
3.	$O^+ + O_2 \rightarrow O_2^+ + O$	$2.1 \times 10^{-11} \{T_n + 2\,T_i/3 \times 300\}^{-0.763}$	*Chen et al.* [1978][a]
4.	$O^+ + N_2 \rightarrow NO^+ + N$	$1.533 \times 10^{-12} - 5.92 \times 10^{-13} (T_{eff}/300)$ $+ 8.60 \times 10^{-14} (T_{eff}/300)^2$ for $300 \leq T_{eff} \leq 1700$ K $2.73 \times 10^{-12} - 1.155 \times 10^{-12} (T_{eff}/300)$ $+ 1.483 \times 10^{-13} (T_{eff}/300)^2$ for $1700 < T_{eff} < 6000$ K	*St. Maurice and Torr* [1978]; *Albritton* [1978]; *Chen et al.* [1978]
5.	$NO^+ + e \rightarrow N + O$	$4.3 \times 10^{-7} (T_e/300)^{-1}$	*Torr and Torr* [1979]
6.	$N_2^+ + O \rightarrow NO^+ + N$	$1.4 \times 10^{-10} (T_i/300)^{-.44}$ for $T_i < 1500$ K	*McFarland et al.* [1974]; *Torr* [1979]
7.	$N_2^+ + e^- \rightarrow N + N$	2.7×10^{-7}	*Abdou et al.* [1984]
8.	$N_2^+ + O \rightarrow O^+ + N_2$	$0.07\, k_6 (T_i/300)^{0.21}$	*McFarland et al.* [1974]
9.	$N_2^+ + O_2 \rightarrow O_2^+ + N_2$	$9.1 \times 10^{-11} \exp(-0.002\, T_{eff})$	*Lindinger et al.* [1974]
10.	$N^+ + O_2 \rightarrow O_2^+ + N$	4×10^{-10}	*Huntress and Anicich* [1976]
11.	$N^+ + O_2 \rightarrow NO^+ + O$	2×10^{-10}	*Huntress and Anicich* [1976]
12.	$N^+ + O_2 \rightarrow NO^+ + O(^1D)$	$\beta = 0.7$	*Langford et al.* [1985]
13.	$O_2^+ + N \rightarrow NO^+ + O$	1.2×10^{-10}	*Fehsenfeld* [1977]
14.	$O_2^+ + NO \rightarrow NO^+ + O_2$	4.4×10^{-10}	*Lindinger et al.* [1974]
15.	$O^+(^2D) + N_2 \rightarrow N_2^+ + O$	8×10^{-10}	*Rowe et al.* [1980]; *Johnsen and Biondi* [1980]
16.	$O^+(^2D) + O \rightarrow O^+(^4S) + O$	5×10^{-12}	*Abdou et al.* [1984]
17.	$O^+(^2D) + O_2 \rightarrow O_2^+ + O$	7×10^{-10}	*Johnsen and Biondi* [1980]
18.	$O^+(^2D) + e^- \rightarrow O^+(^4S) + e^-$	$6.6 \times 10^{-8} (300/T_e)^{.5}$	*Henry et al.* [1969]
19.	$O^+(^2P) \rightarrow O^+(^2D) + h\nu$	0.173 s^{-1}	*Seaton and Osterbrock* [1957]
20.	$O^+(^2P) \rightarrow O^+(^4S) + h\nu$	0.047 s^{-1}	*Seaton and Osterbrock* [1957]
21.	$O^+(^2P) + e^- \rightarrow O^+(^2D) + e^-$	$1.5 \times 10^{-7} (300/T_e)^{.5}$	*Henry et al.* [1969]
22.	$O^+(^2P) + e^- \rightarrow O^+(^2D) + e^-$	$4.7 \times 10^{-8} \cdot (300/T_e)^{.5}$	*Henry et al.* [1969]
23.	$O^+(^2P) + N_2 \rightarrow$ products	4.8×10^{-10}	*Rusch et al.* [1977]
24.	$O^+(^2P) + O \rightarrow$ products	5.2×10^{-11}	*Rusch et al.* [1977]
25.	$He + h\nu \rightarrow He^+ + e^-$	$4.0 \times 10^{-8} - 1.2 \times 10^{7}$ (c)	*Torr and Torr* [1985]
26.	$He^+ + N_2 \rightarrow N^+ + N + He$	1×10^{-9}	*Adams and Smith* [1976]
27.	$He^+ + N_2 \rightarrow N_2^+ + He$	6.5×10^{-10}	*Adams and Smith* [1976]
28.	$O^+ + H \rightarrow H^+ + O$	$2.2 \times 10^{-11} \cdot (T_i)^{.5}$	derived from *Banks and Kockarts* [1973]
29.	$H^+ + O \rightarrow O^+ + H$	$2.5 \times 10^{-11} \cdot (T_n)^{.5}$	derived from *Banks and Kockarts* [1973]
30.	$O^+ + N(^2D) \rightarrow N^+ + O$	5×10^{-11}	*Torr et al.* [1979]
31.	$NO^+ + e^- \rightarrow N(^2D) + O$	$\beta \cdot k_5$ where $\beta = 0.76$	*Kley et al.* [1977]
32.	$N_2^+ + e^- \rightarrow N(^2D) + N$	$\beta \cdot k_7$ where $\beta = 1.9$	*Queffelec et al.* [1985]
33.	$N_2^+ + O \rightarrow N(^2D) + NO^+$	$\beta \cdot k_6$ where $\beta = 1.0$	*Frederick and Rusch* [1977]
34.	$N^+ + O_2 \rightarrow N(^2D) + O_2^+$	$\beta \cdot k_{10}$ where $\beta = 1.0$	assumed
35.	$N(^2D) + O \rightarrow N(^4S) + O$	$\sim 7 \times 10^{-13}$	*Richards et al.* [1981]
36.	$N(^2D) + O_2 \rightarrow NO + O$	6×10^{-12}	*Lin and Kaufman* [1971]
37.	$N(^2D) + e^- \rightarrow N(^4S) + e^-$	$5 \times 10^{-10} (T_e/300)^{.5}$	*Frederick and Rusch* [1977]
38.	$N(^2D) + O_2^+ \rightarrow NO^+ + O$	1×10^{-1}	*Dalgarno* [1970]
39.	$N(^4S) + O_2 \rightarrow NO + O$	$4.4 \times 10^{-12} \exp(-3220/T)$	*Becker et al.* [1969]
40.	$N + NO \rightarrow N_2 + O$	3.4×10^{-11}	*Lee et al.* [1978]
41.	$O_2 + h\nu \rightarrow O(^1D) + O$	$\beta = 1;\ J_\chi(O_2)_{SR} = (1.5-2.8) \times 10^{-6}$	*Torr et al.* [1980]
42.	$O_2^+ + e^- \rightarrow O(^1D) + O$	$\beta\, k_2$ where $\beta = 1.2$	*Abreu et al.* [1986]
43.	$O(^1D) + N_2 \rightarrow O(^3P) + N_2$	$2.0 \times 10^{-11} \exp(107.8\, T_n)$	*Streit et al.* [1976]
44.	$O(^1D) + O_2 \rightarrow O(^3P) + O_2$	$2.9 \times 10^{-11} \exp(67.5/T_n)$	*Streit et al.* [1976]
45.	$O(^1D) \rightarrow O(^3P) + h\nu$	0.00934	*Fischer and Saha* [1983]
46.	$N(^2D) + O_2 \rightarrow O(^1D) + NO$	$\sim 5 \times 10^{-12}$	*Rusch et al.* [1978]; *D. G. Torr et al.* [1981]
47.	$O_2^+ + e^- \rightarrow O(^1S) + O$	$\beta\, k_2$ where $\beta = 0.08$	*Bates and Zipf* [1981]; *Abreu et al.* [1986]
48.	$O_2^+ + N \rightarrow O(^1S) + NO^+$	$\sim 2 \times 10^{-11}$	*Frederick et al.* [1976]
49.	$O(^1S) + O(^3P) \rightarrow O + O$	2×10^{-14}	*Slanger and Black* [1981]
50.	$O(^1D) + O \rightarrow O + O$	8×10^{-12}	*Abreu et al.* [1986]

TABLE 1. (continued)

Reaction Number	Reaction	Rate Coefficient (cm^3 s^{-1}) or Rate (s^{-1})	Reference
51.	$O(^1S) \rightarrow O(^1D + h\nu$	1.07	*Kernahan and Pang* [1975]
	$\rightarrow O(^3P) + h\nu$	0.0444	
52.	$N(^2D) + NO \rightarrow N_2 + O$	7×10^{-11}	*Lin and Kaufman* [1971]
53.	$O(^1S) + O_2 \rightarrow O(^3P) + O_2$	$4.9 \times 10^{-12} \exp(-1730/RT)$	*Zipf* [1979]
54.	$N_2(A^3\Sigma_u^+) + O \rightarrow$ products	2×10^{-11}	*Piper* [1982]
55.	$N_2(A^3\Sigma_u^+) + O \rightarrow O(^1S) + N_2$	$\beta \cdot k_{54}$ where $\beta = 0.37$	*Piper* [1982]
56.	$N_2^{+*} + O \rightarrow O^+ + N_2$	$\sim 2 \times 10^{-10}$[b]	*Abdou et al.* [1984]; *Torr* [1985]
57.	$N_2 + h\nu \rightarrow N^+ + N + e$	$(1.78 - 5.14) \times 10^{-18}$	*Torr and Torr* [1985][c]
	$\rightarrow N_2^+ + e$	$(3.06 - 8.82) \times 10^{-7}$	
58.	$O + h\nu \rightarrow O^+(^4S) + e$	$(0.98 - 2.81) \times 10^{-7}$	*Torr and Torr* [1985][c]
	$\rightarrow O^+(^2D) + e$	$(0.79 - 2.34) \times 10^{-7}$	
	$\rightarrow O^+(^2P) + e$	$(0.45 - 1.38) \times 10^{-7}$	
	$\rightarrow O^+(^4P) + e$	$(1.04 - 3.43) \times 10^{-8}$	
	$\rightarrow O^+(^2P^*) + e$	$(0.46 - 1.42) \times 10^{-8}$	

[a] Since the results of *Chen et al.* [1978] stop at 700°K, we normalize the converted drift tube data parameterized by *St. Maurice and Torr* [1978] at this temperature.

[b] The model computes this rate coefficient as a function of N_2^+ vibrational temperature (T_v). The value reduces to that given by equation (6) when $T_v = T_n$. Inclusion of this process is an option available [see *Abdou et al.*, 1984].

[c] The ranges given for the ionization frequencies indicate the variation over a solar cycle.

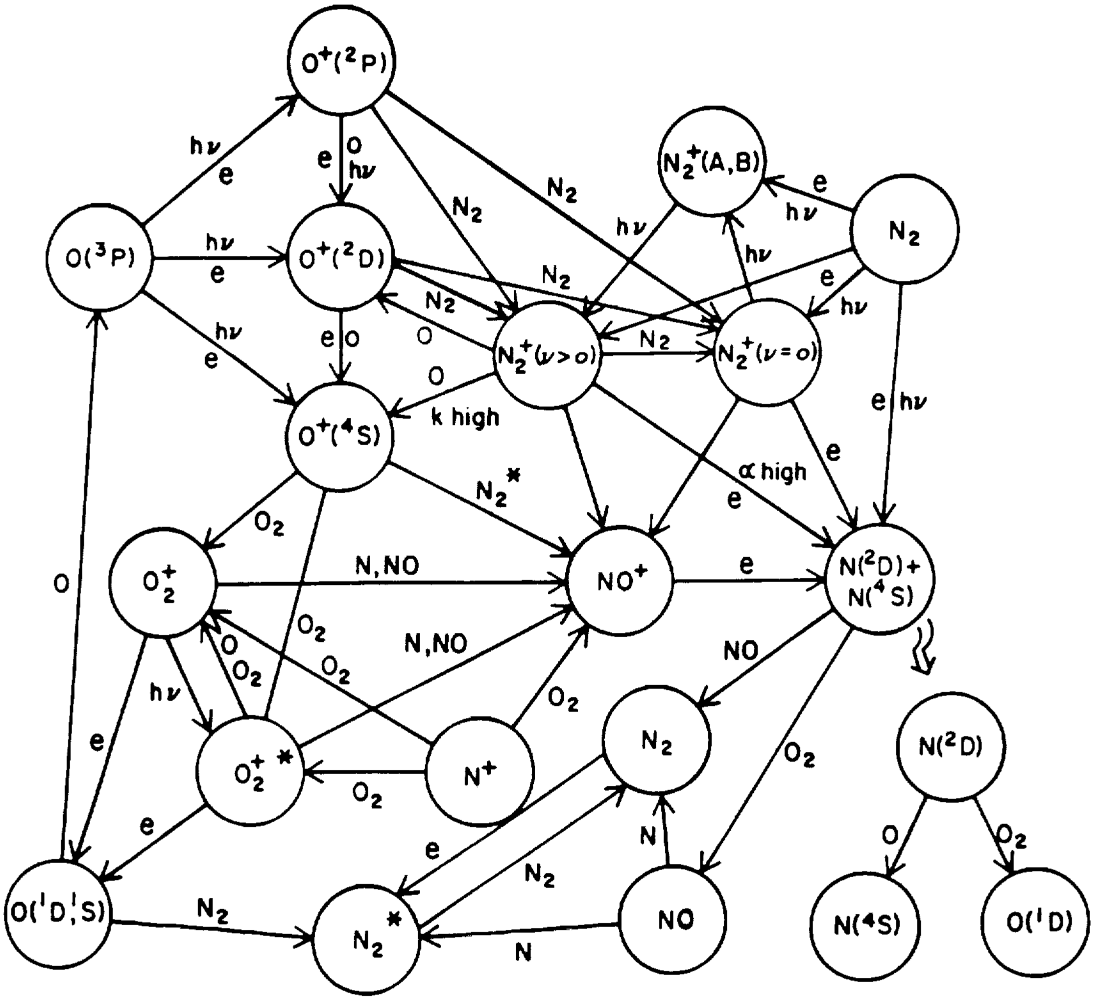

Fig. 3. Schematic of the thermospheric and ionospheric chemistry that is incorporated in the model.

corresponding to solar maximum ($F10.7 = 194$, $Ap = 23$). This study deals only with the airglow, and we do not show results for latitudes higher than $L = 5$.

Details of the results are given in the following section.

MODELING OF THE 7320-Å AIRGLOW EMISSION

The 7320-Å emission arises from the $O^+(^2P)$ state, which is produced in the thermosphere by two mechanisms: photoionization and photoelectron ionization:

$$O + h\nu \rightarrow O^+(^2P) + e$$

$$O + e^* \rightarrow O^+(^2P) + 2e$$

where the photoelectrons may be those produced locally, or those produced in the conjugate hemisphere and transported along the magnetic field lines. The $O^+(^2P)$ is lost by several mechanisms: radiation

$$O^+(^2P) \rightarrow O^+(^4S) + h\nu_{7320\ \text{Å}}$$

collisional deactivation

$$O^+(^2P) + N_2 \rightarrow N_2^+ + O$$

$$O^+(^2P) + O \rightarrow O^+ + O$$

$$O^+(^2P) + e \rightarrow O^+(^2D) + e$$

$$O^+(^2P) + e \rightarrow O^+(^4S) + e$$

This photochemistry has been reviewed by *Torr and Torr* [1982]. It should be noted that since publication of the aeronomically derived values of the rate coefficients by *Rusch et al.* [1977], the solar EUV flux below ≈250 Å was doubled. We estimate that when quenching dominates, the reported intensities may be about 30% too high.

Plate 1 shows the 7320-Å volume emission rate at the peak of the layer as a function of latitude, local time (longitude) and altitude. The upper plot shows the peak volume emission rate as a function of latitude and local time. Because the model has longitudinal variability resulting from both the MSIS [*Hedin* 1987] model atmosphere, and the interhemispheric coupling, this particular plot is shown for 00 UT. This UT is equivalent to placing midnight at 0° longitude, the Greenwich meridian, and noon at 180° longitude, i.e. over the Pacific Ocean. Where the volume emission rate becomes so small as to be effectively zero, the values are not plotted. These regions can be seen near midnight for equatorial latitudes, and represent no production at these times. The graphics tend to smear the northern and southern latitude boundaries by a few degrees to the north and south, respectively. The solutions are only valid, however, within the $L \leq 5$ region illustrated in Figure 5.

The basic features shown in Plate 1 have been discussed by *Torr et al.* [1990] but we will review them here briefly as this plate will be used for the comparison with other cases. Summer is

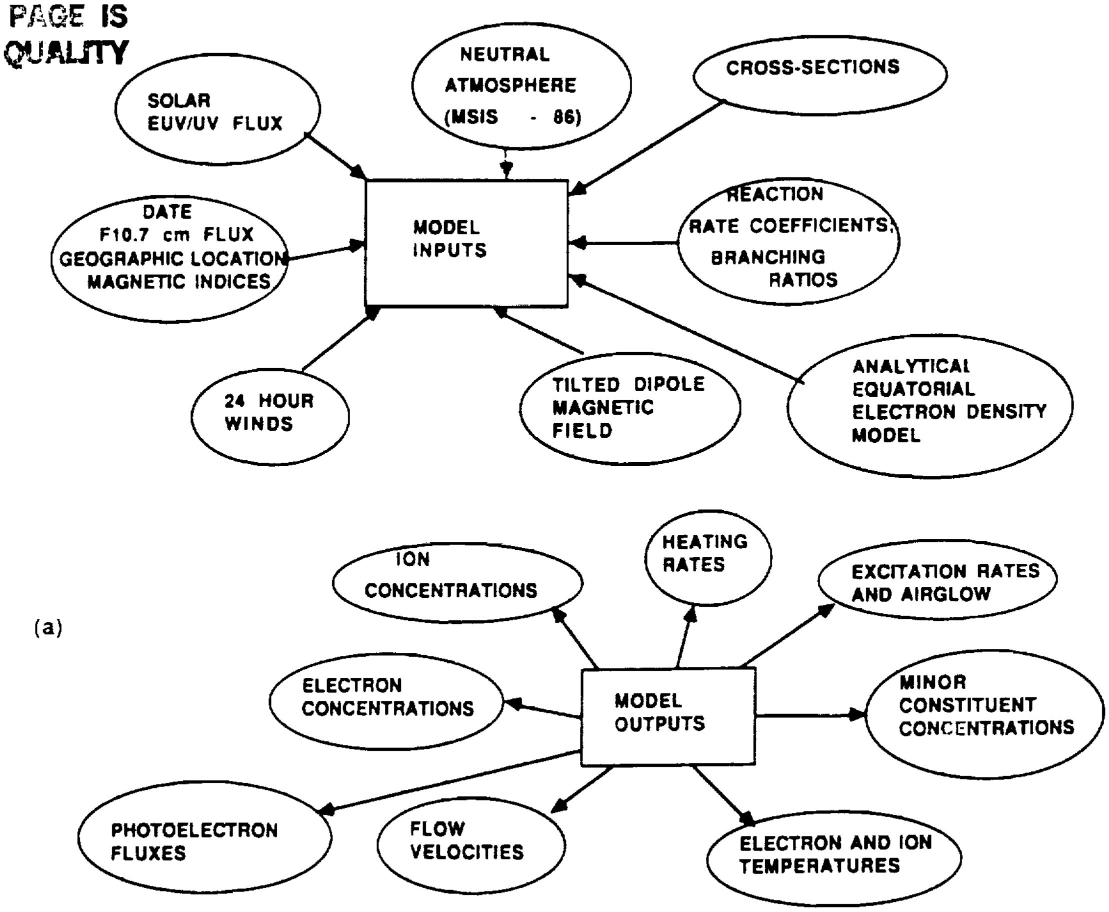

Fig. 4(*a*). Schematic illustration of the major input and output elements of the field line interhemispheric plasma (FLIP) code. (*b*) Illustration of the flow of the solutions.

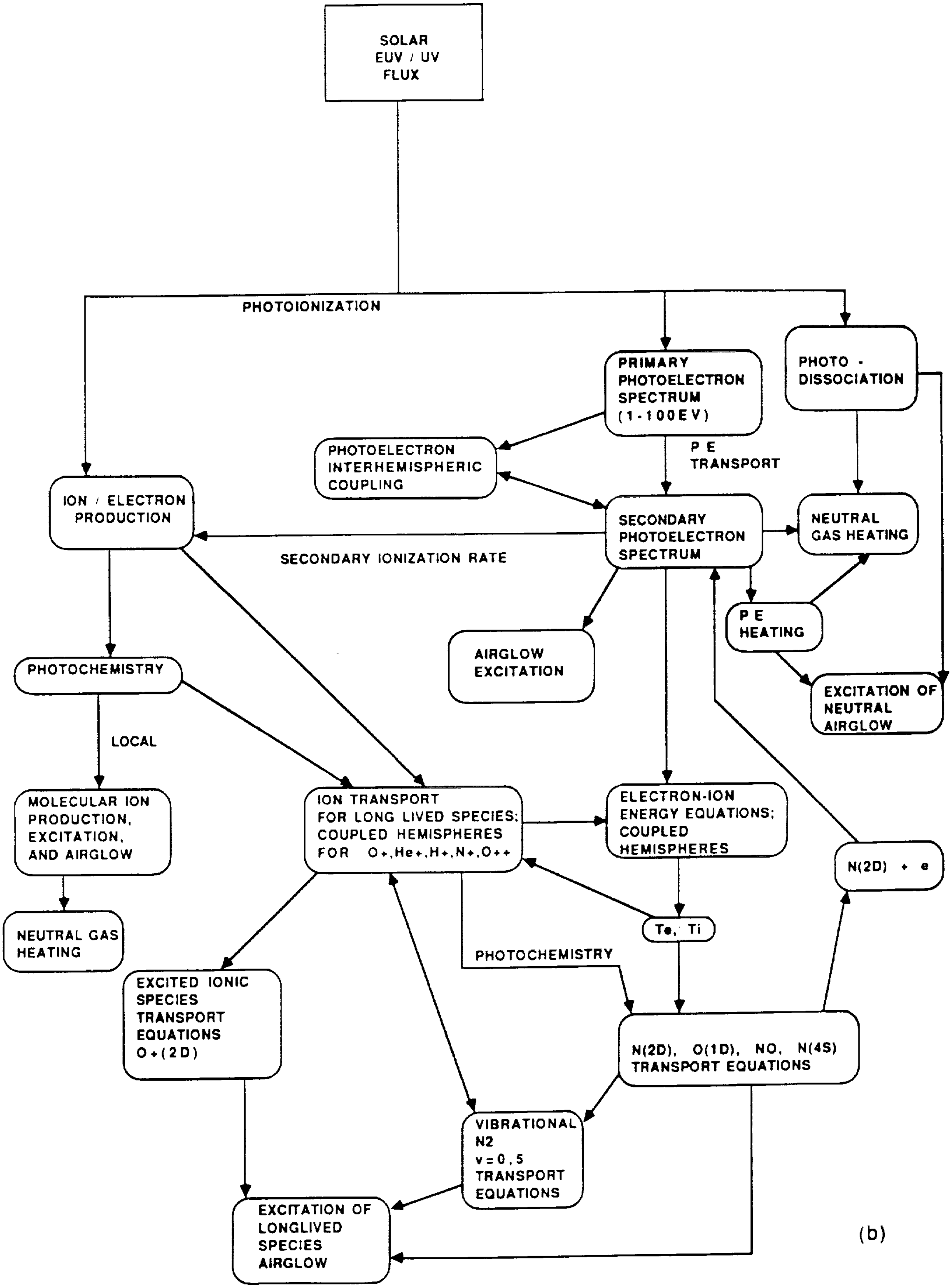

Fig. 4. (continued)

in the southern hemisphere as is immediately seen by the longer duration of the midday peak volume emission rates. Figure 6 shows the production and loss rates at northern and southern mid-latitudes near noon. In both cases the major production mechanism is photoionization with photoelectron impact contributing about 25%. The major high altitude loss mechanism is radiation, while quenching by N_2 dominates at lower altitudes. It is interesting to note in Plate 1 that the midday peak volume emission rates in the winter (northern) hemisphere are somewhat larger than in the summer hemisphere. The reason for this can be seen in Figure 6. While the N_2 peak quenching rate is almost identical in both hemispheres, the N_2 quenching falls off with altitude with a smaller scale height in the winter hemisphere, so that radiation dominates to a lower altitude with the resulting higher emission rate.

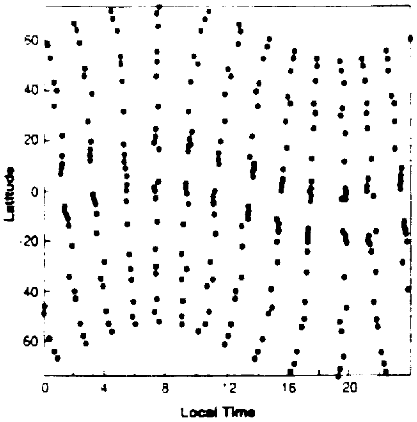

Fig. 5. Locations of grid points at which diurnal altitude solutions were obtained.

At and beyond the terminators (for solar zenith angles larger than 90°) sunlight illuminates increasingly higher altitudes, and the peak altitude rises while the volume emission rate falls sharply. In Figure 7 we show the production and loss rates for a solar zenith angle of 105° in the evening southern hemisphere. The peak UV photoionization has risen to above 600 km. A second peak is formed near 300 km. The latter is a result of photoelectrons which are produced in the ionization process that caused the upper peak. The photoelectrons are transported downward and lose their energy near 300 km in the impact ionization of atomic oxygen. Plate 2 shows the same information as was given in Plate 1, but versus solar zenith angle instead of local time. This plate shows the extent to which seasonal hemispheric asymmetries are reduced when the data are plotted in this format.

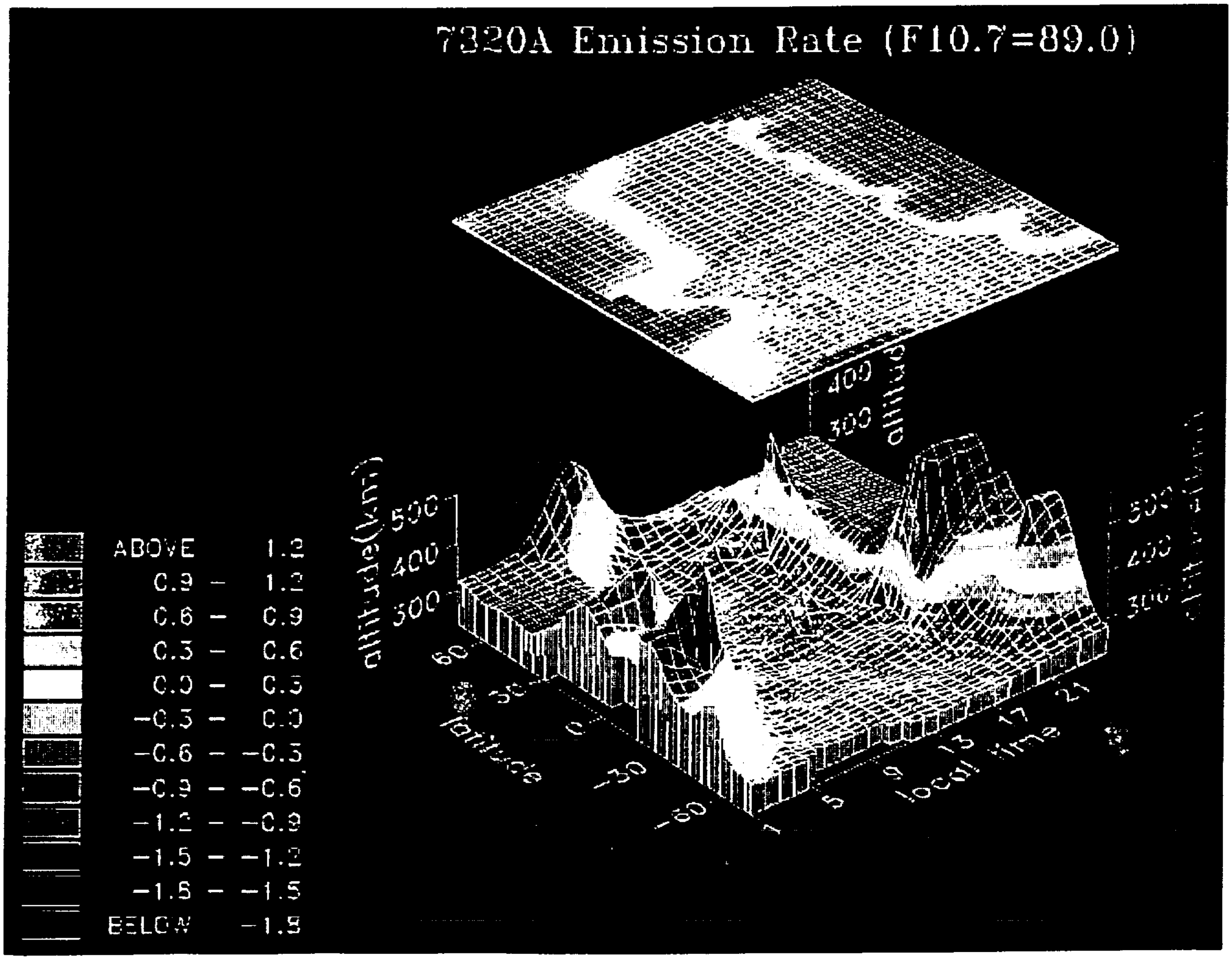

Plate 1. The 7320-Å volume emission rate (photons cm^{-3} s^{-1}) at the peak of the layer as a function of altitude, latitude, and local time (longitude) for 00 UT. The upper plot shows the peak volume emission rate only as a function of latitude and local time. The volume emission rate is on a log scale. The results are only valid within the $L \approx 5$ boundaries shown in Figure 5.

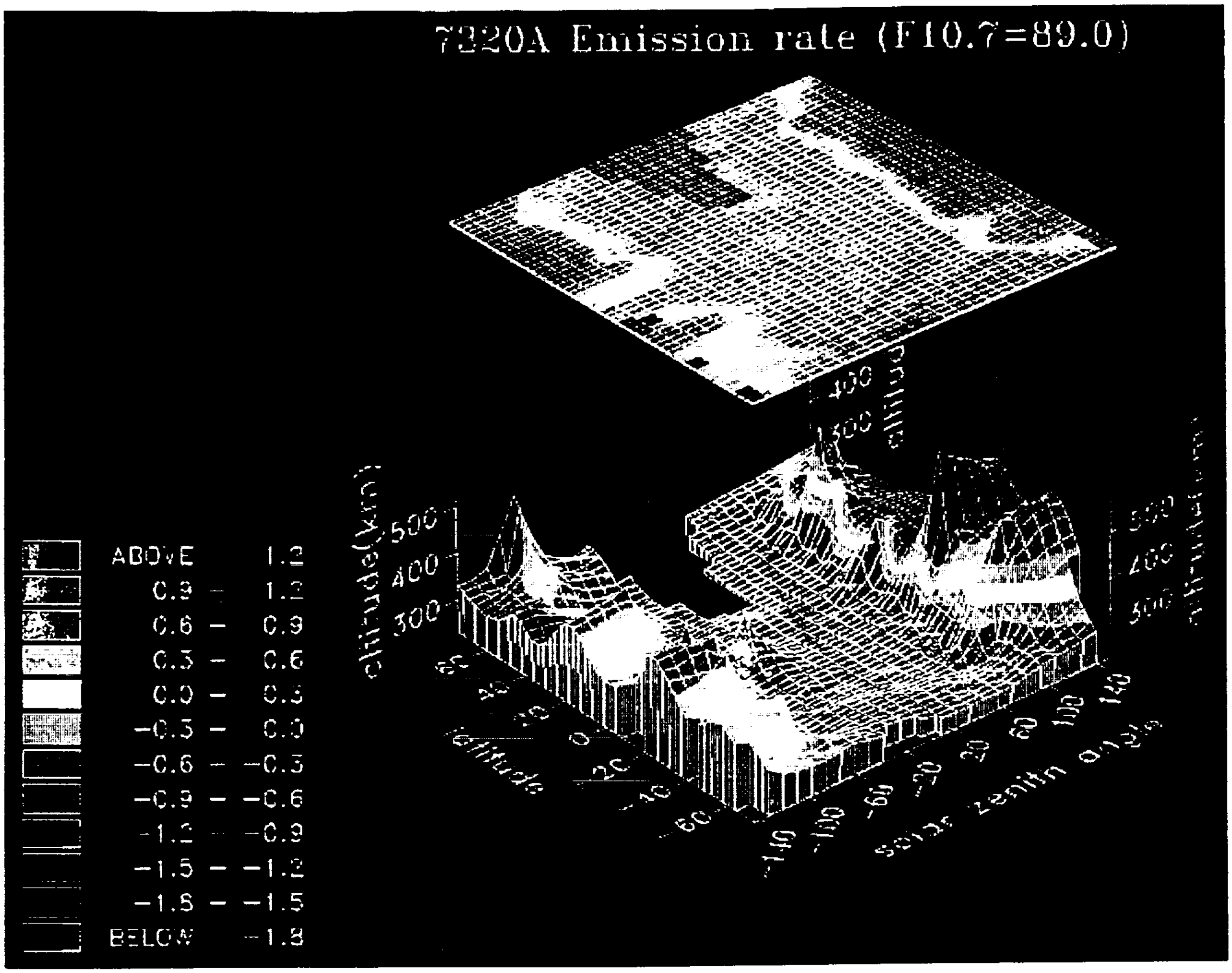

Plate 2. The 7320-Å volume emission rate (photons $cm^{-3} s^{-1}$) at the peak of the layer as a function of altitude, latitude, and solar zenith angle. The volume emission rate is on a log scale.

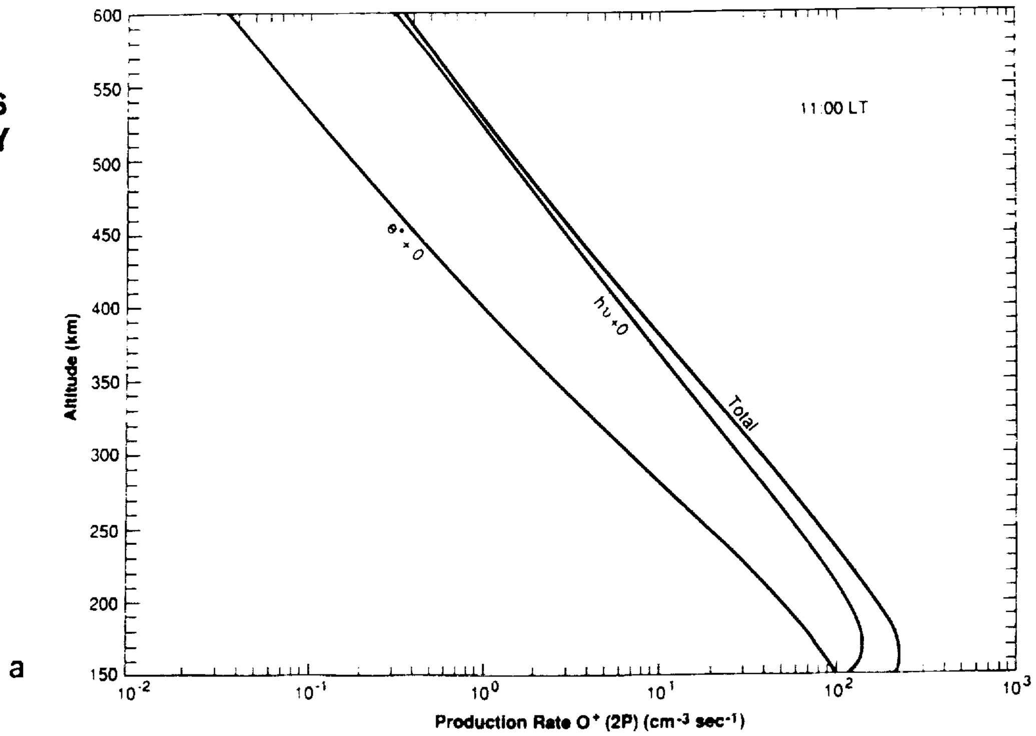

Fig. 6. Midday, mid-latitude production and loss rates for $O^+(^2P)$: (*a*) and (*b*) southern hemisphere for 48°S, 11 LT, $\chi = 28°$; (*c*) and (*d*) northern hemisphere for 40°N, 12 LT, $\chi = 60°$.

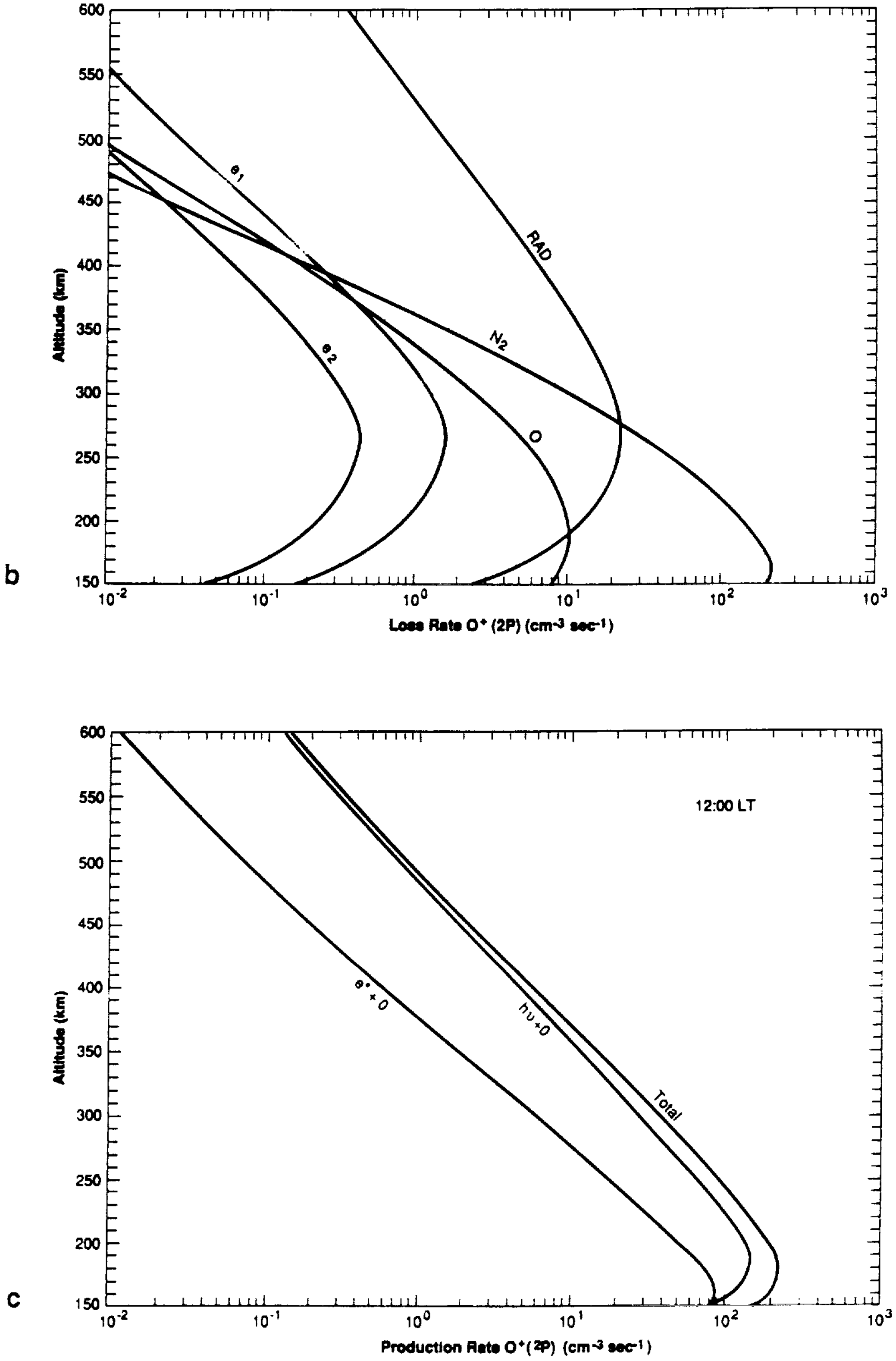

Fig. 6. (continued)

An interesting feature of Plate 1 is the fact that there is significant production (≈ 0.2 cm^{-3} s^{-1}) at high altitudes at midnight in the winter hemisphere. This is due entirely to photoelectrons transported from the summer hemisphere. This conjugate electron production rate together with the loss processes are shown in Figure 8. Without the interhemispheric capability this production source would not be modeled.

Because of the longitudinal asymmetries of the Earth's magnetic field, the conjugate photoelectron production rate varies for different maps generated for different universal times. Plate 3

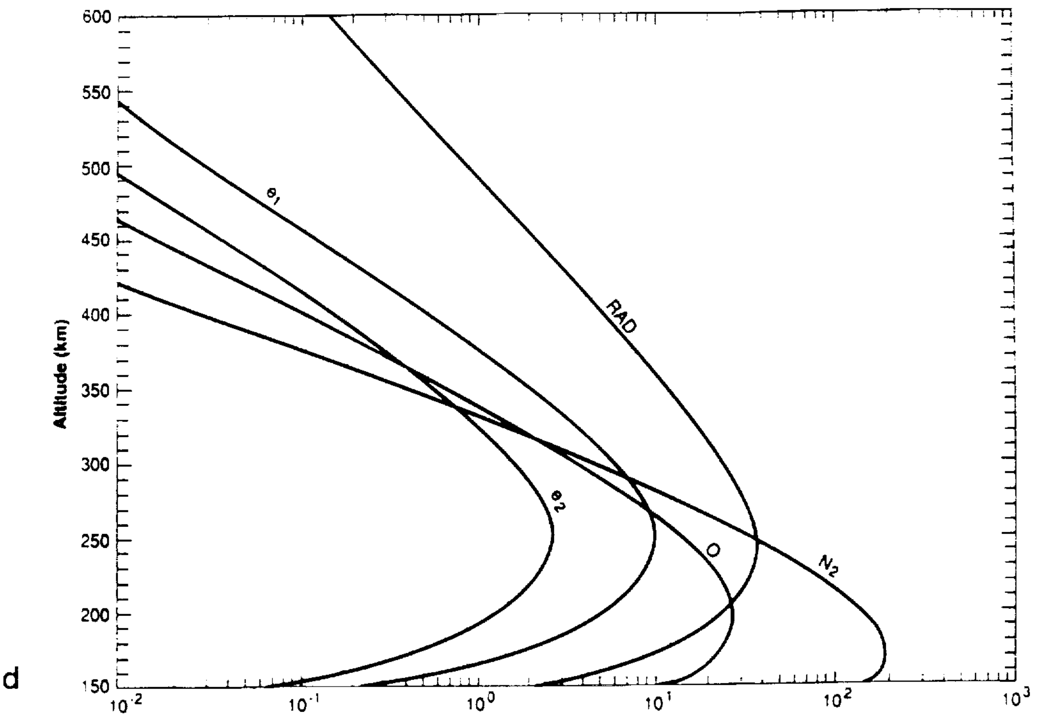

ORIGINAL PAGE IS
OF POOR QUALITY

Fig. 6. (continued)

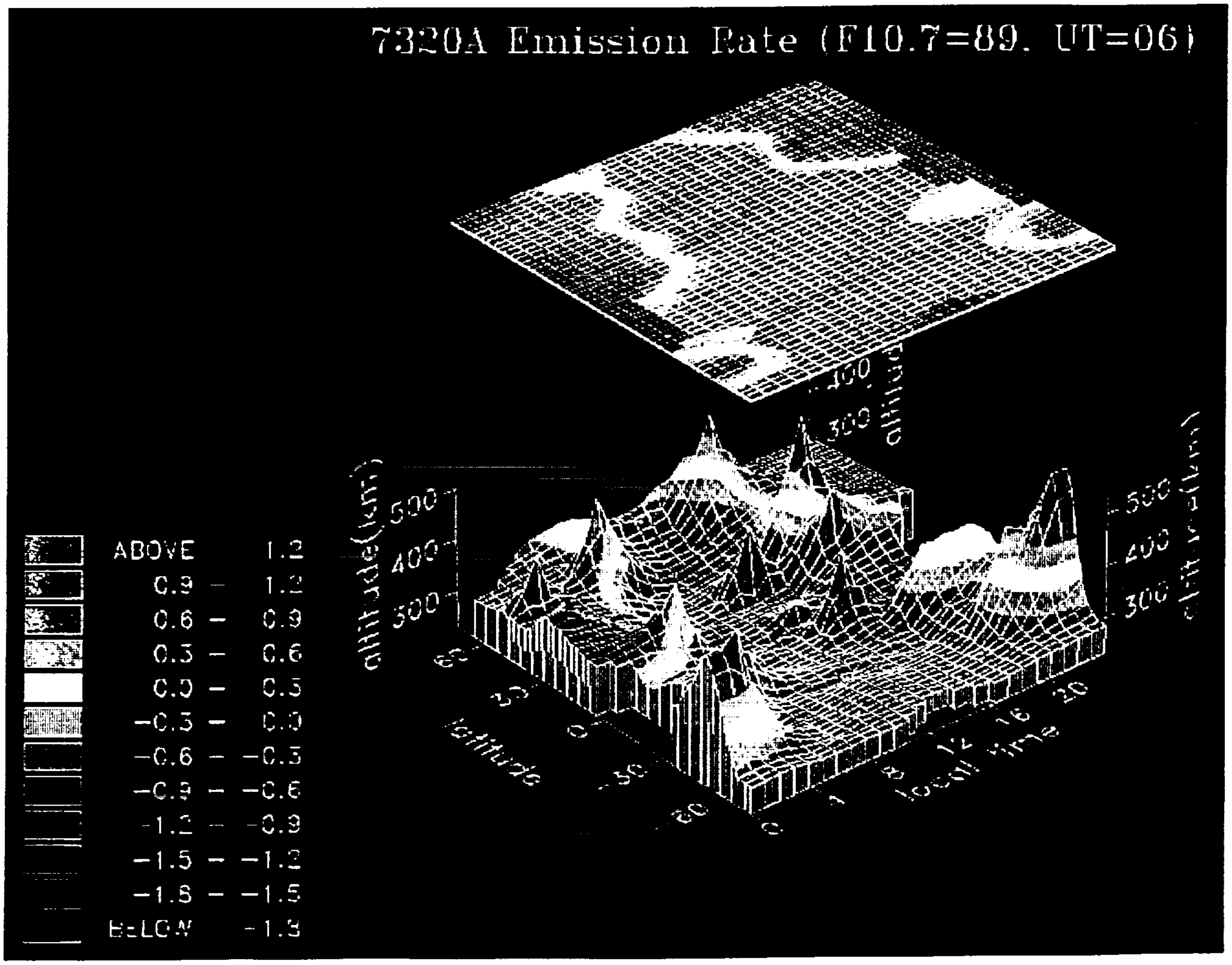

Plate 3. The 7320-Å volume emission rate (photons cm^{-3} s^{-1}) at the peak of the layer as a function of altitude, latitude, and local time for 06 UT. The volume emission rate is on a log scale. The missing areas near the equator at midnight are where the emission rate has effectively gone to zero.

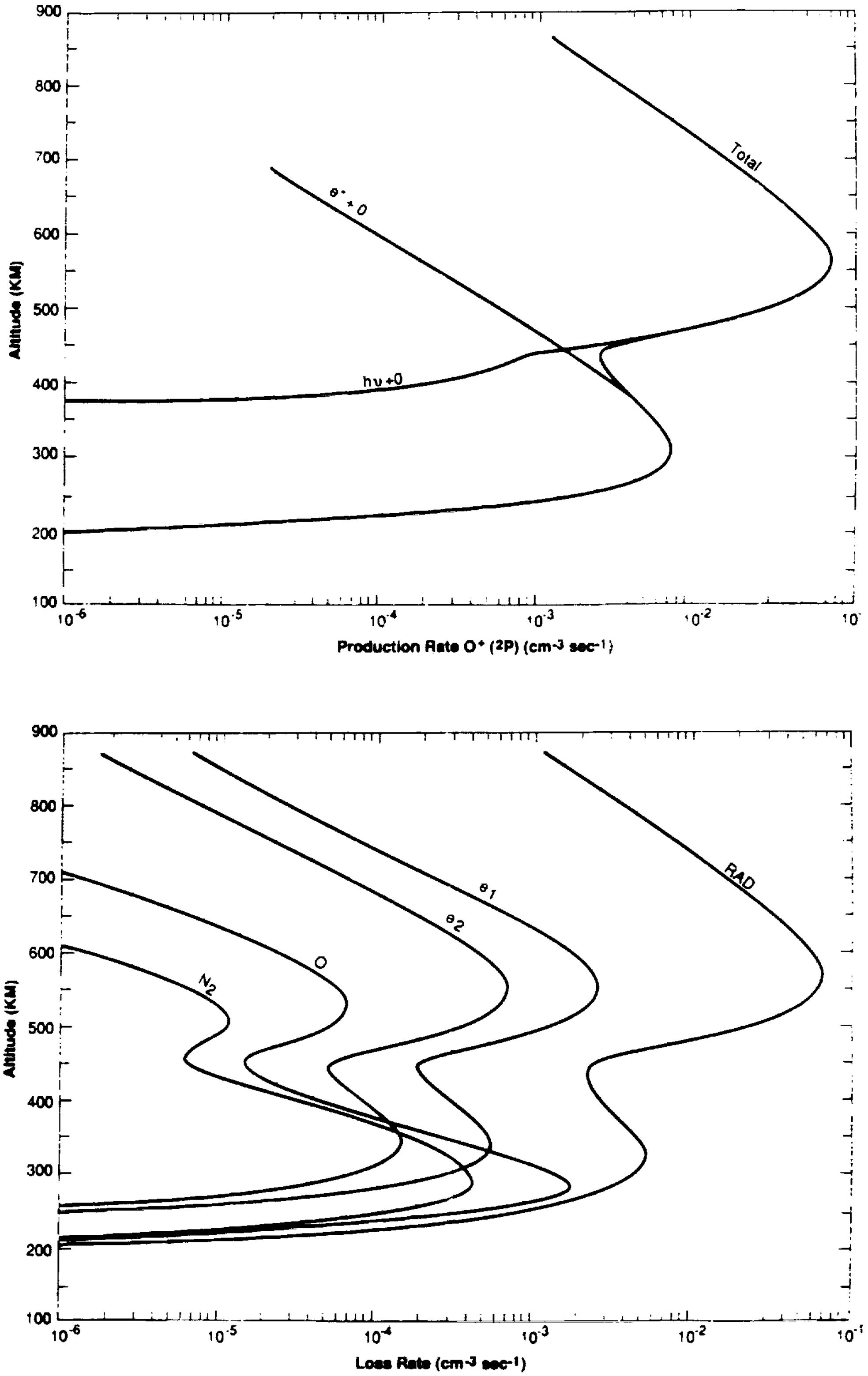

Fig. 7. Production and loss rates for 54°S for a solar zenith angle of 105° (LT = 00).

shows the global plot for the same conditions as Plate 1, but for UT = 0600. This is equivalent to placing midnight at 90°W, over the eastern United States. In this longitudinal sector, higher southern latitudes (solar illuminated) map to lower northern latitudes. Above 50°S the Sun does not set and conjugate electrons are present all through the night near 50°N. Thus the conjugate source is seen to be significantly more pronounced than for 00 UT. Plate 4 shows the integrated volume emission rate, or surface brightness (in rayleighs), with and without the conjugate photoelectron source. The scale has been adjusted to enhance the winter

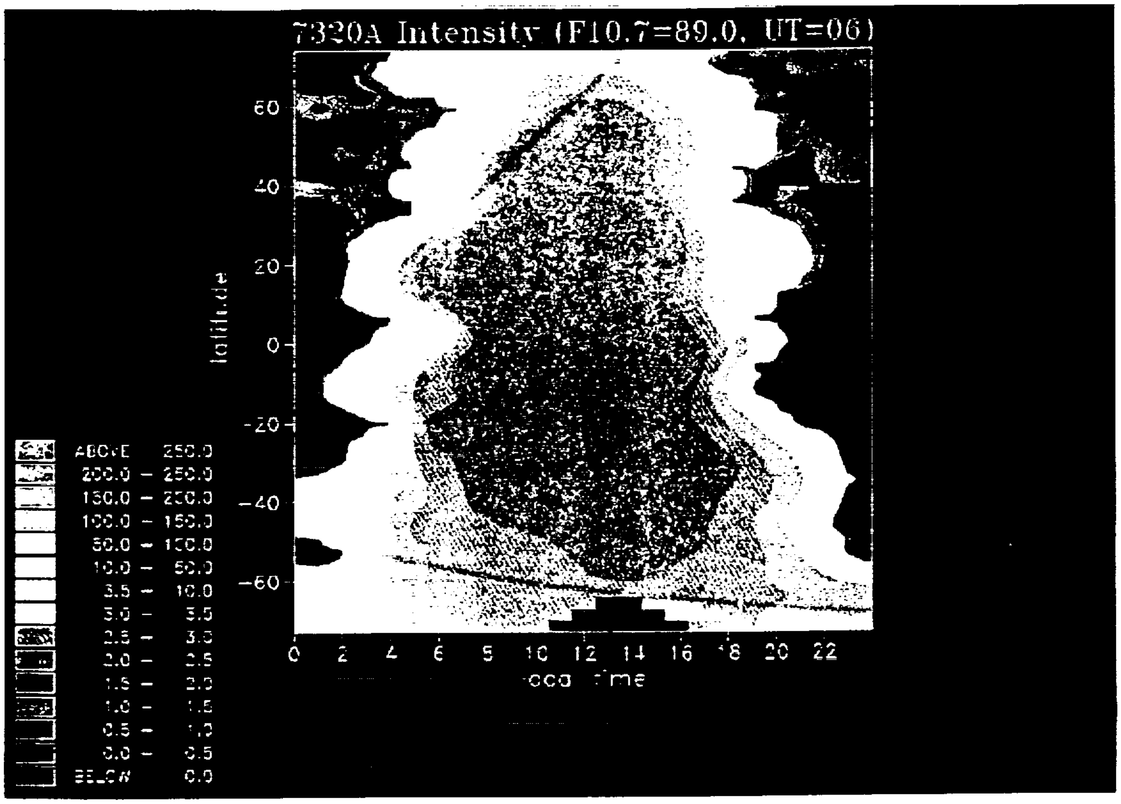

Plate 4*a*. With conjugate photoelectron production.

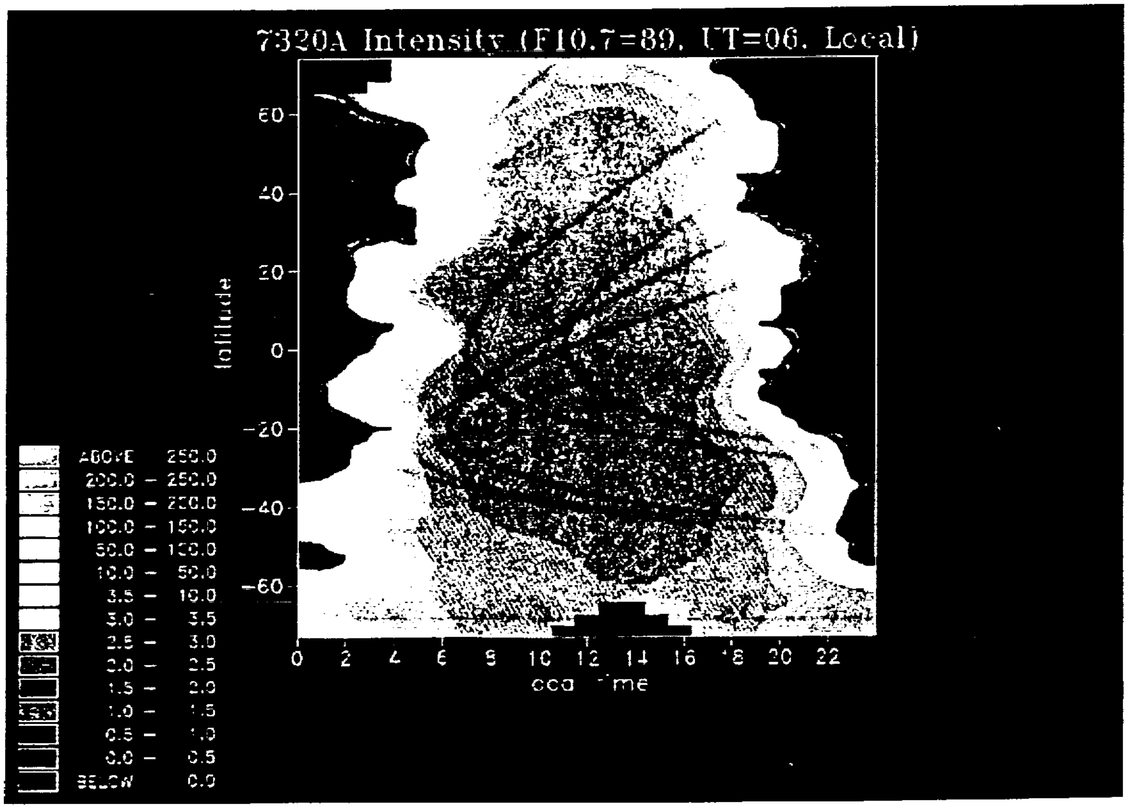

Plate 4*b*. Without conjugate photoelectron production.

Plate 4. Vertical 7320-Å intensity (rayleighs) for solar minimum at UT = 06. The solution is only valid within the $L \leq 5$ boundaries shown in Figure 5.

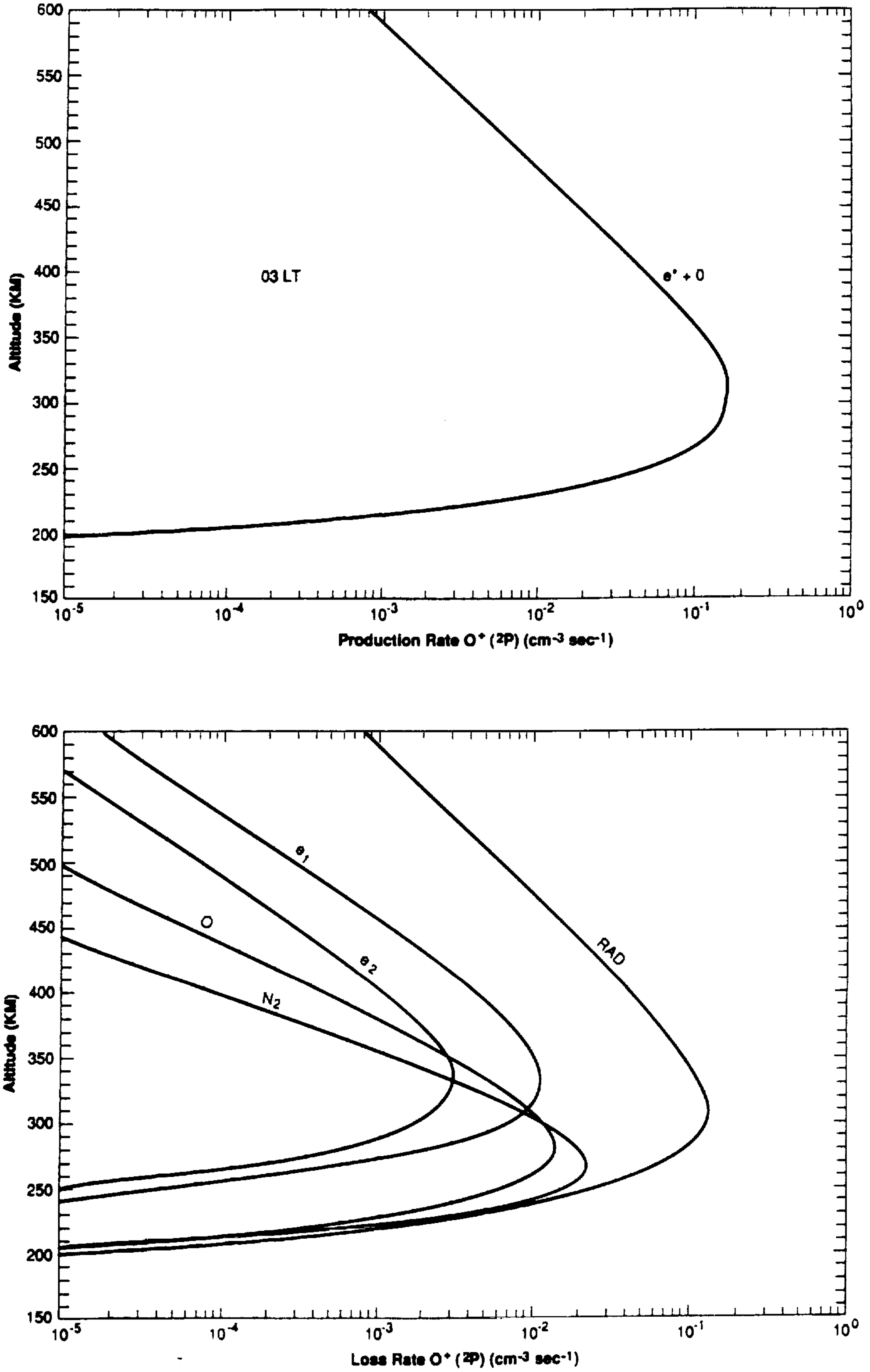

Fig. 8. Conjugate photoelectron production of $O^+(^2P)$ at night in the winter hemisphere (49°N. χ = 137°). The corresponding loss rates are also shown.

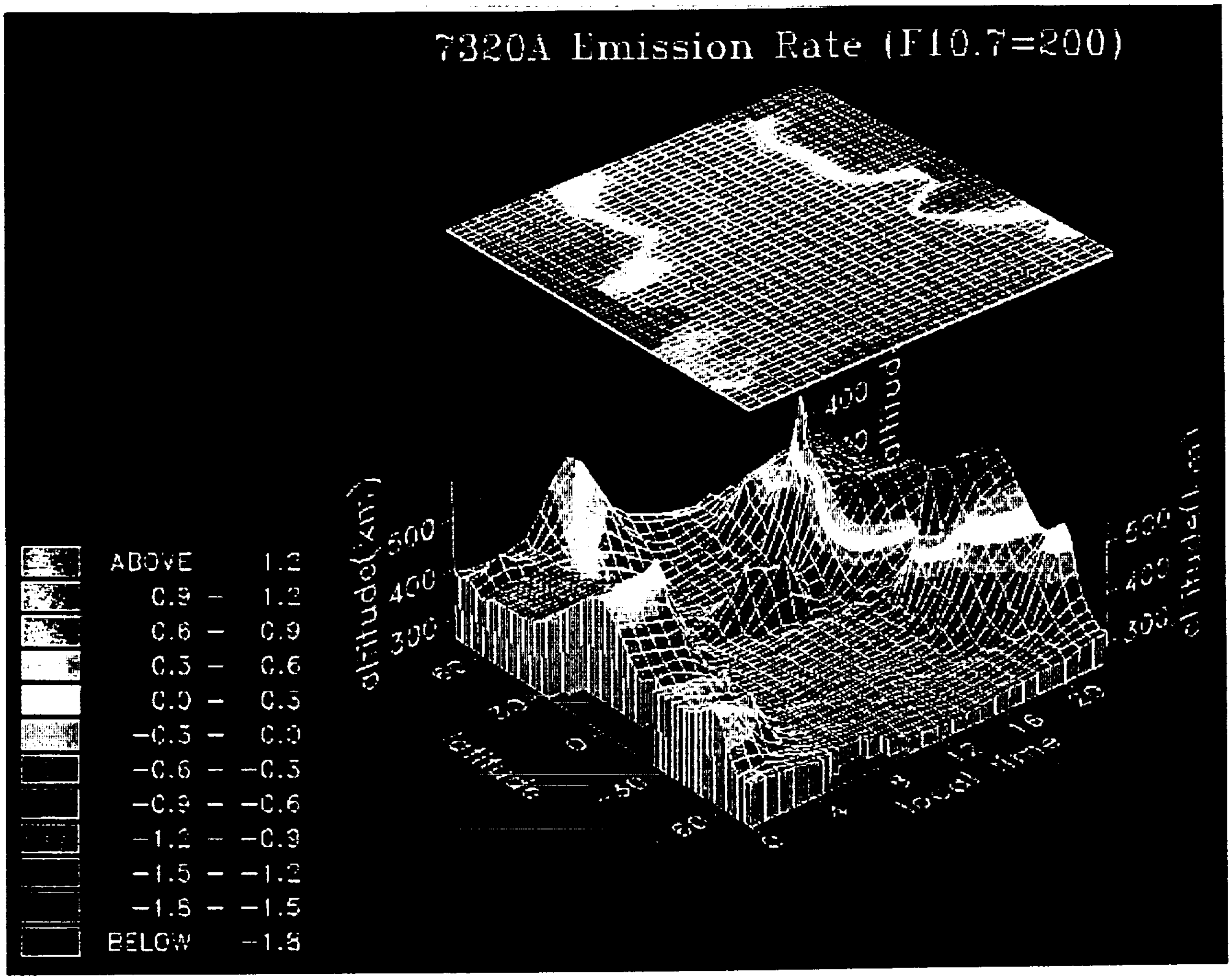

Plate 5. The 7320-Å volume emission rate (photons cm^{-3} s^{-1}) at the peak of the layer as a function of altitude, latitude, and local time for 00 UT. The results are for the same day as Plate 1 (November 28) but for solar maximum conditions. The volume emission rate is shown on a log scale.

nighttime conjugate production. This interhemispheric source results in 2 to 3 R of 7320-A airglow.

Plate 5 shows the same day of year as Plate 1, but for conditions representing solar maximum. The principal differences between these two are in the overall increase in emission rate and the overall increase in altitude of the emission peak. Both of these effects are to be expected on the basis of the solar flux and neutral atmosphere changes.

Plate 6 shows the results of integrating the volume emission rates of the solar minimum and maximum cases (Plates 1 and 5) over altitude to obtain the vertical surface brightness. These intensities (in rayleighs) are what an orbiting instrument would see looking vertically downward on the atmosphere.

MODELING OF THE N_2 3371-Å AIRGLOW

The production mechanism for the excitation of the N_2 second positive system in the dayglow is photoelectron impact:

$$N_2(X^1\Sigma_g^+) + e^* \rightarrow N_2(C^3\pi_u) + e$$

The 3371-A emission arises from the 0–0 band of the second positive system:

$$N_2(C^3\pi_u) \rightarrow N_2(X^1\Sigma_g^+) + h\nu$$

Since the transition is permitted, radiation is the only loss process. The excitation cross sections for the 0–0 band are those of *Imami and Borst* [1974] which are 25% of the total cross section.

Plate 7 shows the results of the semiglobal solution of the 3371-Å volume emission rates. The production rates for noon at midlatitudes are shown in Figure 9. The results shown in Plate 7 follow the behavior anticipated from a simple photoelectron source and radiative loss. The behavior changes after sunset in that the peak production rises in altitude and falls in magnitude. Again, the high latitude conjugate photoelectron source can be seen during the night in the winter hemisphere. While we do not show the 06 UT case here, the conjugate source again becomes more pronounced for the different magnetic field orientation, as it did for the 7320-Å case, because of the more favorable alignment of the magnetic field lines for this purpose.

Plate 8 shows the global model of the peak 3371-Å volume emission rate for solar maximum. What is interesting to note in this case is that, apart from an overall increase in the altitude of the emission peak, the peak emission rate distribution is very similar at solar maximum and solar minimum. However, the difference in the vertical intensity is significant. This is seen in Plate 9 which shows the integrated column surface brightness for solar minimum and maximum. The difference is largely due to the differing scale heights, as can be seen in Figure 9.

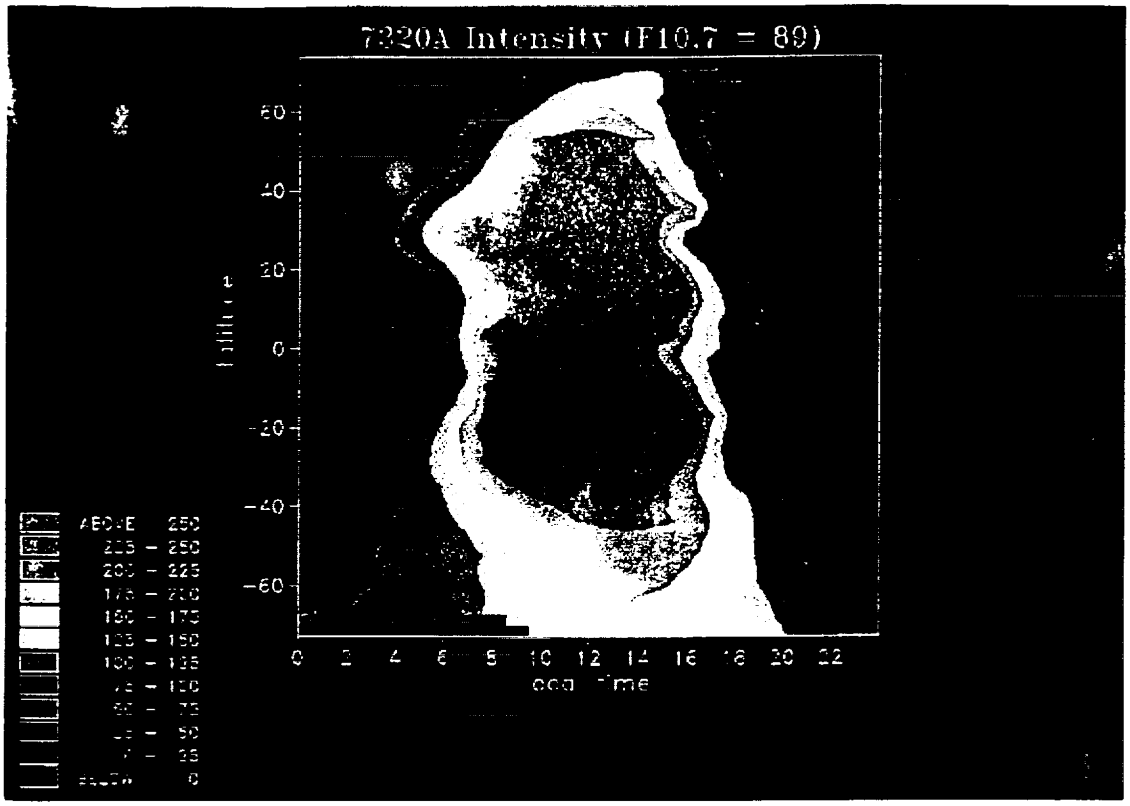

Plate 6*a*. Solar minimum case shown in Plate 1.

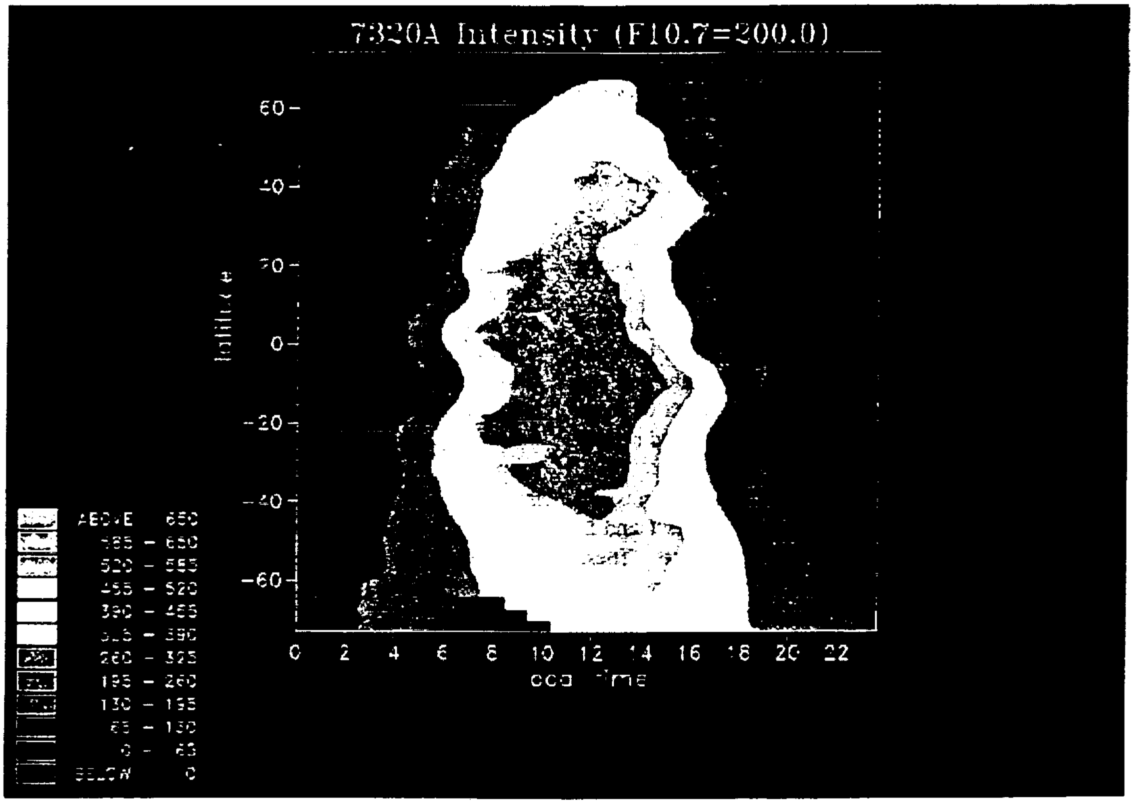

Plate 6*b*. Solar maximum case shown in Plate 5.

Plate 6. Vertical column integrated surface brightness (in rayleighs). The results are only valid within the $L \leq 5$ boundaries shown in Figure 5.

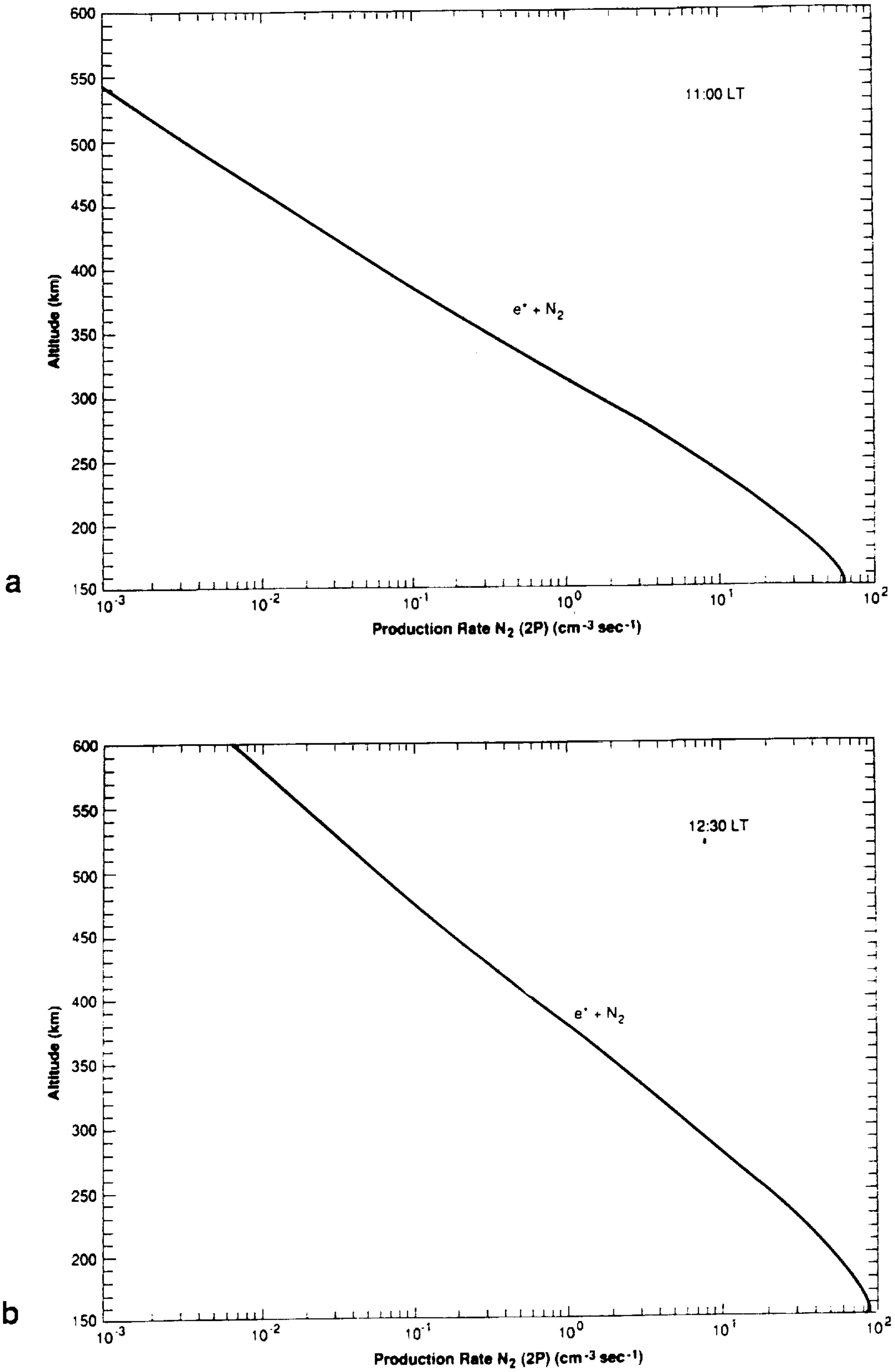

Fig. 9. Production rates for the $N_2(^3C)$ state for 00 UT (*a*) for solar minimum (48°S) and (*b*) for solar maximum (53°S).

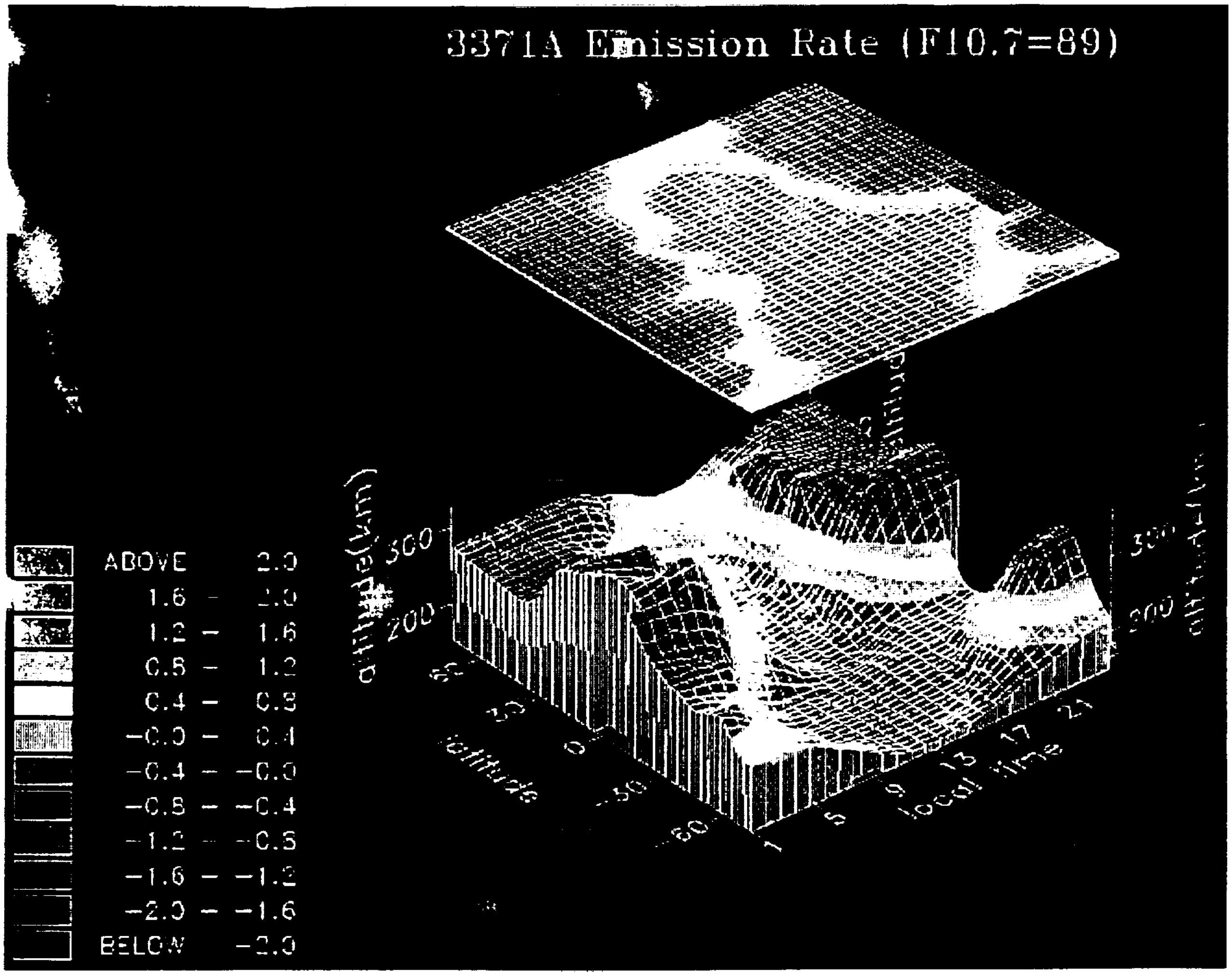

Plate 7 Volume emission rate (photons cm^{-3} s^{-1}) at the peak of the 3371-A layer versus altitude, latitude, and local time (longitude) for near solar minimum conditions. The volume emission rate is plotted on a log scale. The results are only valid within the $L \leq 5$ boundaries shown in Figure 5.

SUMMARY

In this paper we have presented the first interhemispherically coupled models of the $O^+(^2P)$ and $N_2(^3C)$ airglow emission at 7320 A and 3371 A, respectively, covering mid and low latitudes. These are two emissions for which the mechanisms are relatively well understood, allowing us to examine here the morphology. The semiglobal graphical maps clearly illustrate the diurnal, seasonal and solar cyclic variability of these emissions. In both cases, conjugate photoelectrons result in excitation at mid to high nighttime latitudes in the winter hemisphere. The in[illegible]mispheric coupling capability of the model allows us to [illegible] he extent and the longitudinal variability of the conjugate photoelectron effects.

This model provides a capability which will greatly enhance the ability to interpret airglow observations made from spacecraft. Any line of sight geometry can now be projected through the three-dimensional model solution, and by integrating along the projected line of sight, surface brightness (vertical or slant path) can be obtained for comparison with the observations. Furthermore, because of the complex variability exhibited by these emissions over the $L \leq 5$ range, this model also provides a valuable tool for planning of such observations.

Plate 9 Vertical intensity of the 3371-A airglow (in rayleighs) for solar minimum and solar maximum conditions. The solar maximum plot is shown on two scales: one to show the intensity variation and one to allow comparison with the solar minimum plot shown in Plate 9*a*. The results are only valid within the $L \leq 5$ boundaries shown in Figure 5.

ORIGINAL PAGE IS
OF POOR QUALITY

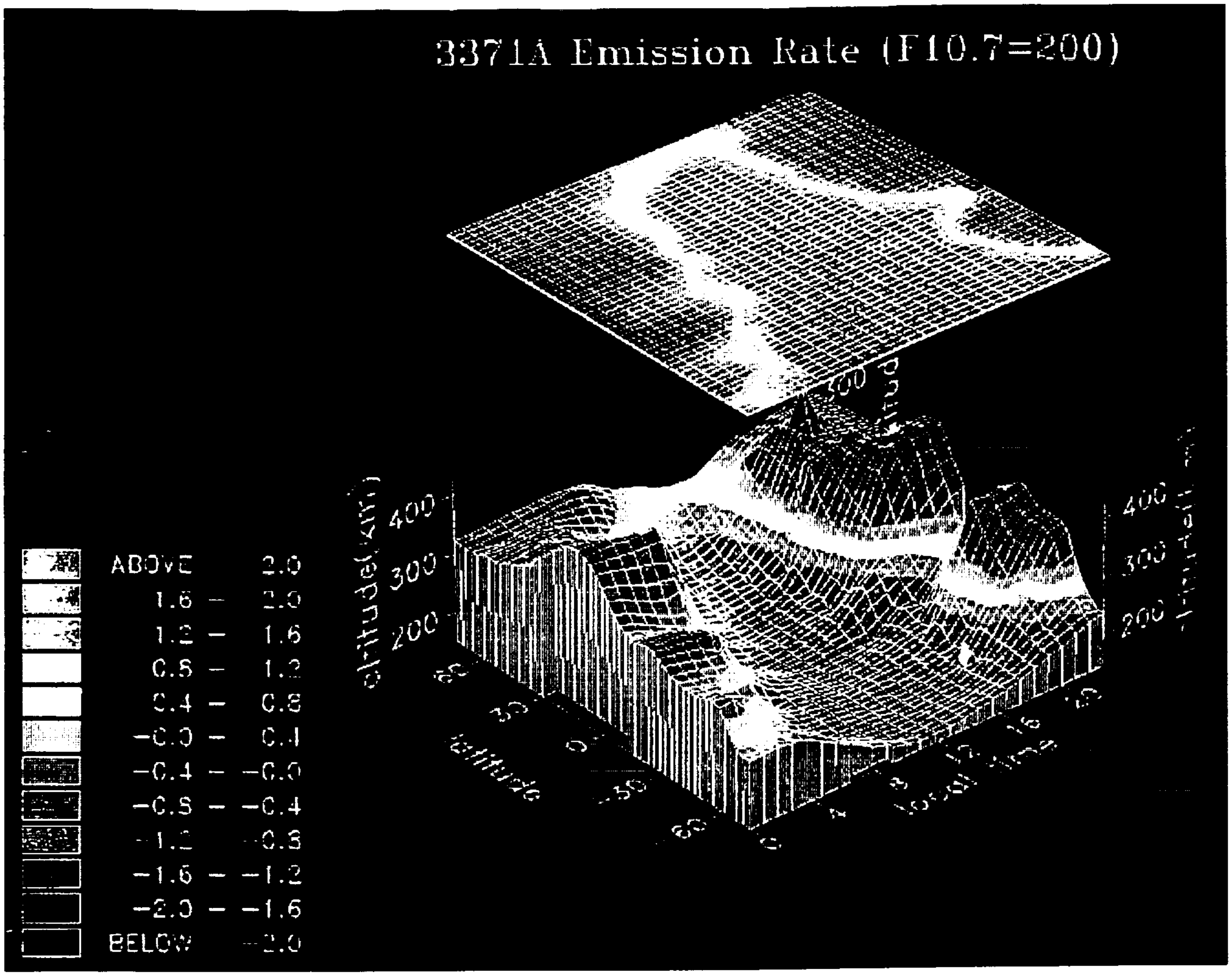

Plate 8. Volume emission rate (photons cm^{-3} s^{-1}) at the peak of the 3371-Å layer for solar maximum conditions. The volume emission rate is plotted on a log scale.

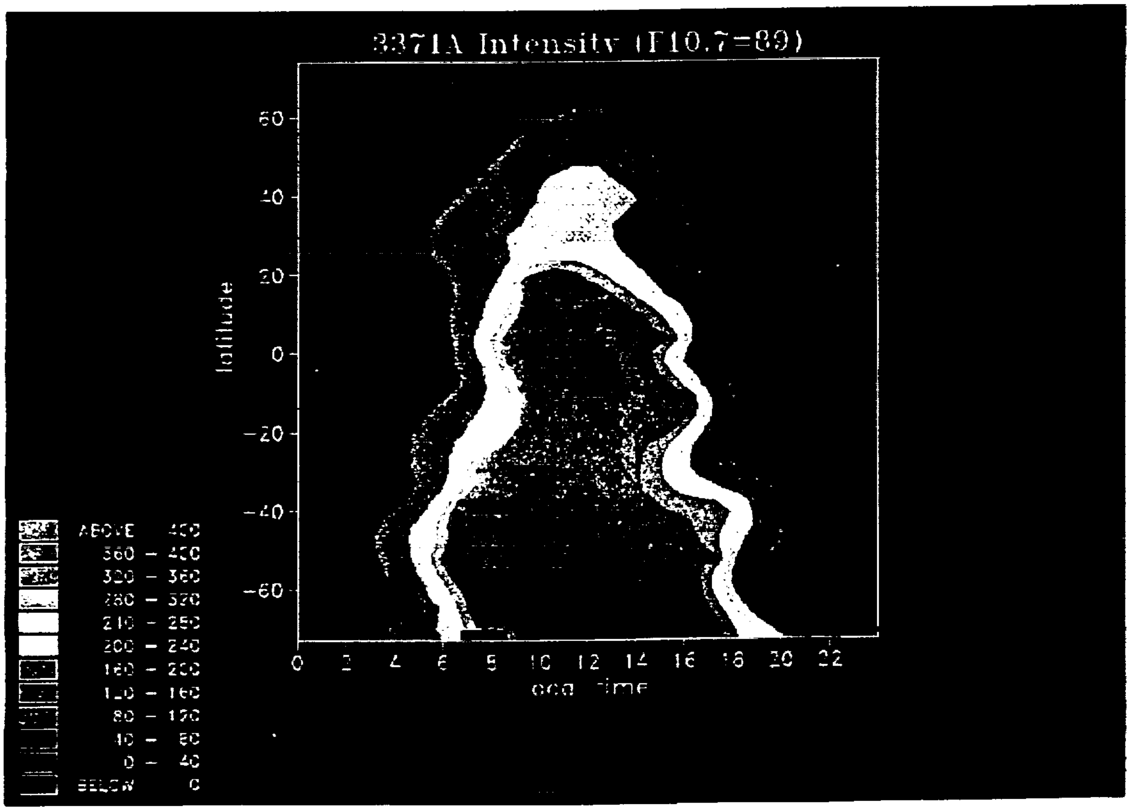

Plate 9*a*
Solar minimum

ORIGINAL PAGE IS
OF POOR QUALITY

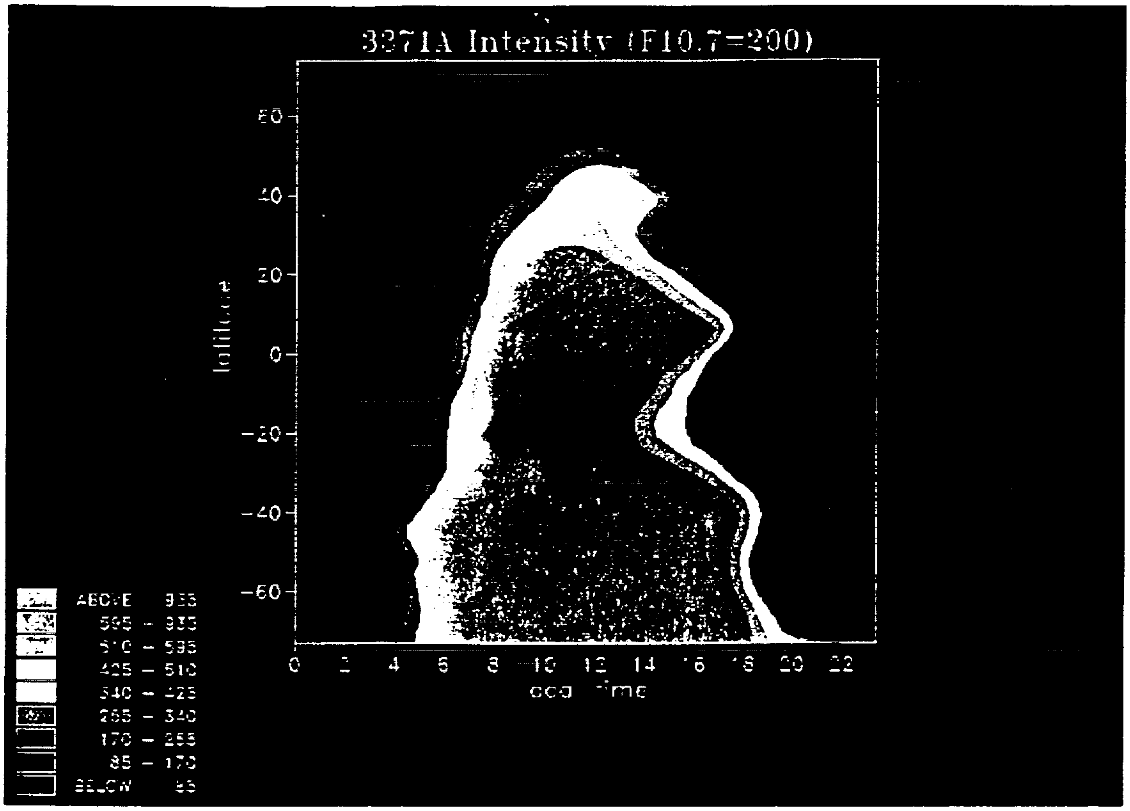

Plate 9*b*. Solar maximum, scaled to brightest intensities.

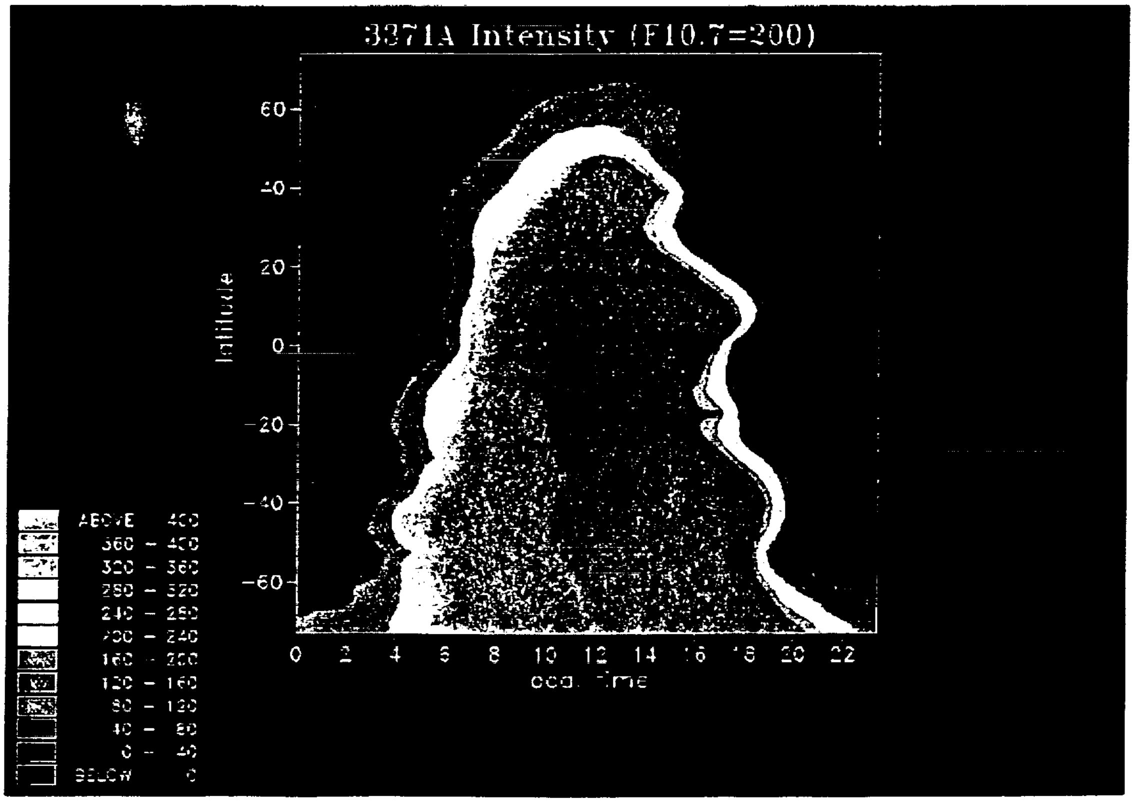

Plate 9*c*. Solar maximum, same scale as solar minimum.

Acknowledgements. This work was supported at the University of Alabama in Huntsville by NASA contract NAS8-37106 and grant NAGW 996, and National Science Foundation grants ATM-8713693, ATM 8907808, ATM-8915898, and ATM-8716036.

The editor thanks S. C. Solomon and another referee for their assistance in evaluating this paper.

REFERENCES

Abdou, W. A., D. G. Torr, P. G. Richards, M. R. Torr, and E. L. Breig, Results of a comprehensive study of the photochemistry of N_2^+ in the ionosphere, *J. Geophys. Res., 89,* 9060, 1984.

Abreu, V. J., J. H. Yee, S. C. Solomon, and A. Dalgarno, The quenching rate of O(^1D) by O(^3P), *Planet. Space Sci., 11,* 1143, 1986.

Adams, N. G., and D. Smith, Production distributions for some ion-molecule reactions, *J. Phys., B9,* 1439, 1976.

Albritton, D. L., Ion-neutral reaction-rate constants measured in flow reactors through 1977, *Atomic Data and Nuclear Data Tables, 22,* 1, 1978.

Anderson, D. N., J. M. Forbes, and M. Codrescu, A fully analytic, low- and middle-latitude ionospheric model, *J. Geophys. Res., 94,* 1520, 1989.

Banks, P. M., and G. Kockarts, *Aeronomy,* Part A, p. 225, Academic, San Diego, Calif., 1973.

Bates, D. R., and E. C. Zipf, The O(^1S) quantum yield from O_2^+ dissociation recombination, *Planet. Space Sci., 28,* 1081, 1981.

Becker, K. H., W. Groth, and D. Z. Kley, The rate constant for the aeronomic reaction N + O_2, *Naturforsch., 24a,* 1280, 1969.

Burnside, R. G., C. A. Tepley, and V. B. Wickwar, The O^+–O collision cross section: Can it be inferred from aeronomical measurements? *Annales Geophysicae, 5A,* 343, 1987.

Chandler, M. O., R. A. Behnke, A. F. Nagy, E. G. Fontheim, P. G. Richards, and D. G. Torr, Comparison of measured and calculated low-latitude ionospheric properties, *J. Geophys. Res., 88,* 9187, 1983.

Chen, A., R. Johnson, and M. A. Biondi, Measurements of the O^+ + N_2 and O^+ + O_2 reaction rates from 300 to 900 K, *J. Chem. Phys., 69,* 2688, 1978.

Dalgarno, A., Metastable species in the ionosphere, *Ann Geophys., 26,* 601, 1970.

Fehsenfeld, F. C., The reaction of O_2^+ with atomic nitrogen and NO^+, H_2O, and NO_2^+ with atomic oxygen, *Planet. Space Sci., 25,* 195, 1977.

Fischer, C. F., and H. P. Saha, Multiconfiguration Hartree-Fock results with Briet-Pauli corrections for forbidden transitions in the $2P^4$ configuration, *Phys. Rev. A, 28,* 3169, 1983.

Frederick, J. E., and D. W. Rusch, On the chemistry of metastable atomic nitrogen in the *F* region deduced from simultaneous satellite measurement of the 5200 Å airglow and atmospheric composition, *J. Geophys. Res., 82,* 3509, 1977.

Frederick, J. E., D. W. Rusch, G. A. Victor, W. E. Sharp, P. B. Hays, and H. C. Brinton, The O I (λ5577 Å) airglow: Observations and excitation mechanisms, *J. Geophys. Res., 81,* 3923, 1976.

Hedin, A. H., MSIS-86 thermospheric model, *J. Geophys. Res., 92,* 4649, 1987.

Hedin, A. E., N. W. Spencer, and T. Killeen, Empirical global model of upper thermosphere winds based on Atmosphere and Dynamics Explorer satellite data, *J. Geophys. Res., 93,* 99959, 1988.

Henry, R. J. W., P. G. Burke, and A. L. Sinfailam, Scattering of electrons by C, N, O, N^+, O^+, and O^{++}, *Phys. Rev., 178,* 218, 1969.

Horwitz, J. L., R. H. Comfort, P. G. Richards, M. O. Chandler, C. R. Chappell, P. Anderson, W. B. Hanson, and L. H. Brace, Plasmasphere-ionosphere coupling, 2, Ion composition measurements at plasmaspheric and ionospheric altitudes and comparison with modeling results, *J. Geophys. Res., 95,* 7949, 1990.

Huntress, W. T., and P. G. Anicich, On the reaction of N^+ ions with O_2, *Geophys. Res. Lett., 3,* 317, 1976.

Imami, M., and W. L. Borst, Electron excitation of the (0,0) second positive band of nitrogen from threshold to 1000 eV*, *J. Chem. Phys., 61,* 1115, 1974.

Johnsen, R., and M. A. Biondi, Laboratory measurements of the O^+(^2D) + N_2 and O^+(^2D) + O_2 reaction rate coefficients and their ionospheric implications, *Geophys. Res. Lett., 7,* 401, 1980.

Kernahan, J. H., and H. L. Pang, Experimental determination absolute A coefficients for "forbidden" atomic oxygen lines, *Can. J. Phys., 53,* 455, 1975.

Killeen, T. L., R. G. Roble, and N. W. Spencer, A computer model of global thermospheric winds and temperatures, *Adv. Space Res., 7,* 207, 1987.

Kley, D., G. M. Lawrence, and E. T. Stone, The yield of N(^2D) atoms in the dissociative recombination of NO^+, *J. Chem. Phys., 66,* 4157, 1977.

Kopp, J. P., D. W. Rusch, R. G. Roble, G. A. Victor, and P. B. Hays, Photoemission in the second positive system of molecular nitrogen in the Earth's dayglow, *J. Geophys. Res., 82,* 555,1977.

Langford, A. O., V. M. Bierbaum, and S. R. Leone, Auroral implications of recent measurement on O(^1S) and O(^1D) formation on the reaction of N^+ with O_2, *Planet. Space Sci., 33,* 1225, 1985.

Lee, J. H., J. V. Michael, W. A. Payne, and L. J. Stief, Absolute rate of the reaction of N(^4S) with NO from 196–400 K with DF-RF and FP-RF techniques, *J. Chem. Phys., 69,* 3069, 1978.

Lin, C. L., and F. Kaufman, Reactions of metastable nitrogen atoms, *J. Chem. Phys., 55,* 3760, 1971.

Lindinger, W., F. C. Fehsenfeld, A. L. Schmeltekopf, and E. E. Ferguson, Temperature dependence of some ionospheric ion-neutral reactions from 300° to 900°K, *J. Geophys. Res., 79,* 4753, 1974.

McFarland, M., D. L. Albritton, F. C. Fehsenfeld, E. E. Ferguson, and A. L. Schmeltekopf, Energy dependence and branching ratio of the N_2^+ + O reaction, *J. Geophys. Res., 79,* 2925, 1974.

Mehr, F. J., and M. A. Biondi, Electron temperature dependence of O_2^+ and N_2^+ ions with electrons, *Phys. Rev., 181,* 264, 1969.

Meriwether, J. W., D. G. Torr, J. C. G. Walker, and A. O. Nier, The O^+(^2P) emission at 7320 Å in twilight, *J. Geophys. Res., 83,* 3311, 1978.

Miller, K. L., D. G. Torr, and P. G. Richards, Meridional winds in the thermosphere derived from measurements of F_2 layer height, *J. Geophys. Res., 91,* 4531, 1986.

Newberry, I. T., R. H. Comfort, P. G. Richards, and C. R. Chappell, Thermal He^+ in the plasmasphere: Comparison of observations with numerical calculations, *J. Geophys. Res., 94,* 15,265, 1989.

Ogawa, H. S., and D. L. Judge, Absolute solar flux measurement shortward of 575 Å, *J. Geophys. Res., 91,* 7089, 1986.

Piper, L. G., The excitation of O(^1S) in the reaction between $N_2(A^3\Sigma_u^+)$ and O(^3P), *J. Chem. Phys., 77,* 2373, 1982.

Queffelec, J. L., B. R. Rowe, M. Morlais, J. C. Gomet, and F. Vallee, The dissociative recombination of $N_2^+(v=0,1)$ as a source of metastable atoms in planetary atmospheres, *Planet. Space Sci., 33,* 263, 1985.

Richards, P. G., Thermal electron quenching of N(^{2}D): Consequences for the ionospheric photoelectron flux and the thermal electron temperature, *Planet. Space Sci., 34,* 689, 1986.

Richards, P. G., and D. G. Torr, An investigation of the consistency of the ionospheric measurements of the photoelectron flux and solar EUV flux, *J. Geophys. Res., 89,* 5625, 1984.

Richards, P. G., and D. G. Torr, Seasonal, diurnal, and solar cyclical variations of the limiting H^+ flux in the Earth's topside ionosphere, *J. Geophys. Res., 90,* 5261, 1985*a*.

Richards, P. G., and D. G. Torr, The altitude variation of the ionospheric photoelectron flux: A comprison of theory and measurements, *J. Geophys. Res., 90, 2877, 1985b.*

Richards, P. G., and D. G. Torr, Thermal coupling of conjugate ionospheres and the tilt of the Earth's magnetic field, *J. Geophys. Res., 91,* 9017, 1986*a*.

Richards, P. G., and D. G. Torr, A method of extracting meridional winds from ionosonde measurements by using ionospheric models, in *Proceedings of the Thermospheric Dynamics Workshop II,* edited by H. G. Mayr and N. J. Miller, *NASA Conf. Pub. 2398,* p. 369, 1986*b*.

Richards, P. G., and D. G. Torr, A factor of 2 reduction in the theoretical F2 peak electron density due to enhanced vibrational excitation of N_2 in summer at solar maximum, *J. Geophys. Res., 91,* 11331, 1986*c*.

Richards, P. G., and D. G. Torr, Ratios of photoelectron to EUV ionization rates for aeronomic studies, *J. Geophys. Res., 93,* 4060, 1988.

Richards, P. G., D. G. Torr, and M. R. Torr, Photodissociation of N_2: A significant source of thermospheric atomic nitrogen, *J. Geophys. Res., 86,* 1495, 1981.

Richards, P. G., D. G. Torr, and P. J. Espy, Determination of photoionization branching ratios and total photoionization cross sections at 304 Å from experimental ionospheric photoelectron fluxes, *J. Geophys. Res., 87,* 3599, 1982*a*.

Richards, P. G., M. R. Torr, and D. G. Torr, The seasonal effect of nitric oxide cooling in the thermospheric UV heat budget, *Planet. Space Sci., 30,* 515, 1982*b*.

Richards, P. G., D. G. Torr, and W. A. Abdou, Effects of vibrational enhancement of N_2 on the cooling rate of ionospheric thermal electrons, *J. Geophys. Res.*, *91*, 304, 1986*a*.

Richards, P. G., D. G. Torr, J. L. Horwitz, and M. R. Torr, Models of the plasmaspheric thermal plasma distribution, *Adv. Space Res.*, *6*, 141, 1986*b*.

Richards, P. G., D. G. Torr, M. J. Buonsanto, and K. L. Miller, The behavior of the electron density and temperature at Millstone Hill during the equinox transition study, September 1984, *J. Geophys. Res.*, *94*, 16,969, 1989.

Rowe, B. R., D. W. Fahey, F. C. Fehsenfeld, and D. L. Albritton, Rate constants for the reactions of metastable O^+ ions wiith N_2 and O_2 at collision energies 0.04 to 0.2 eV and the mobilities of these ions at 300 K, *J. Chem. Phys.*, *73*, 194, 1980.

Rusch, D. W., D. G. Torr, P. B. Hays, M. R. Torr, and A. O. Nier, Determination of the $O^+(^2P)$ ionization frequency using satellite airglow and particle data and its implications on the EUV solar flux, *Geophys. Res. Lett.*, *3*, 537, 1976.

Rusch, D. W., D. G. Torr, P. B. Hays, and J. C. G. Walker, The O II (7319–7330 A) dayglow, *J. Geophys. Res.*, *82*, 719, 1977.

Rusch, D. W., J. C. Gerard, and W. E. Sharp, The reaction of $N(^2D)$ with O_2 as a source of $O(^1D)$ atoms in auroras, *Geophys. Res. Lett.*, *5*, 1043, 1978.

Schunk, R. W., and A. F. Nagy, Ionospheres of the terrestrial planets, *Rev. Geophys.*, *18*, 813, 1980.

Seaton, M. J., and D. E. Osterbrock, Relative O II intensities in gaseous nebulae, *Astrophys. J.*, *125*, 66, 1957.

Slanger, T. G. and G. Black, Quenching of $O(^1S)$ by $O_2(a^1\Delta g)$, *Geophys. Res. Lett.*, *8*, 535, 1981.

St. Maurice, J. P., and R. W. Schunk, Diffusion and heat flow equations for the mid-latitude topside ionosphere, *Planet. Space Sci.*, *25*, 907, 1977.

St. Maurice, J. P., and D. G. Torr, Nonthermal rate coefficients in the ionosphere: The reaction of O^+ with N_2, O_2, and NO, *J. Geophys. Res.*, *83*, 969, 1978.

Streit, G. E., C. J. Howard, O. L. Schmeltekopf, J. A. Davidson, and H. I. Schiff, Temperature Dependence of $O(^1D)$ rate constants for reactions with O_2, N_2, CO_2, O_3, and H_2O, *J. Chem. Phys.*, *65*, 4761, 1976.

Torr, D. G., Refinement of aeronomically determined rate coefficient for the reaction of N_2^+ with O, *J. Geophys. Res.*, *84*, 1939, 1979.

Torr, D. G., The photochemistry of the upper atmosphere, in *The Photochemistry of Atmospheres*, edited by J. S. Levine, pp. 165–278, Academic, San Diego, Calif., 1985.

Torr, D. G., P. G. Richards, M. R. Torr, and V. J. Abreu, Further quantification of the sources and sinks of thermospheric $O(^1D)$ atoms, *Planet. Space Sci.*, *29*, 595, 1981.

Torr, M. R., and D. G. Torr, Recombination of NO^+ in the mid-latitude trough and the polar ionization hole, *J. Geophys. Res.*, *84*, 4316, 1979.

Torr, M. R., and D. G. Torr, The dissociative recombination of O_2^+ in the ionosphere, *Planet. Space Sci.*, *29*, 999, 1981.

Torr, M. R., and D. G. Torr, The role of metastable species in the thermosphere, *Rev. Geophys.*, *20*, 91, 1982.

Torr, M. R., and D. G. Torr, Ionization frequencies for solar cycle 21: Revised, *J. Geophys. Res.*, *90*, 6675, 1985.

Torr, M. R., D. G. Torr, R. A. Ong, and H. E. Hinteregger, Ionization frequencies for major thermospheric constituents as a function of solar cycle 21, *Geophys. Res. Lett.*, *6*, 771, 1979.

Torr, M. R., D. G. Torr, and H. E. Hinteregger, Solar flux variability in the Schumann-Runge continuum as a function of solar cycle 21, *J. Geophys. Res.*, *85*, 6063, 1980.

Torr, M. R., D. G. Torr, and P. G. Richards, A mid-latitude interhemispheric model of the $O^+(^2P)$ airglow emission at 7320 Å, *Geophys. Res. Lett.*, *17*, 65, 1990.

Walker, J. C. G., D. G. Torr, P. B. Hays, D. W. Rusch, K. Docken, G. Victor, and M. Oppenheimer, Metastable ^2P oxygen ions in the daytime thermosphere, *J. Geophys. Res.*, *80*, 1026, 1975.

Young, E. R., P. G. Richards, and D. G. Torr, A flux preserving method of coupling first and second order equations to simulate the flow of plasma between the protonosphere and ionosphere, *J. Comput. Phys.*, *38*, 141, 1980*a*.

Young, E. R., D. G. Torr, P. G. Richards, and A. F. Nagy, A computer simulation of the mid-latitude plasmasphere and ionosphere, *Planet. Space Sci.*, *28*, 881, 1980*b*.

Zipf, E. C., The $OI(^1S)$ state: Its quenching by O_2 and formation by dissociative recombination of vibrationally excited O_2^+ ions, *Geophys. Res. Lett.*, *6*, 881, 1979.

P. G. Richards and D. G. Torr, University of Alabama in Huntsville, Huntsville, AL 35899.

Marsha R. Torr, Space Sciences Laboratory, NASA Marshall Space Flight Center, Huntsville, AL 35812.

S. P. Yung, Boeing Corporation, Huntsville, AL 35899.

(Received October 13, 1989;
revised March 19, 1990;
accepted April 10, 1990.)

GEOPHYSICAL RESEARCH LETTERS, VOL. 17, NO. 1, PAGES 65-68, JANUARY 1990

A MIDLATITUDE INTERHEMISPHERIC MODEL OF THE $O^+(^2P)$ AIRGLOW EMISSION AT 7320 Å

Marsha R. Torr

Space Science Laboratory, Marshall Space Fight Center, Huntsville, Alabama

D. G. Torr and P. G. Richards

Center for Space Plasma and Aeronomy, The University of Alabama in Huntsville

Abstract. The results are reported of the first interhemispheric model of the 7320 Å airglow covering mid- and low latitudes, at all longitudes. A comprehensive model of the ionosphere and thermosphere is used to compute volume emission rates as a function of altitude, latitude, longitude, and local time. Selected results are shown here to illustrate the computational capability. In particular we discuss the diurnal and seasonal variability and interhemispheric coupling of conjugate photoelectrons. The model is particularly well suited for airglow studies, and provides a valuable tool for the comparison, interpretation, and planning of spectroscopic observations made from orbiting platforms for all significant thermospheric emissions.

Introduction

The $O^+(^2P)$ airglow emission at 7320 Å provides a means of determining the $O^+(^2P)$ concentration. Measurements of this emission can be used to determine the atomic oxygen concentration or the solar UV ionization frequency [Meriwether et al., 1978; Rusch et al., 1976]. The photochemistry of this species has been established largely on the basis of the comparison of steady-state altitude profile calculations with surface brightness measurements made from satellites [Walker et al., 1975; Rusch et al., 1977]. Observations of limb brightness are inverted to yield altitude profiles of volume emission rates. The principal sources and sinks of $O^+(^2P)$ have been discussed in detail by Torr and Torr [1982].

Over the years, we have developed a comprehensive model of the ionosphere, thermosphere, and plasmasphere. This model solves the coupled time-dependent energy, momentum, continuity, and photoelectron transport equations from 80 km in one hemisphere, along the field line, to 80 km in the conjugate hemisphere [Young et al., 1980]. The full interhemispheric capability allows for the proper treatment of thermal coupling [Richards and Torr, 1986] and conjugate photoelectrons [Richards and Torr, 1985], which is important in the calculation of airglow emissions. The concentrations of the major neutral species are provided as input from MSIS-86 [Hedin, 1987] to the model which then provides the minor and excited state species and ions [Torr, 1985]. The chemistry of all the emitting species is comprehensively included [Torr, 1985]. Ab initio calculations of the excitation and loss rates are performed for the metastable species [Torr and Torr, 1982] and the vibrational states of molecules and ions [Richards et al., 1986]. The concentrations of odd nitrogen species are also computed together with those of other minor constituents [Torr et al., 1980]. The photochemistry currently used in the model is that defined by Torr [1985] (Tables A-8 through A-12 and A-19 through A-21) with the updates, corrections, and additions summarized in Table 1.

The three-dimensional capability is achieved by running the code for approximately 100 magnetic flux tubes. Because the model is interhemispheric, solutions are obtained simultaneously for the conjugate hemisphere. This yields a total of approximately 200 grid points. The flux tubes are selected along various L-shells for L ≤ 5 and the grid on which the code is run is shown in Figure 1 in geographic space. Because of the large computational requirements, the MSFC CRAY II computer is used. Results are output on a four-dimensional global grid, comprising latitude, longitude, altitude, and local time. Input parameters are date and solar and magnetic indices.

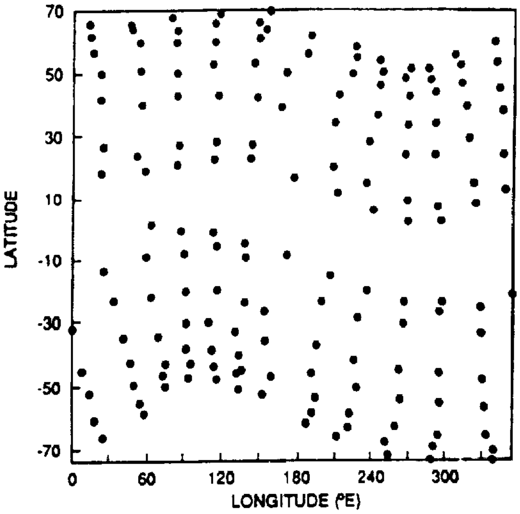

Fig. 1. Location of the conjugate points along L = 1.08 to L = 5 which mark the field lines along which the computations were made.

In this paper we have selected the 7320 Å emission to illustrate the global airglow modeling capability. The calculations have been made for conditions corresponding to November 28, 1983, for which the F10.7 cm flux was 89 and the Ap index was 23. Thus these calculations correspond to a period of relatively low solar activity.

Results

Figure 2 shows the results of the global solution of the 7320 Å emission. The volume emission rate at the peak of the layer is plotted as a function of altitude, latitude, and local time (longitude). This particular plot is shown for 00 UT, which is equivalent to placing midnight at 0° longitude, and noon at 180° longitude.

Several interesting features appear in the results shown in Figure 2. Summer is in the southern hemisphere and the more extensive solar illumination in this hemisphere is immediately evident in the longer duration of the daytime peak values (volume emission rates of the order of 10 photons$\cdot$cm$^{-3}\cdot$s^{-1}). The model results are valid for the latitudinal regime indicated by the envelope of the points shown in Figure 1. The interpolation routine tends to smear the high latitude boundary in Figure 2 by about 3°. Figure 3 shows the production and loss rate profiles for noon at southern midlatitudes. The peak production of $O^+(^2P)$ occurs near 170 km with photoionization the major source. The dominant loss mechanism above 280 km is radiation, and below 280 km it is collisional deactivation by N_2. The combination of these processes results in the emission peak being formed at approximately 260 km.

Paper number 89GL03360.
0094-8276/90/89GL-03360$03.00

TABLE 1. Updates to Photochemical Model of Torr [1985]

Reaction	Rate Coefficient (cm^3 s^{-1}) or s^{-1})	Reference
1) $O^+ + O_2 \rightarrow O_2^+ + O$	$2.1 \times 10^{-11} \left\{ \frac{T_n + 2T_i}{3.300} \right\}^{-0.763}$	Chen et al. [1978]
2) $N_2^+ + O \rightarrow O_2^+ + N_2$	$9.1 \times 10^{-11} \exp(-0.002 \cdot T_{eff})$	Lindinger et al. [1974]
3) $O^+ + N(^2D) \rightarrow N^+ + O$	5×10^{-11}	Torr et al. [1979]
4) $O^+ + H \rightarrow H^+ + O$	$2.2 \times 10^{-11} T_i{\cdot}5$	Banks and Kockarts [1973]
5) $H^+ + O \rightarrow O^+ + H$	$2.5 \times 10^{-11} T_n{\cdot}5$	Banks and Kockarts [1973]
6) $N_2^+ + e^- \xrightarrow{\beta\alpha} N(^2D) + N$	$\alpha = 2.7 \times 10^{-7}$ $\beta = 1.9$	Abdou et al. [1984] Queffelec et al. [1985]
7) $O(^1D) + O_2 \rightarrow O(^3P) + O_2$	$2.9 \times 10^{-11} e^{67.5 T_n}$	Streit et al. [1976]
8) $O(^1D) \rightarrow O(^3P) + h\nu$	$A_{1D} = 0.00934$	Fischer and Saha [1983]
9) $N_2(A^3\Sigma) + O \rightarrow$ products $\rightarrow O(^1S) + N_2$	2×10^{-11} $\beta = 0.37$	Piper et al. [1981] Piper [1982]
10) $N(^2D) + NO \rightarrow N_2 + O$	7×10^{-11}	Lin and Kaufman [1971]
11) $O(^1D) + O \rightarrow O + O$	8×10^{-12}	Abreu et al. [1986]
12) $O(^1S) \rightarrow O(^1D) + h\nu$ $O(^3P) + h\nu$	1.07 0.0444	Kernahan and Pang [1975]

Fig. 2. Three-dimensional plot of the 7320 Å volume emission rate at the peak of the layer versus latitude and local time, for 00 UT. The calculations were done for conditions appropriate for November 28, 1983. The upper panel shows the same results, but without the altitude coordinate, i.e., peak volume emission rate versus latitude and local time. The color code is on a log scale, and the units are photons·cm^{-3}·s^{-1}

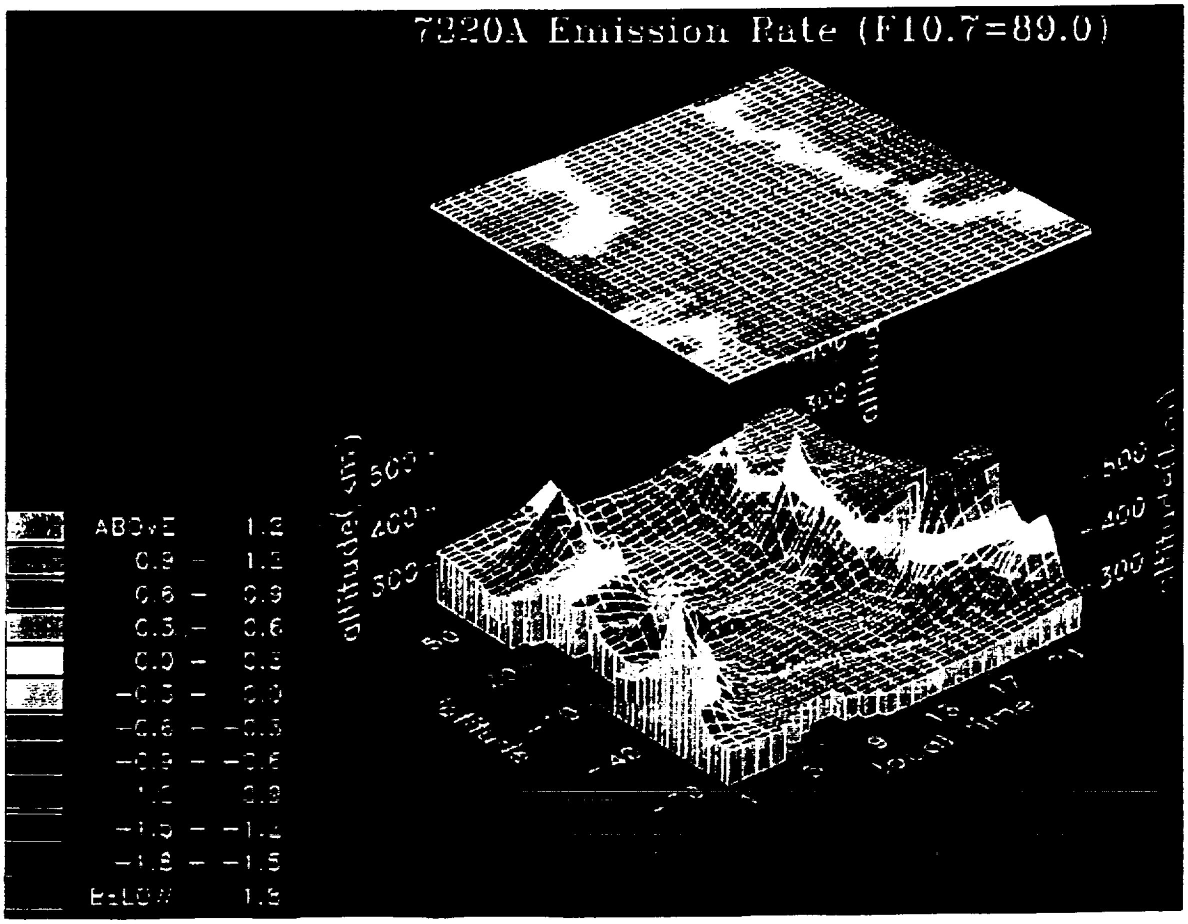

ORIGINAL PAGE IS OF POOR QUALITY

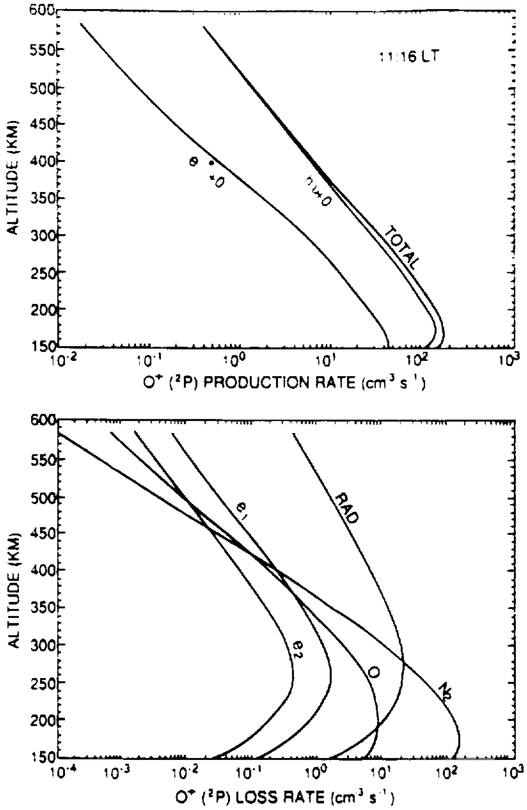

Fig. 3. Sources (a) and sinks (b) of O$^+$(^{2}P) for the location corresponding to 48°S at 11:16 LT in Figure 2. Sources are photoionization and photoelectron impact ionization. Sinks are radiation and quenching by O, N$_2$, and electrons.

At twilight the situation changes rapidly. The photoionization peak rises rapidly in altitude and the production rate falls sharply. Figure 4 shows the production rates for 48°S at 22:23 LT. At this time the solar zenith angle is 107°, so that the high altitudes are illuminated. There is a second peak at about 300 km due to transported local photoelectrons which are produced during the ionization process which created the upper peak. Radiative loss dominates most of the profile. At low latitudes at midnight, the peak production rate tends to zero at very high altitudes. When the production rate effectively drops to zero these values are omitted in Figure 2, so as not to obscure the main results.

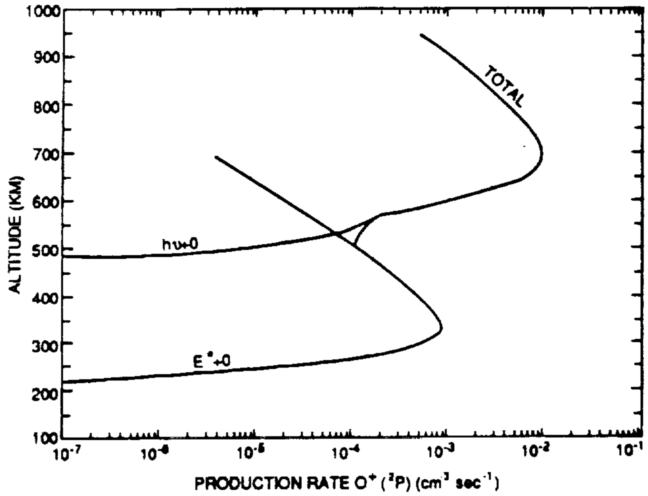

Fig. 4. Sources (a) and sinks (b) of O$^+$(^{2}P) for the location corresponding to 48°S at 22:23 LT in Figure 2.

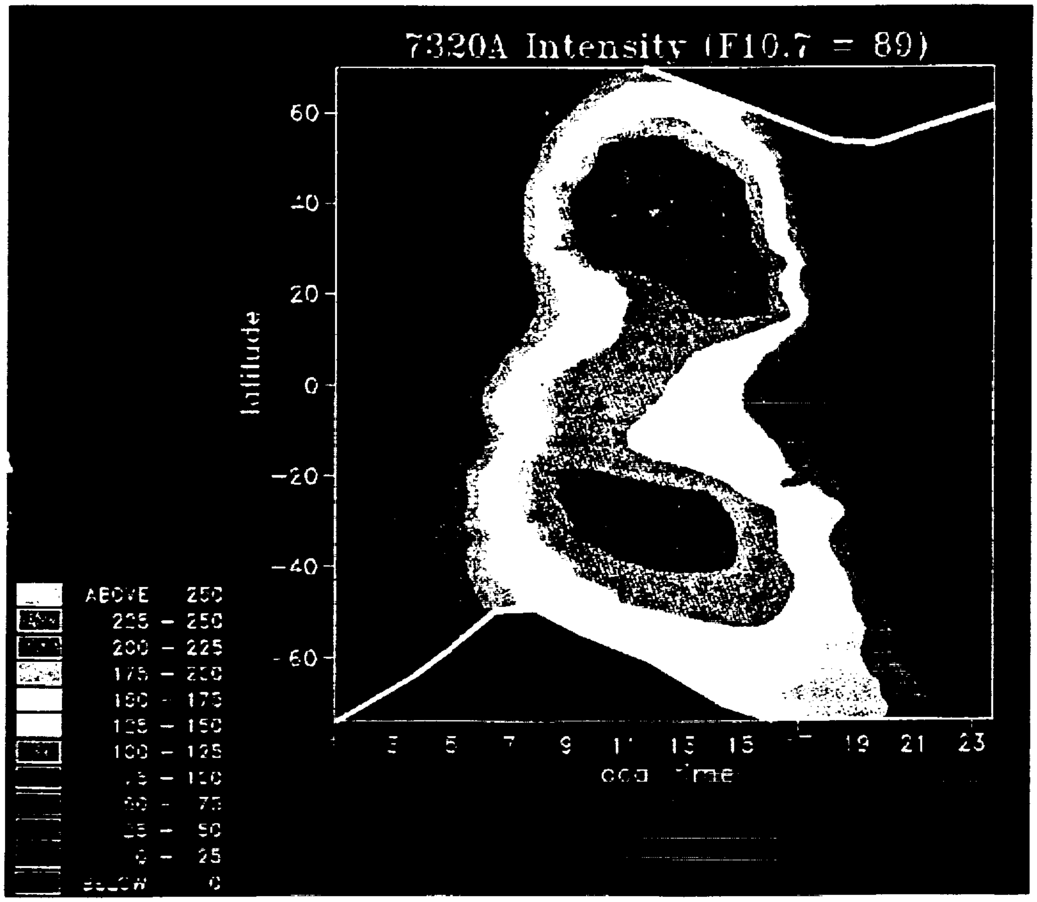

Fig. 5. Vertical column integrated surface brightness (in Rayleighs) for the same case shown in Figure 2.

In the winter (northern) hemisphere the twilights draw closer together but the photochemistry of the daytime and twilight 7320 Å emission is essentially the same as that described above. What is interesting to note here is that there is some production of $O^+(^2P)$ at high latitudes even at midnight. The source is impact ionization by photoelectrons from the sunlit conjugate hemisphere. The conjugate photoelectron source produces a column integrated surface brightness of 2 to 3 R of 7320 Å emission.

Figure 5 shows the global map of the 7320 Å intensity for the same case as Figure 2. This is what would be seen by an instrument looking straight down at the Earth for a fixed UT. The midday intensities in the winter hemisphere are slightly larger than those in the summer hemisphere. This is because the winter hemisphere is somewhat colder, and radiative loss dominates to a lower altitude.

Summary

We have reported the first results of a midlatitude interhemispherically coupled model of the 7320 Å airglow. These results show the diurnal and seasonal variation for conditions representative of near solar minimum. The magnitude and extent of the conjugate photoelectron source is quantified, together with the sources and sinks at selected times. In another paper [Torr et al., 1989] we show further details of the longitudinal and solar cycle variations. This model allows three-dimensional maps of any airglow emission to be generated. Any line of sight geometry can be projected through these maps and the volume emission rate integrated along the viewing direction to enable comparisons with observation. A three-dimensional perspective of airglow emission rates or brightnesses is of relevance to the interpretation of measurements taken from an orbiting vehicle. A satellite flying in a circular orbit through the topology represented in Figure 2 would observe large variations in emission through the structured regions. Semi-global maps of the type produced here provide rapid insight into the sources of the variability.

Acknowledgments. This work was supported by NASA contract NAS8-37106 and NSF grants ATM-8713693 and ATM-8714461 to The University of Alabama in Huntsville. We thank So Po Yung for her assistance in running the code and generating the graphical displays.

References

Abdou, W. A., D. G. Torr, P. G. Richards, M. R. Torr, and E. L. Breig, Results of a comprehensive study of the photochemistry of N^+_2 in the ionosphere, *J. Geophys. Res.*, *89*, 9069, 1984.

Abreu, V. J., J. H. Yee, S. C. Solomon, and A. Dalgarno, The quenching rate of $O(^1D)$ by $O(^3P)$, *Planet. Space Sci.*, *11*, 1143, 1986.

Banks, P. M., and G. Kockarts, *Aeronomy*, Academic Press, Inc., New York, 1973.

Chen, A., R. Johnsen, and M. A. Biondi, Measurements of the $O^+ + N_2$ and $O^+ + O_2$ reaction rates from 300 to 900 K, *J. Chem. Phys.*, *69*, 2688, 1978.

Fischer, C. F. and H. P. Saha, Multiconfiguration Hartree-Fock results with Briet-Pauli corrections for forbidden transitions in the $2P^4$ configuration, *Phys. Rev. A*, *28*, 3169, 1983.

Hedin, A. H., MSIS-86 thermospheric model, *J. Geophys. Res.*, *92*, 4649, 1987.

Kernahan, J. H., and H. L. Pang, Experimental determination of absolute A coefficients for "forbidden" atomic oxygen lines, *Can. J. Phys.*, *53*, 455, 1975.

Lin, C. L., and F. Kaufman, Reactions of metastable nitrogen atoms, *J. Chem. Phys.*, *55*, 3760, 1971.

Lindinger, W., F. C. Fehsenfeld, A. L. Schmeltekopf, and E. E. Ferguson, Temperature dependence of some ionospheric ion-neutral reactions from 300° to 900° K, *J. Geophys. Res.*, *79*, 4753, 1974.

Meriwether, J. W., D. G. Torr, J. C. G. Walker, and A. O. Nier, The $O^+(^2P)$ emission at 7320 Å in twilight, *J. Geophys. Res.*, *83*, 3311, 1978.

Piper, L. G., The excitation of $O(^1S)$ in the reaction between $N_2(A^3\Sigma^+{}_u)$ and $O(^3P)$, *J. Chem. Phys.*, *77*, 2373, 1982.

Piper, L. G., G. E. Caledonia, and J. P. Kennealy, Rate constants for deactivation of $N_2(A)v' = 0,1$ by O_2, *J. Chem. Phys.*, *74*, 2888, 1981.

Queffelec, J. L., B. R. Rowe, M. Morlais, J. C. Gomet, and F. Vallee, The dissociative recombination of $N^+{}_2(\nu = 0,1)$ as a source of metastable atoms in planetary atmospheres, *Planet. Space Sci.*, *33*, 263, 1985.

Richards, P. G., and D. G. Torr, The altitude variation of the ionospheric photoelectron flux: A comparison of theory and measurement, *J. Geophys. Res.*, *90*, 2877, 1985.

Richards, P. G., and D. G. Torr, Thermal coupling of conjugate ionospheres and the tilt of the Earth's magnetic field, *J. Geophys. Res.*, *91*, 9017, 1986.

Richards, P. G., D. G. Torr, and W. A. Abdou, Effects of vibrational enhancement of N_2 on the cooling rate of ionospheric thermal electrons, *J. Geophys. Res.*, *91*, 304, 1986.

Rusch, D. W., D. G. Torr, P. B. Hays, M. R. Torr, and A. O. Nier, Determination of the $O^+(^2P)$ ionization frequency using satellite airglow and particle data and its implications on the EUV solar flux, *Geophys. Res. Lett.*, *3*, 537, 1976.

Rusch, D. W., D. G. Torr, P. B. Hays, and J. C. G. Walker, The OII (7310–7330 Å) dayglow, *J. Geophys. Res.*, *82*, 719, 1977.

Streit, G. E., C. J. Howard, O. L. Schmeltekopf, J. A. Davidson, and H. I. Schiff, Temperature dependence of $O(^1D)$ rate constants for reactions with O_2, N_2, CO_2, O_3, and H_2O, *J. Chem. Phys.*, *65*, 4761, 1976.

Torr, D. G., The photochemistry of the upper atmosphere, in *The Photochemistry of Atmospheres*, ed., J. S. Levine, Academic Press, Inc., New York, pp. 165–278, 1985.

Torr, D. G., M. R. Torr, W. B. Hanson, and J. H. Hoffman, Determination of the sources and sinks of N^+ ions in the thermosphere, *Geophys. Res. Lett.*, *6*, 573, 1979.

Torr, Marsha R., and D. G. Torr, The role of metastable species in the thermosphere, *Rev. Geophys.*, *20*, 91, 1982.

Torr, M. R., P. G. Richards, and D. G. Torr, A new determination of the ultraviolet heating efficiency of the thermosphere, *J. Geophys. Res.*, *85*, 6819, 1980.

Torr, Marsha R., D. G. Torr, P. G. Richards, and S. P. Yung, Mid and low latitude model of thermospheric emissions: 1. $O^+(^2P)$ 7320 Å and $N_2(^2P)$ 3371 Å, *J. Geophys. Res.*, submitted, 1989.

Walker, J. C. G., D. G. Torr, P. B. Hays, D. W. Rusch, K. Docken, G. Victor, and M. Oppenheimer, Metastable ^2P oxygen ions in the daytime thermosphere, *J. Geophys. Res.*, *80*, 1026, 1975.

Young, E. R., P. G. Richards, and D. G. Torr, A flux preserving method of coupling first and second order equations to simulate the flow of plasma between the protonosphere and the ionosphere, *J. Comp. Phys.*, *38*, 141, 1980.

P. G. Richards and D. G. Torr, Center for Space Plasma and Aeronomy, The University of Alabama in Huntsville, Huntsville, AL 35899.

M. R. Torr, Space Science Laboratory, Marshall Space Flight Center, Huntsville, AL 35812.

(Received June 27, 1989;
revised September 20, 1989;
accepted October 25, 1989)

APPENDIX B

NEW HIGH PERFORMANCE FILTERS FOR VACUUM ULTRAVIOLET APPLICATIONS

MUAMER ZUKIC AND DOUGLAS G. TORR
THE UNIVERSITY OF ALABAMA IN HUNTSVILLE
PHYSICS DEPARTMENT
AND
JAMES SPANN AND MARSHA R. TORR
MARSHALL SPACE FLIGHT CENTER
SPACE SCIENCE LABORATORY

OBJECTIVES

TO DEVELOP NARROWBAND HIGH "TRANSMITTANCE" FILTERS FOR THE VACUUM ULTRAVIOLET (VUV) WAVELENGTH REGIME.

GOALS:

TRANSMITTANCE > 30% FOR $130 < \lambda < 200$ nm

BANDPASS ~ 3 nm FWHM

OUT-OF-BAND BLOCKING $< 10^{-3}\%$

APPLICATIONS:

SPECTRAL ISOLATION OF THE TERRESTRIAL EMISSION FEATURES:

H Ly α	121.6 nm
OI	130.4 nm
OI	135.6 nm

AND OTHER FEATURES

CONCEPT FOR THE DEVELOPMENT OF HIGH PERFORMANCE FILTERS

PROBLEMS: LACK OF LOW ABSORPTION FILM MATERIALS IN THE VUV FOR ALL-DIELECTRIC TRANSMISSION FILTERS

⇒ POOR TRANSMISSION, BANDWIDTH AND BLOCKING

ALTERNATIVES: REFLECTIVE COATINGS ARE NOT AS SEVERELY AFFECTED BY ABSORPTION EFFECTS

BUT TYPICAL REFLECTIVE COATINGS HAVE A RELATIVELY BROAD PASSBAND

A MEASURE OF SUCCESS HAS BEEN ACHIEVED PREVIOUSLY BY COMBINING SEVERAL REFLECTORS IN TANDEM

PRINCIPLE: THE RATIO OF IN-BAND TO OUT-OF-BAND REFLECTIVITY (R) INCREASES AS

$(R_{IN}/R_{OUT})^N$ WHERE N = NUMBER OF REFLECTORS

⇒ IMPROVED BANDWIDTH AND OUT-OF-BAND BLOCKING

Our Objective and Commercially Available VUV Narrowband Filters

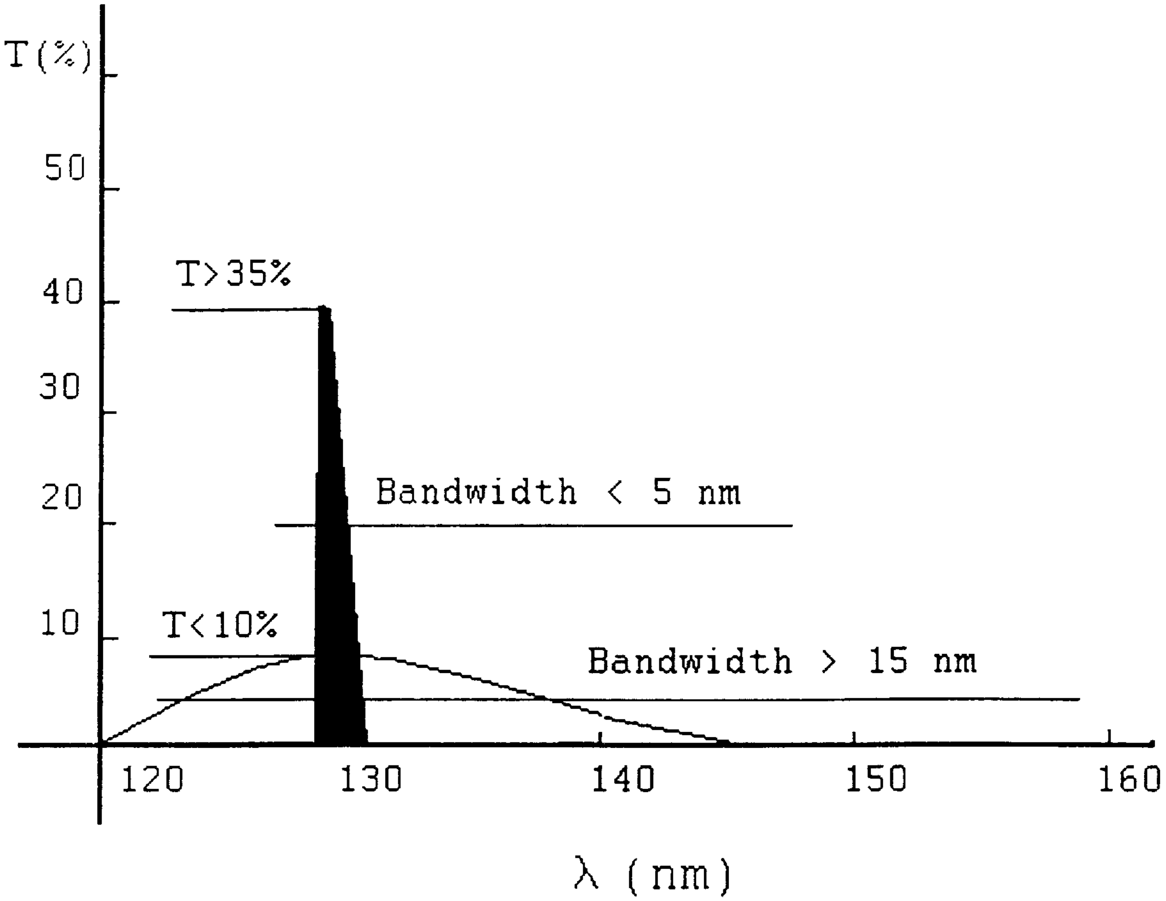

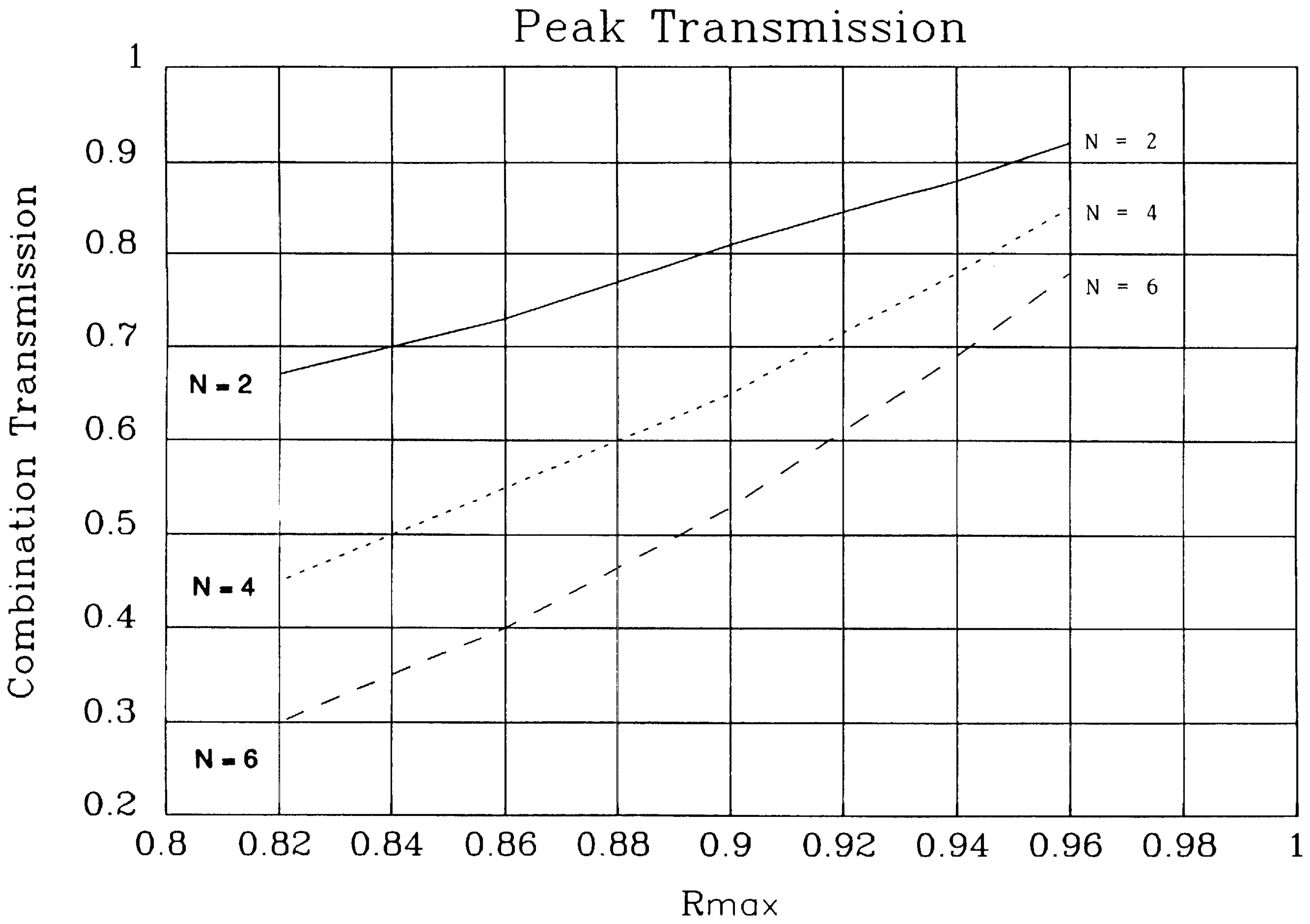
Peak Transmission
Combination Transmission
1
0.9
0.8
0.7
0.6
0.5
0.4
0.3
0.2
0.8
0.82
0.84
0.86
0.88
0.9
0.92
0.94
0.96
0.98
1
Rmax
N = 2
N = 4
N = 6
N = 2
N = 4
N = 6

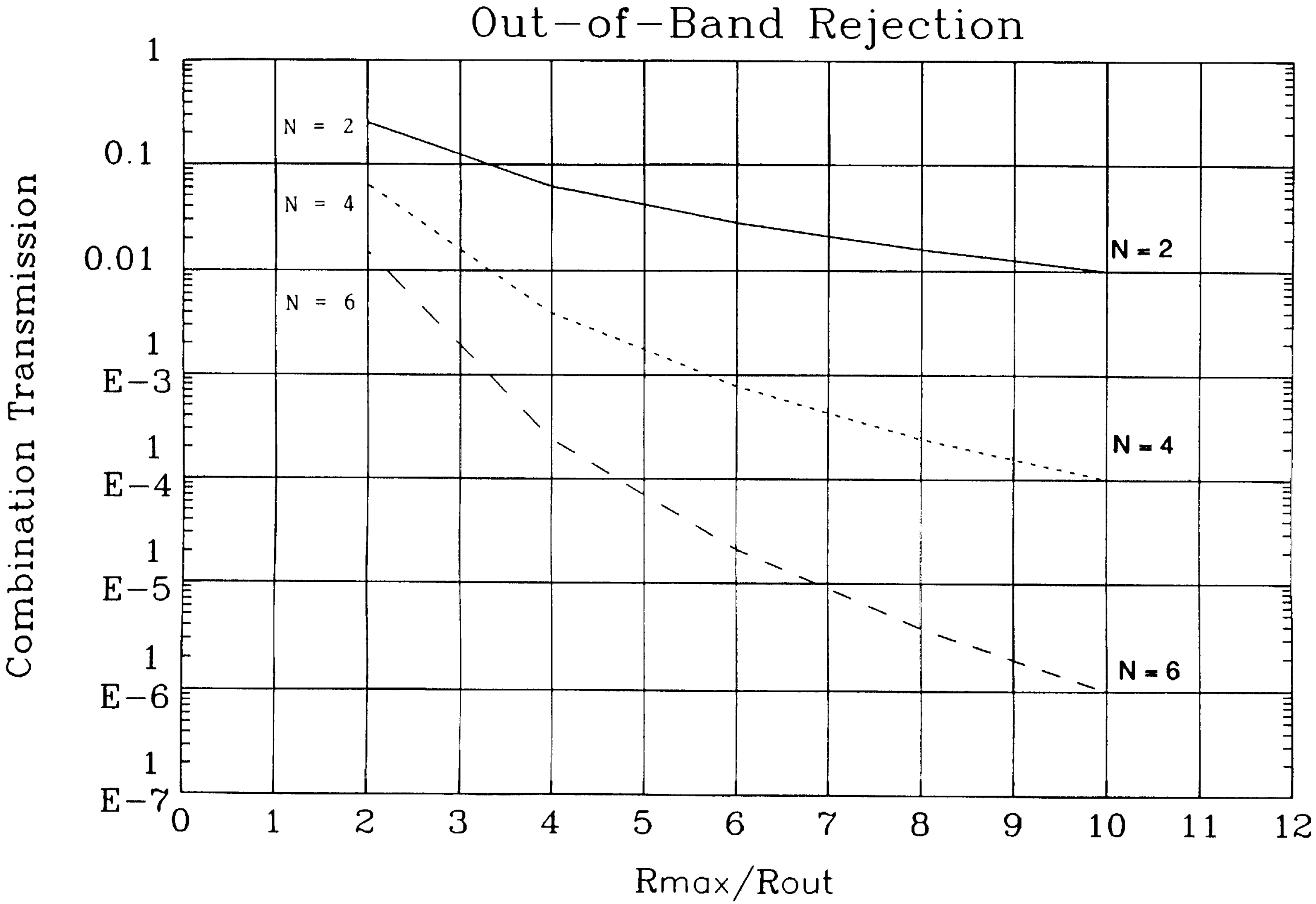
Out-of-Band Rejection
Combination Transmission
1
0.1
0.01
1
E-3
1
E-4
1
E-5
1
E-6
1
E-7
0
1
2
3
4
5
6
7
8
9
10
11
12
Rmax/Rout
N = 2
N = 4
N = 6
N = 2
N = 4
N = 6

QW Multilayers

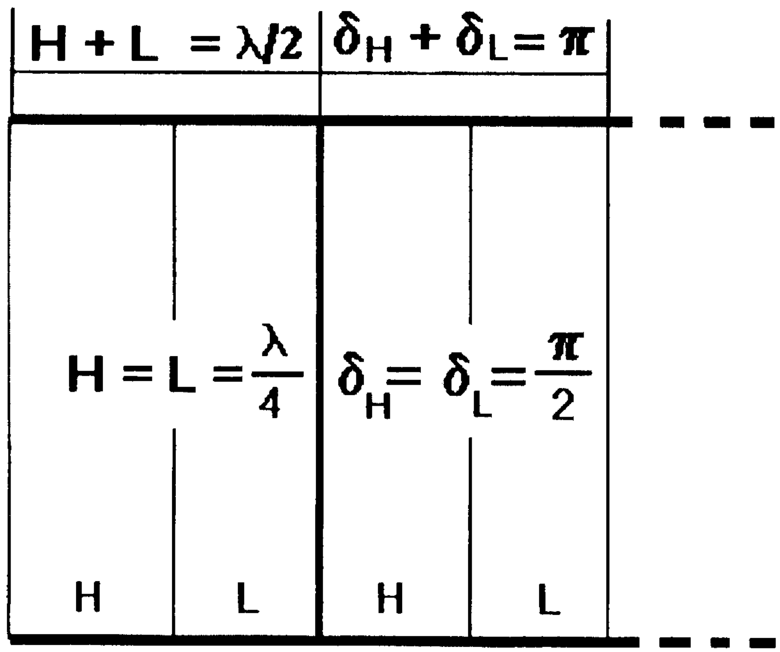

Optical thickness of HL pair

$H + L = \lambda/2$

Phase thickness of HL pair

$\delta_H + \delta_L = \pi$

$H = L = \frac{\lambda}{4}$

$\delta_H = \delta_L = \frac{\pi}{2}$

Disadvantages :

1. High Absorption
2. Low Reflection
3. Large Bandwidth

II Multilayers

Optical thickness of HL pair

$H + L = \frac{\lambda}{2}$

Phase thickness of HL pair

$\delta_H + \delta_L = \pi$

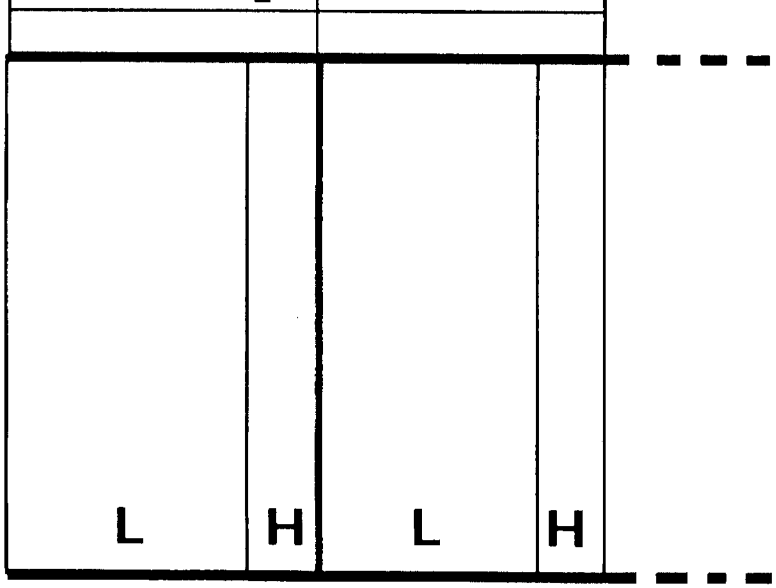

Advantages :

1. Low Absorption
2. High Reflection
3. Narrow Bandwidth

Experimental Arrangement

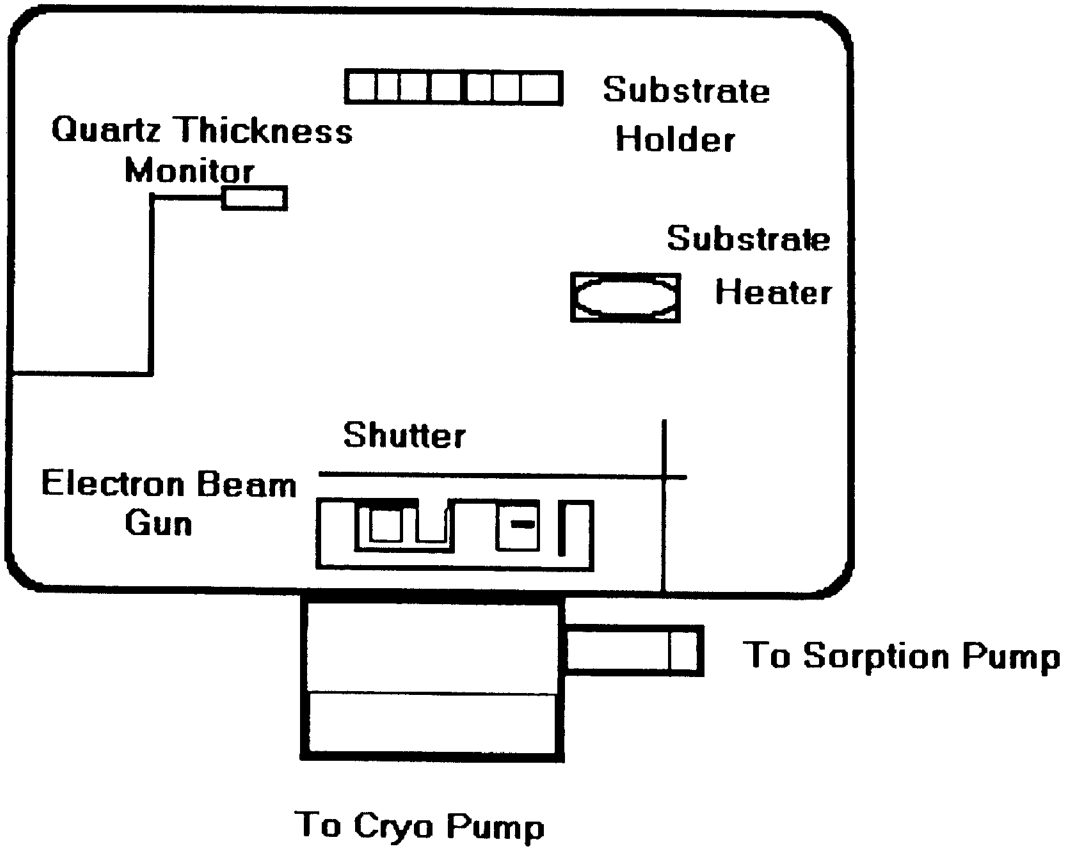

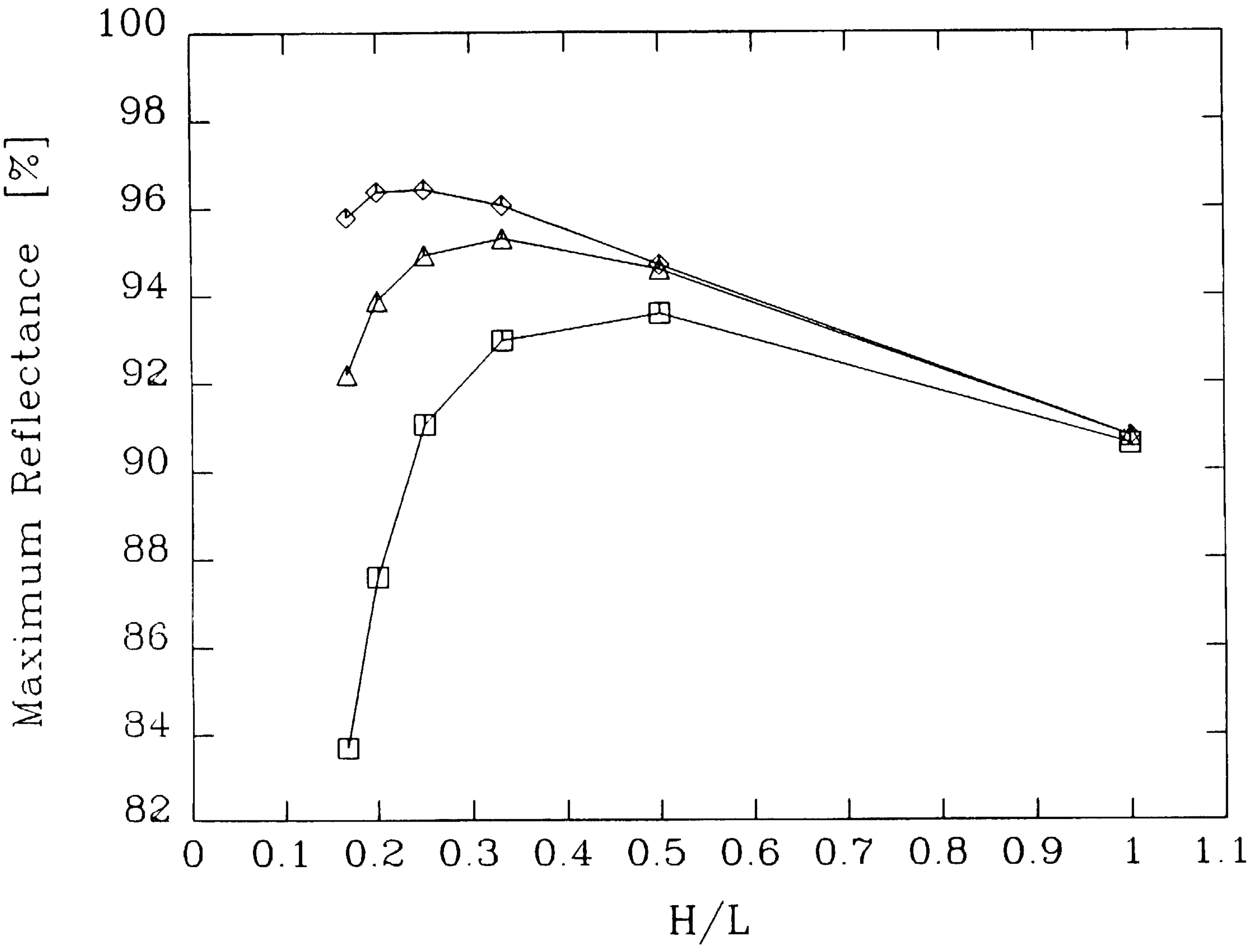

FIGURE 1: THE MAXIMUM REFLECTANCE OF THE Π STACK CALCULATED FOR ZERO ANGLE OF INCIDENCE AT 145 NM. DIAMONDS REPRESENT 99-LAYER, TRIANGLES 55-LAYER, AND SQUARES 35-LAYER STACKS. H = LANTHANUM FLUORIDE, AND L = MAGNESIUM FLUORIDE. THE KOPPELMANN LIMIT IS 90.8%.

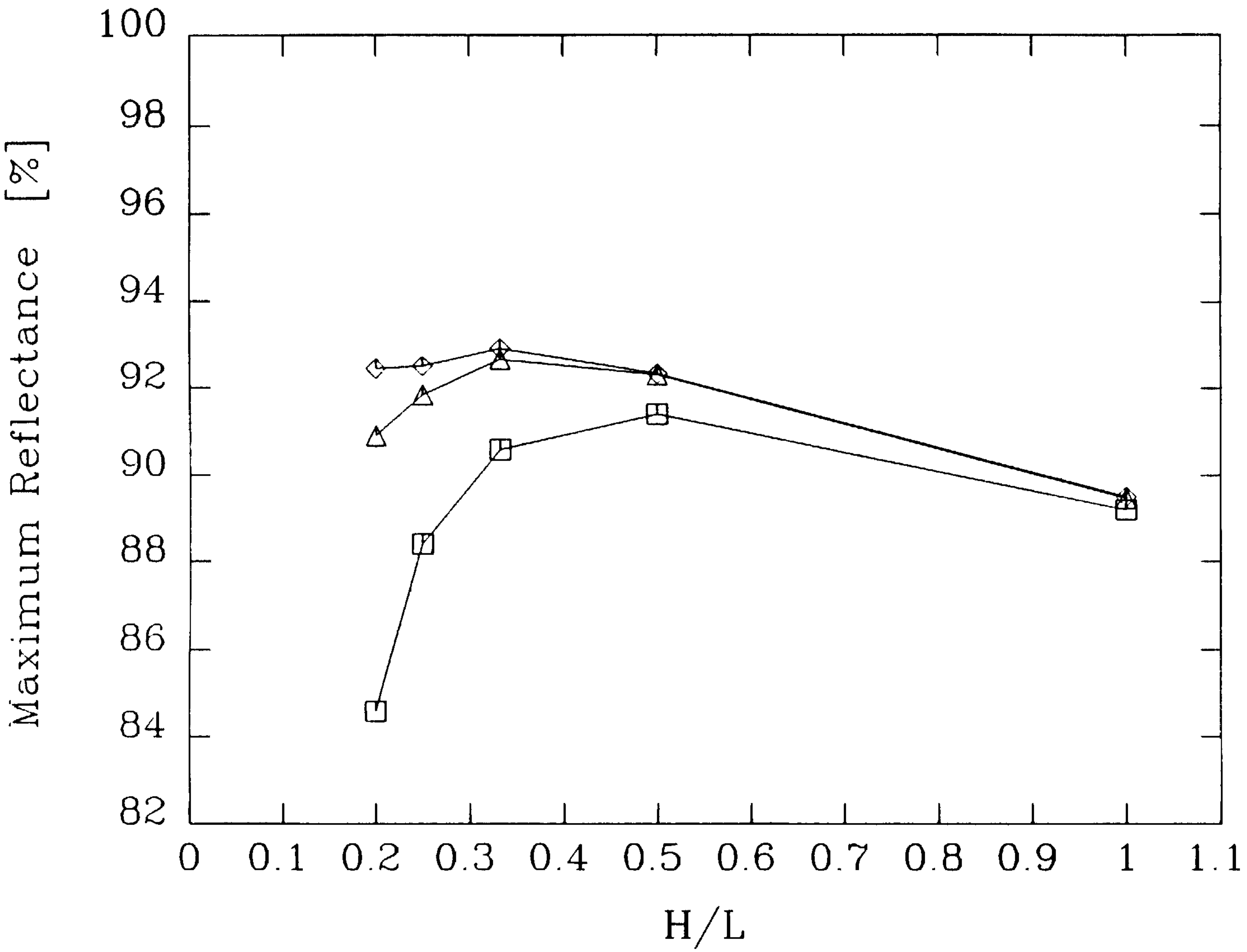

FIGURE 2: THE MAXIMUM REFLECTANCE OF THE Π STACK CALCULATED FOR 45 DEGREES ANGLE OF INCIDENCE AT 135.6 NM. DIAMONDS REPRESENT 99-LAYER, TRIANGLES 55-LAYER, AND SQUARES 35-LAYER STACKS. H = LANTHANUM FLUORIDE, AND L = MAGNESIUM FLUORIDE. THE KOPPELMANN LIMIT IS 89.5%

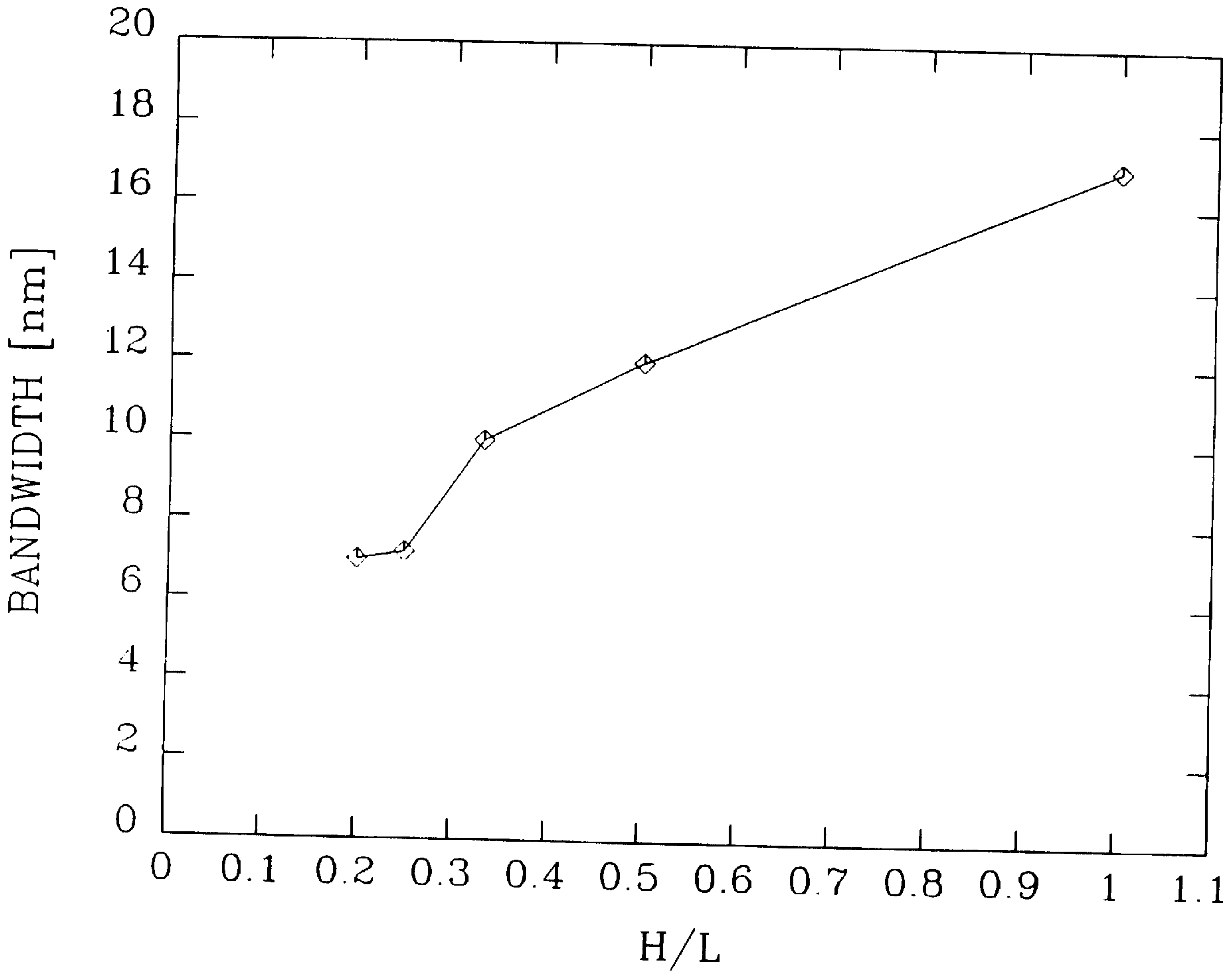

FIGURE 3: THE FULL WIDTH AT HALF OF THE REFLECTANCE MAXIMUM OF THE Π STACKS CALCULATED FOR 45 DEGREES ANGLE OF INCIDENCE. THE MAXIMUM REFLECTANCE OF THE STACKS AS A FUNCTION OF THE H/L RATIO IS SHOWN IN FIGURE 2.

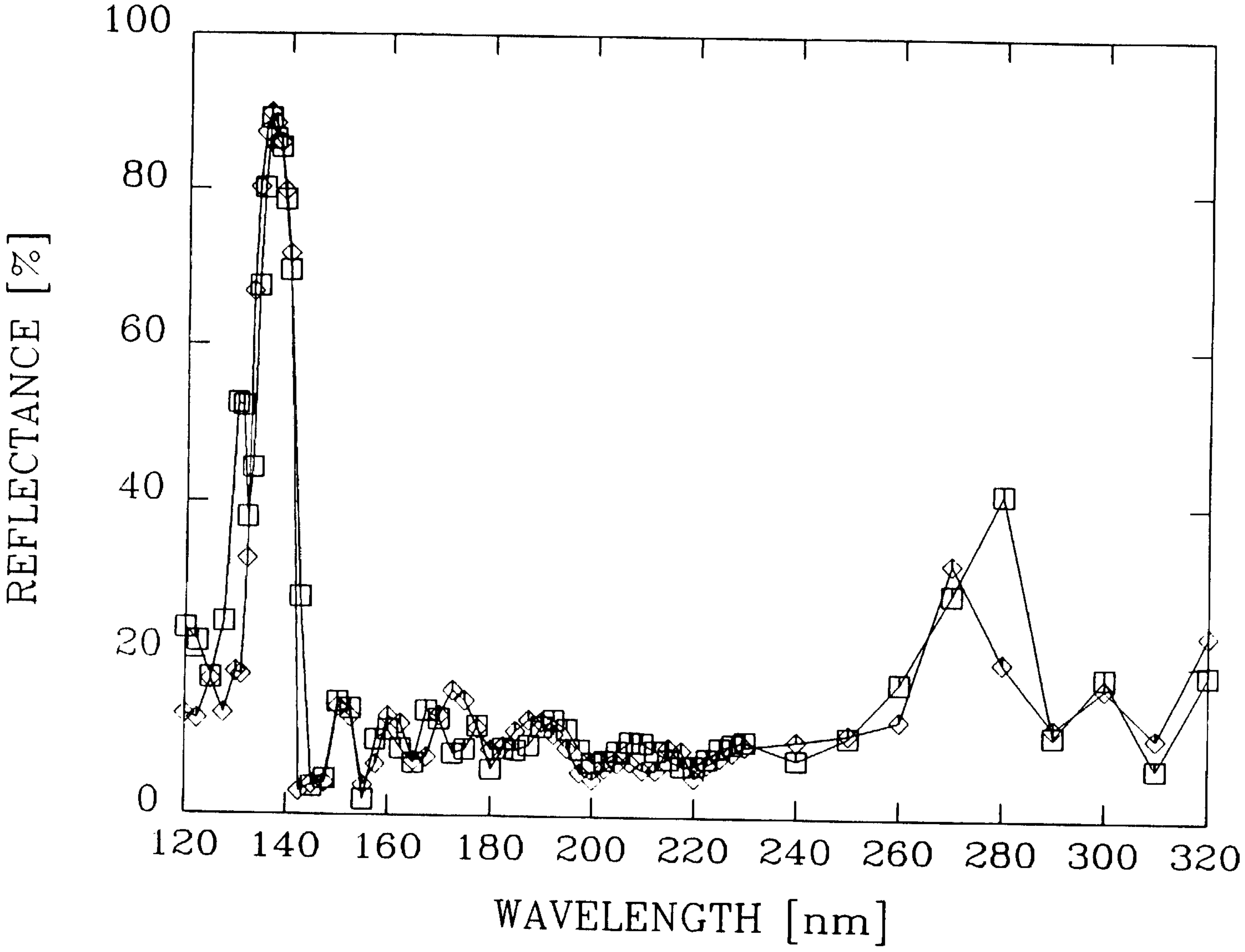

FIGURE 4: THE MEASURED (SQUARES) AND CALCULATED (DIAMONDS) REFLECTANCE OF THE 35-LAYER Π STACK FOR 45 DEGREES ANGLE OF INCIDENCE CENTERED AT 135.6 NM. THE OPTICAL THICKNESS RATIO H/L = 0.25 WITH H = LANTHANUM FLUORIDE, AND L = MAGNESIUM FLUORIDE.

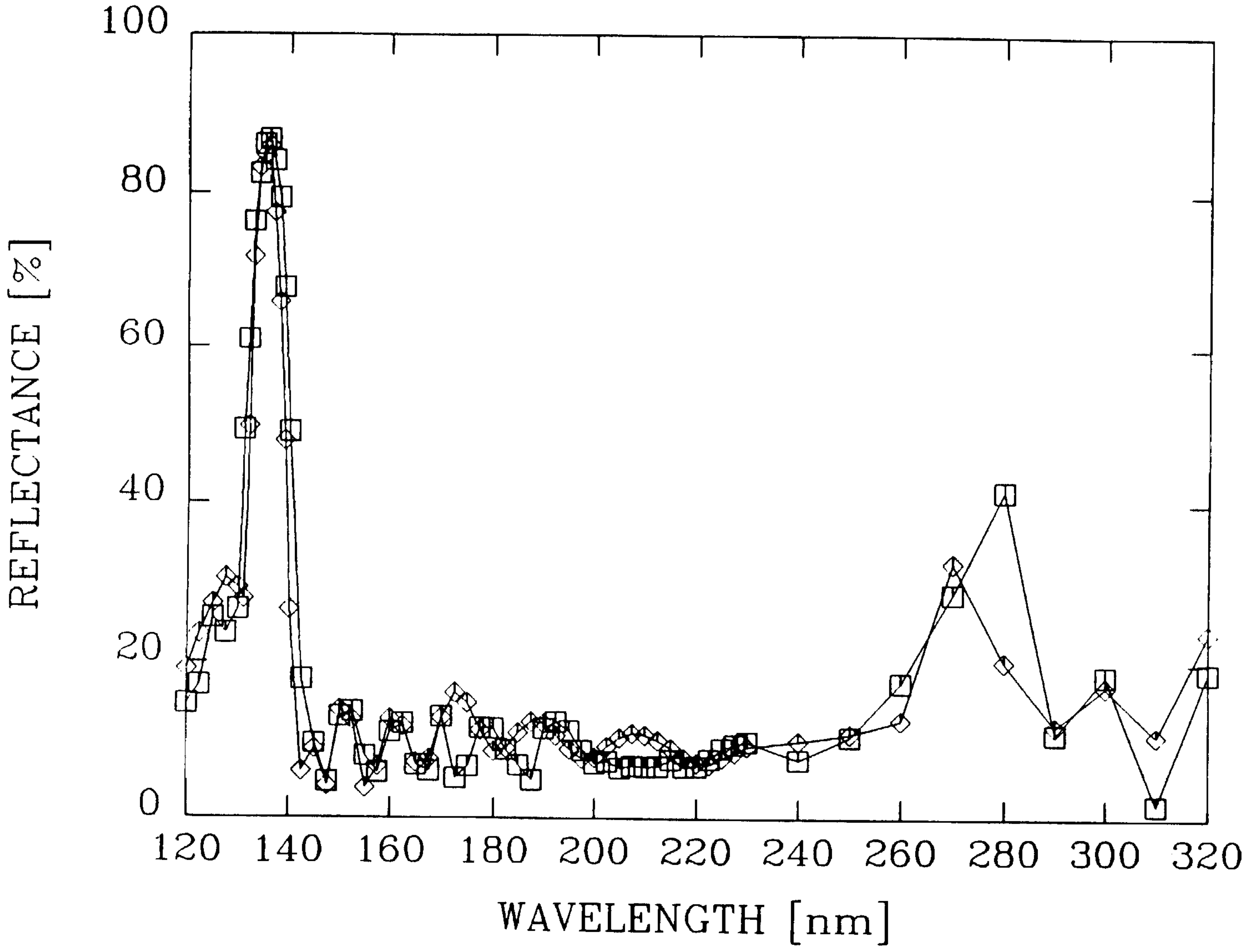

FIGURE 5: THE MEASURED (SQUARES) AND CALCULATED (DIAMONDS) REFLECTANCE OF THE 29-LAYER Π STACK FOR 45 DEGREES ANGLE OF INCIDENCE CENTERED AT 135.6 NM. THE OPTICAL THICKNESS RATIO H/L = 1/3 WITH H = BARIUM FLUORIDE, AND L = MAGNESIUM FLUORIDE.

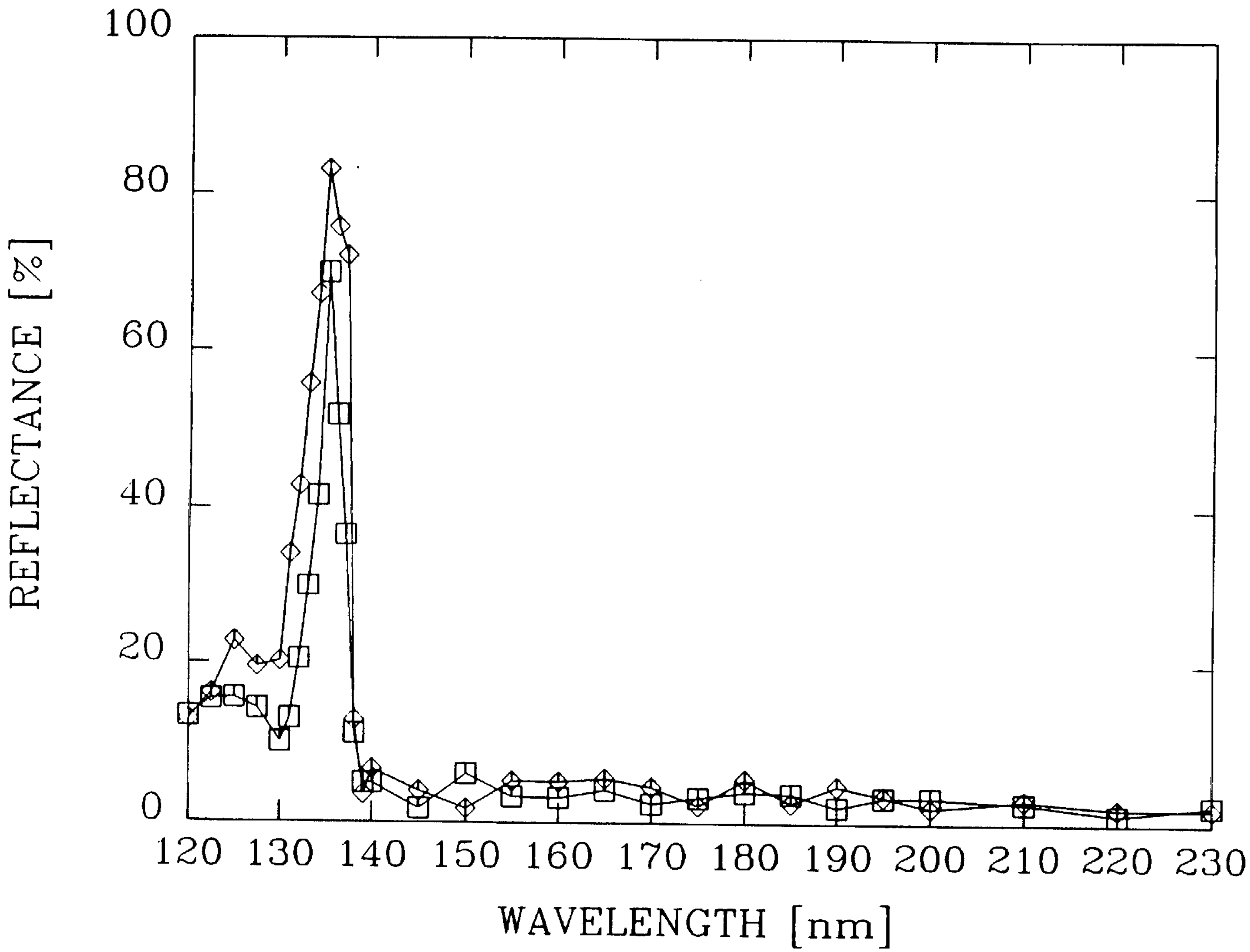

FIGURE 6: THE MEASURED (SQUARES) AND CALCULATED (DIAMONDS) REFLECTANCE OF THE 35-LAYER SECOND ORDER QW STACK FOR 45 DEGREES ANGLE OF INCIDENCE CENTERED AT 135.6 NM. H = BARIUM FLUORIDE AND L = MAGNESIUM FLUORIDE.

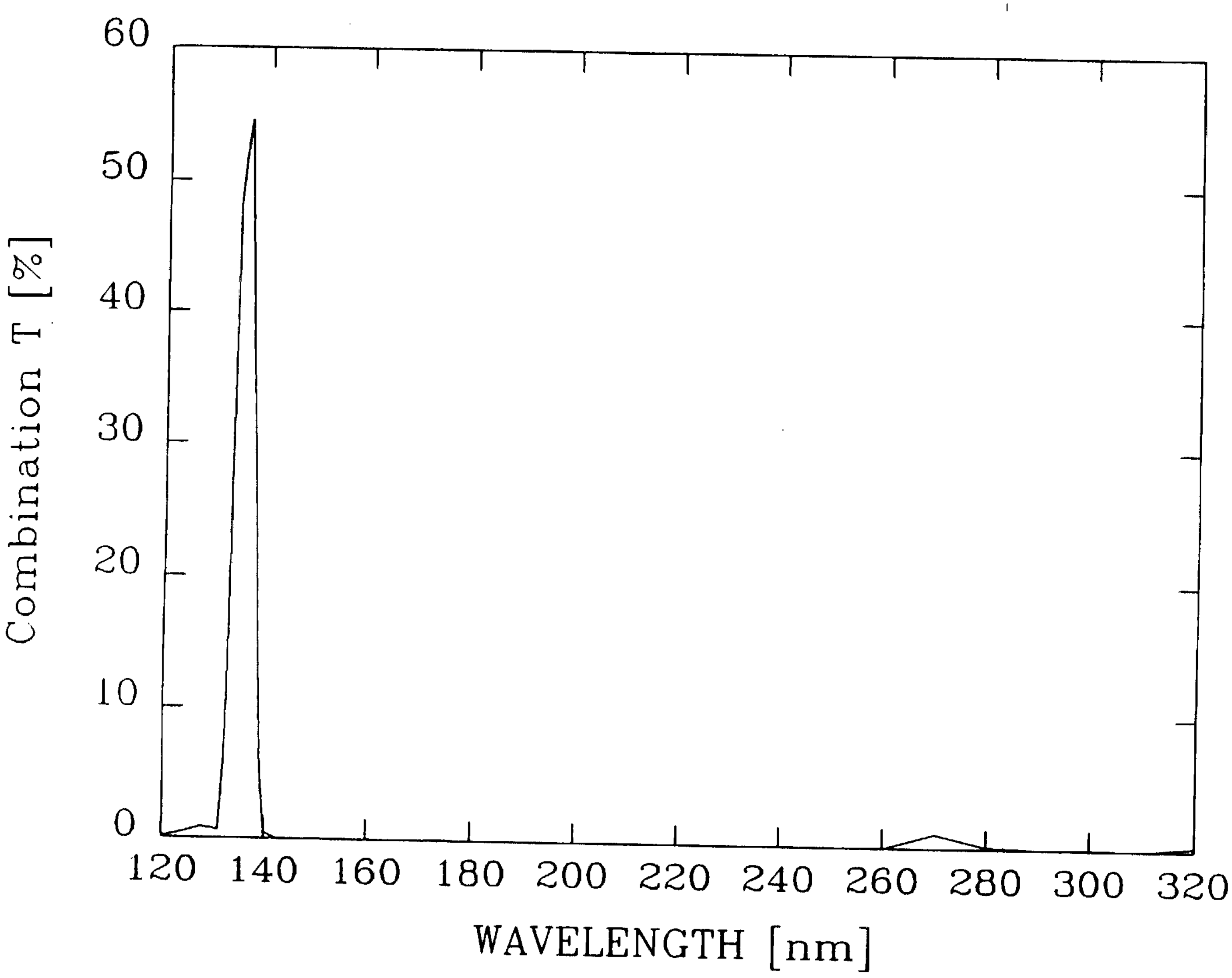

FIGURE 7: THE TRANSMITTANCE OF THE COMBINATION OF FOUR 29-LAYER FILTERS SHOWN IN FIGURE 5. THE BANDWIDTH IS 4.3 NM, AND A PEAK TRANSMITTANCE AT 135.6 NM IS 53.7%.

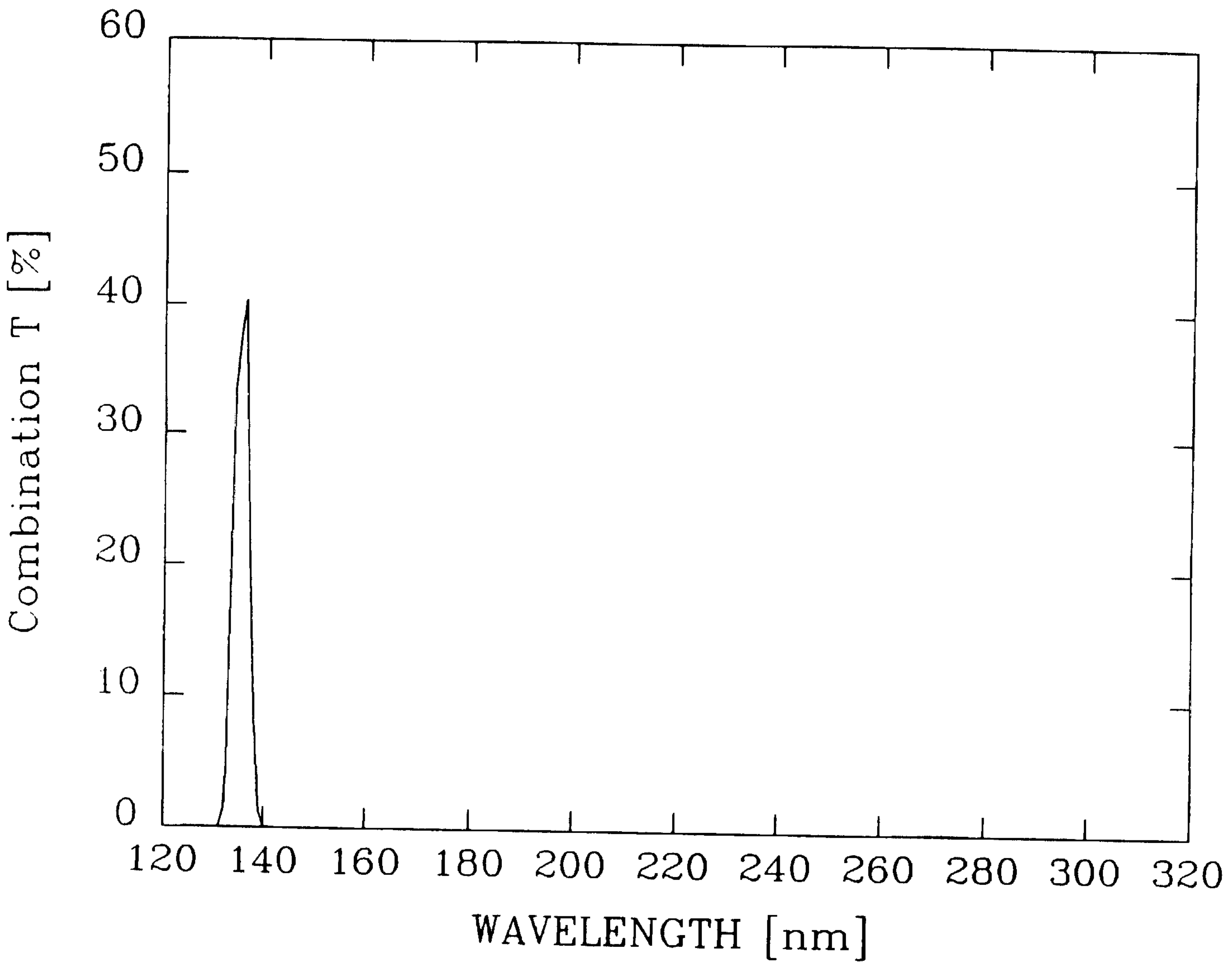

FIGURE 8: THE TRANSMITTANCE OF THE COMBINATION OF SIX 29-LAYER FILTERS SHOWN IN FIGURE 5. THE BANDWIDTH IS 3.2 NM, AND A PEAK TRANSMITTANCE AT 135.6 NM IS 39.3%.

Multiple Reflectors as
Narrowband and Broadband VUV Filters

Muamer Zukic and Douglas G. Torr
University of Alabama in Huntsville
Department of Physics
Research Institute C-10
Huntsville, Alabama 35899

Abstract

We report the development of a new coating design for applications in the vacuum ultraviolet which yields significantly higher reflectivity over selectable bandwidths. We demonstrate that the concept can be used to fabricate high performance narrow and broadband reflection filters, whose spectral properties can be greatly enhanced by utilizing several of these filters in tandem. For example, we have fabricated a narrowband filter at the location of the OI 135.6 nm line with 3.2 nm bandwidth, peak transmittance of 39.3%, and blocking of out-of-band wavelengths is better than 10^{-4}%. The principle of our design approach is to use a combination of high (H) - low (L) refractive index dielectric pairs such that $H + L = \lambda_r/2$ where $H/L < 1$. H and L designate the optical thicknesses of high and low index film materials. This kind of choice for the high-low ratio reduces the effects of absorption for the H films for which the extinction coefficient in the VUV is much higher than for the low index film material MgF_2. The reduced absorption of multilayers with $H/L < 1$, results in a significant increase of reflectivity compared to the classical quarterwave stack for which $H/L = 1$.

Submitted to Applied Optics, 1990

I. INTRODUCTION

Narrowband filters that are commercially available in the vacuum ultraviolet wavelength region from 120 nm to 160 nm have typical transmittance lower than 15%, and full width measured at half of transmittance maximum (FWHM) greater than 25 nm. The peak transmittance of the filters centered at the longer wavelengths from 160 nm - 230 nm lie between 20% and 25% with FWHM $\geq$ 20 nm.[1]

Malherbe[2] reported the design and the spectral performance of a narrowband filter centered at the hydrogen Lyman-α line (121.6 nm) with peak transmittance close to 15% and FWHM = 9 nm. Blocking of the wavelengths longer than 160 nm is better than 10^{-3}%. The filter has relatively high transmittance for the wavelength region from 126 nm - 135 nm; close to 7% at 126 nm and almost 1% at 135 nm. This pass window makes the filter not very useful for terestrial imaging applications if the spectral discrimination of the neighboring atomic oxygen lines at 130.4 nm and 135.6 nm is desired. A narrowband filter centered at 202.5 nm is reported by the same author[3]. The filter has peak transmittance greater than 85% and FWHM = 2.5 nm. However, the blocking zone of the filter is very short and transmittance for wavelengths longer than 220 nm becomes greater than 85%.

The calculated and experimental spectral performance of a Fabry-Perot-type narrowband filter centered at 179 nm was reported by Spiller[4]. The theoretical calculation predicted a narrowband filter with resolution $\lambda_0/\Delta\lambda = 60$ and peak transmittance of 25%, but the measured performance had almost four times smaller resolution and much smaller peak transmittance. Discrepancies between the theoretically predicted and experimentally obtained spectral curves have been ascribed to the excitation of a surface plasma wave traveling along the surface of an aluminum film.

A variable bandwidth transmission filter reported by Elias[5] *et al* had bandwidths from 7 nm to 20 nm with peak transmittance from 20% to 40%, respectively. The filter was centered at 176 nm, and as in the case of other all-dielectric filters, suffered from pass windows in the longer wavelength region.

Narrowband filters for the vacuum ultraviolet wavelength range (VUV) from 120 nm to 230 nm with similar optical properties to those listed above were also reported by some other authors[6-9]. The FWHM bandwidths of some filters that we have developed recently[10] are smaller than 5 nm with peak transmittance greater than 25% centered at wavelengths as low as 135 nm. Since those were all-dielectric filters, the transmittance in the longer wavelength region provided insufficient blocking for some applications.

Currently available VUV broadband filters with bandwidths greater than 10 nm have relatively low transmittance and the shape of the transmittance curve is similar to that of Fabry-Perot-type filters[1,4-8,11]. For most applications a more rectangular shape for the pass band and higher transmittance is required.

Taking all this into account, it is clear that the VUV spectral range lacks high quality narrow and broadband filters such as are available in the visible and infrared parts of the spectrum. The reasons for this are certainly a lack of low absorbing film materials in the VUV for all-dielectric filters, and the coupling of the incident light into plasma surface waves of the metal for metal-dielectric filters.

Hunter[12] achieved a measure of success in solving this problem by combining two or more reflectors in series in order to achieve desired spectral performance for the design of vacuum ultraviolet reflection polarizers and analyzers. The idea is that if sufficiently high reflectivity can be achieved within the passband, then the in-band exponential loss of reflectivity with additional reflective surfaces becomes insignificant compared to the net out-of-band exponential reflectance reduction. However, for the approach to be viable, the ratio of in-band to out-of-band reflectivity at each surface should be the order of 10, eg. 90% and 10%, respectively. Two reflections, for example, then reduce the in-band reflectivity to 81%, whereas the out-of-band reflectivity is reduced to 1%, and so on.

In this paper we report the successful design and fabrication of narrow and broadband reflection filters with the desired 90% reflectance. These filters are then combined into a multiple reflector to provide excellent blocking for out-of-band wavelengths and the desired spectral shape for both narrowband and the broadband applications. For example, narrowband filtering with a bandwidth of 3.2 nm and a throughput at the central wavelength (135.6 nm) of 39.3% was achieved. Blocking of out-of-band wavelengths is better than 10^{-4}%. A multiple reflector was designed to illustrate the performance of a broadband filter centered at 175 nm. In this case a bandwidth of 11 nm and throughput greater than 54% was realized. Out-of-band blocking is better than 3×10^{-3}%.

The next section of this paper reviews the theory of quarterwave (QW), and other multilayer options which we have called Π filters[13]. The design and spectral performance of several narrowband and broadband filters are presented in Section III. Section IV deals with experimental techniques including thin film deposition, and substrate handling and preparation. A summary is given in Section V.

II. ABSORBING MULTILAYERS

A. Reflectance Transmittance and Absorptance

The intensity reflection and transmission coefficients for a plane electromagnetic wave incident on a multilayer stack are given by[14]

$$r = \frac{(M_{11} + M_{12}\eta_S)\eta_0 - (M_{21} + M_{22}\eta_S)}{(M_{11} + M_{12}\eta_S)\eta_0 + (M_{21} + M_{22}\eta_S)}, \tag{1}$$

$$t = \frac{2\eta_0}{(M_{11} + M_{12}\eta_S)\eta_0 + (M_{21} + M_{22}\eta_S)}, \tag{2}$$

where η_0 and η_S, which are the effective optical functions of the incident medium and the substrate, are defined as

$$\eta_0 = n_0 \cos\theta_0, \tag{3}$$

$$\eta_S = n_S \cos\theta_S \tag{4}$$

for s polarization, and as

$$\eta_0 = \frac{\cos\theta_0}{n_0}, \tag{5}$$

$$\eta_S = \frac{\cos\theta_S}{n_S}, \tag{6}$$

for p polarization. Angles, θ_0 and θ_s, for light propagation through the incident medium and the substrate are measured relative to the normal to the film plane. n_0 and n_S are the refractive indices of the incident medium and the substrate, respectively. It is assumed that both the substrate and incident medium have negligible extinction coefficients and therefore real optical functions. The terms $M_{ij}, i, j = 1, 2$ are the elements of the multilayer characteristic matrix $\mathbf{M}$ which is defined as the product of the matrices of the individual layers $\mathbf{M}_l$, where

$$\mathbf{M}_l = \begin{pmatrix} \cos\delta_l & \frac{i}{\eta_l}\sin\delta_l \\ i\eta_l \sin\delta_l & \cos\delta_l \end{pmatrix}. \tag{7}$$

The phase thicknesses of the films δ_l are given by

$$\delta_l = \frac{2\pi}{\lambda_0} N_l d_l \cos\Theta_l, \tag{8}$$

where λ_0 is the vacuum wavelength of the incident light. N_l is the optical function (usually referred to as "optical constant") of the *l-th* layer defined as

$$N_l = n_l(1 + i\kappa_l) = n_l + i n_l \kappa_l = n_l + i k_l, \tag{9}$$

with $\kappa_l = k_l/n_l$, and where n_l is the refractive index, k_l is the extinction coefficient, d_l is the physical thickness, and Θ_l is the complex angle of the light within the *l-th* film.

The reflection and transmission coefficients r and t are complex numbers of the form

$$r = |r| e^{i\phi_r}, \tag{10}$$

$$t = |t| e^{i\phi_t}, \tag{11}$$

where ϕ_r and ϕ_t are the phase changes on reflection and transmission. The intensity reflectance R, transmittance T, and absorptance A of a multilayer are given by

$$R = rr^*, \tag{12}$$

$$T = \frac{\eta_S}{\eta_0} tt^*, \tag{13}$$

$$A = 1 - (R + T). \tag{14}$$

B. Quarterwave Tuned Multilayers

Multilayer stacks formed by high and low index materials alternating throughout a stack are usually referred to as tuned filters or tuned multilayers. The basic design of such a multilayer stack is given in either symmetric [$(HL)^pH$] or asymmetric form [$(HL)^p$]. Symmetric [$(LH)^pL$] and asymmetric [$(LH)^p$] tuned multilayers represent another form of the basic design. H and L designate optical thicknesses of high and low refractive index film materials respectively, and p is the number of (HL) pairs. The form and the symmetry of a stack are determined by the refractive indices of the substrate and incident medium[15].

If the optical thickness of a film (defined as a product of a physical thickness of a film and its refractive index) is equal to one quarter of some reference wavelength λ_r then this film is referred to as a quarterwave (QW) . Applications of QW multilayers are based on the fact that for an incident wavelength $\lambda_0 = \lambda_r$ the beams reflected from the various interfaces will all be in phase, so the reflectance obtained is a maximum.

We have shown that at zero angle of incidence, the maximum reflectance of a QW stack with absorbing film materials is achieved when the number of (HL) pairs p satisfies the following condition[10]

$$p = p_0 = \frac{\pi}{4}\left(\tan^{-1}\left(\frac{\kappa_H - \kappa_L}{1 + \kappa_H \kappa_L}\right)\right)^{-1}, \tag{15}$$

where

$$\kappa_H = \frac{k_H}{n_H}, \tag{16}$$

and

$$\kappa_L = \frac{k_L}{n_L}. \tag{17}$$

n_H and n_L are refractive indices of high and low index film materials, and k_H and k_L are corresponding extinction coefficients. Values of $p \geq p_0$ correspond to numbers of (HL) pairs for which both the absorptance and reflectance of the stack are constant and sum to unity i.e.

$$R + A \rightarrow 1, \tag{18}$$

resulting in a value for the stack transmittance essentially equal to zero.

An alternative description of the optical properties of a QW stack with absorbing films might be given in terms of the standing wave ratio (SWR)[16]. The SWR in general is the ratio of the maximum and minimum amplitudes in a standing wave. In multilayer theory it is the ratio of the maximum to minimum electric field amplitude in the standing wave formed by the interference of the incident and reflected electromagnetic waves. For a symmetrical QW stack[17]

$$SWR = \frac{1+\sqrt{R}}{1-\sqrt{R}} \tag{19}$$

where R is the intensity reflectance of the stack. The SWR saturated level and therefore the maximum reflectance of a QW stack of the form $[(HL)^pH]$ is given by[18]

$$R_K = 1 - 2\pi n_0 \frac{k_H + k_L}{n_H^2 - n_L^2}, \tag{20}$$

where R_K, the ultimate reflectance, is usually referred to as the Koppelmann limit. Thus, the reflectance of a QW stack $R \rightarrow R_K$ as $p \rightarrow \infty$, if film materials forming the stack are absorbing. For non-absorbing film materials $R \rightarrow 1$ as $p \rightarrow \infty$.

It should be emphasized that Eq.(20) was derived with some approximations[18] and it cannot replace an exact calculation of the maximum reflectance of a QW stack. Equation (20) provides an extremely simple relationship between the maximum reflectance obtainable with an absorbing QW stack and the optical properties of film materials forming the stack. However, the value obtained for the maximum reflectance must be treated as an estimate. In addition, R_K is derived for zero angle of incidence and it does not represent the ultimate reflectance for $\theta_0 \neq 0^\circ$. Therefore, we shall reference the exactly calculated reflectance [Eq. (12)] as the "Koppelmann limit" for a QW stack at any angle of incidence.

The Koppelmann limit and how to extend it have been the subject of a number of theoretical and experimental studies[16-21]. Some approaches involve numerical refinement of the film thicknesses in order to reduce the electric field amplitude in the high index materials close to the side of incidence. Other authors, assuming values of the extinction coefficient lower than 10^{-3}, derived approximating formulas for the thicknesses of an optimum (HL) pair which would provide the maximum reflectance.

BaF_2 and LaF_3 are the only available VUV high index film materials identified at this time[22]. They both have values of the extinction coefficient greater than 10^{-2} for wavelengths below 200 nm. This means that most of above mentioned and referenced techniques for the improvement of the Koppelmann limit are not applicable to the VUV wavelength range. Our approach to this problem is to utilize multilayer stacks with the optical thickness ratio $H/L < 1$ instead of standard QW stacks for which $H/L = 1$. MgF_2 film material has values of the extinction coefficient of the order of 10^{-4} for almost entire VUV wavelength region[22], and it is exclusively used as the low index film material for all multilayer designs presented in this paper. Since the extinction coefficient of the high index materials (BaF_2 and LaF_3) is 100 times greater than that of MgF_2, the stacks with $H/L < 1$ have lower absorption and therefore higher reflection than stacks with $H/L = 1$.

C. Thirdwave Tuned Multilayers

The definition of the thirdwave (TW) multilayers is not standardized as in the case of the quarterwave stacks. It is defined here as a tuned multilayer which has one material with optical thickness equal to one third of some reference wavelength, while the optical thickness of the other material is equal to one sixth of a reference wavelength, i.e.

$$n_H d_H = \frac{\lambda_r}{6},$$

$$n_L d_L = \frac{\lambda_r}{3}.$$

Since $k_H/k_L \geq 100$ for presently available high and low index materials in the VUV (LaF_3, BaF_2, and MgF_2), the choice of which material should have the optical thickness of $\lambda_r/6$ is obvious.

The two H and L films in a QW multilayer form an (HL) pair with total optical thickness equal to $\lambda_r/2$ which corresponds to a total phase thickness of the pair $\delta = \pi$. Similarly, an (HL) pair of a TW multilayer has an overall optical thickness equal to $\lambda_r/2$ which again corresponds to a total phase thickness of the pair equal to π. Thus, the principle of a high reflectance at a reference wavelength of a TW tuned multilayer is similar to that of a QW stack. The concept of the TW multilayer leads to other kinds of multilayers which are discussed in the next section.

D. Π Multilayers

We define a Π multilayer as one whose basic (HL) pair has a total optical thickness of $\lambda_r/2$. Optical thicknesses of individual H and L films forming a pair satisfy the following condition

$$H + L = \frac{\lambda_r}{2}, \tag{21}$$

where λ_r is the reference wavelength of the multilayer. The total phase thickness of the pair is equal to π, i.e. $\delta_H + \delta_L = \pi$. Thus, quarterwave and thirdwave stacks are the special cases of Π multilayers. In a quarterwave stack light reflected from all interfaces is in phase, while in a thirdwave and other Π multilayers light reflected from each (HL) pair is in phase. Obviously, quarterwave stacks with low-absorbing film materials (available in the visible and infrared parts of spectrum) provide higher reflectance with fewer layers than other Π stacks. However, in the VUV where low-absorbing high index film materials do not exist, a Π multilayer with smaller physical thickness of H relative to L can provide lower absorptance and therefore higher reflectance of the stack.

Figure 1 illustrates how the Koppelmann limit can be easily extended for zero angle of incidence. It shows maximum reflectances calculated for the 99-, 55-, and 35-layer Π stacks plotted against the ratio of optical thicknesses of high and low index film materials (H/L). The reference wavelength is 145 nm, with MgF_2 as the high, LaF_3 as the low index materials, and fused silica as the substrate. The Koppelmann limit is $R_K = 90.8\%$. The 99-layer filter has the maximum reflectance of 96.5% when the ratio of optical thicknesses $H/L = 1/4$. This ratio corresponds to the optical thicknesses of $H = \lambda_r/10$ and $L = 4\lambda_r/10$. The 55-layer has the maximum reflectance of 95.3% for $H/L = 1/3$ which corresponds to the optical thicknesses of $H = \lambda_r/8$ and $L = 3\lambda_r/8$. The ratio $H/L = 1/2$ provides the maximum reflectance of 93.6% for the 35-layer Π stack. From Fig. 1, it follows that at zero angle of incidence, stacks with the ratio $H/L < 1$ provide a significant improvement in the maximum reflectance over what can be achieved with QW stacks for which $H/L = 1$.

Shown in Figures 2 and 3 are maximum reflectances and bandwidths (full width measured at half of reflectance maximum) respectively, calculated at $\theta_0 = 45^0$ for the 99-, 55-, and 35-layer Π stacks, plotted against the ratio of optical thicknesses of high and low index material (H/L). The reference wavelength is 135.6 nm, with MgF_2 as the low, LaF_3 as the high index material, and fused silica as the substrate. The Koppelmann limit for the QW stack is $R_K = 89.5\%$ $\theta_0 = 45^0$ at angle of incidence. The 99-and 55-layer Π

multilayers (Fig. 2) have a maximum reflectance of 93.0% and 92.7% respectively, when the ratio of optical thicknesses is H/L = 1/3. This corresponds to optical thicknesses of high and low index film materials

$$H = \frac{\lambda_r}{8},$$

$$L = \frac{3\lambda_r}{8}.$$

The 35-layer Π stack (Fig. 1) has a maximum reflectance of 91.4% for H/L = 1/2. The optical thicknesses for this H to L ratio of the Π multilayer are given by

$$H = \frac{\lambda_r}{6},$$

$$L = \frac{\lambda_r}{3}.$$

The lowest decrease of the maximum reflectance occurs for the QW stack when the number of films is decreased from 99 to 35. This result is certainly expected since the saturation level of the SWR decreases with an increase of the multilayer absorption. Of all the multilayers the physical thickness of the high index material (LaF_3 in this particular case) within the multilayer is largest for the QW stack. Therefore, the SWR saturation level for the QW stacks is achieved with fewer layers compared to other Π stacks. As should be expected the bandwidth decreases with a decrease of of the ratio H/L. It is 17 nm for the QW stack and 6.9 nm for the stack with H/L = 1/5 (Fig. 3).

From Figs. 2 and 3, it follows that for the design of a narrowband reflector centered at 135.6 nm, the Π stack with H/L = 1/4 seems to be the most feasible choice. The 35-layer stack with this ratio has optical thicknesses given by

$$n_H d_H = \frac{\lambda}{10}$$

$$n_L d_L = \frac{4\lambda}{10}.$$

Calculated values of the maximum reflectance R_{max} = 88.4% at 135.6 nm and FWHM = 7.2 nm. Figure 4 shows the measured and calculated reflectance of this stack with fused silica as the substrate material. The measured values of the peak reflectance at 135.6 nm is 88.3% while the theory predicts the reflectance peak of 88.4%. The measured bandwidth of 7.2 nm agrees with the theoretical predictions.

Figure 5 shows the measured and calculated reflectance at 45^0 angle of incidence for a 29-layer Π stack with BaF_2 as the high index material and fused silica as the substrate. The ratio H/L = 1/3, and optical thicknesses are given by

$$n_H d_H = \frac{\lambda_r}{8}$$

$$n_L d_L = \frac{3\lambda_r}{8}.$$

The measured reflectance maximum at λ_r = 135.6 nm is 86.0% with bandwidth of 7.2 nm. The theory predicts 86.9% maximum reflectance and 6.8 nm bandwidth.

E. Higher Order Π Multilayer Stacks

The first order QW stacks have wider high reflectance zone than other Π multilayers. The width of the high reflection zone $(\Delta\lambda)_{H.R.}$ of a QW multilayer with non-absorbing film materials is given by[23]

$$(\Delta\lambda)_{H.R.} = \frac{1}{2(m-1)+1}\frac{4\lambda_r}{\pi}\sin^{-1}\left(\frac{n_H - n_L}{n_H + n_L}\right) \tag{24}$$

where m is the order of Π multilayer. For absorbing film materials the width of the high reflection zone is smaller than that calculated using Equation (24). Thus, Equation (24) gives a maximum width for a high reflectance zone obtainable for materials with refractive indices n_H and n_L. Thus, an alternative approach for the design of the narrowband reflectors is to utilize the QW or other Π stacks with higher order m. However, an increase of the order of a Π stack from 1 to, say m, changes a total phase thickness of an (HL) pair from $\pi \rightarrow m\pi$. The total optical thickness of an (HL) pair is increased by $\lambda_r/2$ when the order of a Π stack is increased by unity. Increased physical thickness of both high and low index film materials results in increased absorptance and therefore lower reflectance of the stack. Figure 6 shows the calculated and experimentally obtained reflectance of the second order QW stack centered at 135.6 nm at a 45^0 angle of incidence. BaF_2 is used as the high index material and fused silica as the substrate. The calculated value of the maximum reflectance is 83.1% while the measured value is 69.9%. Discrepancies between the theory and experiment may be explained by the presence of physical factors neglected in the theoretical calculation such as the surface and volume scattering, film and substrate contaminations, and film inhomogeneity. The agreement between the theoretical prediction and experimentally obtained results is much better for the first order filters (Figs. 4 and 5) than for the second order QW stack. This may indicate that thicker films in the QW stack are more affected by the physical factors neglected in the multilayer theoretical calculation.

III. MULTIPLE REFLECTION FILTERS

A. Narrowband

Reflection filters shown in Figures 4 and 5 have measured reflectances at the central wavelength of 86.0% and 88.3%, respectively. They both have relatively high reflectance in the shorter wavelength region and an average reflectance of the order of 10% for the longer wavelengths. The reflectance outside the filter's "pass" zone and the bandwidth of the pass zone can be reduced by means of multiple reflections from two or more reflection filters upon which light is incident at an angle of 45^0. The overall transmissions of combinations of four and six 29-layer filters are shown in Figures 7 and 8, respectively.

The maximum throughput of the 4-filter combination at the central wavelength $\lambda =$ 135.6 nm is 53.7% and the bandwidth of 4.3 nm. The blocking for shorter wavelengths is better than 0.7% and for longer wavelengths is better than $10^{-2}\%$. If further improvement of the blocking for wavelengths outside the pass zone is required, then 6 or more filters can be combined. However, adding more filters will reduce the overall transmittance of the combination. The maximum throughput of the 6-filter combination at the central wavelength is 39.3% with the bandwidth of 3.2 nm. The blocking outside the pass zone is better than $10^{-4}\%$ for longer and better than 0.07% for shorter wavelengths. If a 4 mm thick MgF_2 window is placed at the entrance of the combination than the transmittance of shorter wavelengths may be less than $10^{-4}\%$.

B. Broadband

The pass zone of a broadband filter is bounded by a lower and upper wavelengths. Ideally, the spectral components of the incident light, with wavelengths shorter than the lower and longer than the upper wavelength of the filter, together referred to as the out-of-band spectrum, are rejected. In the design examples that follow, wavelengths of the out-of-band spectrum are rejected by means of multiple reflections from QW stacks. The rejection at shorter wavelengths might be improved by the suitable choice of the window material, placed at the entrance of a multireflector combination. Windows made of BaF_2 and CaF_2 absorb wavelengths below 135 nm, and 125 nm respectively, while fused silica and Al_2O_3 may be used for broadband filters with a lower pass limit above 145 nm[13,24].

Because of the narrower high reflection zone the Π multilayers with $H/L < 1$ are not suitable for the design of broadband reflectors. QW stacks for which $H/L = 1$ are a better choice for the design and fabrication of these filters. Figure 9 shows the measured and calculated reflectance at 45° incident angle for the 25-layer QW stack. The reference wavelength is 175 nm, LaF_3 is used as the high index material, and fused silica as the substrate. The measured peak value of the reflectance is 90.3% and the bandwidth measured at half of the reflectance maximum is 19 nm. The average reflectance for the out-of-band wavelengths is of the order of 10%. The Koppelmann limit for LaF_3 and MgF_2 at this wavelength is $R_K = 94.4\%$, and the theoretically predicted value of the peak reflectance is 91.6%.

The agreement between the theory and the experiment is much better than for the second order QW stack (Fig. 6). Again this may indicate that thicker films in the second order QW stack are more affected by the physical factors neglected in the multilayer theoretical calculation.

Figure 10 shows the transmittance of combinations of four and six of these reflectors. The 4-reflector combination has a peak transmittance of 66.3% and the bandwidth of 11.5 nm. The rejection of the out-of-band spectrum up to 300 nm is better than 0.1%.

If a 4 mm thick fused silica parallel plate is used as the window then the rejection of the shorter wavelengths of the out-of-band spectrum is better than 10^{-3}%. The 6-reflector combination has a peak transmittance of 54.04% with bandwidth of 11 nm. This combination provides much better rejection for out-of-band wavelengths. The transmittance of the combination for out-of-band wavelengths is less than 3×10^{-3}%. If a 4 mm thick fused silica is used as the window than the transmittance of the combination for shorter wavelengths of the out-of-band spectrum is less than 10^{-5}%.

IV. THE EXPERIMENTAL ARRANGEMENT

All depositions are made on 12.7 mm diameter by 2 mm thick MgF_2 and fused silica substrates with root mean square roughness less than 1 nm. The substrates are cleaned by the supplier (Acton Research Corp., Acton, Massachusetts) using the following procedure: optical soap wash, water rinse, ethanol soak then ultrasonic bath, fresh ethanol rinse, and finally a Freon rinse. The substrates are packed in a clean room environment in Delrin holders. They are removed from Delrin holders immediately prior to mounting in the substrate holder for deposition. Mounting in the substrate holder is done in a laminar flow bench. During the transport from the bench to the vacuum chamber the substrate is kept in a flow of dry nitrogen. All depositions are made at the University of Alabama in Huntsville, Optical Aeronomy Laboratory and spectrophotometric measurements are made at the Atomic Physics Branch of the NASA/Marshall Space Flight Center.

The vacuum system consists of a cryo-pump and a sorption pump giving an oil-free environment for all depositions and therefore providing a very low probability for hydrocarbon contamination of the films. The film materials BaF_2 and LaF_3 are prepared for vacuum deposition by CERAC with a typical purity of 99.9% while MgF_2 (99.95%) is standard BALZERS coating material. The films are deposited with low deposition rates of 0.18 - 0.20 nm/sec on the substrates heated to 200°C. The pre-deposition pressure is 7.5×10^{-7} while the deposition pressure varies between 1.7 and 2.3×10^{-6} for all coating materials. The temperature is monitored with a Chromel-Alumel thermocouple attached to an aluminum ring substrate holder. The substrate and the ring holder are placed in the center of a 40 mm diameter by 6 mm thick stainless steel plate. A quartz crystal is used for the film thickness and deposition rate monitoring. The depositions are made with an electron gun. The gun has fixed voltage of 10 KV and low power depositions are maintained by supplying low current to the filament. The source to the substrate distance is 500 mm and the source to the monitor distance is 350 mm.

V. SUMMARY

The idea of utilizing multiple reflections from Π multilayer reflection filters upon which the light is incident at 45^0 angle constitutes the basis of our narrowband and broadband filters. The multiple reflector combinations provide superior spectral performance for both the narrowband and the broadband filters over what is currently available.

The high reflective multilayer coatings for the narrowband reflection filters are designed using Π multilayer stacks with $H/L < 1$ instead of the classical QW stacks for which $H/L = 1$. It is shown that the Π stacks with $H/L < 1$ have higher reflectance and smaller bandwidth than the QW stacks, and are therefore more suitable for the design of narrowband reflection filters. It is demonstrated that the QW stack maximum reflection limit at both $\theta_0 = 0^0$ (Koppelmann limit) and $\theta_0 = 45^0$ can be easily extended for coating materials available in the VUV. A peak reflectance of more than 96% for zero angle of incidence can be achieved for wavelengths as low as 135.6 nm when Π stacks with the ratio $H/L < 1$ are utilized. Stacks with more than 99 layers can provide further improvements of the maximum reflectance, but the lowest value of the H/L ratio is limited by the smallest feasible thickness of the high index films. Furthermore, Π multilayers with $H/L < 1$ are not suitable for broadband reflectors since they generally do not have a width of the high reflectance zone as wide as the QW stacks.

The agreement between the theoretical and experimental results is much better for first order filters (Figs. 4, and 5) than for the second order QW stack (Fig. 6) and for QW stacks centered at longer wavelengths (Fig. 9). This may indicate that thicker films in the QW stack are more affected by the physical factors neglected in the multilayer theoretical calculation such as the surface and volume scattering, film inhomogeneity, and film contamination.

REFERENCES

1. Acton Research Corporation, **Optical Filters,** Catalog (1989).
2. A. Malherbe, "Interference Filters for the Far Ultraviolet", *Appl. Opt.* **13,** 1275-1276 (1974).
3. A. Malherbe, "Multidielectric Components for the Far Ultraviolet", *Appl. Opt.* **13,** 1276-1276 (1974).
4. E. Spiller, "Interference Filters for the Ultraviolet and the Surface Plasmon of Aluminum", *Appl. Opt.* **13,** 1209-1215 (1974).
5. L. R. Elias, R. Flach, and W. M. Yen, "Variable Bandwidth Transmission Filter for the Vacuum Ultraviolet: $La_{1-x}Ce_xF_3$", *Appl. Opt.* **12,** 138-139 (1973).
6. E. T. Fairchild, "Interference Filters for the VUV (1200-1900Å)", *Appl. Opt.* **12,** 2240-2241 (1973).
7. B. K. Flint, "Special Application Coatings for the Vacuum Ultraviolet (VUV)", *Opt. Eng.* **18,** 92-97 (1979).
8. B. K. Flint, "Recent Developments in Ultraviolet Filters and Coatings", *Adv. Space Res.* **2,** 135-142 (1983).
9. W. R. Hunter, "Review of Vacuum Ultraviolet Optics", Proc. **SPIE, 140,** 122-130 (1978).
10. M. Zukic, D. G. Torr, J. F. Spann, and M. R. Torr, "VUV Thin Films Part II: Vacuum Ultraviolet All-dielectric Narrowband Filters", paper accepted for publication in *Appl. Opt.* (Sept. 1, 1990).
11. E. Spiller, "Multilayer Interference Coatings for the Vacuum Ultraviolet" in **Space Optics,** B. J. Thompson and R.R. Shanon eds. Proc. of the Ninth International

Congress of the International Commission for Optics, 581-597 (National Academy of Sciences, Washington, D.C., 1974).

12. W. R. Hunter, "Design Criteria for Reflection Polarizers and Analyzers in the Vacuum Ultraviolet", *Appl. Opt.* **17**, 1259-1270 (1978).
13. M. Zukic and D. G. Torr, "VUV Thin Films", in **Topics in Applied Physics,** K. H. Guenther ed., Chapter VII, Springer-Verlag series on Thin Films, in press (to be published by March 1991).
14. M. Born and E. Wolf, **Principles of Optics,** Chapter 1 (Pergamon Press, Oxford 1983).
15. H. A. Macleod, **Thin-Film Optical Filters,** Chapters 2,5, and 6 (Macmillan, New York 1986).
16. L. Young, "Prediction of Absorption Loss in Multilayer Interference Filters", *J. Opt. Soc. Am.* **52**, 753-761 (1962).
17. C. K. Carniglia and J. H. Apfel, "Maximum Reflectance of Multilayer Dielectric Mirrors in the Presence of Slight Absorption", *J. Opt. Soc. Am.* **70**, 523-534 (1980).
18. G. Koppelmann, "On the Theory of Multilayers Consisting of Weakly Absorbing Materials and Their Use as Interferometer Mirrors", *Ann. Phys.* **5**, 388-396 (in German, Leipzig 1960).
19. J. H. Apfel, "Optical Coatings Design with Reduced Electric Field Intensity", *Appl. Opt.* **16**, 1880-1885 (1977).
20. P. H. Lissberger, "The Ultimate Reflectance of Multilayer Dielectric Mirror", *Opt. Acta* **25**, 291-298 (1978).

21. M. Sparks and M. Flannery, "Simplified Description of Multilayer Dielectric Reflectors", *J. Opt. Soc. Am.* **69**, 993-1006 (1979).

22. M. Zukic, D. G. Torr, J. F. Spann, and M. R. Torr, "VUV Thin Films Part I: Optical Constants of BaF_2, CaF_2, LaF_3, MgF_2, Al_2O_3, HfO_2, and Si_2 Thin Films" paper accepted for publication in *Appl. Opt.* (Sept. 1, 1990).

23. P. Yeh, **Optical Waves in Layered Media,** Chapters 6 and 7, (Wiley, New York 1988).

24. D. F. Heath and P. A. Sacher, "Effects of a Simulated High-Energy Space Environment on the Ultraviolet Transmittance of Optical Materials Between 1050 Åand 3000Å", *Appl. Opt.* **5**, 937-943 (1966).

FIGURE CAPTIONS

Figure 1: The maximum reflectance of the Π stack calculated for zero angle of incidence at 145 nm. Diamonds represent 99-layer, triangles 55-layer, and squares 35-layer stacks. H = Lanthanum Fluoride, and L = Magnesium Fluoride. The Koppelmann limit is 90.8%.

Figure 2: The maximum reflectance of the Π stack calculated for 45 degrees angle of incidence at 135.6 nm. Diamonds represent 99-layer, triangles 55-layer, and squares 35-layer stacks. H = Lanthanum Fluoride, and L = Magnesium Fluoride. The Koppelmann limit is 89.5%.

Figure 3: The full width at half of the reflectance maximum of the Π stacks calculated for 45 degrees angle of incidence. The maximum reflectance of the stacks as a function of the H/L ratio is shown in Fig. 2.

Figure 4: The measured (squares) and calculated (diamonds) reflectance of the 35-layer Π stack for 45 degrees angle of incidence centered at 135.6 nm. The optical thickness ratio H/L = 1/4 with H = Lanthanum Fluoride, and L = Magnesium Fluoride.

Figure 5: The measured (squares) and calculated (diamonds) reflectance of the 29-layer Π stack for 45 degrees angle of incidence centered at 135.6 nm. The optical thickness ratio H/L = 1/3 with H = Barium Fluoride, and L = Magnesium Fluoride.

Figure 6: The measured (squares) and calculated (diamonds) reflectance of the 35-layer second order QW stack for 45 degrees angle of incidence centered at 135.6 nm. H = Barium Fluoride, and L = Magnesium Fluoride.

FIGURE CAPTIONS

(Continued)

Figure 7: The transmittance of the combination of four 29-layer filters shown in Figure 5. The bandwidth is 4.3 nm, and a peak transmittance at 135.6 nm is 53.7%.

Figure 8: The transmittance of the combination of six 29-layer filters shown in Figure 5. The bandwidth is 3.2 nm, and a peak transmittance at 135.6 nm is 39.3%.

Figure 9: The measured (squares) and calculated (diamonds) reflectance of the 25-layer QW stack for 45 degrees angle of incidence centered at 175 nm. H = Lanthanum Fluoride, and L = Magnesium Fluoride.

Figure 10: The transmittance of combinations of four (solid line) and six (dashed line) 25-layer QW stacks shown in Fig. 9.

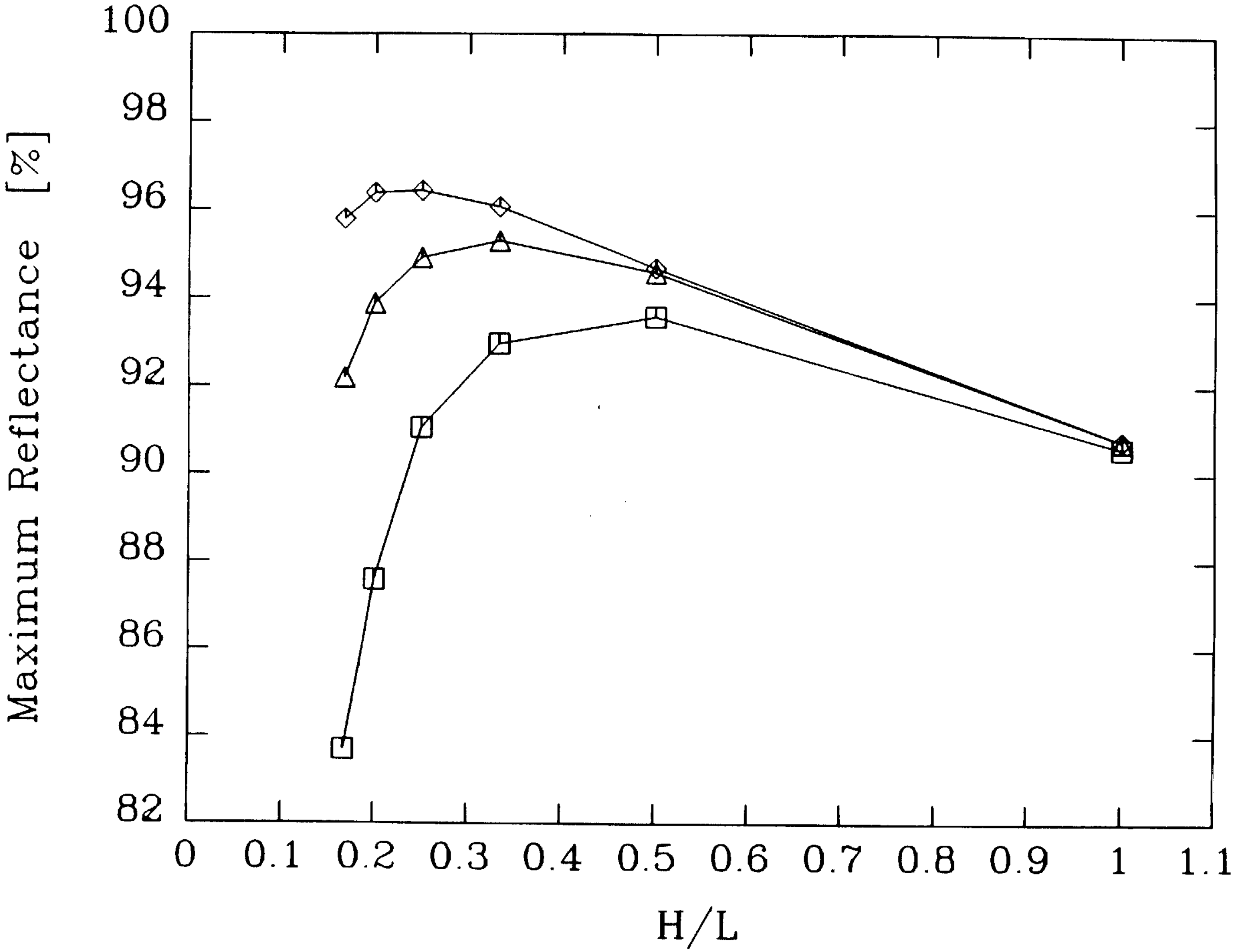

Figure 1: The maximum reflectance of the Π stack calculated for zero angle of incidence at 145 nm. Diamonds represent 99-layer, triangles 55-layer, and squares 35-layer stacks. H = Lanthanum Fluoride, and L = Magnesium Fluoride. The Koppelmann limit is 90.8%.

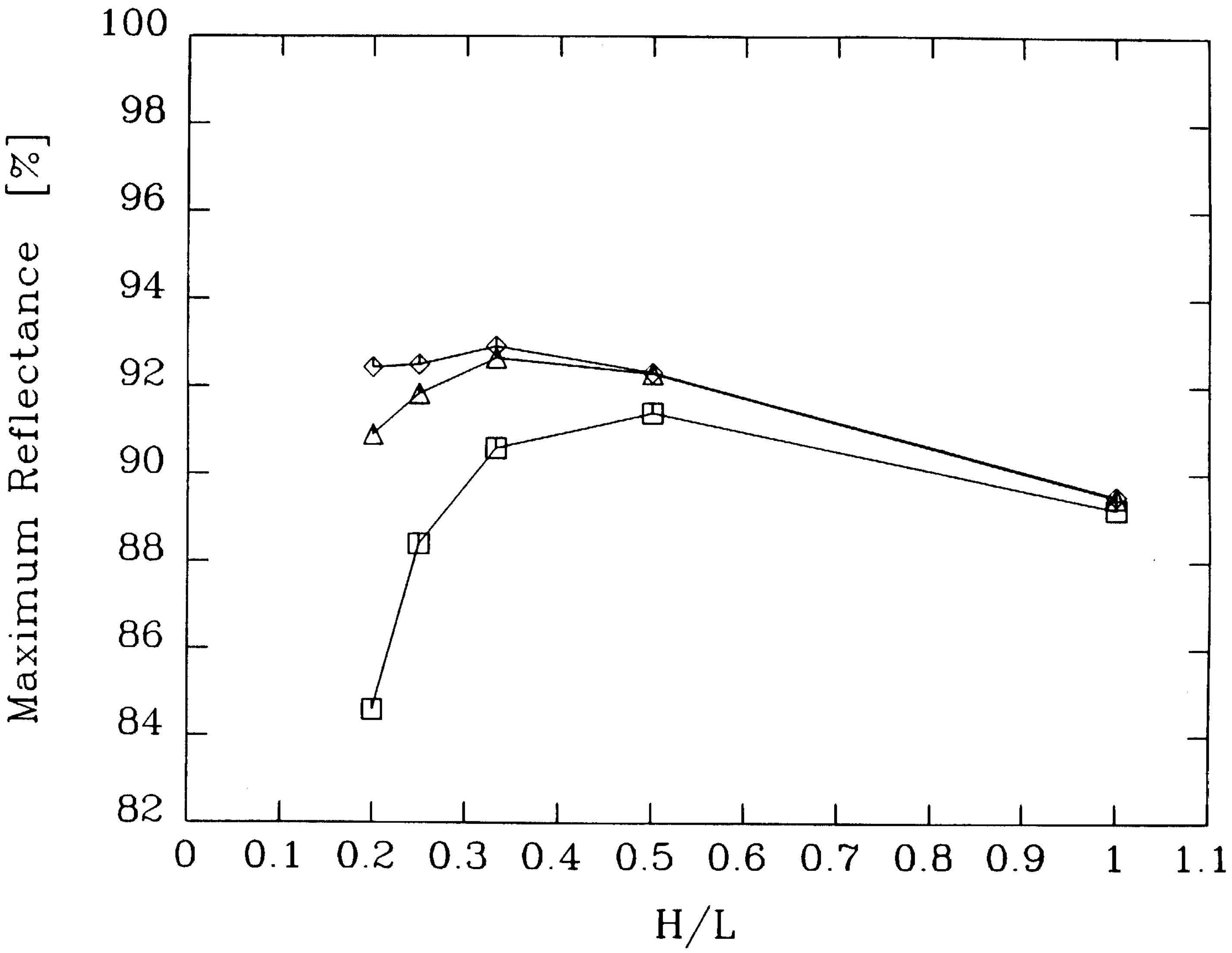

Figure 2: The maximum reflectance of the Π stack calculated for 45 degrees angle of incidence at 135.6 nm. Diamonds represent 99–layer, triangles 55–layer, and squares 35–layer stacks. H = Lanthanum Fluoride, and L = Magnesium Fluoride. The Koppelmann limit is 89.5%.

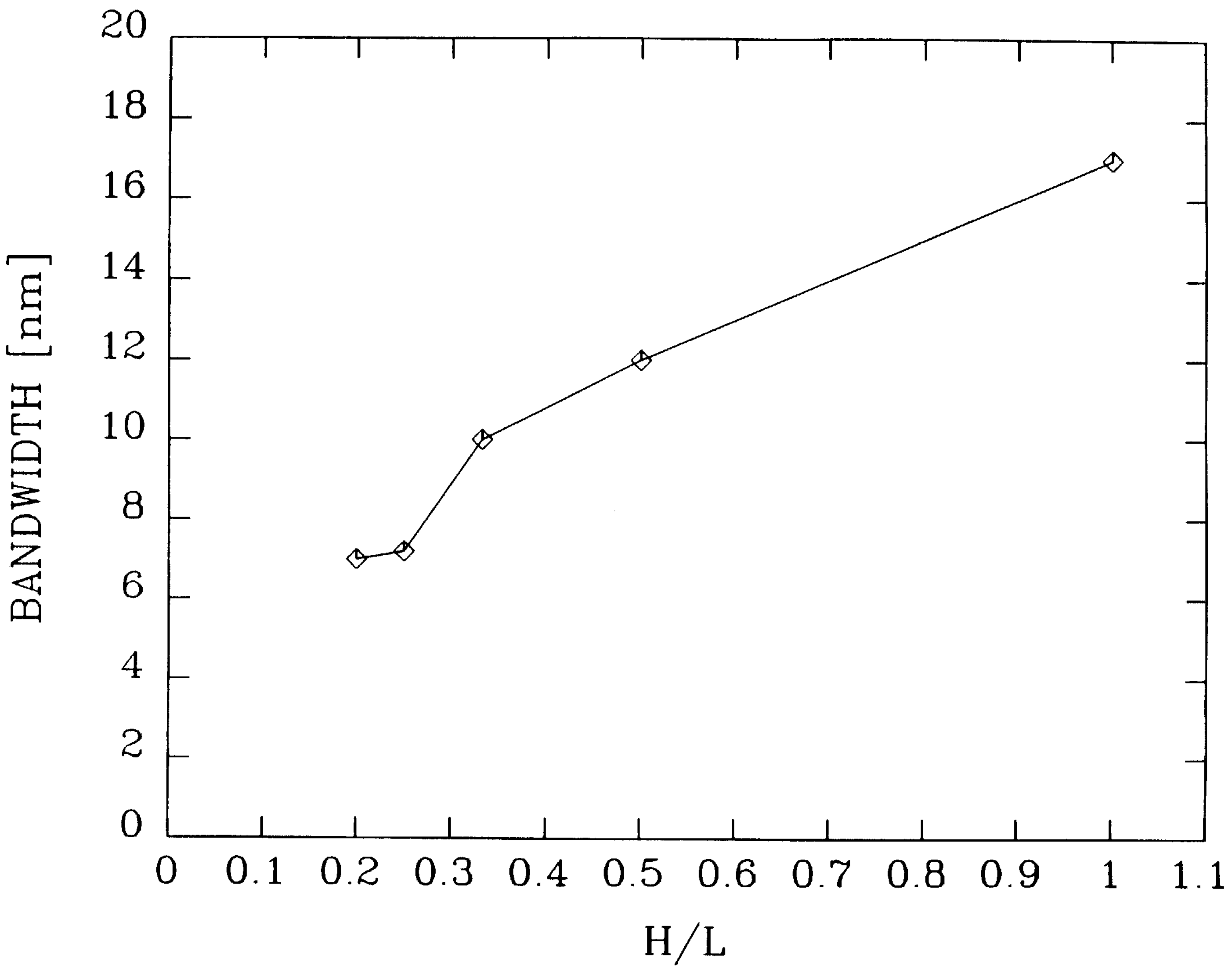

Figure 3: The full width at half of the reflectance maximum of the Π stacks calculated for 45 degrees angle of incidence. The maximum reflectance of the stacks as a function of the H/L ratio is shown in Fig. 2.

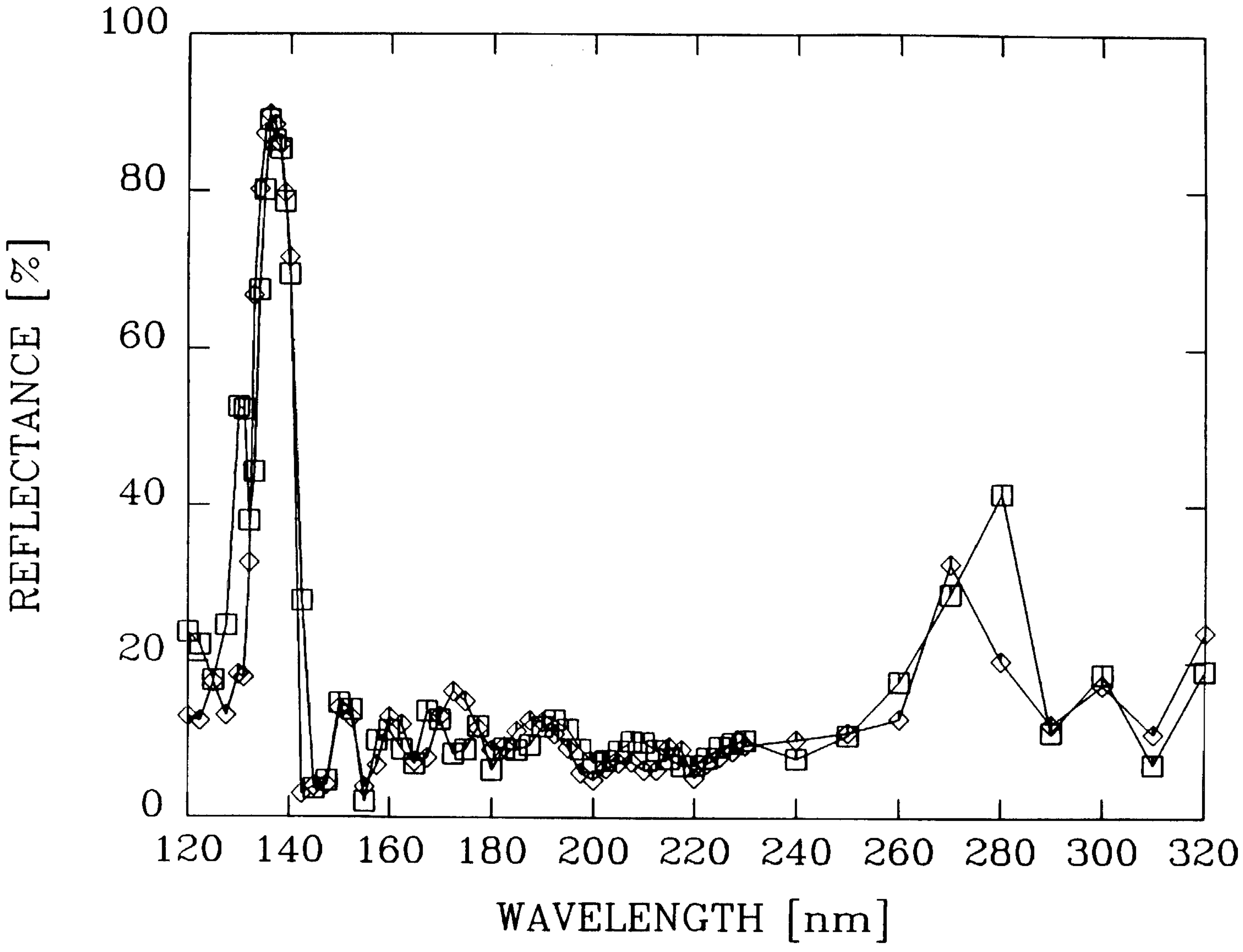

Figure 4: The measured (squares) and calculated (diamonds) reflectance of the 35−layer Π stack for 45 degrees angle of incidence centered at 135.6 nm. The optical thickness ratio H/L = 0.25 with H = Lanthanum Fluoride, and L = Magnesium Fluoride.

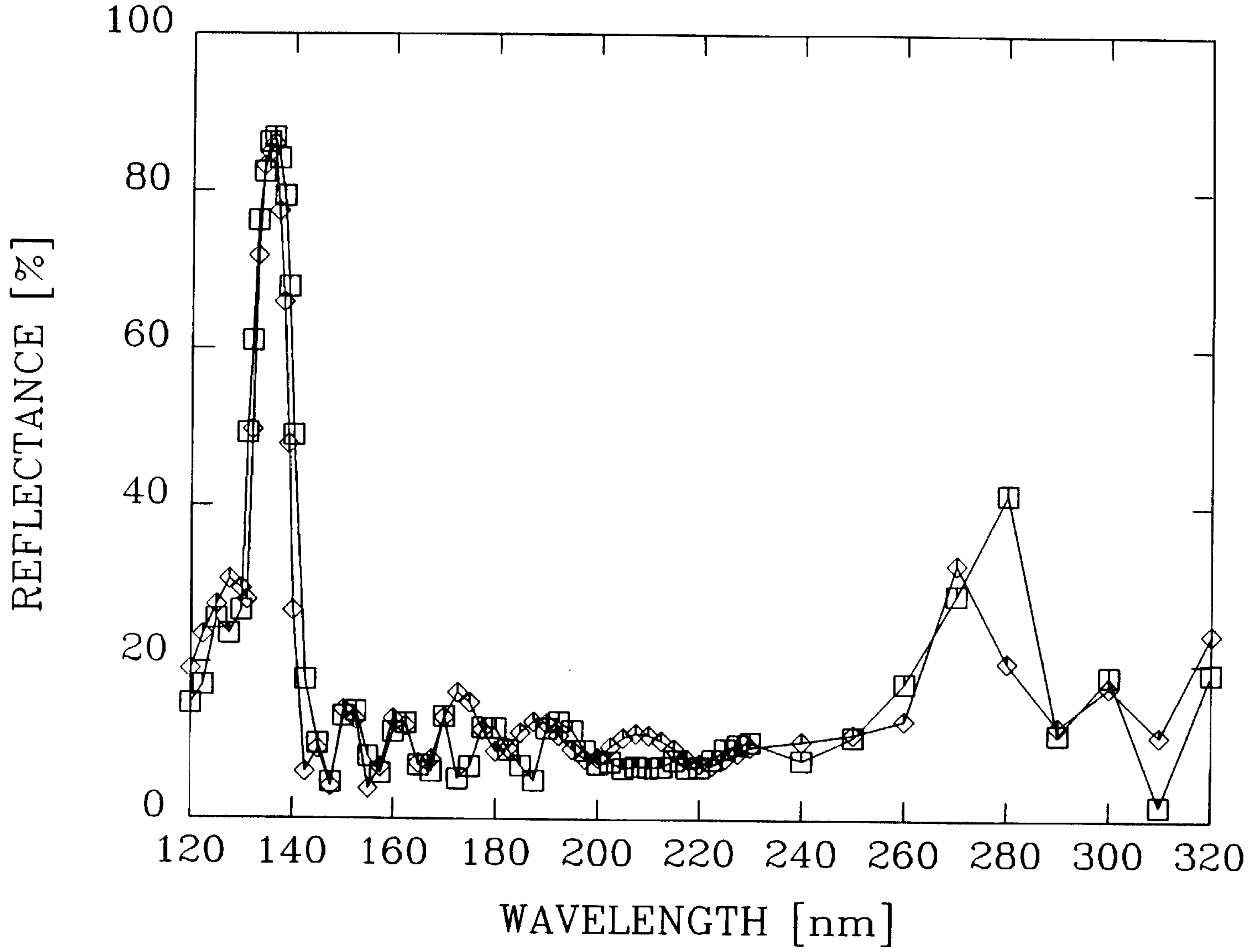

Figure 5: The measured (squares) and calculated (diamonds) reflectance of the 29-layer Π stack for 45 degrees angle of incidence centered at 135.6 nm. The optical thickness ratio H/L = 1/3 with H = Barium Fluoride, and L = Magnesium Fluoride.

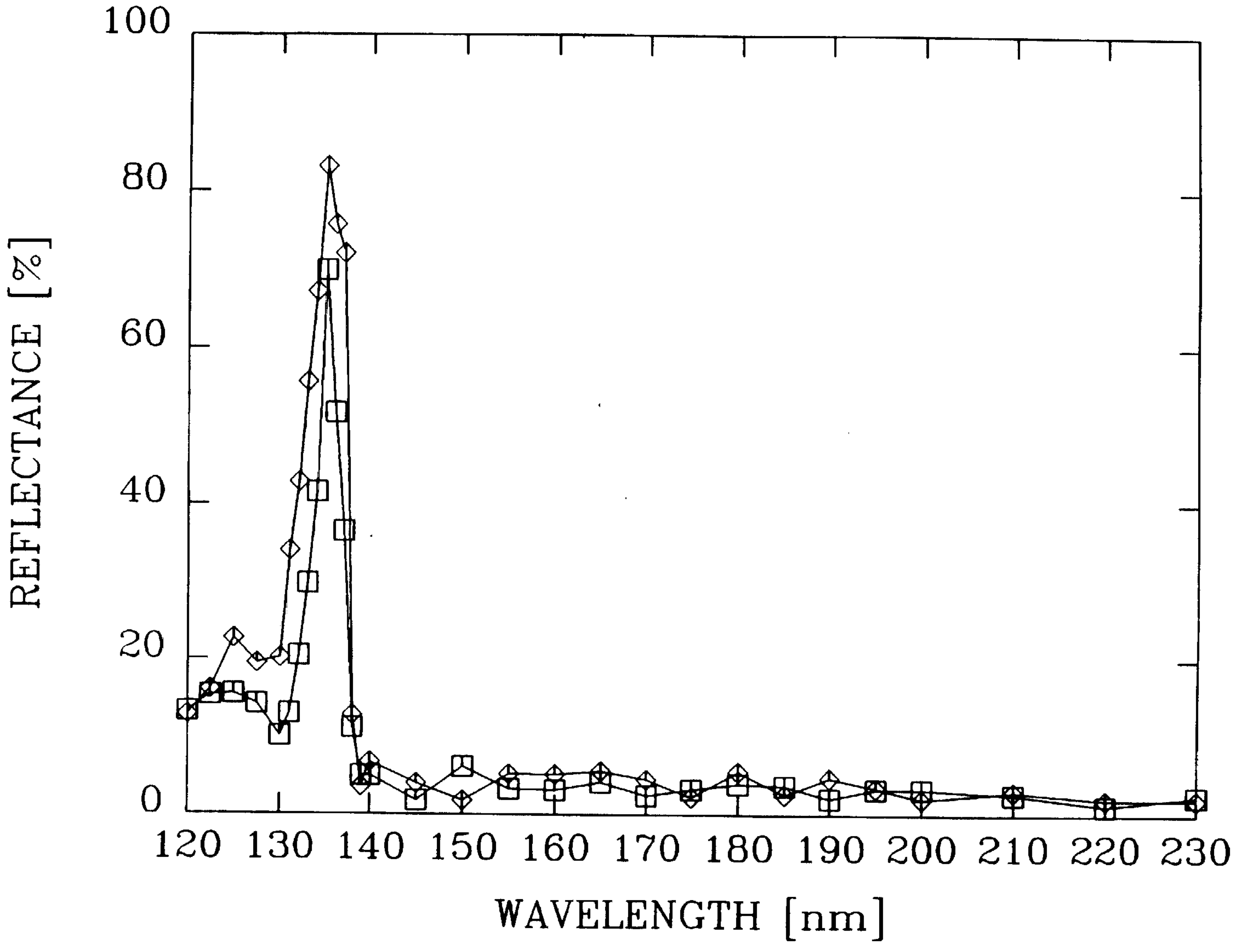

Figure 6: The maesured (squares) and calculated (diamonds) reflectance of the 35-layer second order QW stack for 45 degrees angle of incidence centered at 135.6 nm. H = Barium Fluoride and L = Magnesium Fluoride.

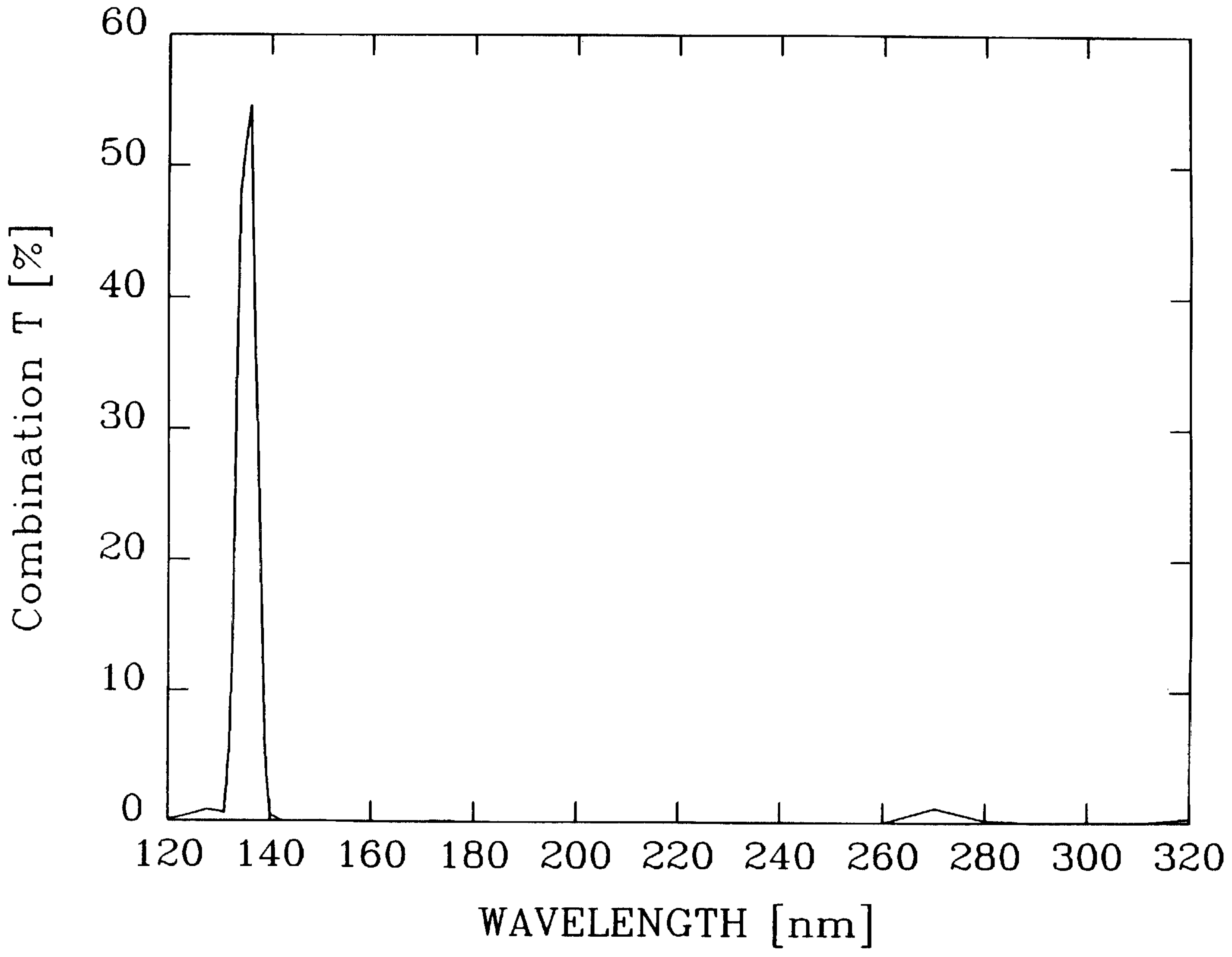

Figure 7: The transmittance of the combination of four 29−layer filters shown in Fig. 5. The bandwidth is 4.3 nm, and a peak transmittance at 135.6 nm is 53.7%.

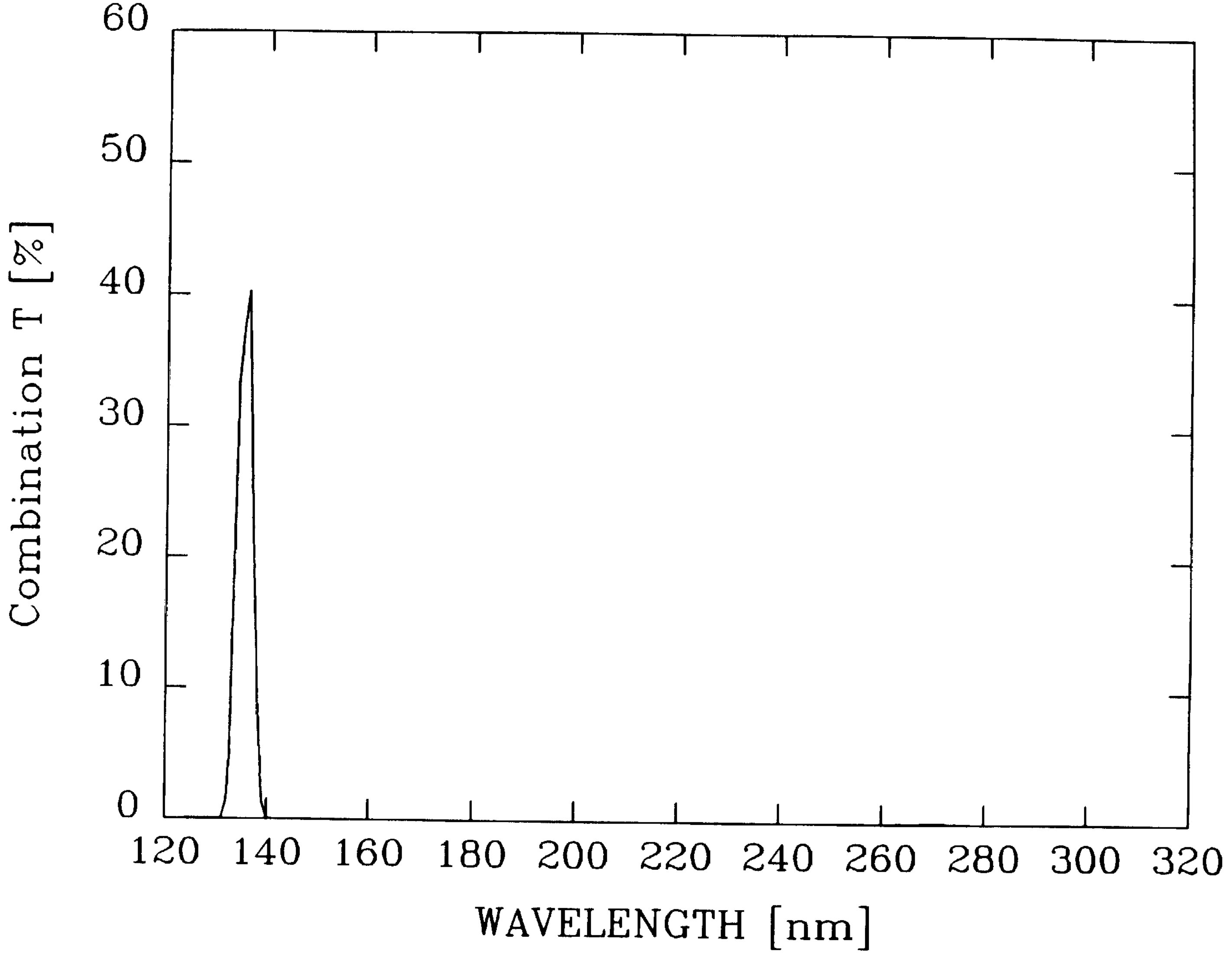

Figure 8: The transmittance of the combination of six 29–layer filters shown in Fig. 5. The bandwidth is 3.2 nm, and a peak transmittance at 135.6 nm is 39.3%.

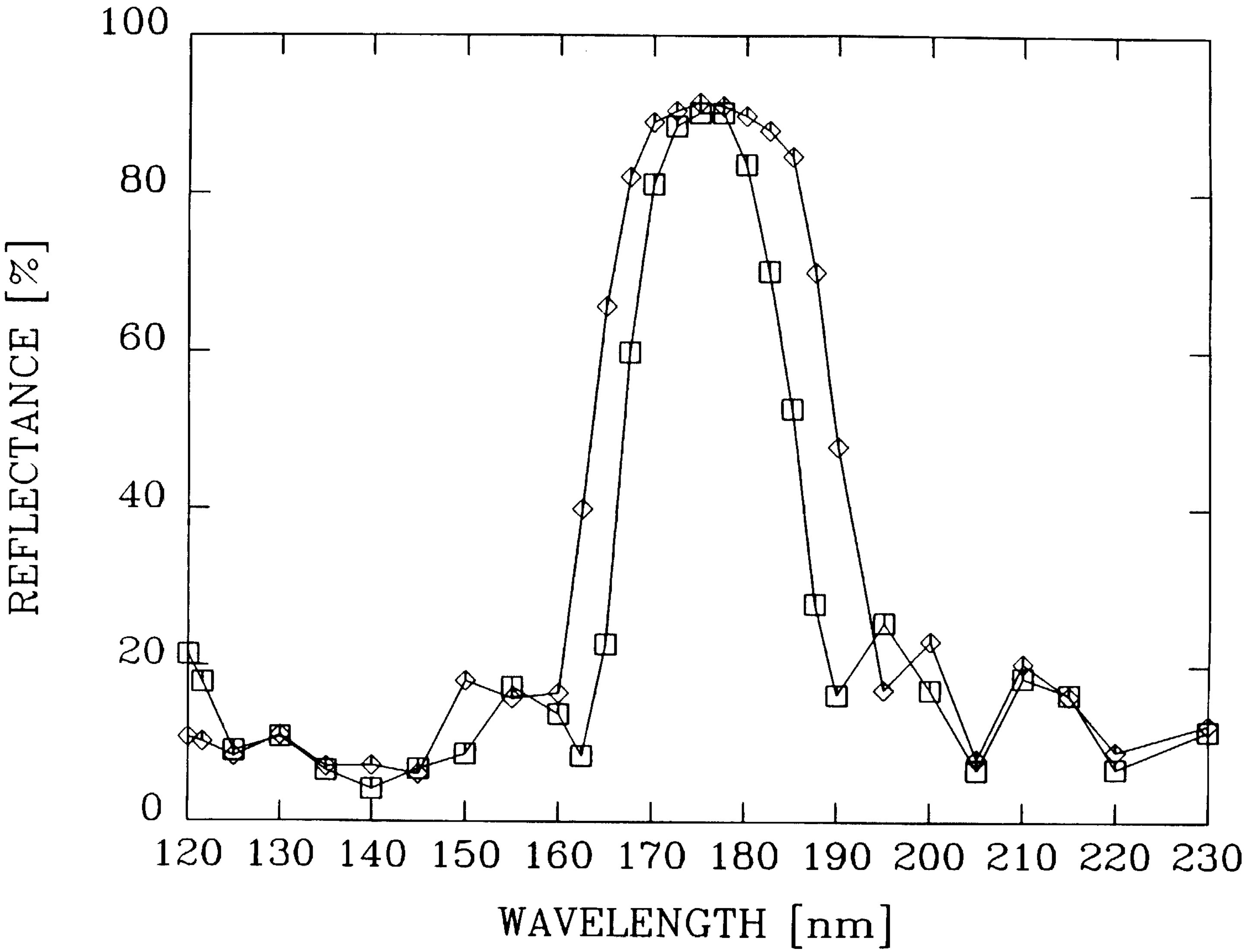

Figure 9: The measured (squares) and calculated (diamonds) reflectance of the 25-layer QW stack for 45 degrees angle of incidence centered at 175 nm. H = Lanthanum Fluoride, and L = Magnesium Fluoride.

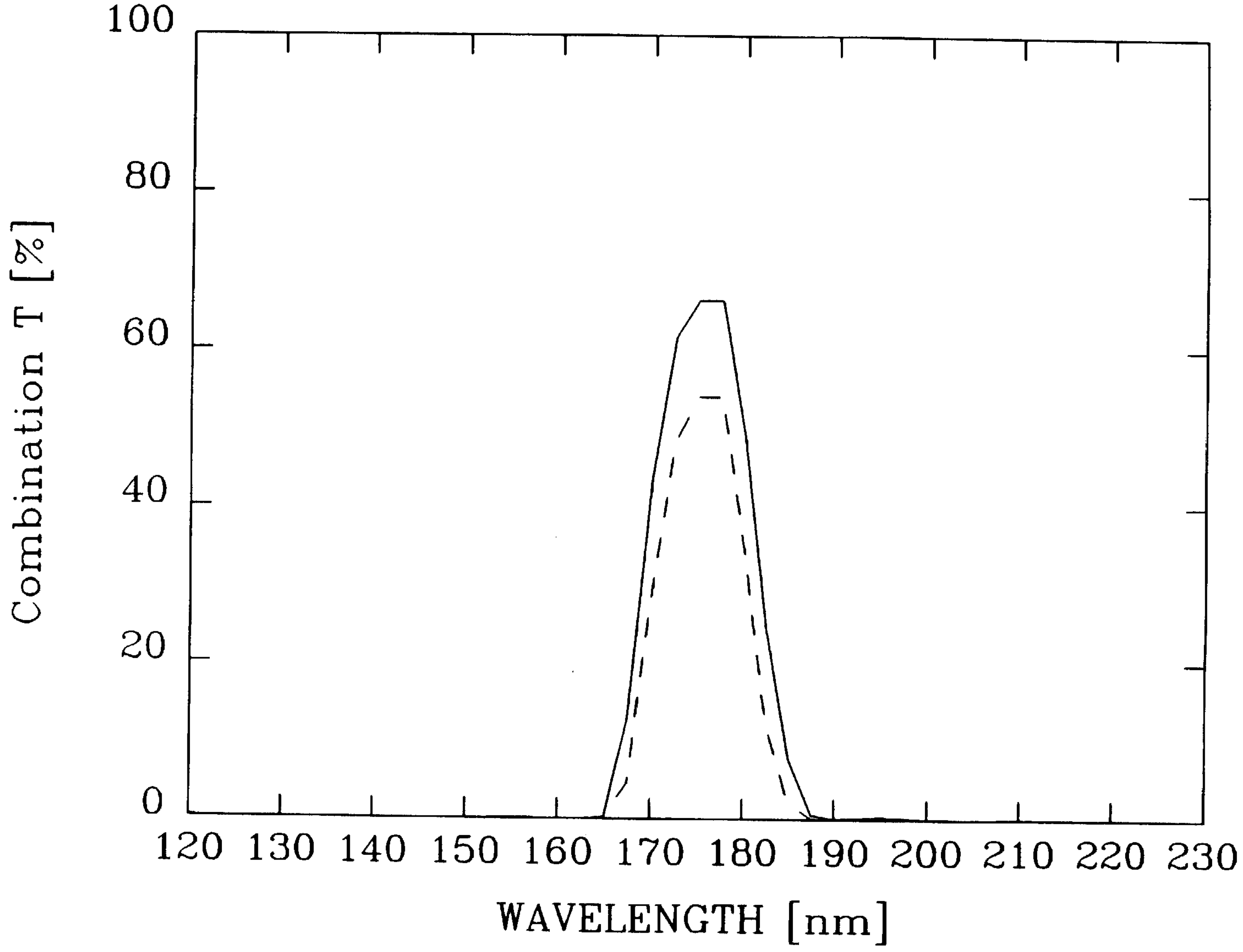

Figure 10: The transmittance of combinations of four (solid line) and six (dashed line) 25–layer QW stacks shown in Fig. 9.

APPENDIX C

High Throughput Narrowband 83.4 nm Self-Filtering Camera

Muamer Zukic and Douglas G. Torr
University of Alabama in Huntsville
Research Institute C-10
Huntsville, AL 35899
Phone: (205) 895-6238 FAX: (205) 895-6717
and
Marsha R. Torr and James F. Spann
NASA/Marshall Space Flight Center
Huntsville, AL 35812
Phone: (205) 544-7591 FAX: (205) 544-5862

Abstract

Photometric imaging of ionospheric/magnetospheric O II emission at 83.4 nm is a primary objective for imaging and tomographic mapping of magnetospheric O^+ ions. However, instrumental sensitivity has been a major barrier to realizing this goal. We report an instrumental design employing a low focal ratio (f/# less than 2) three-mirror camera where the reflecting surfaces act as both narrow-band reflection filters at 83.4 nm and as a high quality imaging system. The design includes multilayer coatings with reflectances that are relatively insensitive to the angle of incident light (0 - 50^0). The peak reflectance per mirror is more than 60% at 83.4 nm with the average reflectance for out-of-band wavelengths of less than 5%. The net reflective transmission for the three mirrors is greater than 20% with 5nm bandwidth and 10^{-2}% rejection for out-of-band wavelengths increasing to $5\text{x}10^{-4}$% at H Ly α (121.6 nm). The low focal ratio combined with high system transmission results in about 2 orders of magnitude improvement in sensitivity over previously reported designs. The camera spot size throughout the entire image plane is less than 50 μm for an 8^0 field of view, improving with smaller fields of view.

EXTREME ULTRAVIOLET IMAGER

APPLICATIONS:

- IMAGING OF IONOSPHERIC/MAGNETOSPHERIC O^+ IONS AT 83.4 NM

→ 3D PROFILES OF O^+ (AND ELECTRON DENSITY) CONCENTRATION THROUGH TOMOGRAPHIC INVERSION OF EUV EMISSIONS

- MEETS A KEY GOAL IN IONOSPHERIC/MAGNETOSPHERIC PHYSICS

OBSERVING PLATFORMS:

ROCKET BORNE AURORAL IMAGING

FREE FLYERS

LUNAR BASED

EUV IMAGER (Continued)

PERFORMANCE

HIGH THROUGHPUT AT 83.4 NM WITH NARROWBAND FILTERING WITH A FACTOR OF 100 IMPROVEMENT OVER CURRENT TECHNOLOGY

NOTE: LACK OF SENSITIVITY IN THE EUV HAS BEEN A MAJOR BARRIER IN THE PAST

DESIGN APPROACH

LOW F/# (F/# = 2) → HIGH THROUGHPUT

NEW 3-MIRROR DESIGN CONCEPT DEVELOPED BY THE CENTER FOR APPLIED OPTICS

SELF-FILTERING SYSTEM:

EMPLOYS NEW THIN FILM TECHNOLOGY

HIGHLY REFLECTIVE MIRROR COATINGS ACT AS NARROWBAND FILTERS

→ HIGH TRANSMISSION OPTICS

→ **IONOSPHERIC/MAGNETOSPHERIC IMAGING NOW BECOMES VIABLE**

HIGHLIGHTS OF PREVIOUS ACCOMPLISHMENTS (Continued)

4. ALGORITHMS FOR THE RETRIEVAL OF NEUTRAL MERIDIONAL WINDS FROM THE HEIGHT OF THE PEAK OF THE IONOSPHERIC F_2 LAYER WILL PROVIDE A DATABASE FOR

→ **GLOBAL THERMOSPHERIC DYNAMICS**

5. DESIGN AND DEVELOPMENT OF NEW HIGH PERFORMANCE FILTERS FOR THE EUV TO VISIBLE AND NEW HIGH PERFORMANCE OPTICAL DESIGNS FOR SPATIAL IMAGING

→ **FACTOR OF 10^2 IMPROVEMENT IN EUV IMAGING**
FACTOR OF 10 IMPROVEMENT IN FAR-UV IMAGING
FACTOR OF 2 IMPROVEMENT IN VISIBLE IMAGING